Links between galaxy evolution, morphology and internal physical processes

Katarina Bodova Kraljic

UNIVERSITÉ PARIS-SUD

ÉCOLE DOCTORALE 127:
ASTRONOMIE ET ASTROPHYSIQUE D'ÎLE DE FRANCE

Laboratoire: SAp, CEA Saclay

Discipline : Science de l'univers

Thèse de doctorat

par

Katarina Kraljic

Links between galaxy evolution, morphology and internal physical processes

Date de soutenance : 23/10/2014

Composition du jury :

Directeur de thèse :	Frédéric Bournaud	Dr. (CEA Saclay)
Président du jury :	François Boulanger	Dr. (Institut d'Astrophysique Spatiale)
Rapporteurs :	Avishai Dekel	Prof. Dr. (The Hebrew University of Jerusalem, Racah Institute of Physics)
	Andreas Burkert	Prof. Dr. (Faculty of Physics of the University of Munich)
Examinateurs :	Stéphane Arnouts	Dr. (Laboratoire d'Astrophysique de Marseille)
	Jérémy Blaizot	Dr. (Observatoire de Lyon)

Thanks

> *You can recognize truth by its beauty and simplicity. When you get it right, it is obvious that it is right–at least if you have any experience–because usually what happens is that more comes out than goes in. The inexperienced, the crackpots, and people like that, make guesses that are simple, but you can immediately see that they are wrong, so that does not count. Others, the inexperienced students, make guesses that are very complicated, and it sort of looks as if it is all right, but I know it is not true because the truth always turns out to be simpler than you thought.*
>
> — Richard P. Feynman, *Sympathetic Vibrations: Reflections on Physics as a Way of Life*

Frédéric

> *You can make something that somebody likes so much that they're depressed, or they're happy, on account of that damn thing you made! In science, it's sort of general and large: You don't know the individuals who have appreciated it directly.*
>
> — Richard P. Feynman, *"Surely You're Joking, Mr. Feynman!": Adventures of a Curious Character*

Florent

David

> *What is communicated can be truth or lie. Communication is a strong force, but also for either good or evil.*
>
> — Richard P. Feynman, *What do you care what other people think?*

> *It is our responsibility as scientists, knowing the great progress which comes from a satisfactory philosophy of ignorance, the great progress which is the fruit of freedom of thought, to proclaim the value of this freedom; to teach how doubt is not to be feared but welcomed and discussed; and to demand this freedom as our duty to all coming generations.*
>
> — Richard P. Feynman, *What do you care what other people think?*

Andi Burkert
&
Avishai Dekel

Alain Sarfati

> *If you're teaching a class, you can think about the elementary things that you know very well. These things are kind of fun and delightful. It doesn't do any harm to think them over again. Is there a better way to present them? Are there any new thoughts you can make about them? The elementary things are easy to think about; if you can't think of a new thought, no harm done; what you thought about it before is good enough for the class. If you do think of something new, you're rather pleased that you have a new way of looking at it.*
>
> — Richard P. Feynman, *"Surely You're Joking, Mr. Feynman!": Adventures of a Curious Character*

to all of you who care

> *So I have just one wish for you–the good luck to be somewhere where you are free [...], and where you do not feel forced by a need to maintain your position in the organization, or financial support, or so on, to lose your integrity. May you have that freedom.*
>
> — Richard P. Feynman, *"Surely You're Joking, Mr. Feynman!": Adventures of a Curious Character*

RPF Thank you.

Thank you
Merci
Grazie
Alain Andi Anita Anna Aurélie Avishai Corentin Daizhong Damien David Emanuele Emeric Florent Francesco François Frédéric Hervé Hervé Jared Jérémy Koryo Marie Marie Mark Maurilio Min Orianne Paniez Pierre-Alain Pierre-Emmanuel Qinghua Qingli Roger Rory Sarah Stéphanie Suzanne Tao Tatyana Taysun Veronica Xinwen Yu-Yen

Hvala
Bakoosh Birg Mooshoo

Ďakujem
Mamka Ocko Tonička Franz Soňa Žeže

Mojim láskam
Stellka & Darko

Abstract

This thesis aims at making the link between galaxy evolution, morphology and internal physical processes, namely star formation as the outcome of the turbulent multiphase interstellar medium, using the cosmological zoom-in simulations, simulations of isolated and merging galaxies, and the analytic model of star formation.

In Chapter 1, I explain the motivation for this thesis and briefly review the necessary background related to galaxy formation and modeling with the use of numerical simulations.

I first explore the evolution of the morphology of Milky-Way-mass galaxies in a suite of zoom-in cosmological simulations through the analysis of bars. I analyze the evolution of the fraction of bars with redshift, its dependence on the stellar mass and accretion history of individual galaxies. I show in particular, that the fraction of bars declines with increasing redshift, in agreement with the observations. This work also shows that the obtained results suggest that the bar formation epoch corresponds to the transition between an early "violent" phase of spiral galaxies formation at $z > 1$, during which they are often disturbed by major mergers or multiple minor mergers as well as violent disk instabilities, and a late "secular" phase at $z < 1$, when the final morphology is generally stabilized to a disk-dominated structure. This analysis is presented in Chapter 2.

Because such cosmological simulations form too many stars too early compared to observed galaxy populations, I shift the focus in Chapter 3 to star formation in a sample of low-redshift galaxy simulations in isolation at parsec and sub-parsec resolution. I study the physical origin of their star formation relations and breaks and show that the surface density threshold for efficient star formation can be related to the typical density for the onset of supersonic turbulence. This result holds in merging galaxies as well, where increased compressive turbulence triggered by compressive tides during the interaction drives the merger to the regime of starbursts.

An idealized analytic model for star formation relating the surface density of gas and star formation rate as a function of the presence of supersonic turbulence and the associated structure of the ISM is then presented in Chapter 4. This model predicts a break at low surface densities that is followed by a power-law regime at high densities in different systems in agreement with star formation relations of observed and simulated galaxies.

The last part of this thesis is dedicated to the alternative cosmological zoom-in technique (Martig et al., 2009) and its implementation in the Adaptive Mesh Refinement code RAMSES. In Chapter 5, I will present the basic features of this technique as well as some of our very first results in the context of smooth cosmological accretion.

Contents

List of Figures

List of Tables

Chapter 1

Motivation

> *The physicists should be ashamed of themselves: astronomers keep asking, "Why don't you figure out for us what will happen if you have a big mass of junk pulled together by gravity and spinning? Can you understand the shape of nebulae?" And nobody ever answers them.*
>
> — Richard P. Feynman, *Tips on physics*

1.1 From Great Debate to Cosmic Zoo

26 April 1920, Smithonian Museum of Natural History in Washington, D.C., two astronomers, Harlow Shapley and Heber D. Curtis, give lectures that will become known as the "Great debate". Among others, the issue of the existence of separate, external galaxies to our Galaxy, Milky Way, is discussed. Shapley supports the generally believed idea at that time, that Milky Way makes up the entire Universe. The result of the debate being inconclusive, the astronomical community has to wait for final answer. In 1925 Edwin Hubble publishes distance measurements (initial one on the discovery of Cepheids in NGC 6822, Hubble, 1925) that destroy the Shapley's Universe and start a whole new adventure for astronomy: the Universe is much larger than our Galaxy and plenty of other galaxies – "island universes" – are located beyond its boundaries. Henceforth, the Universe is understood as a collection of innumerable galaxies spread out in space, farther than the largest telescope could see. Hubble would later be credited with having discovered[1], based also on measurements of V. Slipher (Slipher, 1917), that the Universe is not static (Hubble, 1929, Hubble & Humason, 1931), as was then commonly believed, but expands.

[1] Not only Hubble never really gave an interpretation and the cosmological significance of the empirical determination of the slope in the distance-radial velocity diagram (Kragh & Smith, 2003), but he was certainly not the first to plot such data. Georges Lemaître computed an expansion rate based on observation data in 1927 (Lemaître, 1927), two years before Hubble published the work thanks to which the names "Hubble constant" and "Hubble diagram" would become firmly established.

The Universe was first "made" infinite in space by Hubble, to "become" finite in time soon after thanks to ~~Hubble~~ Lemaître. A completely new era of astrophysics has started.

The discovery of the existence of other galaxies and variety of their morphologies raised many questions. What is the origin of these galaxies? And once formed, how do they evolve? In spite of missing answers to all these questions, galaxies were immediately recognized as important fundamental building blocks of the Universe. One of the first steps towards a coherent theory of galaxy evolution was a classification scheme of galaxies, today known as the Hubble tuning fork, developed by Hubble (Hubble, 1926, 1936), heavily inspired by J. H. Reynolds[2] and Sir James Jeans. Although considered somewhat too simple, the basic ideas of this scheme still hold. Its modern version, as seen by the Hubble Space Telescope in today's Universe, is shown in Figure 1.1. This diagram separates galaxies according to their morphology into ellipticals, lenticular galaxies and spirals which are sub-divided further in function of a presence of a bar into normal and barred spiral.

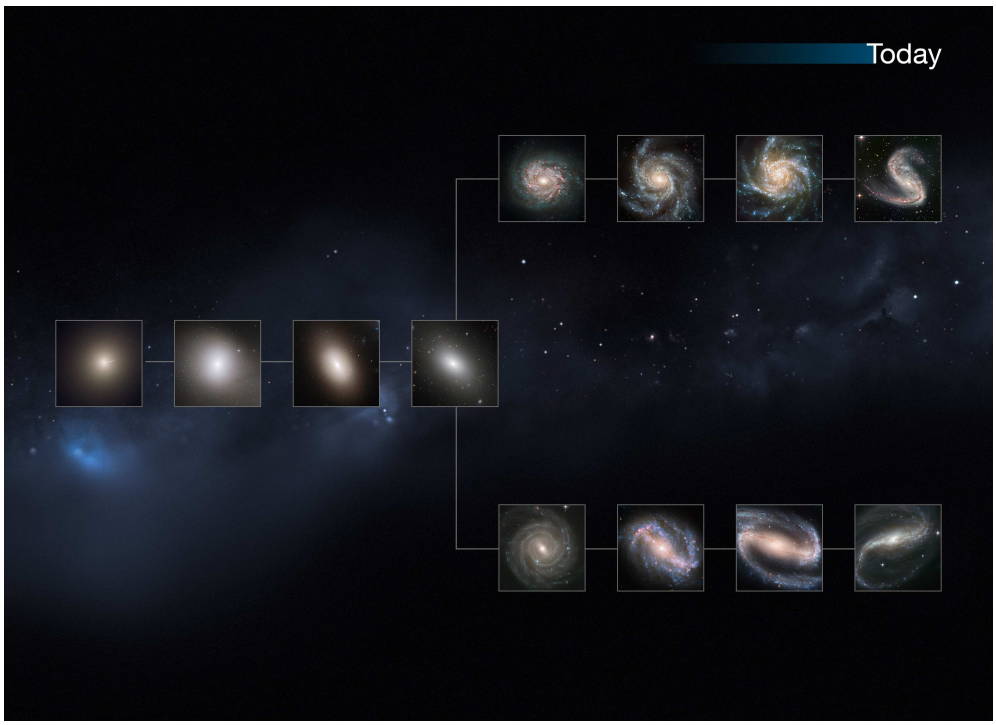

Figure 1.1

Hubble sequence as seen by Hubble Space Telescope in today's Universe. Based on their morphology, galaxies are divided into three main classes: ellipticals (left), lenticular galaxies (middle) and spirals (right). Spiral galaxies are further divided into two sub-classes: normal (top) and barred spirals (bottom). (Credit: NASA, ESA, M. Kornmesser)

ellipticals

Elliptical galaxies are ellipsoidal systems mainly supported by the random motions of their stars. They have no spiral arms and often no obvious galactic disk. Apart from a dense central nucleus, they often exhibit little internal structure of any kind. Most ellipticals contain little or no gas and

[2] John Henry Reynolds (1874 - 1949), British amateur astronomer came up with a galaxy classification scheme in 1920 (Reynolds, 1920), but there is no reference to this work in Hubble's paper published 6 years later. Apparently, "Hubble had a very selective methodology for not referencing earlier scientists who may have presented the original ideas." (Block, 2012)

dust and display no evidence of young stars or ongoing star formation. They are made up mostly of old, low-mass stars with disordered orbits, exhibiting little or no overall rotation.

spirals

Spiral galaxies have highly flattened disks with a spiral arm structure and a central concentration of stars known as the bulge. The flat galactic disks of typical spiral galaxies are rich in gas and dust. They are mainly supported by rotation and exhibit active star formation. Stars form within the spiral arms, while the bulges contain large numbers of old stars. Spiral galaxies are divided into two subclasses, normal and barred spirals, according to whether or not a recognizable bar-like feature is present in the central part of the galaxy. Arms of the normal spiral galaxy emerge from the periphery of the nuclear region, while in barred spirals, arms spring from the extremities of the bar.

lenticulars

Lenticular galaxies represent an intermediate type: they have a bright bulge similar to elliptical galaxies, while they maintain some disk-like structure, but without spiral arms. They have no star forming regions visible, and their light comes almost entirely from old stars. Like spirals, they are sub-divided into two categories, depending on whether or not they show a bar.

Somehow for historical reasons, galaxies at the left of the diagram (elliptical and lenticular) are labeled "early" and those on the right (spiral) "late"-type galaxies.[3]

irregulars

In addition, Hubble found that about 3% of galaxies he examined didn't fit into any of previously described categories due to the clear lack of the dominant nuclei and rotational symmetry. He named them irregular galaxies because their visual appearance did not allow placing them in the context of the tuning fork diagram. Today we know that Hubble missed much more than that. His morphological classification ignores faint dwarf galaxies the detection of which is difficult outside the Local Group and which probably make up a large fraction of the galaxies in the Universe. Dwarf galaxies with significant gas content and ongoing star formation often have very irregular structures, that is why they are called (dwarf) irregulars. On the other hand, dwarfs without gas and with no young stars are typically diffuse. They are called dwarf spheroidals. Finally, brighter galaxies often showing highly distorted or filamentary structure without any resemblance of disk nor ellipsoidal component are called peculiar galaxies. Their appearance suggests that in some cases they represent the result of a close encounter or collision between galaxies.

peculiar galaxies

Since Hubble, various extensions to his original classification have been proposed. While some mainly refine the existing categories reflecting finer details of galaxy substructures (e.g. de Vaucouleurs, 1959, van den Bergh, 1960, Sandage, 1961, de Vaucouleurs, 1974), other propose a more radical revision of galaxy classification based on the kinematic rather than on the apparent morphological aspects (ATLAS^{3D}, Cappellari et al., 2011). However, the notions of spheroid and disk as two principal galaxy components, formation processes of which need to be understood, are still present.

The importance of the Hubble classification lies in the fact that morphology is not the only property of galaxies that varies along the sequence. As we move from left to right, the total galaxy stellar mass decreases: elliptical galaxies are on average more massive than spirals. On the other hand, the star formation increases from left to right. Stars form in a variety of masses. The most massive stars are very bright and hot, which makes them look blue or white. Being very massive, they live for short time during which they can outshine everything else and thus give a galaxy its bluish color. When these massive blue stars die and no new stars are formed for a while, galaxy is left with less massive, cooler, red stars which will make it look red. Thus elliptical galaxies are on average redder than spirals.

The main difficulty in studying galaxy formation and evolution is that observing the evolution of individual galaxies is simply impossible due to the long typical timescales involved, which are much

[3] It was Edwin Hubble who used this terminology, but contrarily to what is thought, he didn't attempt to imply an evolutionary sequence.

longer than that of a human being. But what human beings can do[4], is to look at galaxies at larger distances which is equivalent to looking at galaxies when the Universe was younger. Although we cannot suppose that galaxies seen at different epochs correspond directly to consequent evolutionary stages of the same kind of galaxy observed today, we can try to understand the relation between galaxies at different redshifts[5] by comparing their properties in a statistical sense.

Hubble inferred the morphological sequence by examining more than thousand of galaxies. Today, modern large surveys (e.g. CANDELS, SDSS) provide us with images and spectras of hundreds of thousands of galaxies at different epochs. Distant galaxies show many more peculiar shapes and more perturbed morphologies compared to local galaxies, but interestingly enough, the classification system still applies.

Delgado-Serrano et al. (2010) found that the Hubble sequence 6 billion years years ago (corresponding to redshift ~ 0.65) was different from the one we see today. In the current, local, Universe, about 72% of galaxies are spirals, 15% lenticular, 3% elliptical and 10% have peculiar morphologies. Distant galaxies (6 billion years ago) have much larger fraction of peculiar galaxies, 52%. 4% were elliptical, 13% lenticular and 31% spiral. Thus early-type galaxies (elliptical and lenticular) do not seem to show the evidence of number evolution during the past 6 billion years, while the fraction of peculiar and spiral galaxies show a strong evolution. Almost all evolution seems to be caused by the transformation of peculiar galaxies in the past Hubble sequence into regular spirals in the present-day Hubble sequence.

Lee et al. (2013) explored morphologies of galaxies at even earlier times, when Universe was only 3 billion years old. They found quantitative and qualitative similarity between relatively massive galaxies at this epoch (redshift ~ 2, 11 billion years ago) and their present-day counterparts. They interpret these findings as evidence that the Hubble sequence, as observed today, was already in place.

1.2 Galaxy formation & evolution in a nutshell

It was more than 30 years ago that the prevailing paradigm for galaxy formation was set forth by White & Rees (1978) and Fall & Efstathiou (1980). Meanwhile, the original ideas about formation process of galaxies have been shaped and revised, new ones emerged to modify the existing picture or to revolutionize our understanding of the formation and evolution of structures in the Universe we live in (e.g. Kereš et al., 2005, Dekel & Birnboim, 2006, Dekel et al., 2009, on the accretion of gas). The main purpose of the following Section, partly inspired by text book Mo et al. (2010), is to give a phenomenological and very synthetic overview of some basic processes that are believed to play a role in the galaxy formation and evolution. Their schematic view is represented in Figure 1.3.

cosmology

Every successful theory of galaxy formation and evolution has to fit within the framework of large scales in spacetime, cosmology. Standard cosmological model, based on the theory of General Relativity and the assumption of the spatial homogeneity and isotropy of the Universe, does not itself make formation of structures possible, deviation from perfect uniformity is needed. Quantum fluctuations in the nearly uniformly distributed matter at early times of the history of the Universe

[4] And not only they can, but they do look at galaxies, somehow by definition - "man can be probably classified as *Homo sapiens* since the moment he consciously looked up to the sky" (Jiří Grygar, Czech astronomer, 1936) and because they have a reputation to uphold - "man is different from pig because the former would occasionally look at the stars" (Victor Ambartsumyan, Armenian scientist and astronomer, 1908 -1996).

[5] Because the Universe is expanding, redshift is related to the distance: farther away the object is, larger its receding velocity is, thus larger its redshift is.

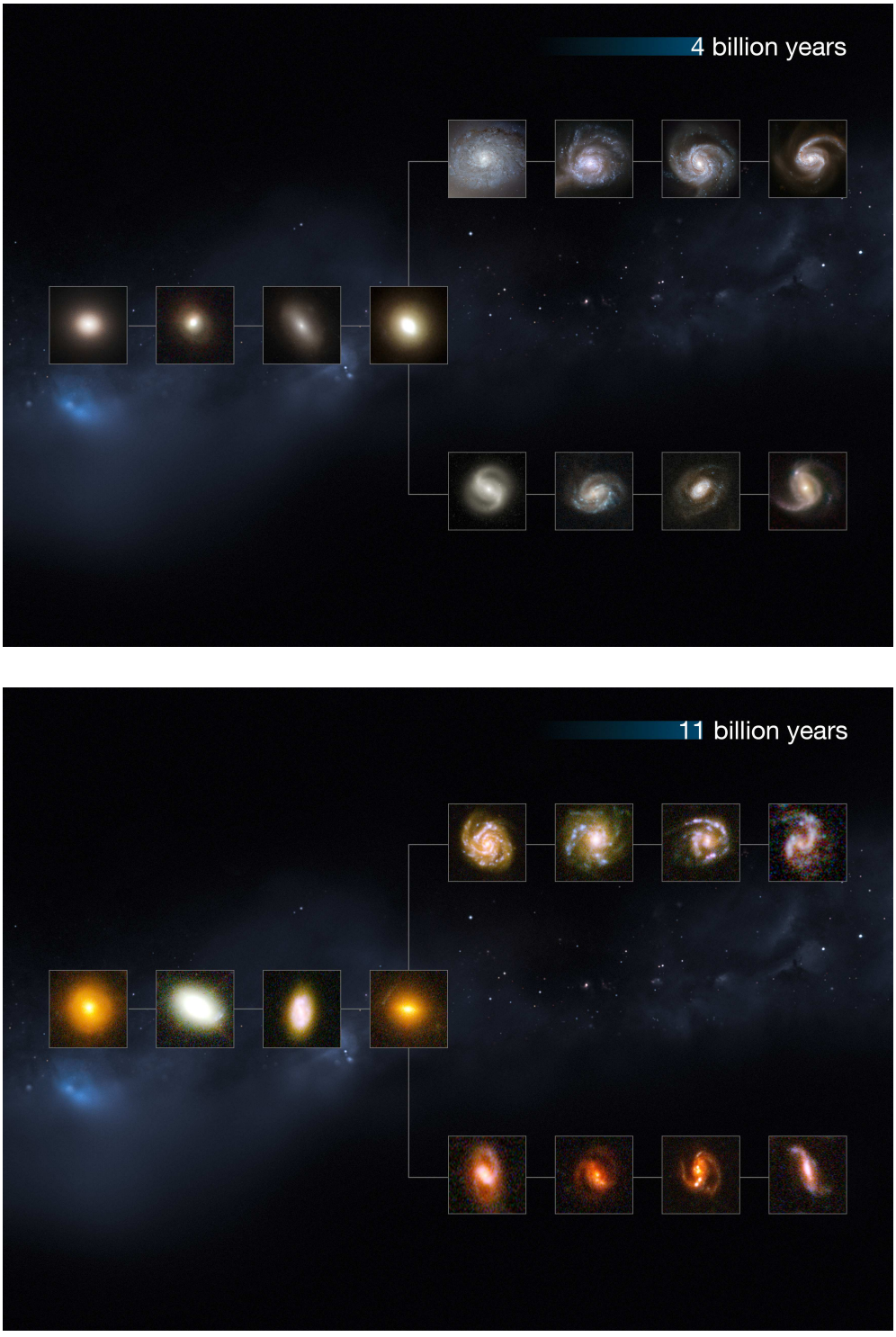

Figure 1.2

Hubble sequence, as seen by Hubble Space Telescope, 4 and 11 billion years ago. This image is illustrative: the individual distances to these galaxies are only approximate. (Credit: NASA, ESA, M. Kornmesser)

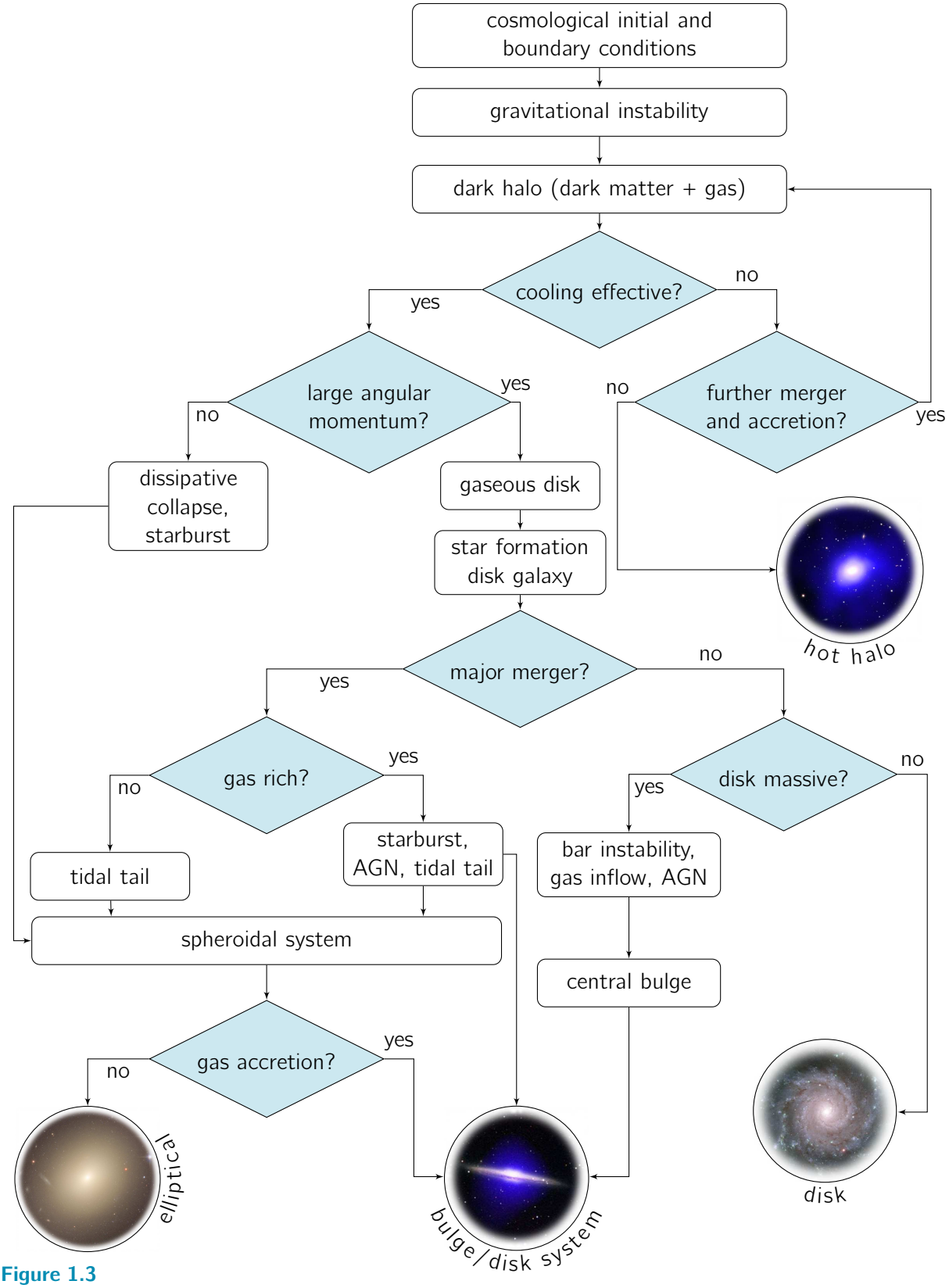

Figure 1.3

Logic flow chart depicting physical processes that are believed to play a role during the formation and evolution of galaxies. Adapted from Mo et al. (2010). Image credit: (bulge/disk) X-ray: NASA/CXC/U. Copenhagen/K.Pedersen, Optical: Palomar DSS; (elliptical): NASA, ESA, and The Hubble Heritage Team (STScI/AURA); (disk) ESO/PESSTO/S. Smartt; (hot halo) CLoGS project.

are believed to be the seeds of the structures we observe today.

gravity

These tiny perturbations in the density field can grow by gravitational interactions. On one hand, regions with density higher than the background increase their density by attracting material from surroundings generating thus over-dense regions. On the other hand, regions whose initial density is lower that the average one, become under-dense by loosing matter. In the initial phase of the structure growth, over-dense regions increase their size due to the overall expansion of the Universe. The perturbations evolve in what is called linear regime. Once these perturbations become big enough, they decouple from the expansion and can collapse – they enter so called non-linear regime.

dark halo

Let us consider a matter that is collisionless, with no, or only weak interactions, evolving solely under the effect of gravity. It will eventually collapse and relax to a quasi-equilibrium state. Such matter exists in the Universe and it is called dark matter. It turns out that 85% of all matter in the Universe is of this kind. Remaining 15% is much less exotic, it is ordinary "baryonic" matter[6]. This matter is collisional: on top of gravity, strong shocks leading to the increase of the temperature can be created during the collapse. Such system can reach hydrostatic equilibrium if self-gravity and pressure gradients are balanced. The outcome of the non-linear gravitational collapse of matter composed of (cold[7]) dark and baryonic matter is what we call dark matter halo with gas shock-heated to virial temperature that may settle into hydrostatic equilibrium in the potential well of the dark matter halo.

hot halo

cooling

Further fate of this object depends on the ability of the gas to cool. Cooling is one of the most important physical processes involved in formation of galaxies. The cooling rate is determined by the density of the gas, its temperature and chemical composition. Details of individual cooling processes are quite complicated. However, the net effect of effective cooling is a loss of pressure support that allows the flow and accumulation of the gas in the center of the dark matter halo, in a protogalaxy. Four main channels through which gas can cool can be distinguished: ① in massive halos with the virial temperature $T_v \gtrsim 10^7$ K, where gas is almost completely ionized, cooling is dominated by emission due to electron-ion interactions (free-free emission, also called Bremsstrahlung); ② in the temperature range $10^4\mathrm{K} < T_v < 10^7\mathrm{K}$, atoms, excited by collisions, decay radiatively to the ground state and/or electrons can recombine with ions while emitting a photon; ③ in haloes with $T_v < 10^4$ K, gas is usually neutral and if heavy elements and/or molecules are present, cooling takes place through deexcitation of the fine and hyperfine structure lines in the former and of rotational or vibrational energy levels in the latter case; ④ at high redshifts ($z \gtrsim 6$), charged particles can transfer part of their energy to cosmic microwave background photons in so-called Compton inverse scattering.

angular momentum

An important ingredient playing a role in determining the outcome of the collapse at this stage is the angular momentum. Dark matter and baryonic material have some amount of angular momentum prior to collapse. If gas keeps sufficient amount of angular momentum during cooling, it spins up

[6] In terms of the mass-energy budget of the Universe, ordinary baryonic matter makes up only 4%, the remaining 96% is dubbed "dark" (e.g. Planck collaboration 2013), reflecting our inability to detect and identify it directly. Within the dark sector, 74% is made of dark energy and remaining 22% of dark matter. Very little is known about the nature and origin of both dark matter and dark energy. The archetype of dark matter is WIMP (Weakly Interacting Massive Particle), a non-baryonic massive particle with little interaction with baryonic matter. Such a particle however doesn't exist in the Particle Physics standard model and thus requires new physics. Moreover, dedicated experiments for both direct and indirect detection have not been successful so far to find evidence of such particles. The situation is even more unclear in the case of dark energy, the unknown from of energy "blamed" for triggering accelerated expansion of the Universe. The observational data is consistent with a cosmological constant Λ, the quantum field theory vacuum. However, the profound nature of dark energy remains mysterious and other explanations such as modified gravity or back-reaction are not ruled out.

[7] dubbed cold because typical velocities of the particles making up this matter at the time of decoupling were non-relativistic

disk formation

while it flows inward and it settles in a cold disk in centrifugal equilibrium at the center of the halo. In this way, the qualitative understanding of the formation of disk galaxies can be obtained.

star formation

Once gas becomes sufficiently dense and is able to cool efficiently, self-gravity can lead to a runaway collapse during which the fragmentation may result into conversion of high-density cold gas into stars. Observations suggest a bimodality in star formation: there seems to be a quiescent mode, typical for disk galaxies and a starburst mode. The latter is characterized by higher star formation rate, defined as the mass of the stars that are formed per year, at fixed mass of gas compared to disks, and is believed to be triggered by galaxy interactions and mergers. Independently of the operating mode, star formation is considered to be among the most important processes affecting the formation and evolution of galaxies.

feedback

During their evolution, stars inject energy, momentum, mass and metals back to the interstellar and if strong enough even the intergalactic medium through different feedback processes. Stellar feedback thus plays an important role in galaxy formation by regulating star formation (e.g. Mac Low & Klessen, 2004), driving interstellar turbulence (e.g. Kim et al., 2001, Joung & Mac Low, 2006, Agertz et al., 2009a, Tamburro et al., 2009) and offering a viable mechanism to generate galactic scale outflows (e.g. Martin, 2005, Oppenheimer & Davé, 2006).

Shortly after their birth, stars emit photons that can ionize the surrounding medium. Young massive stars emit mainly energetic ultraviolet (UV) photons capable of ionizing the cold neutral gas, heating it up to temperatures of about 10^4 K and creating thus the hot ionized bubbles, the HII regions. This process of photoionization modifies the structure and the dynamics of the gas mainly at small, but potentially on galactic scales too.

At early times ($\lesssim$ 4 Myr), gas surrounding stars also receives a momentum flux through dust grains (Murray et al., 2005, 2010). The initial UV or optical photons can be absorbed, then re-emitted in the infrared (IR) flux and undergo multiple scattering, if the region between star and gas is optically thick in the IR, which further enhance the bulk of the momentum supplied by radiation pressure and absorbed by the gas[8].

Stellar winds driven by massive stars ($\gtrsim$ 5 $M_\odot$) is another feedback process that operates immediately after birth of star (Lamers & Cassinelli, 1999). More massive stars ($8 - 40$ $M_\odot$) undergo core-collapse and explode in the form of supernovae (SN) type II at later stages of their evolution ($\gtrsim$ 3 Myr, but mostly around 10 Myr). In addition to type II, SNe of type Ia can occur in binary systems in which one of the stars is a carbon-oxygen white dwarf that accretes mass from its companion and explodes as a supernova. Feedback from SNe represent important source of stellar feedback as it can substantially modify the ability of the gas to form stars. Radiation from SN explosions together with the kinetic energy of the expanding shell transfer energy to the gas which consequently heats up. The amount of gas that can cool efficiently thus decreases which in turn reduces the process of star formation itself.

In addition to stellar feedback, radiation from active galactic nucleus (AGN) powered by accretion of mass onto a supermassive black hole is believed to contribute to the overall feedback budget.

Galaxies and dark matter haloes do not evolve in isolation. Instead, they represent open systems that interact with surrounding environment. Besides outflows driven by various feedback processes, galaxies can accrete baryonic and dark matter from the intergalactic medium through inflows and they can evolve by interacting and merging with other dark matter haloes and galaxies. Indeed, in the cold dark matter scenario, structures form in hierarchical way in so-called "bottom-up" scenario in which structures of lower mass form first. The formation of structures of increasingly higher mass happens

[8] Sufficient opacity to IR radiation is needed so that the available energy is absorbed by the gas rather than radiated away.

only later, by the merging of lower-mass entities, leading to a Universe composed of cosmic voids, sheets and filaments. According to this model, massive galaxies are expected to form by mergers of smaller ones. The outcome of a merger depends on several parameters, e.g. the relative velocity of involved galaxies, their angular momenta, their mass ratio or the impact parameter. If merging galaxies have very different masses, we talk about "minor merger". In such case, the properties of the dominating galaxy do not change significantly. Its dark halo is expected to gain slightly more mass by accretion of the gas from the companion galaxy, where it can cool again and form new stars. Similarly, the stars of less massive galaxy are added to the stellar population of the massive one. If masses of galaxies undergoing a merger are comparable, the consequences for both galaxies are much more radical. During such "major merger", disks are typically destroyed and transformed into a spheroidal component due to a high velocity dispersions attained by the stars (e.g. White, 1978, Negroponte & White, 1983, Barnes, 1988, Hernquist, 1992). Such violent interactions may lead to the ejection of the part of the matter and/or of the gas from the galaxies, observable as tidal tails (e.g. Toomre & Toomre, 1972). If the gas content of merging galaxies is high, the perturbed gas orbits may lead to increased star formation activity, starburst. Gas can also flow into the centers of the galaxies, feeding the super massive black holes and thus triggering the AGN activity. The formation of elliptical galaxies can be understood, at least qualitatively, in this way. This picture is supported by numerical simulations showing that merger of galaxies of comparable masses leads to the formation of an elliptical galaxy regardless of the morphology of progenitors. If a new gas with a significant amount of angular momentum is further accreted to such elliptical, a new disk can form resulting in apparition of a disk-bulge system. Another possible scenario of the formation of disk-bulge system is accretion of cold gas along cosmic filaments that maintains the disk structure. The gravitational fragmentation of such gas-rich and turbulent disks leads to the formation of giant clumps that may merge into a central spheroid. Theory distinguishes two different modes of accretion onto galaxies: the hot and the cold mode. In the hot mode (T$\sim 10^6$ K) the gas is first shock heated before it cools and descends into the center of the halo, while in the cold mode (T$\sim 10^4 - 10^5$ K), the gas is never heated and falls into the center of the halo in a free-fall time. Whether hot or cold mode of accretion operates depends mainly on the mass of the halo. If the mass of the halo is higher than the critical mass, corresponding to the threshold above which a shock is stable, the gas is accreted in the hot mode. On the other hand, the cold mode of gas accretion dominates in lower mass galaxies (baryonic mass $\lesssim 10^{10}$ $M_\odot$). However, at high redshift, even high mass galaxies can be fed by streams of the cold gas that can penetrate their hot halo due to the enhanced density of the gas along the cosmic filaments that can cool efficiently before shock heating develops.

minor merger

major merger

formation of ellipticals

Mergers and accretion are not the only processes that can modify the morphology of galaxies. In dense environments, e.g. in clusters, galaxies may lose their gas due to so-called ram pressure, a pressure exerted on a body which is moving through a fluid medium causing a strong drag force. If the drag force overcomes the galaxy's gravity, its gas is stripped out as it moves through the hot intergalactic medium. When it is a spiral galaxy that loses most of its interstellar gas, its future star formation is greatly reduced, its thin disk can be heated by tidal interactions and it can thus be transformed into a lenticular galaxy, i.e. a disk galaxy with very little or no ongoing star formation. Transformation of spiral galaxy into lenticular is considered to be the standard scenario of formation of lenticular galaxies.

formation of lenticulars

Besides ram pressure (Gunn & Gott, 1972, Quilis et al., 2000), various other processes may lead to the formation of lenticular galaxies. They are all related to galaxy interactions (direct or indirect) and subsequent loss of stellar content. For instance, when interacting galaxies move too fast with respect to each other, the dynamical friction between them is not strong enough to slow them down

enough to cause a merger. Such encounter may however alter their shape and will typically strip off some of outer, weakly bound stars. This process is called galaxy harassment (Moore et al., 1996). Another process commonly affecting galaxies in dense environments is galaxy strangulation (Larson et al., 1980). It is a process of loss of gas due to tidal effects created by the gravitational potential of the cluster into which a galaxy falls. By losing its gas, star formation in the galaxy gradually ceases.

Galaxies can be reshaped also by internal dynamical processes. Of particular importance in evolution of disk galaxies are bars, stellar dynamical structures in the central regions of galaxies, that are believed to form spontaneously due to instabilities in massive and dynamically cold (rotation-dominated) galaxies. Their importance lies in their ability to redistribute angular momentum and mass within the galaxy. They are also efficient in driving gas inwards and thus leading to the formation of dense central ellipsoidal component referred to as pseudobulge, to distinguish it from "classical", merger-built bulge.

bar

central bulge

1.3 Galaxy formation & evolution: where do we stand?

In the current cosmological paradigm, structures form by amplification of primordial fluctuations that are driven by a gravitational instabilities in the expanding Universe. The growth of such instabilities can be studied analytically in the linear regime, and to some extent in weakly non-linear regime too. However, the fully non-linear evolution is mainly studied with the help of numerical simulations.

On large, cosmological scales ($\gtrsim$ 1 Mpc), the hierarchical Cold Dark Matter (CDM) structure formation scenario is reasonably well established by means of gravitational N-body simulations (e.g. Springel et al., 2005, 2006). When compared to observations, very good agreement is found with the large-scale structure statistics derived from these gravity-only simulations.

On smaller scales, however, the details of the formation and evolution of galaxies are much less well understood. The main reason is the difficulty in modeling the baryonic component of the Universe and the complexity and non-linearity of underlying physical processes. The collisional nature of the gas makes modeling of baryons much more complicated than that of dark matter. In addition, plenty of phenomena associated with baryons that have to be consistently taken into account are often not very well understood (e.g. star formation, cooling, effects of feedback).

Simulations of galaxy formation have encountered a number of problems, most notably the central cusp problem, the missing satellites problem and the problem related to the angular momentum, known as the "angular momentum catastrophe".

core-cusp problem

The core-cusp problem refers to the mismatch of the theoretically predicted central densities of dark matter haloes when compared with observations. Dark matter haloes of observed galaxies, especially low-mass ones, are found to have constant or shallow density profiles, called cores (e.g. Moore, 1994, Burkert, 1995, de Blok et al., 2001, Swaters et al., 2003, Spekkens et al., 2005, Oh et al., 2011), while cosmological dissipationless N-body simulations report density distributions, called cusps, that diverge in the centers of dark matter haloes (e.g. Navarro et al., 1997, Moore et al., 1999b, Navarro et al., 2010, Ishiyama et al., 2013). To flatten a central cusp, gravitational potential of dark matter halo has to be modified. This can be achieved by gravitational effects from baryons to dark matter halo, producing an expansion of the dark matter component of the galaxy, thus reducing its central density. Two categories of mechanisms enabling the reduction of the central density profile have been identified: feedback from SNe (e.g. Navarro et al., 1996, Read & Gilmore, 2005, Ogiya & Mori, 2012, Pontzen & Governato, 2012, Teyssier et al., 2013, Martizzi et al., 2012, 2013) and AGN (e.g. Martizzi et al., 2012, 2013), generating galactic winds or redistributing gas, and dynamical friction from massive clumps or disk instabilities (e.g. El-Zant et al., 2001, Goerdt

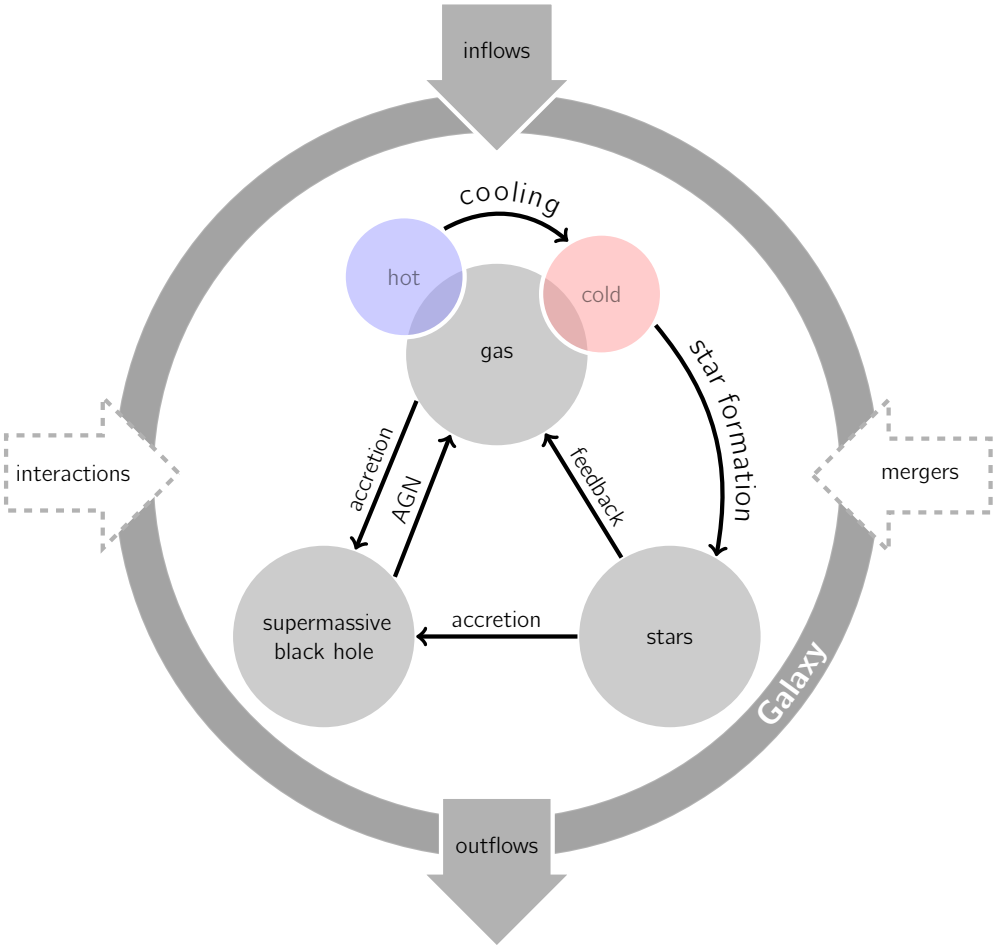

Figure 1.4

A flow chart of the evolution of individual galaxy. The galaxy containing gas, hot and cold, stars and a supermassive black hole, is represented by the gray circle. Hot gas is transformed into cold gas by cooling. This cold gas can be transformed into stars which inject energy, mass and metals into gas. Supermassive black hole can accrete both hot and cold gas, but also stars (a star drifting too close to a supermassive black hole is most likely ripped to shreds by intense tidal stresses and it is the shredded material that is accreted) and release energy in the form of AGN activity, affecting the gaseous component. Moreover, galaxy can accrete gas from intergalactic medium through inflows, can lose gas through outflows driven by feedback (stellar and/or AGN) and can interact or merge with other galaxies. Adapted from Mo et al. (2010).

et al., 2010, Inoue & Saitoh, 2011). Stellar feedback, especially in the form of repeated supernovae episodes transferring energy from gas into dark matter component orbits, seem to be a dominant process for core flattening (Pontzen & Governato, 2012), as opposed to dynamical friction for which massive infalling baryonic clumps are required in order to be able to soften a central dark matter cusp. This suggest that the core-cusp problem may[9] no longer be a major challenge to the CDM paradigm[10].

[9] It is worth noting that the proposed solutions are model dependent, i.e. they depend on the way star formation, feedback and baryonic physics in general are modeled.

[10] Similarly to other small scale problems, one of their most popular solution beyond the CDM model is the warm

missing satellites

Another problem related to dark matter haloes is the missing satellite problem. Briefly stated, this problem refers to the disagreement between the number of satellite galaxies observed in the Local Group compared to the large number of subhaloes predicted by CDM. In the hierarchical CDM scenario, small dark matter haloes collapse first, when the universe is dense, and thus have high density core concentrations. When these small dense haloes later merge to form larger structures, a significant fraction of them survive the tidal stripping due to gravitational interactions with merging haloes. Both semi-analytic model (Kauffmann et al., 1993) and numerical calculations (Klypin et al., 1999, Moore et al., 1999a) have shown that the Milky Way-size haloes should host a large number of satellite subhaloes in disagreement with the observed low number of dwarf galaxies.

too big to fail

One especially puzzling feature of the missing satellite problem is the prediction of the existence of subhaloes that are too massive and dense compared to any of the observed Milky Way brightest satellites. This discrepancy between simulations and the observed internal kinematics of the brightest Milky Way satellites has been dubbed the "too big to fail" problem (Boylan-Kolchin et al., 2011, 2012, Tollerud et al., 2014). Specifically, simulations have shown that the most massive subhaloes have systematically larger central masses compared to those measured in the brightest satellites of the Milky Way. So not only the number of luminous satellites predicted by dark matter-only simulations is too high, the overall distribution in masses of those satellites is also too high.

Solution to the missing satellites problem is searched on the side of theory, where different physical mechanisms allowing the suppression of the galaxy formation are explored, but also on the side of observations, since dwarf satellites are very faint objects that are difficult to detect and the observational completeness is an important issue. On the side of theory, several mechanisms of the suppression of star formation leading to large number of unobservable low-mass subhaloes are studied: the photoionization (Quinn et al., 1996, Gnedin, 2000, Benson et al., 2002, Hoeft et al., 2006, Wadepuhl & Springel, 2011, Pfrommer et al., 2012), efficient especially in low mass haloes (with mass below $\sim 10^9$ $M_\odot$, Okamoto et al., 2008), the injection of energy into the surrounding gas in more massive haloes by supernovae (e.g. Dekel & Woo, 2003, Governato et al., 2007) and young stars, and the tidal effects due to the presence of a baryonic disk. While these mechanisms offer a promising solution to the low-mass regime of the missing satellites problem, they fail at massive end – they are not able to solve the "too big to fail" problem (see e.g. Garrison-Kimmel et al., 2013, for inability of supernova feedback to solve the problem alone). However, some recent works (Brooks et al., 2013, Del Popolo et al., 2014) have suggested that when all the above mentioned effects associated with baryonic physics are combined together, both the number and masses of satellites can potentially be brought into agreement with observations.

planar satellites distribution

Finally, another potential problem concerning satellite galaxies is related to their spatial distribution. Observations of dwarf galaxies in the Milky Way (Lynden-Bell, 1976, Metz et al., 2007, 2008, 2009, Pawlowski et al., 2012) and Andromeda (Metz et al., 2007) galaxy suggest that their distribution may not be isotropic, but rather disk-like. While some authors (Kroupa et al., 2005, Pawlowski et al., 2012) point out that such a satellite system distribution is highly incompatible with the expected theoretical one if the satellites are to trace an isotropic dark matter host halo, others (Zentner et al., 2005, Lovell et al., 2011) find instead that quasi-planar distribution of satellites is a natural outcome in cosmological simulations of the ΛCDM model. Nonetheless, recent study of the greatly improved sample of satellites in the Andromeda galaxy (Conn et al., 2013, Ibata et al., 2013)

dark matter paradigm, with the sterile neutrino – naturally arising from a minimal extension of the neutrino sector within the Particle Physics standard model – as the most popular candidate. However, Schneider et al. (2014) have recently shown that a realistic warm dark matter scenario does not really do better than cold dark matter in alleviating these potential inconsistencies.

reported the existence of a planar subgroup in a significant fraction of the population (roughly 50%). Two classes of possible solutions, accretion and in-situ formation, are discussed in the literature, however there does not seem to be a consensus on whether the presence of co-planar structures of dwarf galaxies represents a real challenge for current galaxy formation models.

In recent years, the discovery of a number of additional faint satellite galaxies (e.g. Irwin et al., 2007, Simon & Geha, 2007, Belokurov et al., 2008, 2010) alleviated to some extent the problem of missing satellites by suggesting the existence of many more satellite galaxies in the Local Group beyond our ability to detect them. The completeness corrections related to the sky coverage, luminosity bias and surface brightness limits point towards an empirical evidence that there is a much larger population of dwarf galaxies to have been discovered (see Bullock, 2010, and references therein). These findings indicate that the missing satellite problem may not be as severe as previously thought, and may have been solved completely within the framework of CDM paradigm.

angular momentum catastrophe

Angular momentum governs the structure of disk galaxies that are rotationally supported systems. As described in the previous Section, in the current paradigm of the galaxy formation proposed by White & Rees (1978) and Fall & Efstathiou (1980), disk galaxies form by gravitational instability through cooling and condensation of baryons inside dark matter haloes if they retain most of their angular momentum in the assembly process. Dark matter haloes are supposed to acquire angular momentum via tidal torques (Peebles, 1969, Fall & Efstathiou, 1980) from interacting structures and since baryons experience the same tidal forces as dark matter, they are expected to have the same distribution of specific angular momentum as their parent dark matter haloes.

However, hydrodynamic numerical simulation, aimed at investigating the process of galaxy formation, have shown that merging substructures lose a significant fraction of their angular momentum by transferring it to the outer halo via dynamical friction and tidal stripping (e.g. Maller & Dekel, 2002). As a consequence, baryons associated with these substructures end up in the central parts of the galaxy leading to the formation of small, centrally concentrated disks dominated by large bulges (e.g. Navarro & Benz, 1991, Navarro & White, 1994, Navarro & Steinmetz, 2000). This problem is usually denoted with the name of "angular momentum catastrophe". Moreover, there is at least one other problem related to angular momentum – the mismatch between the specific angular momentum distribution of simulated haloes and the one observed within real galaxies (van den Bosch et al., 2001).

overcooling

The origin of the angular momentum transfer problem is related to the overcooling problem in the CDM model (e.g. White & Rees, 1978, White & Frenk, 1991). In the hierarchical bottom-up scenario, low-mass dense haloes cool very efficiently. This leads, in absence of heating sources, to rapid condensation of small, dense gas clouds which are slowed down due to the energy and angular momentum loss by dynamical friction against the surrounding dark matter halo (Navarro & Steinmetz, 2000). Cooling is expected to be so efficient at early times that most of the gas should have been converted to stars well before the assembly of present-day galactic disks.

Several solutions have been proposed to these problems. They are all based on the same idea which is to prevent the cooling of the gas in the early assembly process of haloes and thus prevent or delay the collapse of protogalactic gas cloud that allows to reduce the angular momentum loss of the gas as it settles into the disk.

One possible mechanism is photoionization due to the cosmic UV background, the accumulated UV radiation from the previous generations of massive stars and quasars filling the intergalactic space since the reionization epoch ($z \gtrsim 6$). Photoionization was already mentioned as a possible solution to the missing satellites problem. Indeed, such radiation seems to be efficient at heating the gas and preventing it from cooling in low-mass systems playing thus a role in the formation of dwarf galaxies

(e.g. Quinn et al., 1996, Gnedin, 2000, Hoeft et al., 2006).

The most discussed mechanism preventing efficient gas cooling and condensation is the feedback from SNe and evolving stars as it is also believed to be able to remove low-angular-momentum material from the central part of galaxies. This idea is not new, already White & Rees (1978) speculated that enough energy feedback from supernovae could prevent the overcooling and thus reduce the angular momentum loss. Some early simulations (e.g. Weil et al., 1998) with suppressed gas cooling at early stages of galaxy assembly process confirmed the elimination of the angular momentum problem. Since then, various different feedback implementations were used in simulations.

Even though efficiency of SNe feedback was shown to depend strongly on the details of assumptions of individual models (e.g. Navarro & White, 1993, Kay et al., 2002, Scannapieco et al., 2006), the overall impact of SN feedback is found to depend on total galaxy mass. In large systems, feedback may be able to reduce star formation by a factor of a few by heating the gas, while smaller systems are more strongly affected: strong galactic winds may be generated and star formation may be reduced more substantially. In a dwarf galaxy, supernovae could remove a significant fraction of gas and thus reduce the star formation by generating outflows (Dekel & Silk, 1986, Efstathiou, 2000). The gas is found to be blown away only in low mass systems with gas mass $\lesssim 10^6$ $M_\odot$ (Mac Low & Ferrara, 1999), while for higher mass dwarfs, with the halo mass above 10^{10} $M_\odot$, the mass ejection efficiency seems to be very low in quiescent isolated galaxies (Dubois & Teyssier, 2008). On the other hand, in the fully cosmological context, by resolving a multiphase interstellar medium and the energy injection from multiple SNe in clustered star-forming regions, Governato et al. (2010) succeeded to achieve strong outflows from supernovae explosions removing low angular momentum gas from system with the halo mass of $\sim 10^{10}$ $M_\odot$. Realistic dwarf galaxies – bulgeless and with a shallow central dark matter profile – were thus obtained as a natural outcome of galaxy formation in the CDM scenario.

However, the exact role of SNe feedback on the formation of disk-dominated spiral galaxies is unclear. In some limited number of cases, simulations in fully cosmological context have been able to reproduce individual examples of rotation-dominated stellar disks with significant exponential component (e.g. Robertson et al., 2004, Okamoto et al., 2005, Governato et al., 2007). But once no criteria favoring the disk formation (e.g. relatively high spin parameters, quiet merger histories) are applied in the cosmological zoom-in resimulations, no Milky Way-like or other late-type spirals are formed (Scannapieco et al., 2009). Combining energy and kinetic SNe feedback (both type Ia and type II) with the external UV radiation can lead to an improvement in the form of reduction of the bulge, however the formation of bulge-less disk galaxies remains elusive (Stinson et al., 2010, Piontek & Steinmetz, 2011).

These studies indicate that the physical processes playing a role in the formation and evolution of a galaxy are much more complex and other mechanisms in the interstellar medium (ISM) in addition to supernovae are important. Agertz et al. (2011) have investigated the impact of the small-scale physics ($\lesssim 100$ pc[11]) on disk properties. To mimic this unresolved physics such as the conversion of atomic gas into molecular, turbulence on small scales and different radiative effects, the parameter of the star formation efficiency per free-fall time is varied. Comparison with the effect of supernova feedback has shown that this star formation efficiency, thus the underlying small-scale star formation physics, is more successful way of regulating star formation and obtaining realistic galaxies. Increased value of the injected energy per supernova could result into more realistic bulge-to-disk ratio, but gas disk would become significantly distorted. On the other hand, low star formation efficiency ($\sim 1\%$) leads to the successful formation of galaxies with extended disk, flat rotation curves and moderate

[11]While such resolution is reached in zoom-in cosmological simulations dedicated to the study of individual galaxies, larger sample at this resolution allowing statistical studies is still out of reach.

bulge, in agreement with observed disk properties of Milky Way-like galaxies.

too many baryons

However, obtained stellar disks are much more massive than expected for a given halo mass. This is an additional problem models of galaxy formation are facing. Stellar mass to halo mass relations from abundance matching techniques have shown that the majority of simulations lock too many baryons into stars to be viable models for galaxy formation (e.g. Guo et al., 2010). A recent exception is the simulation of Guedes et al. (2011), in which baryon conversion efficiency in agreement with predictions from abundance matching technique was obtained together with a morphology reasonably close to that of a Milky Way-like disk galaxy. The adopted feedback model is still phenomenological, including a strong SN feedback and high star formation efficiency, contrarily to Agertz et al. (2011), and the merging history of the simulated galaxy is particularly quiet.

In spite of significant progress, it is far from clear, that the supernovae feedback is capable of solving the overcooling problem. In addition, even if SNe could avoid the loss of angular momentum, other problems, like the mismatch of the angular momentum profiles, remain (e.g. van den Bosch et al., 2001). Maller & Dekel (2002) proposed that the transfer of angular momentum by the process of dynamical friction and tidal stripping could solve the mismatch of the distribution of specific angular momentum within galaxies between observations and simulations, and thus help to alleviate the angular momentum catastrophe.

These findings suggest that other mechanisms of stellar feedback in addition to supernovae are needed. Indeed, the feedback from massive young stars in form of stellar wind, radiation pressure and HII photoionization injecting the energy and momentum into the ISM before their explosion as SNe have been shown to play a key role in regulating star formation (Hopkins et al., 2011, Stinson et al., 2013, Agertz et al., 2013, Roškar et al., 2013). The early pre-SN energy and momentum injection changes qualitatively the effectiveness of stellar feedback globally by changing the ISM properties prior to the SNe explosions: dense gas becomes more disperse in star forming regions which reduces radiative losses of thermal feedback from SNe and consequently increases the efficiency of stellar feedback itself. Even though the overall structure and properties of the ISM are found to depend on the implementation and choice of parameters, the main reason being the small scales at which these feedback processes operate (such scales are close to the resolution limit of the simulations where numerical effects play a role), inclusion of SNe together with pre-SNe sources into the stellar feedback budget can solve the problem related to galaxy stellar mass mentioned above. Hopkins et al. (2013a) have shown that such complete stellar feedback is both necessary and sufficient to explain the observed relation between galaxy stellar and halo mass at all redshifts. Some previous studies, e.g. Guedes et al. (2011), in which a Milky Way-like galaxy was successfully reproduced at redshift z=0, were still converting too many baryons into stars at higher redshifts. It it this buildup of stellar mass across cosmic time that is problematic in all simulations up to date. Fine tuning of star formation or feedback parameters often allows to recover present-day parameters of galaxies in agreement with observations. What turns out to be difficult is to keep good match with observations at different redshifts. The largest and the most realistic cosmological hydrodynamic simulation to date, Illustris (Genel et al., 2014), succeeded at obtaining a good agreement for the history of cosmic star formation rate (SFR) density at $z > 1$ when compared to the observed values. However, at $z \lesssim 1$, in spite of adjusting the free parameters of feedback modeling, the observed rapid decrease of the cosmic SFR density is not recovered. This suggests that additional suppression of star formation is required, especially for massive haloes ($\approx 10^{12}$ $M_\odot$) which are the main contributors to the cosmic SFR density at $z \lesssim 4$.

cosmic SFR density

In summary, a successful model of galaxy formation has to result into a system matching not only the stellar mass constraints inferred from observations, it should also reproduce morphological

aspects consistent with observed galaxies. Despite the ability of the "full" feedback scheme to satisfy the stellar mass constraints, the simultaneous formation of a thin, morphologically undisturbed disk stays impossible (Roškar et al., 2013). The formation of disk galaxies similar to the Milky Way remains an outstanding problem of galaxy formation models.

We have just seen that the inclusion of the effects of energetic stellar feedback processes in galaxy formation simulations may cure a number of problems they are facing. It is not clear whether any of these processes is dominant, having the strongest impact on the ISM, or all mechanisms are needed to obtain a more realistic ISM and consequently more realistic population of galaxies. Modeling of baryonic processes is difficult as they add non-linearly to modify the observed properties of the multiphase ISM and consequently of galaxies themselves. Additional difficulty arises from the necessity to couple huge range of scales to model consistently the formation and evolution of galaxies: from large cosmological (Mpc) scales, governing the accretion, interactions and merging history down to smallest, sub-parsec scales, where the physical processes like stellar feedback originate. Current state-of-the-art cosmological simulations of galaxy formation are still not able to cover all these scales. Moreover, correct modeling of different stellar feedback processes requires a good knowledge of the process of star formation itself. In spite of great progress both on the side of theory and modeling as well as on the side of observations, formation of stars is still poorly understood.

1.4 Outline

In this thesis, I study links between galaxy evolution, morphology and internal physical processes, namely star formation as the outcome of the turbulent multiphase ISM.

In Chapter 2, I study the evolution of the morphology of galaxies in the suite of zoom-in cosmological simulations, performed by Martig et al. (2012), through the analysis of a particular disk instability, bars. The simulation sample focuses on Milky-Way-mass galaxies in low-density environments, with a broad variety of mass growth histories. I analyze the evolution of the fraction of bars with redshift, its dependence on the stellar mass and accretion history of individual galaxies. In our models, fraction of bars declines with increasing redshift, with observable bars being rare and weak down to $z \simeq 1$ and almost absent from the progenitors of present-day spirals at $z > 1.5$, in agreement with the observed bar fraction evolution. The characteristic epoch of bar formation in galaxies of the studied mass range, namely redshift $z \simeq 0.8 - 1$, is found to correspond to the epoch at which today's spirals acquire their disk-dominated morphology. I show how the obtained results suggest that the bar formation epoch corresponds to the transition between an early "violent" phase of spiral galaxies formation at $z > 1$, during which they are often disturbed by major mergers or multiple minor mergers as well as violent disk instabilities, and a late "secular" phase at $z < 1$, when the final morphology is generally stabilized to a disk-dominated structure.

Simulations used in this study reproduce correct morphologies in agreement with observed properties of galaxies with present-day stellar masses in the $10^{10} - 10^{11}$ $M_{\odot}$ range, in field and loose group environments. At $z = 0$, the simulated galaxies span a large range of Hubble types from bulge-dominated galaxies to nearly bulgeless disks, with most of them having pseudo-bulges and 70% of them hosting a bar, while at $z = 2$, they are very perturbed, with disks, if present, often thick and sometimes unstable and clumpy. Moreover, sizes of simulated galaxies are in reasonably good agreement with observed scaling relation between stellar mass and radius. However, as many cosmological simulations, they convert too many baryons into stars (the galaxy formation efficiency is on average three times higher than the observed one) to be a viable model for galaxy populations. To gain a better understanding of the process of star formation, I have performed a series of low-

redshift galaxy simulations at parsec resolution in isolation, presented in Chapter 3, and studied the physical origin of their star formation relations and breaks. The analyzed sample includes simulations representative of the Large and Small Magellanic Clouds, to which a simulation of a Milky Way-like galaxy (Renaud et al., 2013) is added, reproducing the observed star formation relations and the relative variations of the star formation thresholds. In particular, the role of interstellar turbulence, gas cooling, and geometry in drawing these relations at 100 pc scale are studied. I will show that the surface density threshold for efficient star formation can be linked to the typical density for the onset of supersonic turbulence. When averaged over entire galaxy, observed star-formation relations seem to show evidence of bimodality according to which normal disk galaxies convert their gas into stars within a depletion time up to 10 times longer than galaxy mergers in starburst phase. I will show the evolution of a model of merging galaxies resembling Antennae galaxies (Renaud et al., 2014), but being a fairly representative case of many other mergers, in the Σ_{gas}–Σ_{SFR} plane, form the sequence of disks in the pre-merger phase to the sequence of starbursts reached during the interaction. I will also present the resolved analysis of these merging galaxies at 100 pc scale in the Σ_{gas}–Σ_{SFR} plane revealing qualitatively similar role of interstellar turbulence identified in models of isolated galaxies.

In Chapter 4, I present an idealized analytic model for star formation (Renaud, Kraljic & Bournaud, 2012), relating the surface density of gas and star formation rate as a function of the presence of supersonic turbulence and the associated structure of the ISM. This model predicts a break at low surface densities that is followed by a power-law regime at high densities that can be flattened under the effects of stellar feedback. The strength of this model is its ability to explain the observed diversity of star formation laws and thresholds in different systems: nearby spirals, the Small Magellanic Cloud, high redshift disks, low and high redshift mergers and Giant molecular clouds.

The alternative cosmological zoom-in technique (Martig et al., 2009), used to produce the analyzed sample of galaxies presented in Chapter 2, has the advantage to model properly the properties of the star-forming interstellar medium in spite of relatively low resolution of $\sim$ 100 pc (typically reached in this kind of simulations). However, it is not able to treat gas around, and possibly also inside galaxies correctly – it neglects thermal pressure, especially in hot halos which may play crucial role in modeling high mass systems. This can be remedied by coupling the resimulation method with a grid-based hydrodynamic code which is known to model fluid dynamics better than particle based codes. In Chapter 5, I will present the basic features of the resimulation technique as well as its implementation in the Adaptive Mesh Refinement code RAMSES (Teyssier, 2002). As a perspective for this ongoing project, I will discuss some of our very first results and future analysis in the context of smooth cosmological accretion.

A brief summary is presented in Chapter Conclusion.

Chapter 2

The two-phase formation history of spiral galaxies traced by bars

> *"Where is an interesting bar where lots of things are going on?" I thought that things went on in bars.*
>
> — Richard P. Feynman, *"Surely You're Joking, Mr. Feynman!": Adventures of a Curious Character*

2.1 Introduction

When studying morphological evolution of galaxies, different structural features can be considered. Here, we focus on bars. Bars are one of the most easily quantified[1] substructures in spiral galaxies, and are hence often used as tracers of galaxy evolution. They are also very frequent – most spiral galaxies today contain a central bar, although with largely variable amplitudes (Block et al., 2002, Whyte et al., 2002). Spiral arms are equally common in optical light, but are much weaker in the

[1] This is because bars are located in the central regions of galaxies which are bright even for distant galaxies. In addition, compared to other structural features of galaxies, bars are less affected by dust extinction (e.g. Eskridge et al., 2000).

near-infrared light that more closely traces the stellar mass distribution, and the strength of bars is generally easier to quantify independently of the imaging sensitivity.

bar formation

Both the formation of bars and their time evolution are connected to the baryonic and dark matter properties of their host galaxies, and their mass assembly history. It is commonly accepted that bars develop spontaneously due to instabilities in rotationally supported self-gravitating stellar disks. Once these are sufficiently massive and dynamically cold (rotation dominated) to be gravitationally unstable, with typical Toomre stability parameters $Q \simeq 1.5 - 2.0$[2] (Toomre, 1963, Combes & Sanders, 1981, Gerin et al., 1990, Combes & Elmegreen, 1993), stellar bars form relatively rapidly (e.g. Hohl, 1971, Ostriker & Peebles, 1973, Athanassoula, 2003). However, the onset of bar instability can be delayed by either random motions of stars in dynamically hot (dispersion dominated) disk (Athanassoula & Sellwood, 1986, Athanassoula, 2002, Sheth et al., 2012) or a presence of a massive spheroid (halo or bulge component) due to its strong contribution to the gravitational force that reduces the non-axisymmetric forcing of the bar (Ostriker & Peebles, 1973, Athanassoula & Sellwood, 1986, Athanassoula, 2013).

Apart from this canonical (spontaneous) bar instability, galactic bars can be triggered by large density fluctuations in the disk (Sellwood, 1989), by tidal interactions (Noguchi, 1987, Berentzen et al., 2004, Curir et al., 2006), halo substructure (Romano-Díaz et al., 2008) or a non-axisymmetric dark matter halo distribution (Dubinski & Chakrabarty, 2009). The gaseous content can also trigger bars: gas helps to form outer spiral arms, which can remove angular momentum from the inner regions and strengthen a bar seed (Bournaud et al., 2005).

Bars, just like spirals, are dynamic patterns – waves and can thus transport energy and angular momentum. Indeed, once formed, bars evolve through the exchange of angular momentum with the dark matter halos (Weinberg, 1985, Debattista & Sellwood, 2000), as well as with stellar and gaseous disks (Friedli & Benz, 1993, Bournaud & Combes, 2002, Bournaud et al., 2005). Since the bar (spiral structure within the corotation[3]) is a disturbance with negative angular momentum and negative energy, feeding it with energy or angular momentum will damp it, while taking energy or angular momentum away from it, will excite it (Lynden-Bell & Kalnajs, 1972).

bar strengthening

Thus when bars lose the angular momentum, they can grow stronger (Athanassoula, 2002, 2003). They will also slow down, meaning that their pattern speed will decrease (e.g. Weinberg, 1985, Little & Carlberg, 1991, Debattista & Sellwood, 2000, Athanassoula, 2003, Martinez-Valpuesta et al., 2006), and grow somewhat longer. Since bars tend to end near the CR, when a bar slows down, CR moves out which naturally leads to the increased bar length.

Lynden-Bell & Kalnajs (1972) also showed that angular momentum is transferred from the inner to the outer parts of the disk and that it is mainly the material near resonances that will emit or absorb it. This means that material at ILR will lose angular momentum, while material at CR and OLR will gain it. Thus bar can lose its angular momentum by transferring it through gravitational torques to the outer disk (e.g. Sellwood, 1981), but also through dynamical friction when interacting

[2]We focus here on non-axisymmetric instabilities, like spirals and bars. For $Q \lesssim 1$, gas disks are gravitationally unstable and may lead to the formation of axisymmetric instabilities such as rings and clumps, observed in high redshift galaxies where even dynamically hot disks can be unstable due to their high dense gas fractions.

[3]In realistic galaxy potentials, following resonances typically occur: corotation (CR), inner Lindblad resonance (ILR) and outer Lindblad resonance (OLR). Corotation, in which the density pattern such as a bar rotates at the angular velocity that is equal to the angular velocity of revolution of the star, and thus repeatedly sees the star in the same way, is the strongest of a series of resonances. If a bar rotates at angular velocity for which the star executes two radial oscillations for each revolution, we talk about ILR (for potentials typical for disk galaxies, there can be zero, one or two ILRs depending on the pattern speed). OLR is like ILR, except that the star drifts backward with respect to the rotating frame while it executes two radial oscillations for each revolution.

with the massive dark matter halo (e.g. Sellwood, 1980, Weinberg, 1985, Athanassoula, 2003). This friction can be viewed as the gravitational attraction on the perturber (bar) of the density excess that develops behind it as it moves. Consequently friction can be thought of as the torque between the perturber and the halo response. An interesting consequence of the transfer of angular momentum from the bar to the halo was discussed by Weinberg & Katz (2002) who argued that such exchange could reduce the central density of the dark matter halo by a substantial factor. However, because the disk has only a finite amount of angular momentum to give to the halo, the possible density reduction is quite modest (Holley-Bockelmann et al., 2005, McMillan & Dehnen, 2005). In addition, the mass distribution of the disk contracts as it loses angular momentum. The resulting deepening of the potential well leads to the halo compression, which actually seems to overwhelm the slight density reduction (Colín et al., 2006).

bar weakening or destruction

Bars can weaken or be destroyed when they gain the angular momentum (Bournaud et al., 2005). Transfer of the angular momentum to the outer parts of the disk allows the gas to flow towards its inner parts. As gas clouds move on their orbits, they eventually collide where gas streams intersect (especially near resonances) and shocks develop. Shocks convert some kinetic energy of the bulk motion in the gas into heat, which can be radiated away. Because the shocks are nearly radial, gas impacts them at a steep angle. Therefore, much of the velocity that is lost in the shock is azimuthal. The gas loses energy and falls toward the center.

Furthermore, as shocks are produced when gas accelerates as it approaches and decelerates as it leaves the potential minimum of the bar, gas tends to pile up near the ridge line of the bar. Incoming gas overshoots a little before it plows into the departing gas, so the shocks are nearly radial but offset from the ridge line of the bar in the forward (rotation) direction. This causes the gas to be attracted backwards, towards the bar major axis and thus to lose angular momentum to the bar.

The infalling gas may provide material to nuclear disks and black holes (Knapen et al., 2000, Laine et al., 2002, Laurikainen et al., 2004). It can also lead to the growth of central mass concentrations which can further weaken or even destroy a bar by destroying the bar's orbital structure (Hasan & Norman, 1990, Pfenniger & Friedli, 1991, Hasan et al., 1993, Shen & Sellwood, 2004). However, central concentrations with low-enough mass and/or low-enough mass growth rates could have little effect on real bars (Athanassoula, 2005).

Another, maybe more natural mechanism of bar destructions are galaxy interactions. When a satellite galaxy merges with a disk galaxy, a bar, if it exists, can be destroyed while the disk survives (Pfenniger, 1991, Athanassoula, 1999). A necessary condition for this to happen is sufficiently dense and massive satellite in order to severely impact the bar geometry, in particular stable orbits supporting the bar (Athanassoula et al., 2013).

bar reformation

Gas thus plays an important role in the process of bar destruction by losing its angular momentum to the bar and by producing a central mass concentration. On the other hand, if bars are formed in conditions where they are intrinsically short-lived, sufficient accretion of external gas onto the disk could enable their survival or reformation (Bournaud & Combes, 2002). In addition, galaxy interactions could in theory trigger bar (re-)formation (Gerin et al., 1990, Miwa & Noguchi, 1998, Berentzen et al., 2004), although observations do not show a clear environmental dependence of the bar in disk galaxies (van den Bergh, 2002, Aguerri et al., 2009, Barway et al., 2011, Lee et al., 2012).

bar driven substructures

We have so far discussed processes having an impact on a bar, by making it stronger, weakening or even destroying it, and finally processes making reformation of a bar possible. In turn, bar influences the evolution of a galaxy it lives in. Barred spiral galaxies are rich in different substructures like inner and outer rings, lenses, spiral arms or pseudobulges in the central parts. These features can be understood, at least qualitatively, as results of secular evolution driven by non-axisymmetric

gravitational potentials, such as a bar. We have seen that by driving the gas inwards, bar contributes to the formation of central mass concentrations. If the gas spiraling inward encounters the ILRs, it may accumulate on orbits defined by the resonance instead of flowing all the way to the center of the galaxy. Gas that accumulates at the CR may form the "inner" ring often seen at the ends of bars, gas in the outer part of a galaxy may accumulate at the OLR (Schwarz, 1981). Such rings are places where gas collects and shows signs of ongoing star formation (Kormendy, 1982).

Bars can also thicken through vertical resonances, leading to the formation of pseudo-bulges–i.e., bulges with relatively low concentration and substantial residual rotation (e.g. Bureau & Freeman, 1999, Kormendy & Kennicutt, 2004, Martinez-Valpuesta et al., 2006).

Thus bars are not steady-state structures, they can rather be thought of as features evolving within a galaxy by directly driving its structural evolution which in turn has an impact on its structure and dynamics. Hence, the fraction of barred galaxies and the redshift evolution of this fraction are fundamental tracers of the evolution history of galaxies: this indicates when disks became sufficiently massive and self-gravitating to be bar-unstable, and whether the conditions for bars being long-lived or reformed were met.

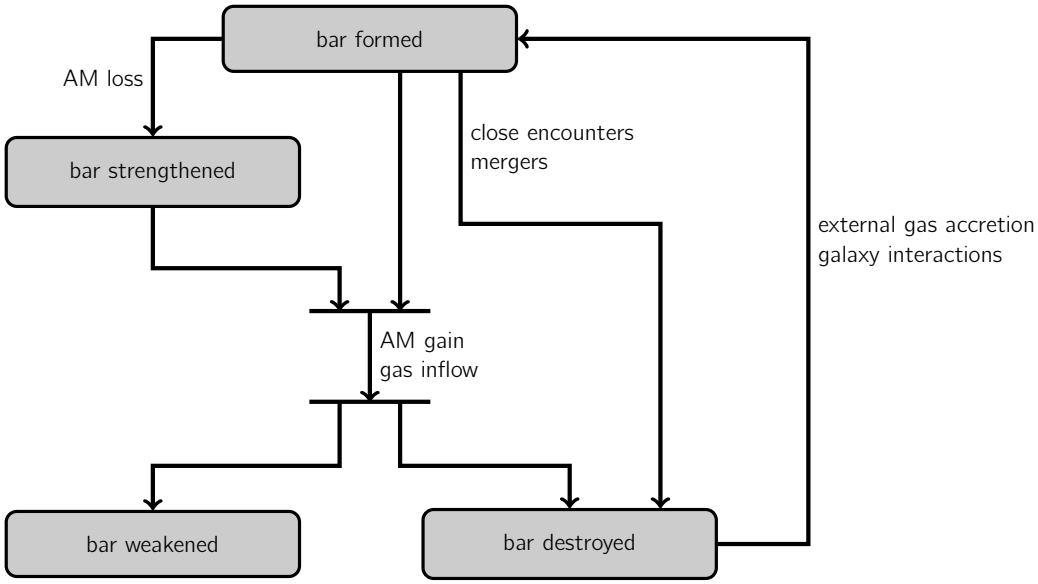

Figure 2.1

"State" diagram of bar evolution. Once bars are formed, they interact with other components – stars, gas and dark matter halo – by exchanging energy and angular momentum (AM), redistributing thus the mass within the galaxy. Bar can be reinforced when it loses angular momentum, while it can weaken or be destroyed when it gains angular momentum. Infalling gas spiraling toward the center of galaxy due to energy and angular momentum loss can also weaken a bar or even destroy it, if sufficient mass accumulates in the central part. Bar destruction can happen via galaxy mergers too. Once destroyed, disk can become bar unstable if sufficient amount of gas is accreted. Other possible mechanism for bar triggering are galaxy interactions.

In the nearby universe, the bar fraction in disk galaxies is very high. Depending on classification techniques, the fraction of strong bars in the optical light is at least 50% (Barazza et al., 2008). Optical classifications reveal roughly one third of strongly barred galaxies, one third of weakly or moderately barred galaxies, and one third of optically unbarred galaxies (de Vaucouleurs et al., 1991). The bar fraction is at least 80% in the near-infrared, where weak bars are not obscured by dust and

more easily distinguished from spiral arms (Eskridge et al., 2000, Block et al., 2002, Whyte et al., 2002, Menéndez-Delmestre et al., 2007).

At higher redshifts, the first searches for bars found a very low bar fraction at $z > 0.5$ (e.g. Abraham et al., 1999), possibly because of small number statistics. Their work also illustrated the difficulties in identifying bars at high redshift: the observed optical light traces the ultraviolet emission, in which bars are harder to detect, even locally. Near-infrared data revealed a number of barred galaxies at $z \geq 0.7$ (Sheth et al., 2003, Elmegreen et al., 2004, Jogee et al., 2004). The first sample large enough to robustly quantify the redshift evolution of the bar fraction without being affected by resolution and band-shifting bias up to $z \simeq 0.8$ was studied by Sheth et al. (2008) in the COSMOS field. These observations indicate that the bar fraction drops by a factor of about three from $z = 0$ to $z = 0.8$. This result holds both for all observable bars and for strong bars separately, and using either visual classifications or quantitative estimates of the bar strength. Sheth et al. (2008) also found a downsizing like behavior for bar formation, i.e., more massive galaxies tend to get barred at higher redshifts. This trend can explain why previous studies, such as Jogee et al. (2004), using shallower data targeted to more massive systems, observed higher bar fractions–but still consistent with a declining bar fraction (see also Elmegreen et al., 2004). Only recently the work on the evolution of the bar fraction was extended to higher redshifts ($0.4 \leq z \leq 1.0$: Melvin et al. 2014; $0.6 \leq z \leq 1.6$: Herrington et al. 2012) confirming the decreasing trend, consistent with previous studies.

In this Chapter, we study the evolution of bars in a sample of cosmological zoom-in simulations of 33 galaxies with present-day stellar masses ranging from 1×10^{10} to 2×10^{11} $M_{\odot}$, in field and loose group environments. The simulation technique and structural evolution of these galaxies (bulge and disk fractions, angular momentum evolution) are presented in Martig et al. (2012). In Section 2.2, simulations and methods for the identification of bars and morphological analysis are presented. In Section 2.3, we analyze the redshift evolution of the bar fraction in the whole sample and in disk-dominated galaxies, using quantitative measurements of the bar strength. The main result, the emergence of bars along the cosmic time that traces the epoch of thin disk formation subsequent to the growth of spheroids and thick disks, is presented in Section 2.4. Section 2.5 studies the lifetime of bars and its dependence on external gas accretion. In Section 2.6, we quantify the contribution of bars in the late growth of bulges, comparing these to unbarred galaxies. Finally, a possible scenario for the two-phase formation history of spiral galaxies traced by bars is discussed in Section 2.7. Finally, a short summary can be found in Section 2.8.

2.2 Simulations and analysis

2.2.1 Simulation sample

The simulation sample comprises 33 field and loose group galaxies modeled at 150 pc resolution from redshift five down to redshift zero with present-day stellar masses ranging from 1×10^{10} to 2×10^{11} $M_{\odot}$. Full description of the zoom-in technique can be found in Martig et al. (2009, 2012), here we recall only its main features. Dark matter halos are selected in a large volume, dark-matter-only simulation, performed using ΛCDM cosmology with the adaptive mesh refinement code RAMSES (Teyssier, 2002). For each selected halo the zoom-in simulation is performed by recording and replicating the mass inflow through a spherical boundary at the final virial radius of that halo. The boundary conditions used for the zoom-in simulation thus replicate all minor and major mergers as well as diffuse infall, as imposed by the initial dark matter only cosmological simulation.

The gravitational softening of zoom-in simulations is 150 pc and the mass resolution is $10^4 - 10^5$ $M_\odot$ (1.5×10^4 $M_\odot$ for gas, 7.5×10^4 $M_\odot$ for stars, and 3×10^5 $M_\odot$ for dark matter particles). Gravity (for gas, stars, and dark matter) is modeled with the particle-mesh code described in Bournaud & Combes (2002, 2003), while interstellar gas dynamics uses the code based on a sticky particle scheme (studied in the context of bar evolution in Bournaud et al., 2005). The drawback of this scheme is in neglecting of thermal pressure, especially in hot halos, which is not crucial in the mass range we study. On the other hand, it has the advantage of modeling the properties of supersonic turbulent pressure in cold gas phases, which is the physically dominant pressure term in the star-forming interstellar medium (e.g. Burkert, 2006) and is hardly modeled by other hydrodynamic techniques unless resolutions of 1–10 pc and low thermal cooling floors are reached (Teyssier et al., 2010, Bournaud et al., 2011a, Hopkins et al., 2011). The local star formation rate follows the Schmidt (1959) law, $\rho_{\rm SFR} \propto \epsilon\rho^{1.5}$, where ϵ is the star formation efficiency for which the value of 2% is adopted. The density threshold above which the star formation takes place is set to 0.03 $M_\odot$ pc^{-3} (i.e., one atom per cubic centimeter), corresponding to the minimal density for diffuse atomic cloud formation (Elmegreen, 2002). Energy feedback from supernova explosions using a kinetic scheme (20% of the energy of the supernovae is distributed to neighboring gas particles within a radius of 70 pc in the form of a radial velocity kick) as well as the continuous gas mass loss from stars (Jungwiert et al., 2001, Martig & Bournaud, 2010) are included.

The $z = 5$ seed for the central galaxy and the incoming companions are implemented with arbitrary disk+bulge models; tests have shown that the seed properties at $z = 5$ have no substantial impact on the structural evolution from $z = 2$ out to $z = 0$, because rapid evolution and mass growth at $z > 3$ washes out the initial assumptions.

In our study, we focus on the redshift range from $z = 2$ to $z = 0$. At $z = 0$, typical mass and SFR of simulated galaxies are $4 - 5\times10^{10}$ $M_\odot$ and 3 $M_\odot$ yr^{-1} at $z = 1$, 2×10^{10} $M_\odot$ and 5 $M_\odot$ yr^{-1} and at $z = 2$, $2 - 3\times10^9$ $M_\odot$ and 10 $M_\odot$ yr^{-1}, respectively. Hence, a broad range of mass growth histories is covered by the sample.

2.2.2 Bar analysis

The method used to determine the presence, length, and strength of a bar is based on the azimuthal spectral analysis of surface density profiles. This is obtained by considering the stellar surface density of each galaxy in polar coordinates, decomposed into Fourier components in the form

$$\Sigma(r,\theta) = \Sigma_0(r) + \sum_m A_m(r)\cos(m\theta - \Phi_m(r)), \tag{2.1}$$

where $\Sigma(r,\theta)$ is the stellar surface density, θ is the azimuthal angle given in a rotating frame in which the bar is fixed, and r is the radial distance. $A_m(r)$ and $\Phi_m(r)$ are the associated Fourier amplitude and phase, respectively. $\Sigma_0(r)$ is the azimuthally averaged profile of the stellar surface density. The analysis is performed on a face-on projection: the spin axis of the whole stellar content of the galaxy is used to define the corresponding line of sight. The center of mass of the stars within the central 10 kpc is taken to be the center of the galaxy for the Fourier analysis.

A typical signature of the presence of a bar is the prominence of even components, especially $m = 2$, within the bar region. The identification of a bar is possible by studying the phase $\Phi_2(r)$ which is constant with radius in the bar region, as opposed to a two-armed spiral mode (Φ_m varies linearly with radius for an m-armed spiral mode).

bar identification

After a careful examination of the whole sample at different redshifts, we decide that a bar is present if $\Phi_2(r)$ is constant to within $\pm5^\circ$ around the median value over a large-enough region,

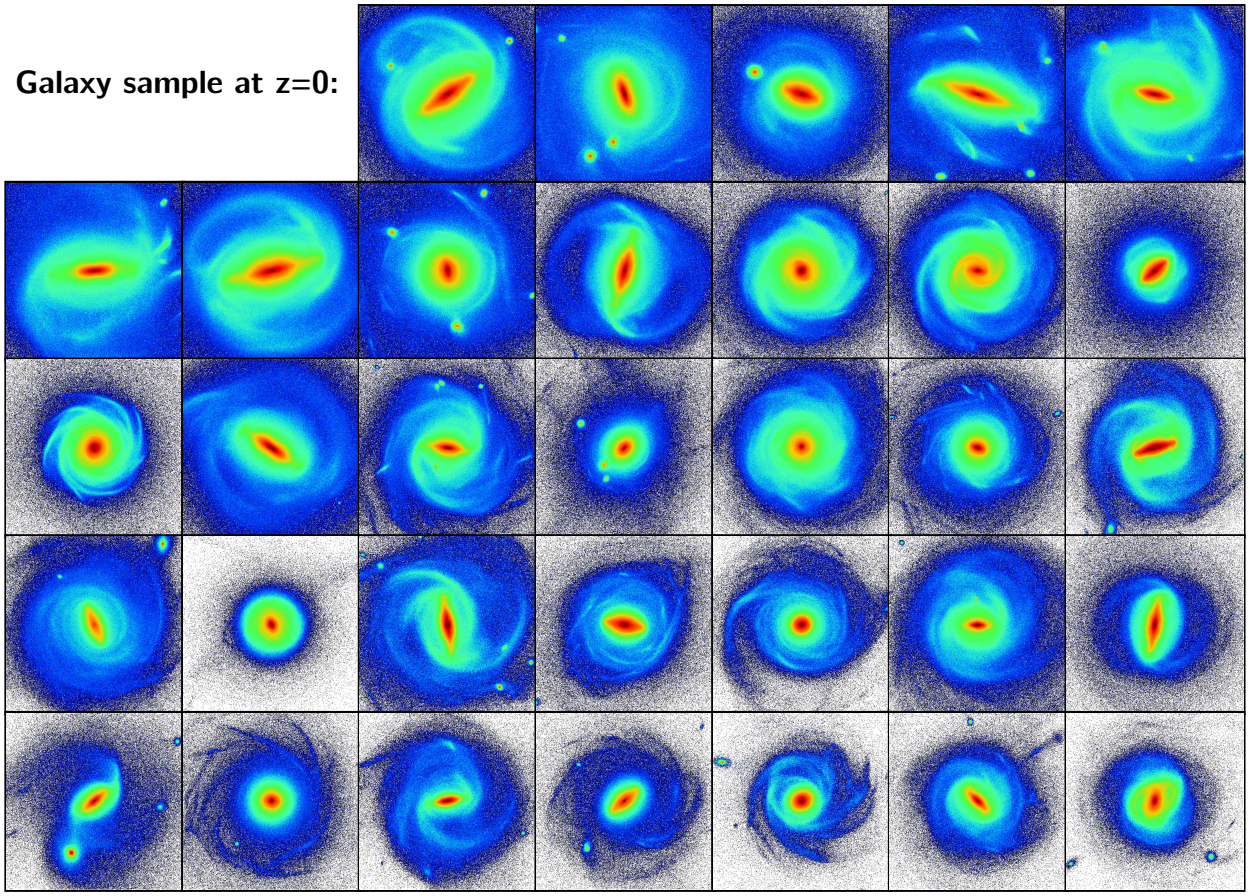

Figure 2.2

Stellar surface density maps (face-on 50×50 kpc^2 projections) of all 33 galaxies in our sample at redshift $z = 0$.

hereafter the "bar region". This bar region should start at radii between 900 pc and 1500 pc, and cover a radial range of at least 1500 pc. We search the starting point of the bar region at $r \geq 900$ pc because central asymmetries or off-centering in the central resolution elements can cause variations of Φ_2 at smaller radii even for visually barred systems, while starting the search at 900 pc is found to never exclude systems that are visually identified as barred. We stop the search at 1500 pc as no bar identified visually starts its $\Phi_2 \simeq$ constant region at larger radii. We impose the bar region (Φ_2 constant to within $\pm 10°$) to cover a radial range of at least 1500 pc because this selects all bars identified visually and this excludes spiral arms, as the latter typically have a variation of Φ_2 of a few tens of degrees over a few kpc. The choice of cutoff in the bar length is given mainly by the resolution. We require the bar to lie within at least three resolution bins used in Fourier analysis. Moreover, typical lengths of significant bars are, in general, ≥ 2 kpc (Barazza et al., 2008). Smaller bars are usually either nuclear bars (which are not the focus of this study) or weak ones. We could possibly miss some of these short and weak bars, but this does not have any impact on our conclusions on bars that would be strong enough to be observed at $z > 0$.

Once a bar region meeting the previous criteria is found, the galaxy is classified as barred. The strength of the bar, measuring the contribution of the bar to the total gravitational potential of the galaxy, is a quantity that is not defined in a unique manner. Different definitions have been used so

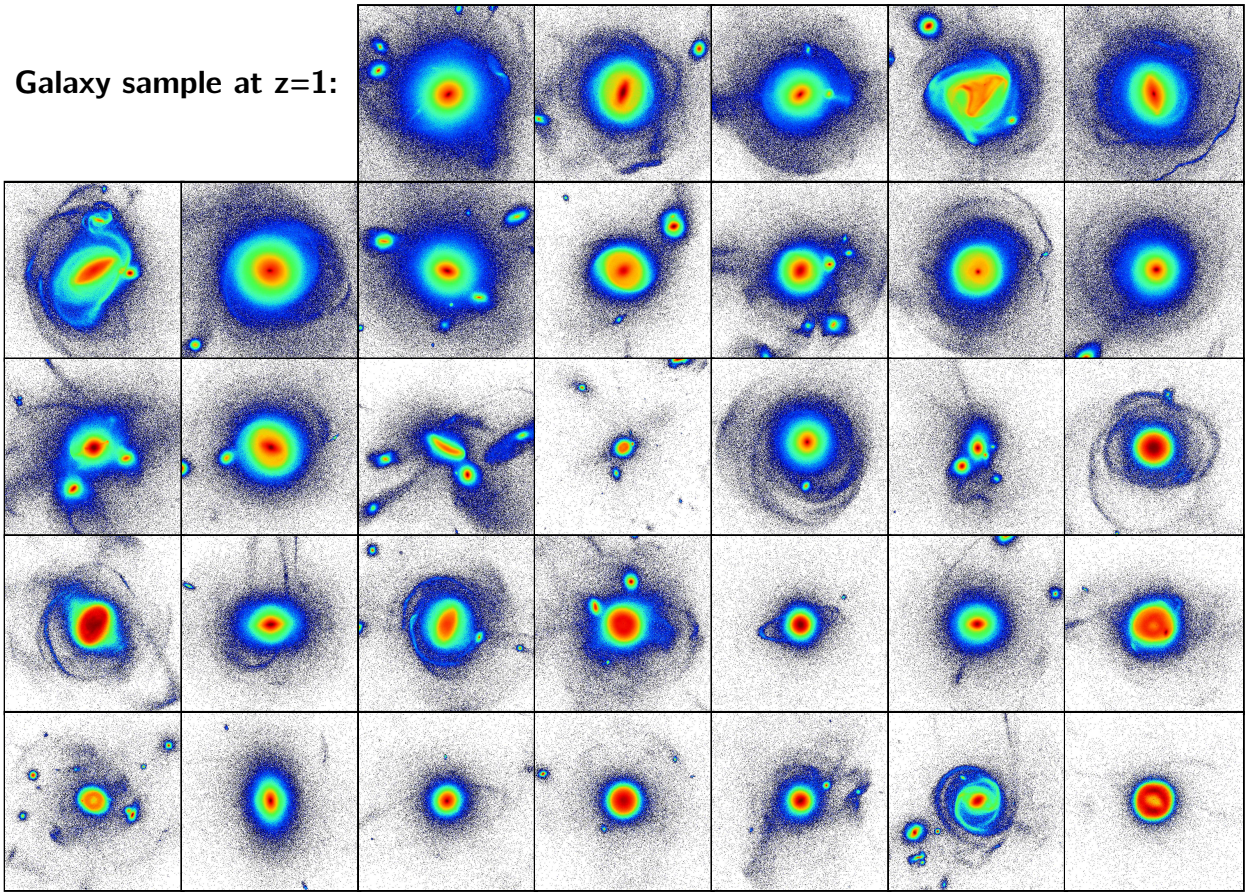

Figure 2.3

Stellar surface density maps (face-on 50 × 50 kpc^2 projections) of all 33 galaxies in our sample at redshift $z = 1$.

far and typically any function of the bar mass, length and axis ratio can be used. We measure the bar strength S following the definition proposed by Aguerri et al. (1998):

bar strength

$$S \equiv r_{\rm bar}^{-1} \int_0^{r_{\rm bar}} \frac{A_2}{A_0}\, {\rm d}r, \tag{2.2}$$

where $r_{\rm bar}$ is the outer radius of the bar region.

Figure 2.5 shows two examples of barred and unbarred galaxies and their corresponding radial profiles of Φ_2. With this technique, the automated identification of barred galaxies is in agreement with all the cases that have been visually examined.

We classify bars into strong bars and weak bars by considering the strength S according to Equation (2.2). In the following, we will distinguish:

① all detected bars, including very weak and short bars,

observable bar

② observable bars, with a strength $S \geq 0.2$, which is the typical detection limit used in observations up to high redshift (e.g. Sheth et al., 2008) – even at z = 0, weaker bars may be confused with spiral arms unless the Φ_2 phase can be probed accurately with very deep imaging (e.g. Block et al., 2002), and

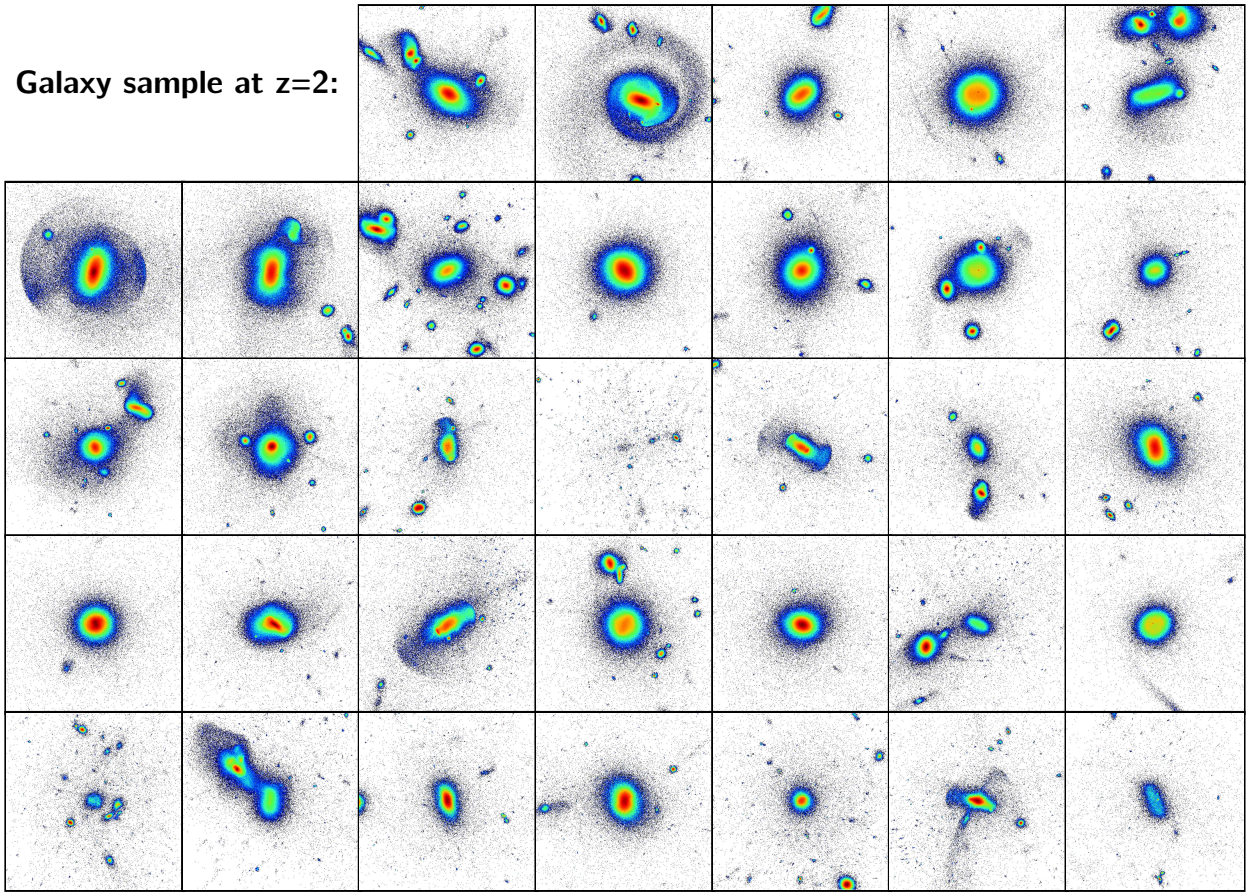

Figure 2.4

Stellar surface density maps (face-on 50×50 kpc^2 projections) of all 33 galaxies in our sample at redshift $z = 2$.

③ strong bars with $S \geq 0.3$, unless specified otherwise. strong bar

At this stage, the identification of bars can still be confused with flattened early-type galaxies, especially for weak bars. A spheroid-dominated galaxy, in the face-on projection defined by the stellar spin axis, can have flattened isophotes in its central regions, which could be identified as a "bar" with our definition, while this corresponds to a triaxial (part of) stellar spheroid rather than a real bar: such an example is shown in Figure 2.6. This occurs only with weak bars, and there are few spheroid-dominated galaxies in our sample at z = 0, so the problem is unimportant there, but such cases are somewhat more frequent at increasing redshift. We thus need to distinguish such "fake" bars from real (if weak) bars. We find that examining two edge-on projections of the stellar mass density unambiguously solves the problem for our whole sample. Real weak bars are found in galaxies with a massive disk component, hence edge-on projections of the stellar density are substantially flat. "Fake" bars are found in galaxies that are spheroid-dominated (at least in the central few kpc) and the edge-on projections are quite round (see Figure 2.7 for an illustration). We thus decide that galaxies for which the strength S of the $m = 2$ mode in two orthogonal edge-on projections[4] is greater or

[4] In these projections, the $m = 2$ mode strength is not a bar strength, but traces the presence of an edge-on disky component in the stellar mass distribution.

equal to 0.3 correspond to real weak bars in disky stellar systems. Other cases are almost round in all projections ($S < 0.3$ in all projections) and are considered to be spheroid-dominated galaxies with "fake" bars, i.e., moderately flattened central regions.

These "fake" bars are rare at low redshift (about 6% of all galaxies) and represent less than 15% of all galaxies at $z > 1.5$. Visual inspection of the results showed that at most two thirds of the "fake" bars are successfully removed by the technique described above at any redshift, so any remaining contamination of the bar fraction would be quite minor. Moreover, most of the results studied in this paper relate to the fraction of bars among disk-dominated galaxies at various redshifts (based on a Sérsic index measurement (Sérsic, 1963), see Section 2.2.3), which is not contaminated by "fake" bars. Indeed, these "fake" bars are flattened spheroid-dominated galaxies, which are naturally removed from the Sérsic index-selected sample of disk-dominated galaxies.

It has been shown by Bournaud et al. (2005) that the $m = 2$ modes are not strongly affected by the dissipation parameters used in sticky-particle codes. We have performed additional checks to estimate the impact of the centering of the galaxy on the result of the Fourier analysis. Changing the in-plane coordinates of the center used for the Fourier decomposition by as much as 300 pc, we do not find any significant change in the detection and strength of bars classified as observable (as defined above). Some galaxies identified as unbarred can appear weakly barred, and weak bars may not be detected anymore, when the center used for the Fourier decomposition is moved by as much as 300 pc. Such ambiguous cases are quite rare for centering offsets smaller than 300 pc. The overall rate of misclassification due to the galaxy off-centering is not larger than 15% and affects mostly bars that would not be observable at high redshift.

2.2.3 Morphology analysis: disk identification

In order to distinguish disk-dominated galaxies from earlier-type ones, we fit the radial profile of the stellar mass surface density with a Sérsic profile of the form

$$\Sigma(r) = a_0 \exp\left[-a_1 \left(\frac{r}{r_0}\right)^{\frac{1}{n}}\right], \tag{2.3}$$

where a_0, a_1 are normalization constants, n is the Sérsic index, r is the radius, and r_0 is the scale length. The fitted range is $r_{50} \leq r \leq 2 \times r_{90}$ for unbarred galaxies and $bar \leq r \leq 2 \times r_{90}$ (or $bar \leq r \leq 2.5 \times i_{25}$ if the length of the bar is shorter than r_{90}) for barred galaxies[5], where r_{50} and r_{90} are radii containing 50% and 90% of mass, respectively, bar is the corrected length of the bar (length of the $bar - 900$ pc), and i_{25} the 25^{th} isophote. The scale-length r_0 is set to the value of r_{50} for each galaxy. Galaxies with a Sérsic index $n \leq 2$ are classified as disk-dominated. The ranges for our set of simulated galaxies are chosen to produce a satisfactory match to the observed morphology of these galaxies on one side and to stay relatively simple with comprehensible physical interpretation on the other side. Indeed, the present classification is reproducible in observations and it agrees with the classification based on a decomposition of disk and bulge components in the six-dimensional phase space by Martig et al. (2012) for the vast majority of the sample. The galaxies presently classified as disk-dominated have a bulge-to-total mass fraction below 35%.

disk dominated

Note that the identification of a disk component to reject "fake bars" (Section 2.2.2) was based on a different criterion. There, we used edge-on projections as we aimed at probing the presence of a substantial disky component hosting the bar, without requiring it to dominate the stellar mass

[5] because the barred region can significantly alter the Sérsic index measurement

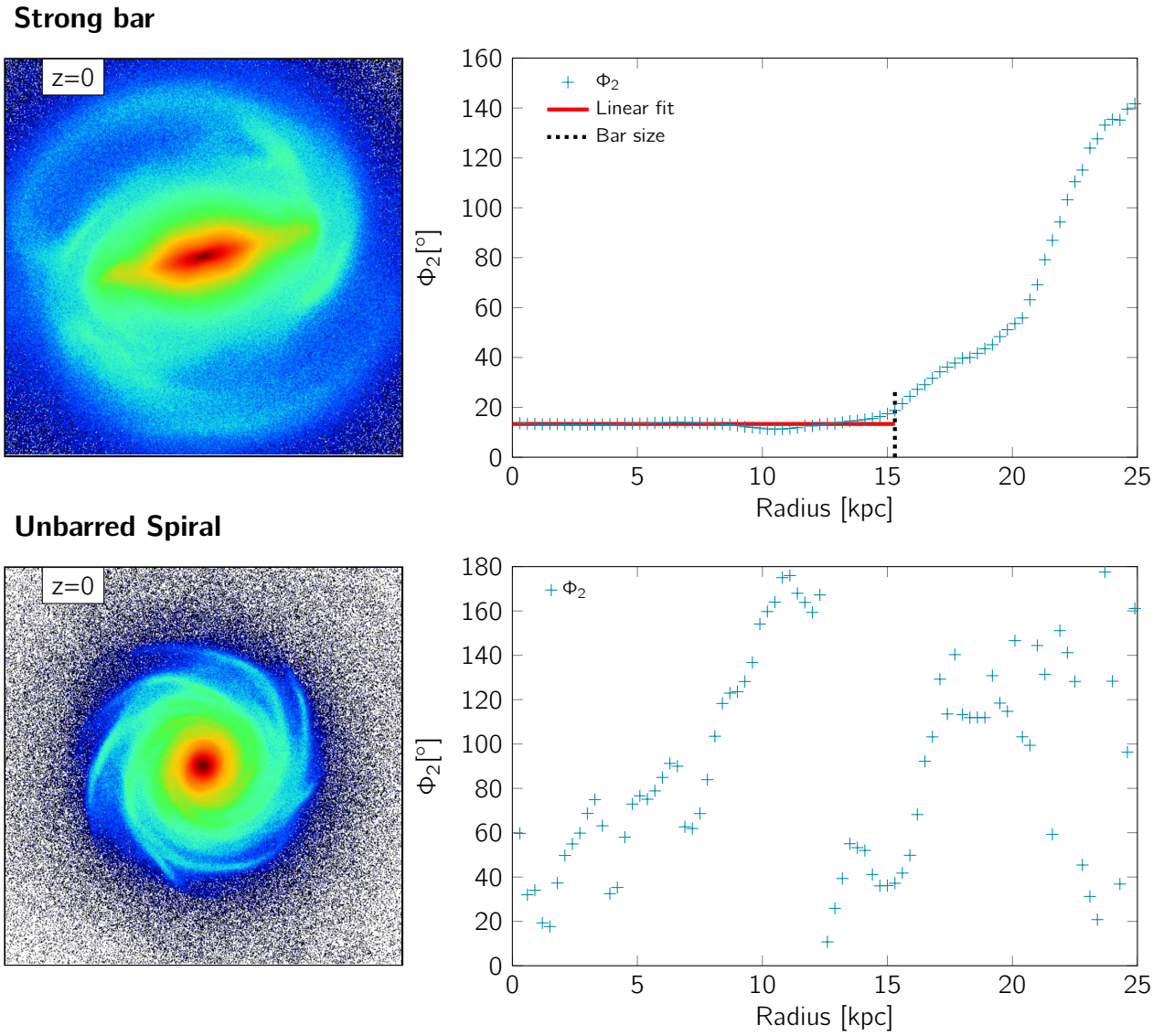

Figure 2.5

Examples of the fitting method results (left panels) and the corresponding surface density maps (right panels) viewed face-on (50×50 kpc^2) for two galaxies in our sample. The top panel shows a (strongly) barred galaxy with the region where the phase Φ_2 is almost constant identified as the bar region, while the bottom panel corresponds to an unbarred galaxy for which no region of constant Φ_2 is detected. The color-coding scale of surface density map is logarithmic going from $\sim 10^{0.5}$ M$_\odot$pc^{-2} for dark blue to $\sim 10^4$ M$_\odot$pc^{-2} for dark red.

distribution. Here, we want to probe whether the whole galaxy is dominated by a disk component typically twice as massive (at least) than the bulge, and we use the Sérsic index of the face-on projection for this. As the Sérsic profile is fitted to the stellar mass density, it is not sensitive to the nuclear concentrations of star formation. Nevertheless, we checked the consistency of the identification with the bulge-to-total ratios obtained by Martig et al. (2012).

Figure 2.8 shows the evolution with redshift of the fraction of disk-dominated galaxies within all 33 simulated galaxies. At $z = 0$, 70% of galaxies are found to be disk-dominated. Their bulge fraction is 23% (from the Martig et al., 2012, decomposition), consistent with classifying them as

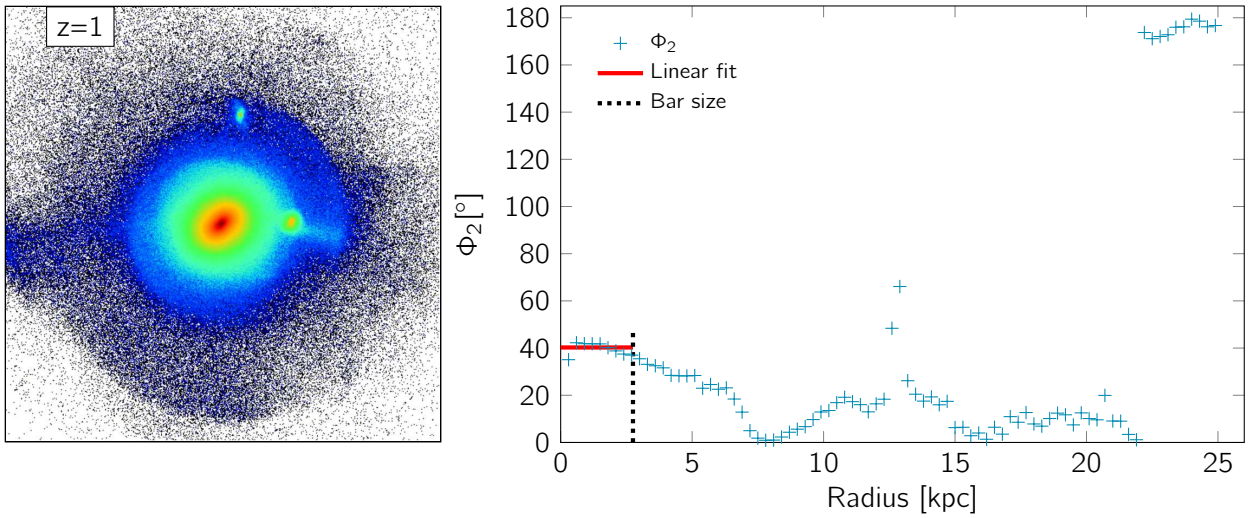

Figure 2.6

Example of a possible "fake" bar. A region of constant Φ_2 is identified at $r \leq 2.7$ kpc (right panel), corresponding to the detection of a short bar. However, the face-on density map (left panel, 50×50 kpc^2) suggests that the identified region could instead be the core of an elliptical, i.e. a "fake" bar. The color coding of the projected density map is the same as in Figure 2.5.

"spiral galaxies". The remaining 30% are galaxies with an average bulge-to-total ratio of 0.43 and could be classified as early-type S0 galaxies. Fraction of disk-dominated galaxies is found to decrease with redshift, down to a fraction of 20% at $z = 1$.

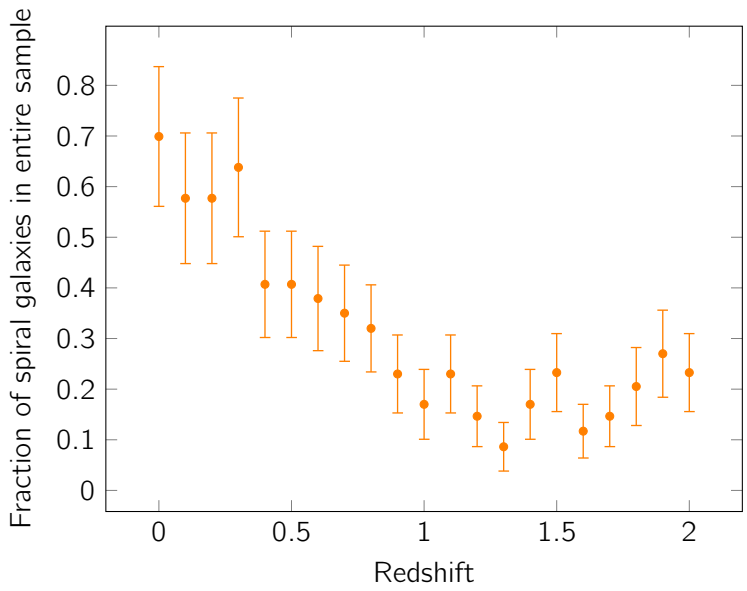

Figure 2.8

Evolution with redshift of the fraction of galaxies classified as spirals according to their Sérsic index. At $z = 0$, about two thirds of galaxies are found to be disk-dominated, while for $z > 1$ this fraction is ~ 0.2 with $\pm$ 1 σ fluctuations. The error bars on measured fractions are Poissonian, the average error bar is attributed to zero fractions.

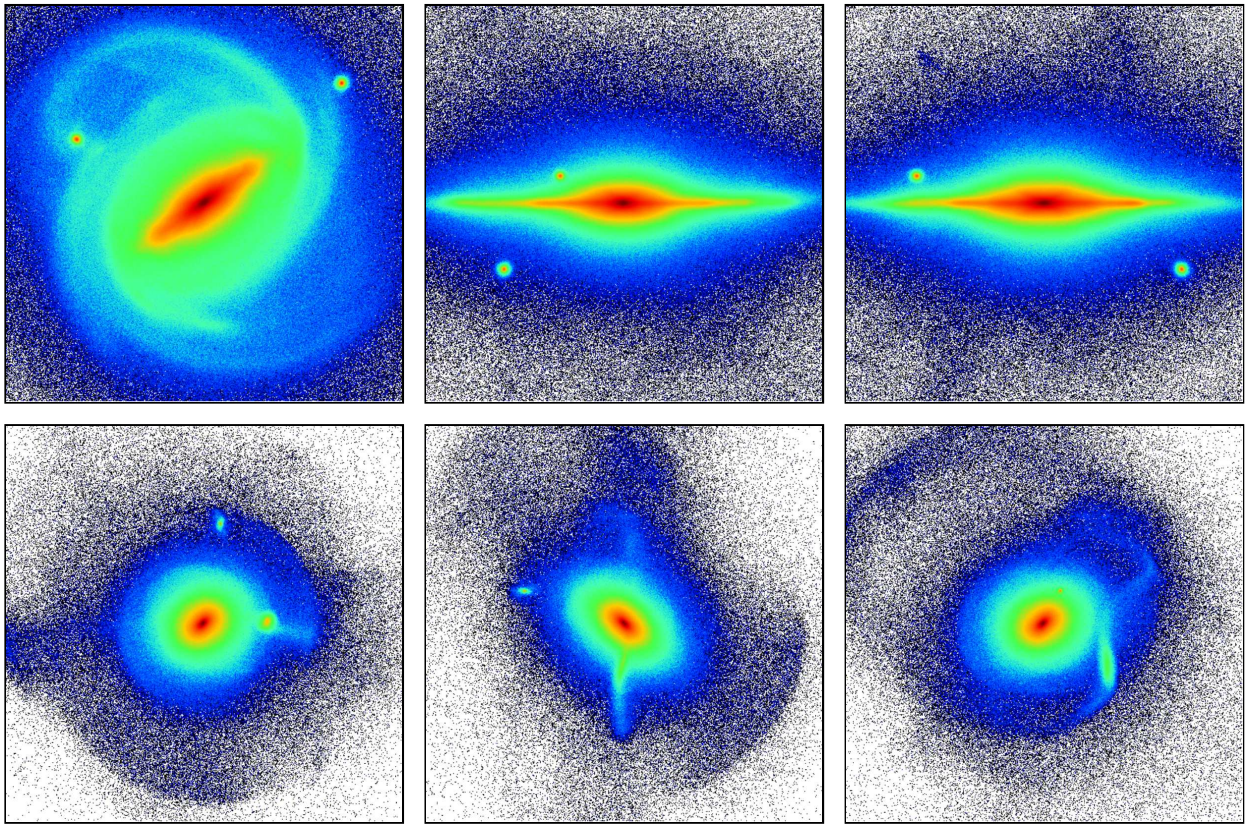

Figure 2.7

Examples of surface density maps (50×50 kpc^2) in three different projections for two simulated galaxies. The corresponding redshift is $z = 0$ and $z = 1$ for galaxies in the top and bottom panels, respectively. If a potential bar is identified in the face-on projection, then the two orthogonal edge-on projections are used to discriminate real bars from triaxial cores in spheroids or "fake" bars. The color coding of the projected density map is the same as in Figure 2.5.

2.3 The bar fraction and its redshift evolution

2.3.1 Bar fraction history

The redshift evolution of the bar fraction among galaxies classified as spirals (i.e., disk-dominated) is shown in Figure 2.9. The total bar fraction (with all values of the bar strength included) among spiral galaxies declines with increasing redshift. At redshift zero, 80%–90% of spiral galaxies contain a bar, while at $z \simeq 1$ this fraction drops to about 50%, and to almost zero at $z \simeq 2$. Similarly, the observable bar fraction (including bars with strength $S \geq 0.2$) and strong bar fraction ($S \geq 0.3$) decline from about 70% at $z = 0$ to 10%–20% at $z \simeq 2$. At $z > 1.5$, observable and strong bars are virtually absent.

The above reported bar fractions are measured among spiral (disk-dominated) galaxies, that is why the steady decline of the total, observable, and strong bar fractions from $z = 0$ to $z \sim 1 - 2$ cannot be attributed to a decline of the fraction of disk-dominated galaxies. As was already mentioned, the fraction of disk galaxies declines with increasing redshift (Figure 2.8), and consequently, the bar fraction among all galaxies declines even more rapidly with redshift (from $\approx 60\%$ at $z = 0$ to less than 5% at $z = 1$ for strong bars, Figure 2.10), but the decline of the bar fraction occurs even

considering only disk-dominated galaxies.

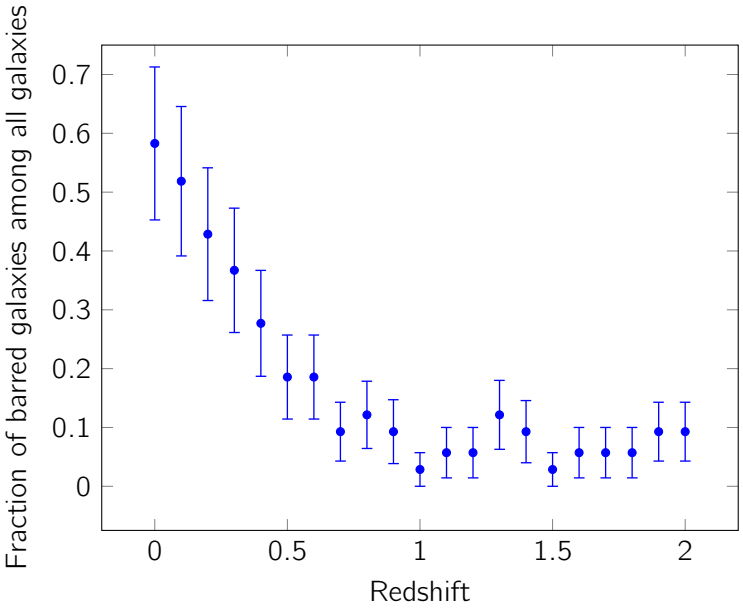

Figure 2.10
Evolution with redshift of the fraction of barred galaxies among all galaxies, where only strong bars ($S \geq 0.3$) are considered. Note that the bottom panel of Figure 2.9 showed strong bars among galaxies classified as disk-dominated (Sérsic index $n < 2$).

In Figures 2.11 and 2.12, we compare our data to the observations of the $z = 0 - 0.8$ sample in COSMOS and the Sloan Digital Sky Survey (SDSS) by Sheth et al. (2008), and the $z = 0.6 - 1.6$ sample from the CANDELS survey by Herrington et al. (2012) (only in Figure 2.11). Models and data are in quantitative agreement for the redshift evolution of the fraction of both observable and strong bars[6]. Note that Sheth et al. (2008) used an ellipse-fitting method to measure bar strengths, as opposed to Fourier decomposition method that we used. However, this technique was shown to lead to quantitative results consistent with Fourier decomposition method (Block et al., 2002, Laurikainen et al., 2002), as well as to visual estimates by Sheth et al. (2008) themselves. Note also, that the fraction of bars that could be robustly observed at $z > 0$, i.e. bars having a strength larger than 0.2, is lower than the total fraction of bars identified in the simulations, including the weakest bars, especially at redshift $z \sim 1$ (compare the top panel of Figure 2.9 and e.g. Figure 2.11), nevertheless, both fractions follow a similar evolution with redshift.

Observations of the bar fraction are typically limited to redshift $z \lesssim 0.8$. To date, two exceptions exists, the CANDELS sample by Herrington et al. (2012) with the studied redshift range $z = 0.6 - 1.6$ and a recent HST-COSMOS sample by Melvin et al. (2014), exploring the bar fraction within the redshift range $z = 0.4 - 1.0$. Our models agree with the observed trends up to those redshifts, and suggest that the observed decline should continue at higher redshifts, with observable bars being almost absent at $z \geq 1$.

[6]Defined in Figure 2.12 as bars having the strength $S \geq 0.4$, for consistency with Sheth et al. (2008).

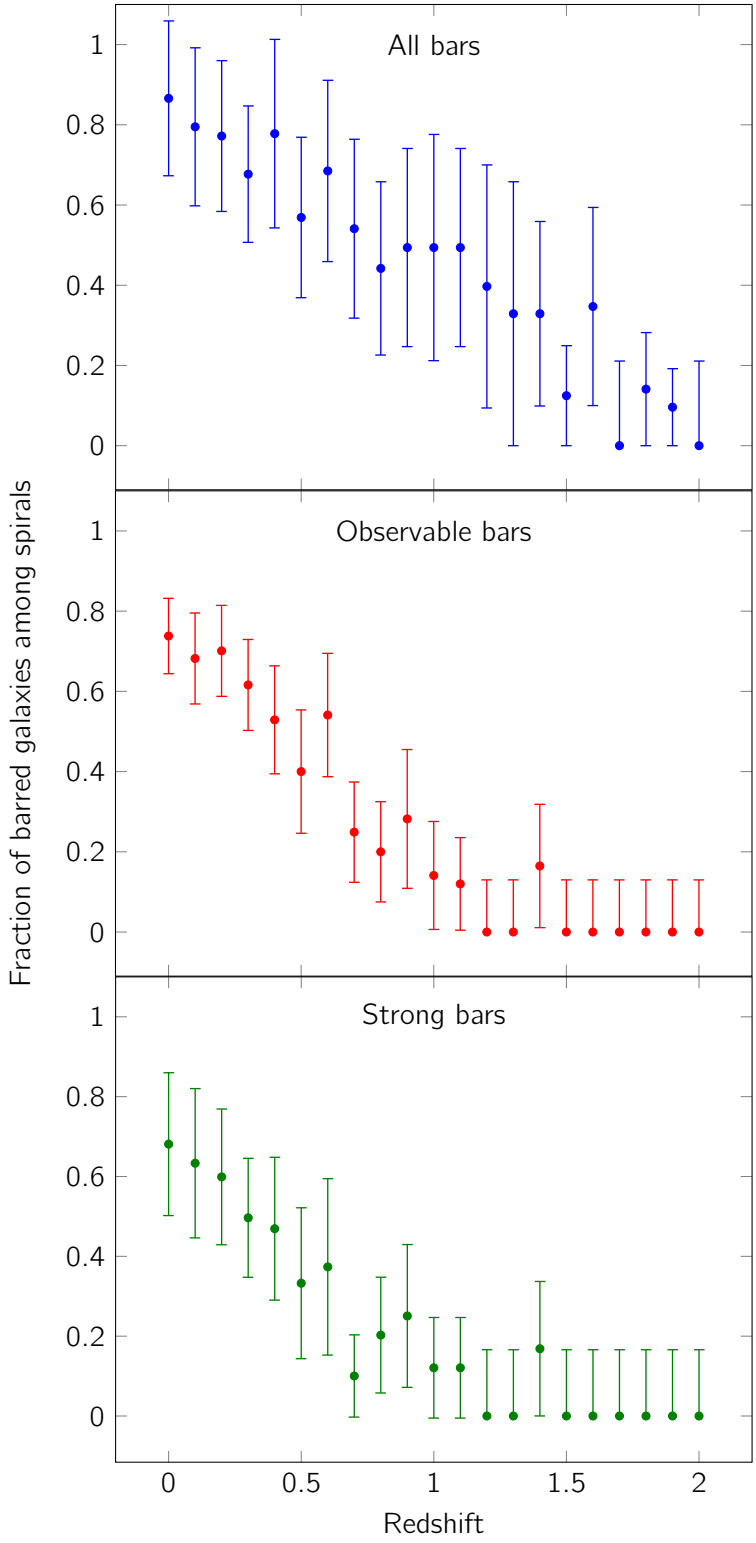

Figure 2.9

Evolution with redshift of the total bar fraction including even weak bars (top panel), observable bar fraction (middle panel), and strong bar fraction (bottom panel) among spiral galaxies (i.e., galaxies with a Sérsic index $n < 2$).

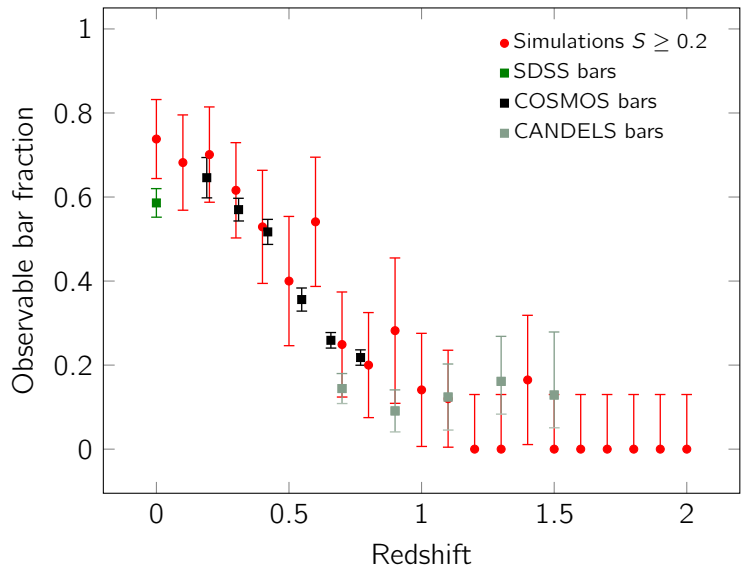

Figure 2.11
Comparison of the redshift evolution of the bar fraction in spiral galaxies with COSMOS and SDSS data (Sheth et al., 2008) and CANDELS data (Herrington et al., 2012). The lower limit on the bar strength of simulated galaxies is set to 0.2, so that only observable bars are shown. The error bars are calculated as in (Sheth et al., 2008), assuming binomial statistics.

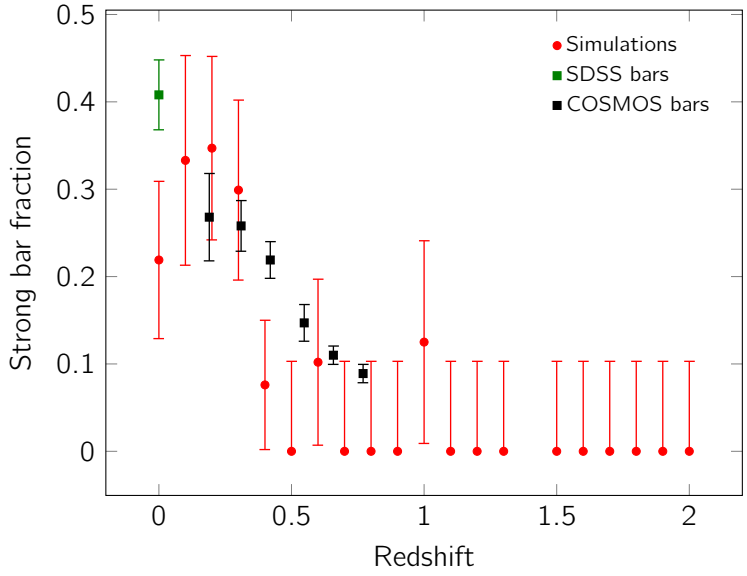

Figure 2.12
Comparison of the redshift evolution of the fraction of strong bars (we are here considering strengths greater than 0.4) in spirals of COSMOS and SDSS data (Sheth et al., 2008). The error bars are calculated as in Figure 2.11.

2.3.2 Stellar mass dependence

We next examine the mass dependence of the redshift evolution of the bar fraction. To this purpose we divide galaxies into two mass bins, above and below the median mass of the sample in each redshift bin. The redshift bin size was adjusted so that the Poissonian error in each bin does not exceed 20%. Figure 2.13 (left panel) shows the redshift evolution of the total bar fraction among spiral galaxies for low-mass and high-mass systems separately.

downsizing

We find that bars form later in lower-mass galaxies, in a "downsizing"-like mode, which is consistent with the observations of Sheth et al. (2008). As a possible explanation, these authors proposed that merging activity, which is more common at high redshift, could affect low-mass systems more severely by heating them and thus delaying or preventing bar formation. However, mergers alone cannot account for the observed trend in our models. First, major mergers of spiral galaxies often result in the formation of spheroid-dominated galaxies, even at high redshift (Bournaud et al., 2011a). We

find that the majority of disk galaxies are barred today, and bar formation is found in our sample even when considering only disk-dominated galaxies with low Sérsic indices, so the process should be independent of the occurrence of major mergers. Second, minor mergers and interactions can cause the destruction *or* formation of a bar, depending in particular on the orbital parameters (Gerin et al., 1990, Berentzen et al., 2003, 2004). Since bars at high redshift ($z \gtrsim 1$) are rare, any net effect of mergers and/or interactions should be bar formation in previously unbarred systems, rather than bar destruction in previously barred systems.

Our results suggest that the epoch of bar formation is the typical epoch at which galaxies start to be dominated by a kinematically cold, thin stellar disk (see Section 2.4). Thus a possible explanation of the "downsizing" of bar formation we see over the entire sample could be, that these modern spiral disks themselves form later in lower-mass galaxies (see Figure 2.13). The continuation of rapid mass accretion onto lower-mass systems down to lower redshift could keep their disk violently unstable, with giant clumps and irregular structures rather than bars, as further discussed in Section 2.7. More massive spiral galaxies seem to be largely in place and already disk-dominated at $z \sim 1$ (e.g. Sargent et al., 2007).

We also find that at intermediate redshift ($z \lesssim 0.6$), the fraction of bars in high-mass systems stays roughly constant from $z \sim 0.6$ to $z = 0$ at a relatively high value of ∼70%, while in low-mass galaxies continues to increase with decreasing z. At high redshift ($z > 1$), the most massive disk galaxies do contain some bars (although relatively rare, and in general too weak to be easily observable), while lower-mass disk galaxies are systematically unbarred.

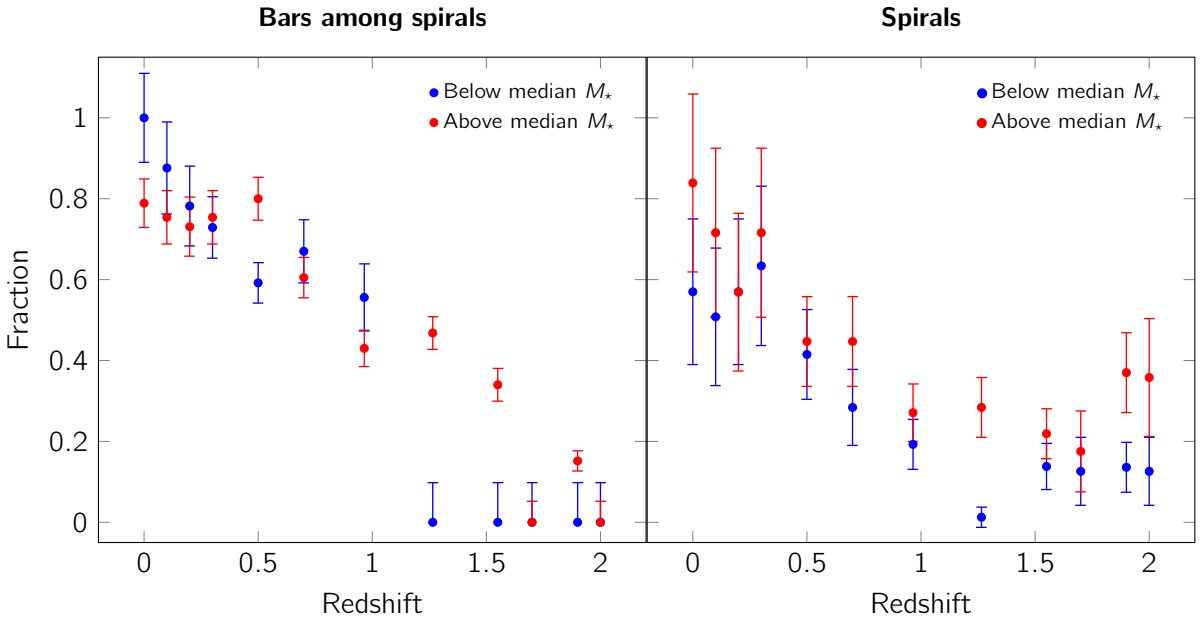

Figure 2.13

Evolution with redshift of the fraction of barred galaxies among spiral galaxies (left) and spiral galaxies among all galaxies (right) according to their mass. In each redshift bin, galaxies are classified as having a stellar mass above or below the median value, which is 6×10^{10} $M_\odot$ at $z = 0$, 2.5×10^{10} $M_\odot$ at $z \sim 1$, and 4×10^9 $M_\odot$ at $z = 2$. Those ∼ 70% of galaxies in our sample that are not classified as spirals at $z \geq 1$ are not just ellipticals, but also compact objects, irregular clumpy types and some mergers.

2.4 The emergence of massive thin disks

We have found that while the total bar fraction and strong bar fraction are both high at low redshift, they become very small or close to zero at $z \geq 1$. Moreover, most of the bars found at $z > 1$ in the simulations are quite weak and would not even be considered with a bar strength threshold at $S = 0.2$, hence they would be hardly observable at high redshift (see Figure 2.11).

In Figure 2.8, we have shown the redshift evolution of the fraction of disk-dominated[7] galaxies in our simulation sample. Surprisingly, this evolution is quite similar to the redshift evolution of the fraction of strong bars or moderate (observable) bars (see Figure 2.8 compared to the bottom panel of Figures 2.9 and 2.11). This suggests that the epoch of bar formation is also the epoch at which galaxies that are presently spirals start to be dominated by stellar disks. Indeed, at higher redshift, the progenitors of these present-day spirals are sometimes disk-dominated, but are often spheroid-dominated, or have irregular morphologies such as clumpy disks (i.e., short-lived unstable disks), or are interacting and merging systems (see Martig et al., 2012, for a thorough study of the structural evolution of the simulated galaxies in the same sample).

violent phase

secular phase

Our results, together with those obtained in Martig et al. (2012), indicate that the present-day spiral galaxies grow mostly through two phases. During an early "violent" phase at $z > 1$ systems are often disturbed by major mergers or multiple minor mergers as well as violent disk instabilities (giant clumps). During this phase, the galaxy morphology can evolve from disk-dominated to a spheroid without being necessarily stabilized toward the final disk-dominated structure. At $z < 1$, present-day spirals evolve mostly through a "secular" phase when the morphology is generally stabilized to a disk-dominated structure (Martig et al. 2012). The bulge growth is then only slow and limited as important mergers and violent disk instabilities become rare, and almost absent after $z \simeq 0.7$.

Martig et al. (2012) have shown, that there is no correlation between the morphologies and the disk/bulge fractions between this early violent phase ($z > 1$) and the present day. The bulge/disk fractions become more and more tightly correlated with the final $z = 0$ values when the systems enter the secular phase after $z \approx 1$ (see Figures 2.14a and 2.14b). Stars formed or accreted in the early violent phase end up mostly in the thick disk, stellar halo, and bulge at redshift zero. On the other hand, stars that form in the secular phase at $z < 1$ mostly grow the modern thin spiral disk, with a substantial, but non-dominant contribution to late bulge growth, especially in barred systems (see Section 2.6 for late secular bulge growth).

For the vast majority of galaxies in our sample, spanning stellar masses of 1×10^{10} to 2×10^{11} $M_{\odot}$, the epoch of bar formation covers a relatively narrow redshift range $z \simeq 0.7-1$. The comparison with the structural evolution shows that the (observable) bar fraction is constantly very low in the early violent phase of spiral galaxy formation. During this phase disk-dominated systems can be present, but are generally destroyed/reformed over short timescales, and uncorrelated with the final disk fraction. But once spiral galaxies enter their secular phase at $z \leq 1$, bars rapidly form and consequently the bar fraction rapidly raises. This corresponds to the epoch at which the final thin spiral disk starts to form and dominate the stellar structure of these galaxies: the disk and bulge fractions can continue to evolve down to $z = 0$, but in this phase the disk is not destroyed/reformed anymore, although the bar itself may sometimes be destroyed/reformed. At this point, the formation of a long-lived massive thin disk allows the bar to form in most of the progenitors of today's spirals.

The interpretation of the bar fraction in our simulation sample is primarily that the epoch of the emergence of bars traces the epoch at which modern thin disks are established and start to dominate the stellar mass distribution of present-day spirals. Observations have so far confirmed the redshift

[7] According to criterion defined in Section 2.2.3.

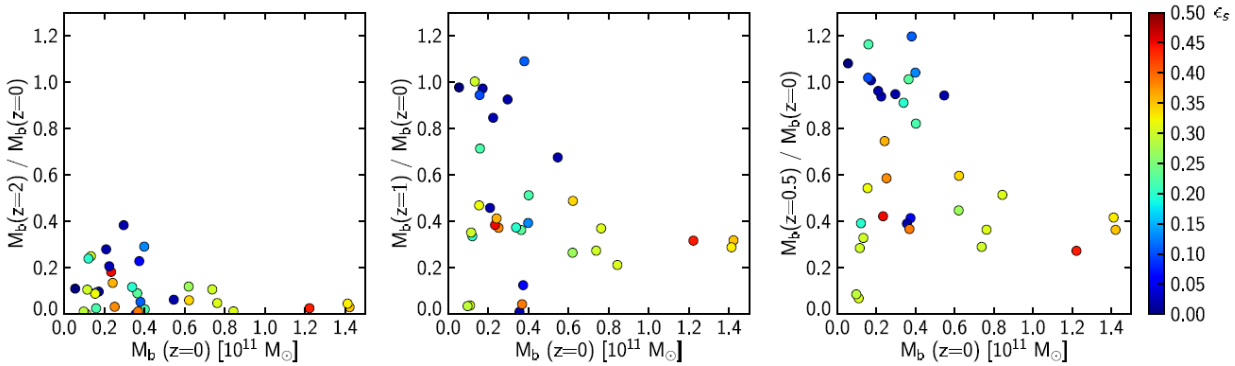

(a) Evolution of the mass of the dispersion-dominated component with redshift

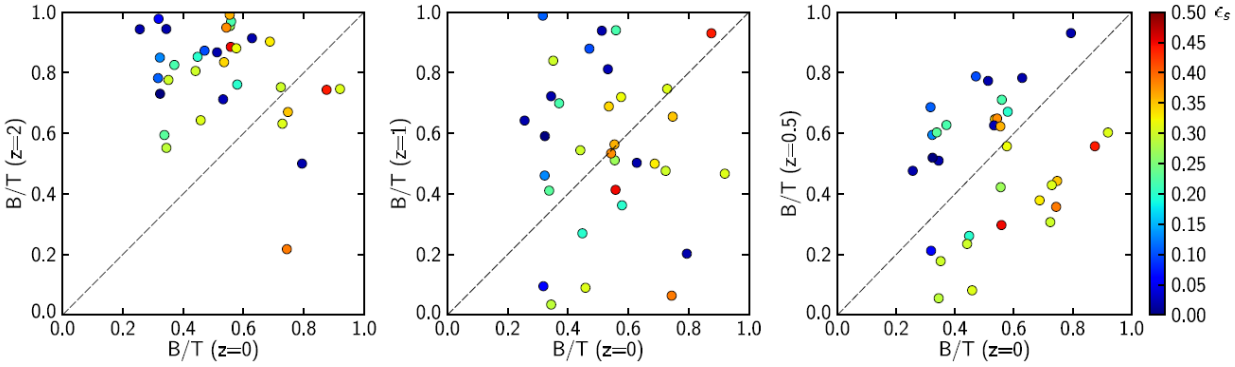

(b) Evolution of the B/T ratio with redshift

Figure 2.14

From Martig et al. (2012). (a) Evolution of the mass of the dispersion-dominated component (bulge+bar) with redshift. The panels show the fraction of the mass of this component that was already in place at different redshifts (left: $z = 2$; middle: $z = 1$; right: $z = 0.5$) as a function of the final (at $z = 0$) bulge+bar mass. The color coding indicates the value of ϵ_s (the average circularity[8] for stars in the central spheroid component, with value zero corresponding to a non-rotating component) at $z = 0$ for each galaxy, it is thus related to the amount of rotation in the central regions, i.e., to the presence of a bar or a rotating bulge. (b) Evolution of the bulge+bar(B)-to-total(T) ratio with redshift. The panels show B/T at different redshifts (left: $z = 2$; middle: $z = 1$; right: $z = 0.5$) as a function of B/T at $z = 0$. The color code is the same as in Figure 2.14a.

evolution of the bar fraction up to $z \sim 1 - 1.5$. If this trend is confirmed for higher redshifts that need to be probed, it could suggest that the same interpretation applies to observed bars, namely that their emergence traces the typical epoch at which spiral galaxies establish their modern disk-dominated structure at $z = 0.8 - 1$ (for present-day stellar masses in the $10^{10} - 10^{11}$ $M_\odot$ range). This hypothesis of a two-phase formation history traced by the emergence of bars is further discussed and illustrated with representative examples in Section 2.7.

[8] $\epsilon = j/j_{\rm circ}(R)$, with $j_{\rm circ}(R)$ defined as the angular momentum a particle would have if it were on a circular orbit at its current radius

2.5 Bar lifetime

In Section 2.3.1, we have seen that bars start to steadily appear at redshift $z \sim 0.8 - 1$. A closer examination of individual bars formed in this redshift range reveals that their strength often remains roughly constant down to redshift $z \sim 0$. Interesting question to ask is whether this is because the conditions are favorable for the strength being intrinsically constant, or would those bars become weaker or even destroyed in complete isolation if they would not have been maintained by external infall as proposed by Bournaud & Combes (2002). To try to answer this question, we examine the influence of the external accretion on the lifetime of a bar in a realistic cosmological context (unlike the idealized accretion used by Bournaud & Combes 2002).

Four galaxies, hereafter labeled Galaxy 1 to Galaxy 4, with representative bar strength histories are selected in our sample. We next run new simulations for these galaxies without external accretion once their bar has formed.

long-lived bar

In Figure 2.15, the two galaxies (Galaxy 1 and 2) with very similar redshift evolution of the bar strength with and without accretion are shown. The bar forms at $z \sim 1.3$ and $z \sim 1$ in these galaxies, respectively. Once formed, the bar keeps roughly constant strength down to $z \sim 0$ in both cases, with and without accretion. These bars are intrinsically long-lived and their evolution is not significantly influenced by late mass accretion.

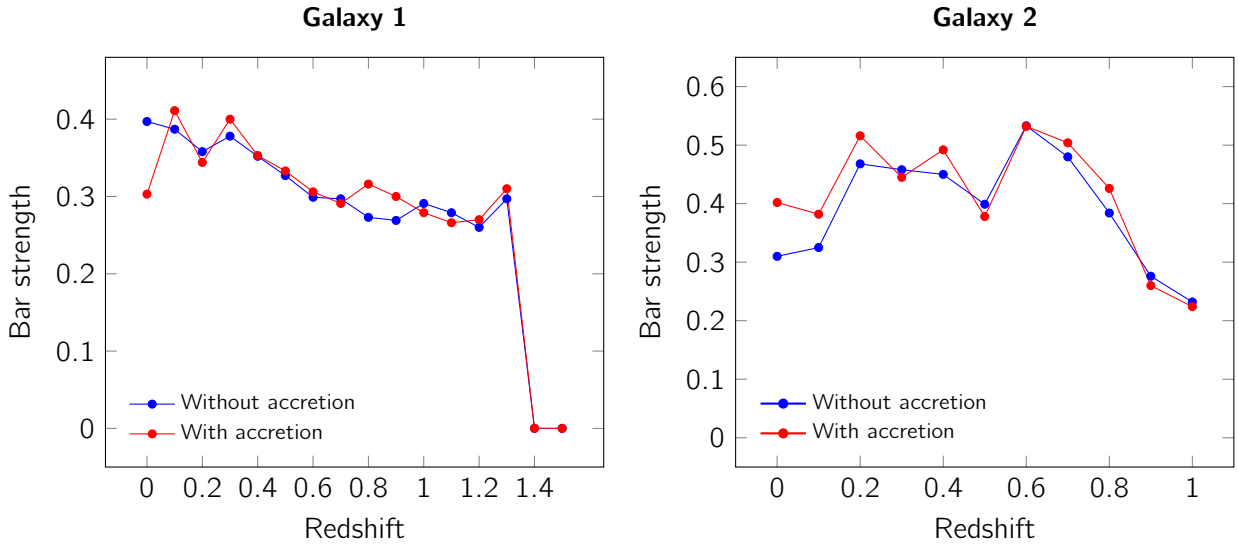

Figure 2.15

Examples of two galaxies with similar redshift evolution of bar strength with and without accretion. In both cases, the two galaxies host long-lived strong ($S \gtrsim 0.3$) bars that form at $z \gtrsim 0.8$. The strength of bars does not evolve significantly. The external accretion hence does not seem to be needed to maintain a strong bar down to $z = 0$. Here and in all following figures, the null value for the bar strength is to be interpreted as no bar detection rather than the exact value obtained by Equation (2.2).

short-lived bar

In Figure 2.16, the two other galaxies (Galaxy 3 and 4), with the bar strength evolution this time influenced by the external accretion, are shown. Galaxy 3 (left panel) hosts a weak bar (with $S \lesssim 0.2$) that dissolves and reforms several times in the simulation with accretion. When the external accretion is shut down, the bar evolution is different, but the overall trend is similar: bar undergoes several episodes of dissolution and formation. When the bar forms, it remains weak without significant

evolution in the strength parameter.

Galaxy 4 (right panel) represents an example, in which external accretion is necessary to maintain a strong bar down to $z = 0$. In the simulation with accretion, this galaxy forms a bar at $z \sim 0.8$. The bar initially grows in strength, but it becomes strong (with $S > 0.3$), it stays strong down to $z \sim 0$. Without the external accretion, the bar maintains similar strength ($S \gtrsim 0.3$) down to $z \sim 0.2$, after which it weakens significantly.

Hence, bars that form after $z \sim 0.8 - 1$ are mostly long-lived, often without requiring external accretion, which is probably explained by the fact that these bars form once the gas fraction is relatively low (it is easier to dissolve bar when gas fraction is high). There are, however, cases where the bar evolution is influenced by external mass infall and late cosmological accretion below redshift one, including cases where the presence of a strong bar at $z = 0$ is only achieved through external accretion.

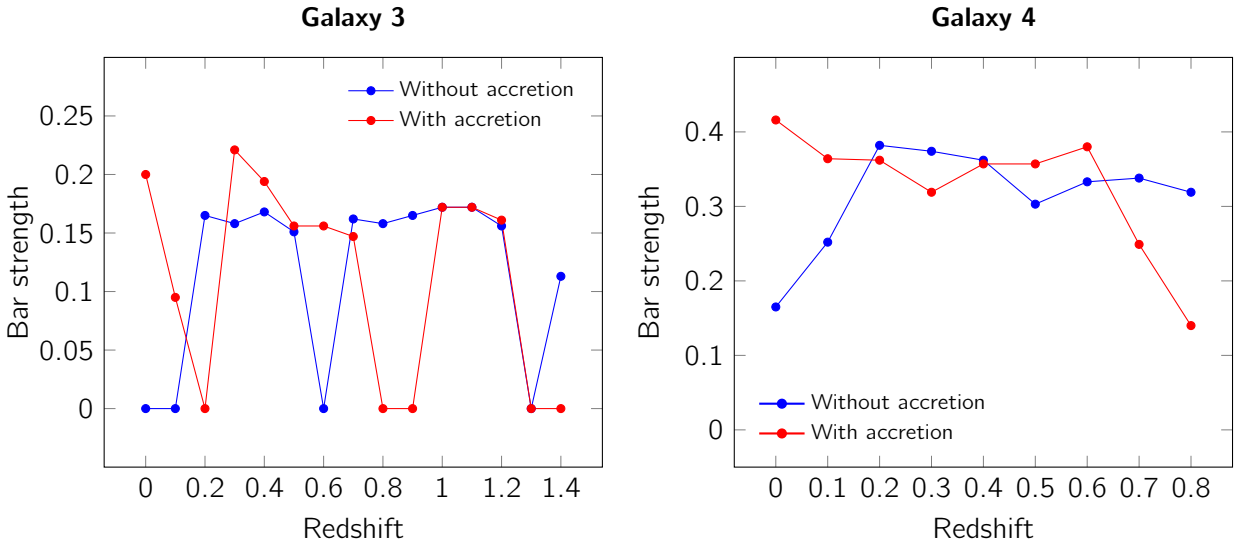

Figure 2.16

Examples of two galaxies with different redshift evolution of bar strength with and without accretion. Galaxy 3 (left panel) hosts a weak bar that forms at $z > 1$. Detailed redshift evolution of the bar strength in fiducial simulation is different than in the case without external accretion, but the overall behavior is similar: the bar undergoes several episodes of formation and dissolution. Galaxy 4 (right panel) hosts a strong bar from $z \sim 0.6$ down to $z \sim 0$ in fiducial simulation, but weakens significantly from $z \sim 0.2$ when external accretion is shut down.

At the opposite, there are bars that form early ($1 < z < 2$), but these are relatively rare and have shorter lifetimes. They can either dissolve spontaneously, as is the case of the Galaxy 5 in Figure 2.17, or be destroyed by mergers, which is the case for the two other galaxies shown in this figure (Galaxies 6 and 7).

The shorter bar lifetime at $z > 1$ compared to $z < 1$ can be explained by the higher gas fractions at these early epochs, making it easier to dissolve a bar by gravitational torquing and mass concentration (Bournaud et al., 2005). The early bars (formed at $z > 1$) tend to undergo several cycles of formation and destruction more commonly at higher redshifts, where they are also more rare. After the reformation, bars eventually persists down to redshift zero, owing to late cosmological infall and buildup of a massive thin disk.

Overall, it appears that external gas accretion is required to maintain low-redshift bars only in a limited fraction of the sample, but is generally required to reform early bars at $z \sim 1$, which tend to be intrinsically short-lived.

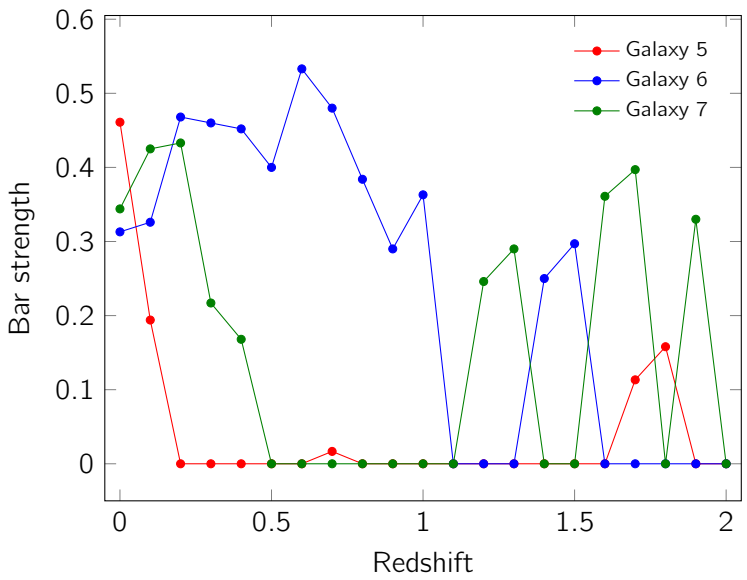

Figure 2.17
Examples of three simulated galaxies with an early bar formation ($1 < z < 2$). Galaxy 5 (red) hosts a bar that is destroyed spontaneously, rapidly after its formation at $z \sim 2$. A new bar reforms at low redshift ($z \sim 0.2$). The bars developed at $z \gtrsim 1$ in Galaxies 6 and 7 (blue and green) are destroyed by mergers, but reform later. The early formed bars seem to be short-lived, although they can reform later. The high frequency at which the bar is destroyed and reformed between $z > 1$ and $z < 2$ in Galaxy 7 is rather rare.

2.6 The role of bars in (pseudo-)bulge growth

Bars have been proposed by several authors (e.g. Athanassoula, 2005, Heller et al., 2007, Fisher et al., 2009) to play an important role in the formation of the pseudo-bulge by triggering the gas inflows to the central regions of the galaxy. In this Section, we address the impact of the bar in the growth of the bulge.

The identification of the bulge is made using GALFIT (Peng et al., 2002, 2010) for 28 (out of 33 analyzed so far) galaxies at $z = 0$. The remaining five galaxies are excluded from the study because their complex structure did not make it possible to achieve a satisfying and unique GALFIT decomposition. Relatively low Sérsic indices of the majority of bulges indicate that they are pseudo-bulges rather than classical, merger-built bulges (see Martig et al., 2012, for a detailed study of the simulated galaxies in our sample).

We compute the averaged normalized distribution of the redshift formation of stars that are present in the bulge of a given galaxy at $z = 0$. For galaxies that host a bar, this distribution is computed with respect to the moment of the apparition of the bar, which is thus interpreted as the average redshift at which the bar forms.

In Figure 2.18, we show the normalized age distribution of stars in the bulge for barred and unbarred galaxies (left and right panels, respectively), together with the theoretical mass accretion rate that scales with redshift as $(1+z)^{2.25}$ (Neistein et al., 2006). We note a slightly larger excess of stars in barred galaxies with respect to the infall rate as compared to that of unbarred galaxies.

If we quantify the impact of the influence of a bar on the growth of the bulge in terms of the ratio of the area of the distribution over the region between the redshift $z = 0$ and the average redshift of the bar formation over a redshift range of $0 \leq z \leq 2$, we find 24% for barred galaxies and 11% for galaxies without a bar. This very qualitative comparison suggests that the presence of a bar has an impact on the growth of the bulge.

Even though it is difficult at this stage to quantify the effect of the bar on the bulge more precisely, both qualitative and quantitative study suggest that the bar plays a role in the growth of the bulge as the cosmological accretion rate of baryons alone does not seem to be sufficient to explain this overabundance of stars forming in the pseudo-bulge at late epochs.

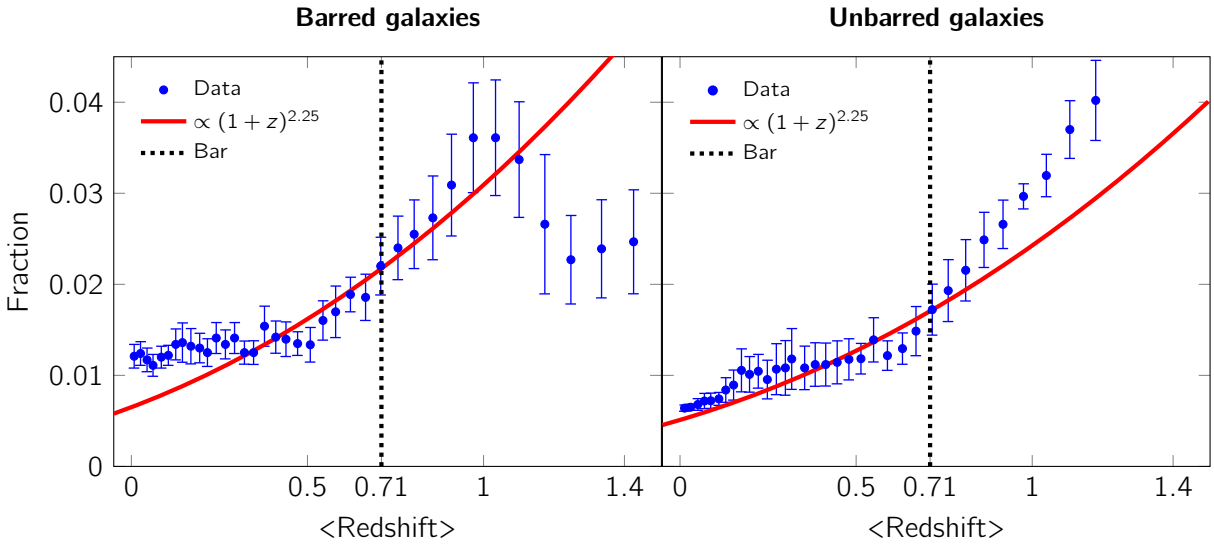

Figure 2.18

Normalized bulge stellar age distribution. The two panels show the age distribution for stars in the bulge at $z = 0$ for barred (left panel) and unbarred (right panel) galaxies. The fitted theoretical total mass accretion rate that scales as $(1 + z)^{2.25}$ (Neistein et al., 2006) is shown too (the red line). The black dashed line represents the average time at which the bar is formed. All stars located to the left of this line are stars younger than the bar. We show this average bar formation redshift also for unbarred galaxies for comparison.

2.7 Bars as tracers of spiral galaxy formation

In our models, bars in present-day spirals are rare and only weak at high redshift ($z > 1$), but once they emerge at $z \sim 1$, they rapidly become ubiquitous at lower redshift. We have suggested (see Section 2.4) that this epoch of the bar emergence corresponds to the transition between an early "violent" phase, characteristic for high redshift down to $z \simeq 0.8 - 1$, and a late "secular" phase at lower redshifts. Indeed, the morphology of the progenitors of today's spirals evolves rapidly and is uncorrelated with their final structure in the proposed "violent" phase at $z > 1$ (see Martig et al., 2012), with mostly the thick disk and stellar spheroids forming in this phase, while after $z < 1$ the thin disk grows and the structural parameters such as the bulge and disk fractions become well correlated with their final values at $z = 0$.

The evolution of bars can be influenced by different effects of the dark matter halo (see e.g. Berentzen & Shlosman, Machado & Athanassoula, 2006, 2010 for the effects of the shape of halo; and Weinberg & Katz, Sellwood, 2007, 2008 for the effects involving more general halo properties). During its evolution with redshift, dark matter halo affects the evolution of the entire galaxy, in particular the bar, which in turn influences the halo itself. Bar formation can thus be reinforced or delayed depending on exact halo properties. However, such effects should be resolved by our

simulations. The key epoch of bar formation appears to correspond mostly to the evolution of baryonic properties in our analysis.

In Figure 2.19, we show three representative examples of morphological evolution at different redshifts. One, which is disk-dominated at $z > 1$, but where violent disk instabilities, including giant clumps, destroy this early disk into a thick disk and spheroid. Second one, which is spheroid dominated with a major merger at $z \sim 2$, and a third one which is also spheroid dominated with several minor mergers at $z \simeq 1 - 2$. This is illustrative of the "violent phase" at $z > 1$. Other works have shown that high-redshift disks have high gas fractions and are violently unstable with giant clumps and transient features, but do not frequently develop bars (e.g. Bournaud et al., 2007, Ceverino et al., 2010, Bournaud et al., 2014). In addition, such instabilities destroy any thin disk that would have started to grow, while major mergers that can reform some disk components (e.g. Robertson et al., 2006) mostly convert disks into spheroids, even in high-redshift conditions (Bournaud et al., 2011a).

Hence, no massive thin disk can stabilize and develop a substantial bar before redshift one in the majority of our sample, as in the two representative examples shown in Figure 2.19. After $z = 1$, mergers with mass ratios larger than 5:1 are almost absent from our sample, diffuse gas accretion occurs at a much lower rate and the rate of stellar bulge growth drops too. Consequently, between $z = 1$ and $z = 0.5$, a massive thin disk can form and start to dominate the mass distribution, as probed by the formation of spiral arms in the face-on images shown in Figure 2.19. This thin disk grows secularly down to $z = 0$ and generally gets barred by $z \simeq 0.5$ (strongly in the two first cases, weakly in the third one).

These three cases illustrate the transition between a phase characterized by frequent mergers and disk instabilities, an early violent phase, and a phase dominated by slower mass infall, a late secular phase. We have also seen that this transition, occuring when the massive thin disk forms, is traced by the emergence of bars. Overall, the epoch of bar formation in our simulations probes the epoch at which spiral galaxies have formed the bulk of their disk, stellar halo, and thick disk, and start to be dominated (in terms of stellar mass) by their final thin disk with only slow (secular) evolution down to $z = 0$.

In observations, the bar fraction also decreases with increasing redshift, and although it could be probed in detail only up to $z \simeq 1$ (with one exception up to ~ 1.5 - Herrington et al. 2012), it is in close agreement with our models so far. If confirmed observationally, could the emergence of bars at $z \simeq 0.8 - 1$ also correspond to the epoch at which spiral galaxies acquire their final morphology and start being dominated by their thin rotating stellar disk? And could a transition between a violent phase of galactic assembly, with rapid episodes of merging and violent instabilities building a thick disk and spheroids, be followed by a calm secular phase of thin disk growth and evolution, with the typical transition at $z \simeq 0.8 - 1$? These issues are further discussed in the remainder of this Section.

Let us start with a discussion about chemical properties of disk galaxies that seem to be consistent with such a two-phase assembly process. Thick disks are often observed around spiral galaxies (Dalcanton & Bernstein, 2002, Seth et al., 2005), without ongoing star formation and no or almost no young stellar populations (Yoachim & Dalcanton, 2006, Ibata et al., 2009). In particular, the Milky Way thick disk contains no or almost no stars younger than 8 Gyr (Gilmore et al., 1985, Reddy et al., 2006). This is consistent with events disrupting any cold rotating disk into a thick disk occuring only at redshifts higher than $z \sim 1$, while the thin disk would not have been significantly disrupted/thickened after this epoch. Also the enhanced α element abundances in the thick disk and central bulge (Lecureur et al., 2007, Zoccali et al., 2007) suggest that their star formation occurred mostly as brief events (not longer than a few 10^8 yr), and that the formation of stars belonging to the present-day thin disk occurred at later epochs with longer timescales (see also Chiappini, 2009).

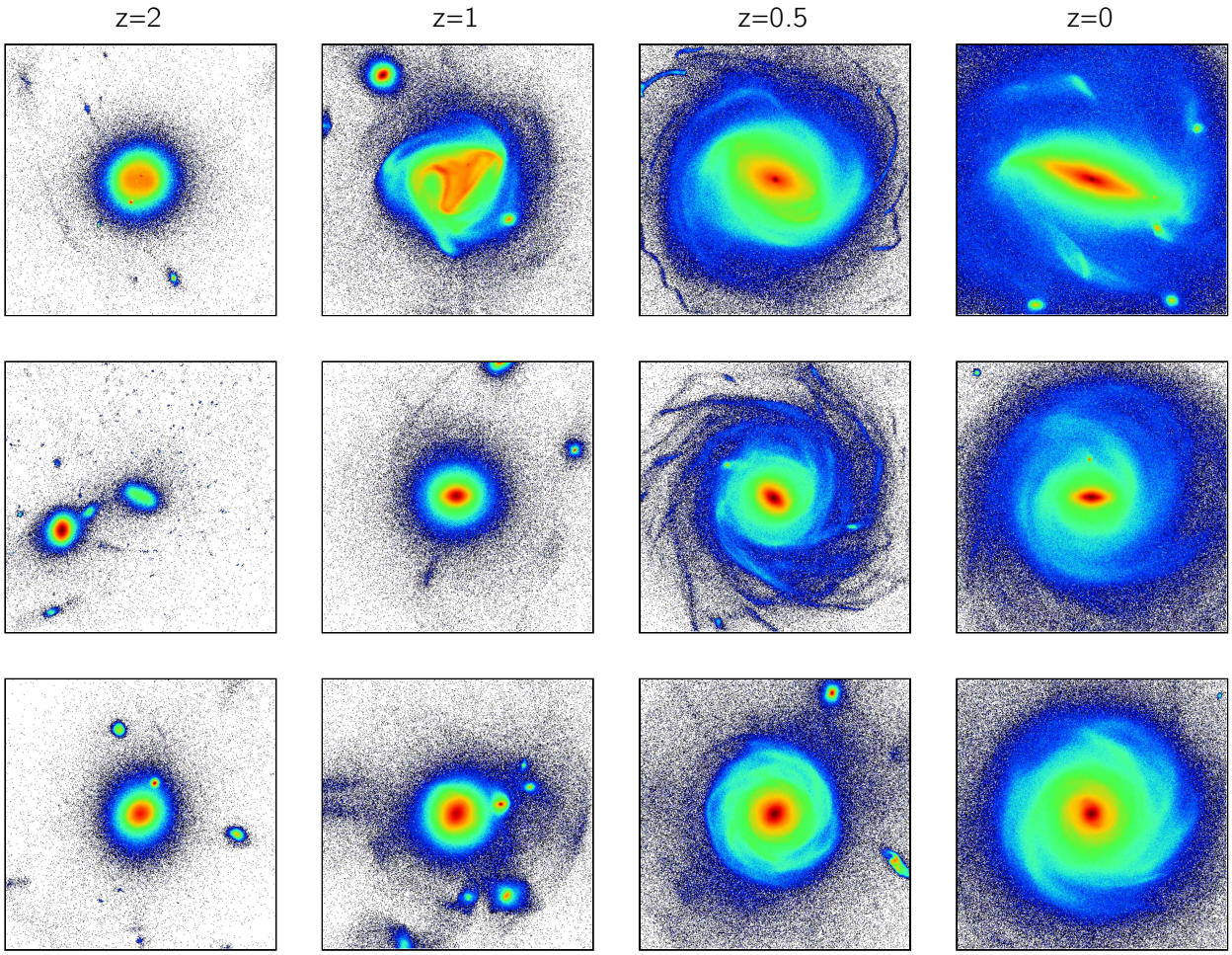

Figure 2.19

Examples of morphological evolution from $z = 2$ down to $z = 0$ for three simulated galaxies. Stellar density maps (face-on 50×50 kpc^2 projections) are shown for $z = 2$, 1, 0.5, and 0. Galaxies evolve rapidly during the "violent" phase at $z \gtrsim 1$ when they frequently undergo phases of violent disk instabilities (top panels) and major mergers (middle panels). The morphology at $z = 0$ and $z \gtrsim 1$ is uncorrelated with early spheroids being possible progenitors of today's spirals (bottom panels). Once galaxies enter the late "secular" phase at $z < 1$, their structural parameters become more tightly correlated with the final disk morphology.

These brief events could have been mergers or violent instabilities characterized by giant clumps in rapidly accreting galaxies, that grow both a bulge and a thick disk (Bournaud et al., 2009) over short timescales, while a thin disk component can form and remain stable after, with lower gas infall rates.

Results from gas kinematics and/or optical and near-infrared spectroscopy used in direct searches for disks are also consistent with $z \simeq 1$ as the typical redshift for the emergence of modern thin spiral disks, along with their bars. Near-infrared spectroscopy of a $z \sim 3$ sample of star-forming galaxies, with masses typical for the progenitors of Milky-Way-like galaxies and present day spirals (AMAZE and LSD; Maiolino et al., 2010, Gnerucci et al., 2011), reveals only a minor fraction of rotating disks. The majority of these galaxies are mergers or irregular systems dominated by high velocity dispersions. A similar survey of star-forming galaxies in a comparable mass range at a median redshift $z \simeq 1.2$ (MASSIV; Epinat et al., 2012) finds that about 40%-50% of the galaxies in their sample

are rotating disks. Similarly, the IMAGES survey, at $z \simeq 0.6 - 0.8$, finds a majority of rotating disk galaxies (Yang et al., 2008) in a sample that still covers masses typical for the progenitors of today's spiral galaxies ($10^{10} - 10^{11}$ $M_\odot$). This survey furthermore suggests that many of these $z \simeq 0.6 - 0.8$ galaxies have formed their disks only recently, after experiencing violent events such as major mergers (Hammer et al., 2009), and that they will undergo only slow evolution of their global properties, such as their Tully-Fisher relation, down to $z = 0$ (Puech et al., 2010).

Another argument comes from morphological studies that are also consistent with redshift $z \sim 1$ marking the emergence of modern thin disks. Elmegreen et al. (2007b, 2009) found the Hubble Ultra Deep Field sample at $z > 1$ to be dominated by irregular morphologies corresponding to major mergers and interactions and "clumpy" unstable disks, which are typically forming thick disks, bulges, and stellar halos (Bournaud et al., 2009), rather than thin spiral disks. Some cold spiral disks are also found in this sample, but their fraction is quite low before $z = 1$. The situation is largely different at $z \simeq 0.7$ when the fraction of clumpy irregular disks drops steadily and stable spiral disks, progenitors of present-day $10^{10} - 10^{11}$ $M_\odot$ galaxies, rapidly become more numerous. For somewhat more massive galaxies, Sargent et al. (2007) found that a large fraction of massive disks are in place around redshift one, but substantially fewer than at lower redshift.

This combination of findings provides support for our suggestion that the emergence of galactic bars at $z \simeq 0.8 - 1$ traces the transition between an early "violent" and a late "secular" phase in the formation history of spiral galaxies. During the "violent" phase, stars that belong to the modern thick disk, bulge, and halo form in systems that do not have a permanent disk-dominated structure, while the "secular" phase is characterized by the thin disk growth and evolution with ubiquitous bars and limited pseudo-bulge growth. The downsizing of bar formation (Sheth et al., 2008, Section 4.2; Cameron et al., 2010) could, according to this scenario, correspond to the later termination of the violent phase and later disk stabilization in lower-mass galaxies. For these galaxies, both merging activity and violent disk instabilities should persist down to lower redshift (Bournaud et al., 2012, and references therein). Alternatively, bars could grow more rapidly in more massive systems once their cold, thin disk is stabilized (Elmegreen et al., 2007a). To conclude, our model is so far consistent with the observed evolution of the bar fraction. Further validation could be obtained by confirming the drop in the bar fraction, especially at $z \sim 1$ and above, with almost only weak bars (strength ≤ 0.2) being present at $z > 1$ for the mass range studied here.

2.8 Summary

A study of a sample of cosmological zoom-in simulations of 33 Milky Way mass galaxies in field and loose group environments from $z = 2$ down to $z = 0$ was presented. To determine the presence of a bar, the method based on the decomposition of the stellar surface density profiles into Fourier components was used. The disk/spheroid structure of the modeled galaxies was further analyzed using the Sérsic index of the surface density profile. Our main results are summarized as follows.

① The total bar fraction among spiral galaxies declines with increasing redshift. It drops from almost 90% at $z = 0$ to about 50% at $z \simeq 1$ and to almost zero at $z \simeq 2$. The fraction of observable (with strength $S \geq 0.2$) and strong bars ($S \geq 0.3$) declines from about 70% at $z = 0$ to 10%-20% at $z = 1$ and to zero at $z = 2$. This result holds for galaxies with a mass range of $2 \times 10^9 - 8 \times 10^{10}$ $M_\odot$ at $z \sim 1$ and $4 \times 10^{5-1} \times 10^{10}$ $M_\odot$ at $z \sim 2$, i.e., typical progenitors of Milky-Way-like spirals. For more massive galaxies, the bar fraction could

however remain higher at $z \sim 2$ if the downsizing of bar formation observed in our sample still holds for higher masses/redshifts.

② The epoch of bar formation traces the epoch of the emergence of the final thin disk of spiral galaxies. This corresponds to the termination of an early "violent" phase at $z > 1$, characterized by frequent mergers, violent disk instabilities and rapidly evolving structure, forming thick disks, bulges, and stellar halos. It is followed by a "secular" phase at $z < 0.8$, dominated by the slower growth and evolution of modern thin disks and limited bulge growth at late times. The $z = 0.8 - 1$ transition epoch is found for the mass of typical Milky Way progenitors, and tends to move to higher redshift for more massive systems.

③ We find that in general there is only a minor contribution of bars in the late growth ($z < 1$) of (pseudo-)bulges in spiral galaxies and this late growth is dominated by continued cosmic infall and minor mergers rather than by bars. However, there are some cases where the bar-induced pseudo-bulge is important, as in observed "peanut-shaped" bulges.

④ Finally, early bars (formed at $z > 1$) are often short-lived and may reform several times. Bars formed below $z \sim 1$ are found to persist down to $z = 0$, some of them being intrinsically short-lived but maintained by late cosmological gas infall.

According to our model, the scarcity of significant bars at $z \geq 1$, if confirmed observationally, would indicate, that present-day spirals and Milky Way-like galaxies have formed and stabilized their modern thin spiral disk only relatively late in their growth history, typically at $z \simeq 0.8 - 1$. At earlier times, they would be mostly forming their spheroidal components, like bulges and halos, and thick disk, under the effect of both hierarchical merging and violent instabilities in rapidly accreting systems. The continuation of this violent phase with mergers, rapid cold gas accretion, and disk instabilities down to lower redshift in lower-mass galaxies (e.g. Bournaud et al., 2012) could then explain a "downsizing"-like behavior for bar formation.

Chapter 3

Star formation laws and thresholds

The role of turbulence - simulations

> *If you will never say that a law is true in a region where you have not already looked you do not know anything. If the only laws that you find are those which you have just finished observing then you can never make any predictions. Yet the only utility of science is to go on and to try to make guesses.*
>
> — Richard P. Feynman, *The Character of Physical Laws*

Cosmological simulations of galaxies, including the morphological study presented in the previous Chapter, reproduce morphologies in agreement with observed properties of galaxies of comparable masses and environments. However, similarly to many other cosmological simulations, they suffer from problems related to their stellar content: their fraction of baryons converted in stars is too high compared to observationally deduced values. Observational results representing serious challenge

for galaxy evolution models are all in one way or another related to star formation and buildup of stellar mass over cosmic time. Simply reducing the net cosmological inflow (corrected for outflows) through heating processes and/or feedback driven outflows cannot be the entire solution. Gas fraction is typically already too low in simulated galaxies at high redshift and even recent Illustris simulation with strong AGN feedback that matches the observed star formation indicator at high redshift fails at redshift zero. Gas is required for the late star formation inside galaxies. One is thus naturally led to ask the question how well do we understand the process of star formation itself. This Chapter is dedicated to star formation through the small-scales analysis in a sample of idealized galaxy simulations.

3.1 Introduction

galaxy formation efficiency

Galaxy formation seems to be a very inefficient process[1]: only a small fraction of baryons in the Universe are converted into stars, with the peak of a galaxy formation efficiency[2] being at around 20 % in dark matter haloes with the mass of about 6×10^{11} $M_{\odot}$, and dropping very rapidly towards both higher and lower mass (e.g. Guo et al., 2010, Moster et al., 2013). In haloes of low mass, such low efficiency is believed to be due to supernova-driven galactic winds capable to expel gas from these objects with low escape velocities (e.g. Larson, 1974, White & Rees, 1978, Dekel & Silk, 1986, Efstathiou, 2000). At high mass end, it is feedback from the active galactic nuclei, that is considered to play a major role in reducing the galaxy formation efficiency (e.g. Tabor & Binney, 1993, Silk & Rees, 1998, Benson et al., 2003, Croton et al., 2006).

Comparison of typical values of galaxy formation efficiency required in a ΛCDM universe with values obtained in galaxy simulations reveals, that they lock too many baryons into stars to be a viable models for galaxy formation (Guo et al., 2010). Even though most of the newer simulations show a good agreement with the efficiencies needed to reproduce the observed stellar mass functions at redshift zero, almost all of them have far too high efficiencies at higher redshifts. This indicates that these simulations typically form too many stars too early ($z > 3$), while at late times ($z \lesssim 2$) star formation is quenched too strongly, lacking late star formation, so that most of the stellar mass at $z = 0$ is already present at high redshift (Behroozi et al., 2013, Moster et al., 2013).

gas fractions

This too rapid conversion of gas into stars at $z > 2$ is suggested to explain the discrepancy in gas fraction between simulated and observed galaxies. While observations point toward high gas fractions ($\gtrsim 50\%$) in star-forming galaxies at redshift $z \approx 1-2$ (Daddi et al., 2010a, Tacconi et al., 2010, Tacconi et al., 2013; but note criticism from Narayanan et al., 2012 due to the usage of locally-calibrated CO-to-gas conversion factors), many cosmological simulations find much lower gas content (down to 10%) in similar mass and redshift ranges (e.g. Ceverino et al., 2010, Kereš et al., 2012).

main sequence

Additional constraints come from the observed tight correlation between the star formation rate (SFR) and the stellar mass ($M_{\star}$) in star forming galaxies, the so-called star formation main sequence (SFMS) with an intrinsic scatter ~ 0.3 dex (Daddi et al., 2007, Elbaz et al., 2007, Noeske et al., 2007, Salim et al., 2007). Galaxy formation models struggle to reproduce the observed SFMS especially at $z \simeq 2$. A recent exception is the Illustris simulation (Vogelsberger et al., 2014), in which a good agreement with observations is obtained at $z = 0$, however, at intermediate redshifts $z \sim 1-3$, the

[1] A variety of different methods establishing the link between the properties of the evolving population of dark matter haloes and galaxies they host, such as dark matter halo abundance matching (e.g. Vale & Ostriker, 2004, Guo et al., 2010), kinematics of satellite galaxies (More et al., 2009) or gravitational lensing (Mandelbaum et al., 2006), point towards the same conclusion.

[2] defined as the fraction of all baryons associated with the halo which are locked into stars

normalization of SFMS is significantly lower compared to observations (Sparre et al., 2014). Similarly, the galaxy specific star formation rates (SFR/$M_\star$) are underestimated in this redshift range, showing a tension with observations which is common to hydrodynamic simulations and theoretical models.

Various feedback mechanisms are commonly proposed solutions for delaying the early star formation in galaxy simulations. Being implemented via subgrid recipes, these processes are very uncertain elements of models and their exact role is still debated. Outflows induced by feedback from active galactic nuclei may reduce the star formation activity, however they make the problem of low gas fractions even worse (Dubois et al., 2012). Recent Illustris simulation (Vogelsberger et al., 2014) succeeded to obtain a good agreement with observations for the cosmic star formation rate density at high redshifts, however in spite of choosing parameters resulting in more energetic AGN feedback compared to previous studies, star formation is not quenched sufficiently at late times. Moreover, due to the small scatter of the SFMS, repeated episodes of outflows followed by inflows of cosmic or recycled gas does not seem to be a viable solution neither.

Conceptually different kind of solution was recently proposed by Gabor & Bournaud (2014) invoking the coupling between infalling gas streams and the gas disk as a possibility to maintain high gas fraction simultaneously with delayed high-redshift star formation. Their model suggests that if the coupling is strong, star formation efficiencies can be lower by a factor of three while keeping gas fractions above 40 % until $z < 2$. Further investigation of this mechanism is needed, as previous models suggest that the inflow-disk coupling is weak (e.g. Hopkins et al., 2013b).

In summary, the state-of-the-art cosmological simulations of galaxy evolution struggle at reproducing the above mentioned observational results simultaneously in different redshift and mass ranges. Galaxies in simulations typically lock too many baryons into stars and even if they reproduce correct stellar mass at redshift zero, they form too many stars at high redshifts. A simple solution of gas removal at early times through outflows driven by strong feedback introduces a non-trivial challenge, as gas needs to be present in galaxies in sufficient quantities in order to sustain low-redshift star formation at observed rates. While more sophisticated stellar feedback certainly is a necessary ingredient of any successful galaxy evolution model, a better understanding of star-formation process at small scales is a must.

I will now focus on the conversion of gas into stars which is a fundamental and among the most important physical processes affecting the formation and evolution of galaxies and for which questions about its efficiency and triggering mechanism remain open. Thus in addressing star-forming galaxies, the problem reduces to our fundamental ignorance of star formation.

Observations of galaxies have shown a close correlation, known as the Schmidt-Kennicutt relation, between the surface density of star formation rate ($\Sigma_{\rm SFR}$) and the surface density of gas ($\Sigma_{\rm gas}$) (e.g. Kennicutt, 1989, Wong & Blitz, 2002). The details of this scaling relation are found to vary with the environment. Spiral galaxies convert their gas into stars with longer depletion times than galaxies in a merger phase (Daddi et al., 2010b, Genzel et al., 2010, Saintonge et al., 2012), but more rapidly than dwarf galaxies (Leroy et al., 2008, Bolatto et al., 2011). In addition, the observed relation varies for different tracers. It is shallower for molecular gas than for total (molecular and atomic) gas (Gao & Solomon, 2004, Bigiel et al., 2008, Heyer et al., 2004), but steeper when the atomic gas is considered solely (Kennicutt, 1998, Kennicutt et al., 2007, Schuster et al., 2007, Bigiel et al., 2008). Several other observations (e.g. Kennicutt, 1989, Martin & Kennicutt, 2001, Boissier et al., 2003) have suggested the existence of a critical surface density, the so-called break, below which $\Sigma_{\rm SFR}$ in spiral galaxies drops: star formation is inefficient compared to the regime at high surface densities, well described by a power-law. Consequently, a composite relation of star formation seems to be a better description for the $\Sigma_{\rm gas}$–$\Sigma_{\rm SFR}$ relation, rather than a single power-law.

break

However, the origin of the break, and the transition to a different regime of star formation at high surface densities, remain a matter of debate. Some models evoke the Toomre criterion for gravitational instability (e.g. Quirk, 1972, Kennicutt, 1989, Martin & Kennicutt, 2001) or rotational shear (Hunter et al., 1998, Martin & Kennicutt, 2001) to interpret the existence of the break. Elmegreen & Parravano (1994) emphasize the need for the coexistence of two thermal phases in pressure equilibrium and Schaye (2004) argues that it is the transition from the warm to the cold gas phase, enhanced by the ability of the gas to shield itself from external photo-dissociation, that triggers gravitational instabilities over a wide range of scales. Self-shielding plays an important role also in the model of Krumholz et al. (2009), where it sets the transition from atomic to molecular phase at a metallicity-dependent Σ_{gas}. Dib et al. (2011) shows that feedback from massive stars is an important regulator of the star formation efficiency in protocluster forming clouds. Based on this, Dib (2011) proposes that the break in the Σ_{gas}–Σ_{SFR} relation can be related to a feedback-dependent transition of the star formation efficiency per unit time, as a function of the gas surface density (but see Dale et al. 2013 reporting a possibly low impact of the stellar feedback on the star formation rate and efficiency). Renaud et al. (2012) have recently proposed an analytic model in which the origin of the star formation break is related to the turbulent structure of the interstellar medium (ISM). In this model, a threshold in the local volume density, resulting in the observed surface density break corresponds to the onset of supersonic turbulence that generates shocks which in turn trigger the gravitational instabilities and thus star formation.

Different mechanisms are invoked in theoretical works to explain the scaling relations, such as gravity (Tan, 2000, Silk & Norman, 2009), turbulence of the interstellar medium (e.g. Elmegreen, 2002, Mac Low & Klessen, 2004, Krumholz & McKee, 2005, Hennebelle & Chabrier, 2011, Padoan & Nordlund, 2011, Federrath & Klessen, 2012, Renaud et al., 2012, Federrath, 2013), feedback from massive stars (Dib, 2011) and the interplay between the dynamical and thermal state of the gas (Struck & Smith, 1999).

In addition to these theoretical studies, several galaxy simulations modeling the ISM found a reasonable agreement with observations, using various recipes for star formation and stellar feedback (Li et al., 2006, Wada & Norman, 2007, Robertson & Kravtsov, 2008, Tasker & Bryan, 2008, Dobbs & Pringle, 2009, Koyama & Ostriker, 2009, Agertz et al., 2011, Dobbs et al., 2011, Kim et al., 2011, Monaco et al., 2012, Rahimi & Kawata, 2012, Shetty & Ostriker, 2012, Halle & Combes, 2013). Among them Bonnell et al. (2013) resolved the small scale physics of star formation in the context of galactic scale dynamics. The observed correlation between Σ_{gas} and Σ_{SFR}, together with the break of Σ_{SFR} are often reproduced in simulations, but it remains unclear to what extent the star formation rate estimates depend on the parameters of individual models and underlying assumptions, and what are the fundamental drivers for the observed relations.

The work presented in this Chapter aims at providing a better understanding of the star formation relations and threshold by studying the local properties of simulated galaxies. To this purpose, we use a series of galaxies simulated in isolation (Section 3.2), described in Section 3.3. One may wonder why the sample of galaxies simulated in cosmological context, presented in Chapter 2 is not used instead. One issue is the resolution, but more importantly, these simulations suffer from the same shortcoming as many other similar modern cosmological simulations, their fraction of the cosmic baryons found in stars is too high compared to observations (average of 0.62 compared to the observed fraction of ~ 0.2; e.g. Behroozi et al. 2010). In this study, we focus mainly on three parameters: the Mach number, the star formation density threshold and the thickness of the star-forming regions. The method used in deriving parameters needed for the analysis is described in Section 3.4. Our main results reflecting the dependence of star formation on different parameters are plotted in the Σ_{gas}–

Σ_{SFR} parameter space, and can be found in Sections 3.5 and 3.6. Comparison with observation is presented in Section 3.7 and in Section 3.8, the local star formation density threshold interpretation is discussed. We next apply some of previous analysis to a system of merging galaxies in Section 3.9. Finally, we conclude with the summary in Section 3.10.

3.2 Simulation technique

To model a set of isolated galaxies, the Adaptive Mesh Refinement (AMR) code RAMSES (Teyssier, 2002) is used. Physical parameters of modeled galaxies are described in Section 3.3.

The dark matter and stellar components are modeled as collisionless massive particles, sensitive only to the gravitational interaction, and evolved using a particle-mesh solver. The gas is described by a density/velocity/pressure/energy field discretized on an adaptively refined grid. The dynamics of the gaseous component is computed by solving the Euler equations on the adaptive grid using a second-order Godunov scheme.

To model astrophysical objects, such as cosmic filament, galaxies or individual star forming clouds, a wide dynamical range is needed. The entire simulated volume often does not require the same level of refinement. Empty, information-poor regions do not need as fine resolution as high density regions where physically interesting things are going on. The AMR technique is able to handle such situations, by allowing the highest resolution in the densest regions, while keeping a low resolution in the low density volumes. The refinement strategy for all our simulations is based on the density criterion of stars and gas. Starting from the coarse level, each AMR cell is refined into 2^3 new cells if ① the number of collisionless particles contained in the current cell exceeds a certain fixed number $n_{\rm refine}$ (a few 10 in our sample of isolated simulations), ② or the baryonic mass in that cell is higher than a certain value ($= n_{\rm refine} \times M_{\rm sph}$, with $M_{\rm sph}$ being a mass at given level of the AMR grid; 3×10^2 $M_\odot$ at highest refinement level in our sample of isolated simulations), ③ or the local thermal Jeans length is smaller than four times the current cell size.

In order to account for the unresolved physics due to finite resolution, the so-called Jeans polytrope ($T \propto \rho$) is added at high densities, corresponding to the scales smaller than the maximal resolution (see Section 3.2.2). This additional thermal support ensures that the thermal Jeans length is always resolved by at least four cells (in our case) and thus avoids numerical instabilities and artificial fragmentation (Truelove et al., 1997).

3.2.1 Star formation & Stellar feedback

In the Jeans' formalism (Jeans, 1902), the collapse of interstellar gas clouds and subsequent star formation occur when the internal gas pressure is not strong enough to prevent the gravitational collapse. This happens once the mass of gaseous cloud exceeds a certain critical mass, so-called Jeans' mass. During the simulations, stellar particles are formed by conversion of gas. However, because we do not resolve individual stars,[3] each stellar particle represents a population of stars with different masses.

These particles are used for the injection of stellar feedback, but are not used in the post processing analysis of the SFR, which is recalculated from the density of gas (see Section 3.4).

[3] This is mainly due to limited computational resources and missing of the proper treatment of the physics associated with the formation of individual stars, which is usually the case in this kind of galaxy simulations.

The conversion of gas into stars is modeled by adopting the Schmidt (1959) relation of the form

SFR density

$$\rho_\star = \epsilon \frac{\rho}{t_{\rm ff}} \propto \epsilon \rho^{3/2} \quad \text{for } \rho > \rho_0, \tag{3.1}$$

where $\rho_\star$ is the local star formation rate (SFR) density, ρ is the density of gas in the cell, ϵ is the star formation efficiency per free-fall time $t_{\rm ff} = \sqrt{3\pi/(32G\rho)}$ and ρ_0 is local, volume density star formation threshold. At each time-step Δt, in cells of size Δx eligible for star formation, a new stellar particle of mass $n_\star M_\star$ is created, where $n_\star$ follows a Poisson law with the mean value of $\rho_\star \Delta t (\Delta_x)^3 / M_\star$ (Katz, 1992).

The values of the star formation efficiency ϵ and the star formation threshold density ρ_0 that we have adopted here (see Table 1) are adjusted to match the observed global SFR for local galaxies: $\approx 1-5$ $M_\odot yr^{-1}$ for the Milky Way (Robitaille & Whitney, 2010) and ≈ 0.4 $M_\odot yr^{-1}$ for the Large Magellanic Cloud (e.g. Skibba et al., 2012), on average. SFR of the simulated Small Magellanic Cloud is ≈ 0.5 $M_\odot yr^{-1}$, on average, which is higher than the observed value (e.g., 0.05 $M_\odot yr^{-1}$ obtained by Wilke et al. 2004), perhaps because of different structures, but a one-to-one match is not seeked.

feedback

The stellar feedback from the massive end of the stellar mass function is included only, the OB-type stars with mass > 4 $M_\odot$, which for a Salpeter (1955) initial mass function corresponds to 20% of the mass of each stellar particle created. Pre-supernova feedback, in the form of photo-ionization and radiative pressure is included in the case of the Milky Way simulation only (Renaud et al., 2013), while supernova (SN) feedback in used in all simulations. SN feedback is implemented as a Sedov blast (Dubois & Teyssier, 2008), either in a kinetic or thermal scheme. The choice of the SN feedback scheme is determined by treatment of the heating and cooling processes (see Section 3.2.2): every time the gas follows an equation of state (EoS), the total energy of SN (10^{51} erg) is injected in the kinetic form, since thermal feedback would have no effect.

Thermal energy injection via supernovae is inefficient in the dense environments where the cooling times are short and thus most of the injected energy is rapidly radiated away. To remedy this energy loss, the radiative cooling is usually temporarily turned off, often together with star formation (e.g. Thacker & Couchman, 2000, Stinson et al., 2006, Governato et al., 2007, Agertz et al., 2011, Guedes et al., 2011, Scannapieco et al., 2012). We use the revised feedback prescription as proposed by Teyssier et al. (2013). In order to take the non-thermal processes due to not resolved sub-parsec scales into account, the dissipation timescale of non-thermal processes is set to 1 Myr[4]. This is longer than timescales corresponding to the thermal component, consequently the feedback energy can be stored for longer time and released to the gaseous component more gradually. This approach is used in simulations of Large and Small Magellanic Cloud which do not include radiation pressure from young stars and photoionization. The main reason is that this pre-SN feedback is believed to help to maintain the multi-phase structure of the ISM in galaxies with a reasonable fraction of gas at densities where the thermal heating from supernovae has a larger effect.

To compute the SFR, numerical simulations typically use the assumption of the proportionality of the SFR to the gas density over the dynamical or gravitational free-fall timescale, giving rise to the Schmidt relation with the power law exponent of 3/2 in the form we used in our simulations, but there are also models using different exponents in the Schmidt relation. To avoid spreading star formation in all gas available in the simulation, some additional criteria have to be applied. We have applied commonly used density threshold, however, other types of restrictions are possible. These include restriction of star formation to gas which is locally self-gravitating, or Jeans unstable, or below some

[4]The typical turbulence dissipation timescale expected for the subgrid structures not resolved in our simulations.

temperature limit, or in converging flow, or which has a short cooling time, or which is in molecular form, or which satisfies a combination of some of these criteria. Hopkins et al. (2013c) have recently studied the consequences of different star formation criteria in galaxy simulations including stellar feedback and have found that while the total SFR is almost independent of them, the spatial and density distribution of star formation are affected. To decide which prescription describes better the real conditions of star formation, simulations have to be compared with observations. However, due to the degeneracy of the total SFR in these models, observations of star formation on different resolved scales are needed.

From the point of view of numerical implementation of star formation, different techniques exist as well. Instead of treating the stellar particles as collisionless massive particles with a fixed mass, sensitive only to the gravitational interaction, sink particles, capable of accreting bound gas can be used. Various implementations of this method, introduced by Bate et al. (1995) in smoothed particle hydrodynamic codes, are today available in grid-based codes (e.g. Krumholz et al., 2004). Sink particles enable to follow collapse and fragmentation of high-density gas regions in simulations further in time, over many dynamical times and measure directly the mass of gravitationally collapsing gas that is available for star formation.

3.2.2 Metallicity & Equation of state

The cooling and heating processes occurring in the ISM depend on the metallicity. In our models, the gas cooling due to atomic and fine-structure lines, and radiation heating from an uniform ultraviolet background are modeled following Courty & Alimi (2004) and Haardt & Madau (1996), respectively, naturally leading to a multiphase ISM. For better computational efficiency, gas is prevented to cool below the temperature of 500 K. Metallicity is a parameter fixed for each simulation and represents the average metal mass fraction in the galaxy.

Heating and cooling processes can often substantially slow down the simulation. This is mainly due to the Courant et al. (1928) criterion for numerical schemes solving the advection of the flow on a grid, which dictates the length of the time step in order to obtain stable solution. The principle behind the condition is that the length of discrete time steps at which some quantity of the flow moving across a discrete spatial grid is to be computed has to be less than the time needed for the flow to travel between adjacent grid points. Consequently, treatment of a hot gas phase requires a small time step, which can lead to a significant slowing down of the simulation.

A piecewise polytropic EoS of form $T \propto \rho^{\gamma-1}$ with the polytropic index γ can be applied instead. In such case, a pseudo-cooling (PC) EoS (Figure 3.1), fitting the heating and cooling equilibrium of gas at 1/3 solar metallicity (Bournaud et al., 2010, Teyssier et al., 2010) can be used. This EoS is defined as follows:

pseudo-cooling

$$T(\rho) = \begin{cases} 4 \times 10^6 \left(\frac{\rho}{10^{-3}\ \mathrm{cm}^{-3}}\right)^{5/3-1}\ \mathrm{K} & \text{for } \rho < 10^{-3}\ \mathrm{cm}^{-3} \\ 10^4\ \mathrm{K} & \text{for } 10^{-3}\ \mathrm{cm}^{-3} < \rho < 0.3\ \mathrm{cm}^{-3} \\ 10^4 \left(\frac{\rho}{0.3\ \mathrm{cm}^{-3}}\right)^{1/2-1}\ \mathrm{K} & \text{for } \rho \geq 0.3\ \mathrm{cm}^{-3}. \end{cases} \tag{3.2}$$

In the above definition of the EoS, the capacity of the gas to shield itself from the surrounding radiation is neglected. At densities around $0.1 - 1\ \mathrm{cm}^{-3}$ and temperatures of several hundreds K, self-shielding (SS) becomes important: the molecular fraction of the gas increases, enabling it to cool down to even lower temperatures (Dobbs et al., 2008). This can be modeled by the alternative

self-shielding

EoS (Figure 3.1):

$$T(\rho) = \begin{cases} 4\times10^6 \left(\frac{\rho}{10^{-3}\ \mathrm{cm}^{-3}}\right)^{5/3-1}\ \mathrm{K} & \text{for } \rho < 10^{-3}\ \mathrm{cm}^{-3} \\ 10^4\ \mathrm{K} & \text{for } 10^{-3}\ \mathrm{cm}^{-3} < \rho < 10^{-1}\ \mathrm{cm}^{-3} \\ 10^4 \left(\frac{\rho}{0.1\ \mathrm{cm}^{-3}}\right)^{-1}\ \mathrm{K} & \text{for } 10^{-1}\ \mathrm{cm}^{-3} \leq \rho < 10\ \mathrm{cm}^{-3} \\ 10^2 \left(\frac{\rho}{10\ \mathrm{cm}^{-3}}\right)^{4/5-1}\ \mathrm{K} & \text{for } \rho \geq 10\ \mathrm{cm}^{-3}. \end{cases} \tag{3.3}$$

In both definitions, the low density regime of index $\gamma = 5/3$ corresponds to the diffuse hot virialized gas in the stellar halo. In the density range $10^{-3}\ \mathrm{cm}^{-3} < \rho < 10^{-1}\ \mathrm{cm}^{-3}$ the gaseous galactic disk, assumed to be optically thin, is modeled by a quasi-isothermal gas representing the equilibrium between UV background heating and cooling processes.

Jeans polytrope

In addition, a Jeans polytrope of index $\gamma = 2$ is added at high densities. Due to the finite resolution, there will always be some small physical scales that are not resolved. Truelove et al. (1997) have shown that not accounting for this effect can lead to artificial fragmentation of a self-gravitating gas if the Jeans length, corresponding to the collapsing scale length of a sound wave perturbation, is not resolved at least by four resolution elements. Ideally, every time this criterion is not satisfied, new refinement should be activated. Obviously, this cannot be done indefinitely. A possible solution to this problem is to increase artificially the Jeans length, so that it stays resolved by at least four cells at the finest resolution level. This is equivalent to setting a resolution dependent pressure floor $P_{\mathrm{Jeans}} = \alpha(\Delta_{x,min})^2\rho^2$, leading to the introduction of a lower limit in the EoS, the so-called Jeans polytrope:

$$T_{\mathrm{Jeans}}(\rho) = \alpha\mu(\Delta_{x,min})^2\rho\ \mathrm{K}, \tag{3.4}$$

with $\alpha = 16G/(\gamma\pi)$, dominating the high density regions in $T-\rho$ plane. For a given spatial resolution $\Delta_{x,min}$ the Jeans polytrope becomes active at densities above $\approx 2761\ \mathrm{cm}^{-3} \times (\Delta_{x,min}/1\ \mathrm{pc})^{-4/3}$ in the case of PC and $\approx 1023\ \mathrm{cm}^{-3} \times (\Delta_{x,min}/1\ \mathrm{pc})^{-5/3}$ in the case of SS. The corresponding temperatures are $\approx 107\ \mathrm{K} \times (\Delta_{x,min}/1\ \mathrm{pc})^{2/3}$ and $\approx 40\ \mathrm{K} \times (\Delta_{x,min}/1\ \mathrm{pc})^{1/3}$ for PC and SS, respectively.

3.3 Galaxy sample

3.3.1 Initial conditions

We study models of a spiral galaxy resembling the Milky Way (hereafter MW), a disk galaxy similar to the Large Magellanic Cloud (LMC) and an irregular dwarf galaxy comparable to the Small Magellanic Cloud (SMC). We propose models representing systems with different morphological and physical properties rather than trying to reproduce fine details for these galaxies. Each simulation is performed in isolation and without cosmological evolution.

The details of the MW simulation can be found in Renaud et al. (2013). Here, this simulation is analyzed at resolution comparable to the resolution of other galaxy simulations in our sample, which is 1.5 pc, i.e. not at its maximal resolution. The parameters of all simulations are summarized in Table 1.

Simulations are labeled in a way to stress their principal difference which is related to EoS or metallicity parameter. Simulations in which the heating and cooling processes are evaluated have the value of metallicity in subscript. If the EoS is used instead, the subscript indicates the name of the equation of state. The most realistic cases are the $\mathrm{LMC}_{1.0\mathrm{Z}_\odot}$ and the $\mathrm{SMC}_{0.1\mathrm{Z}_\odot}$ simulations for

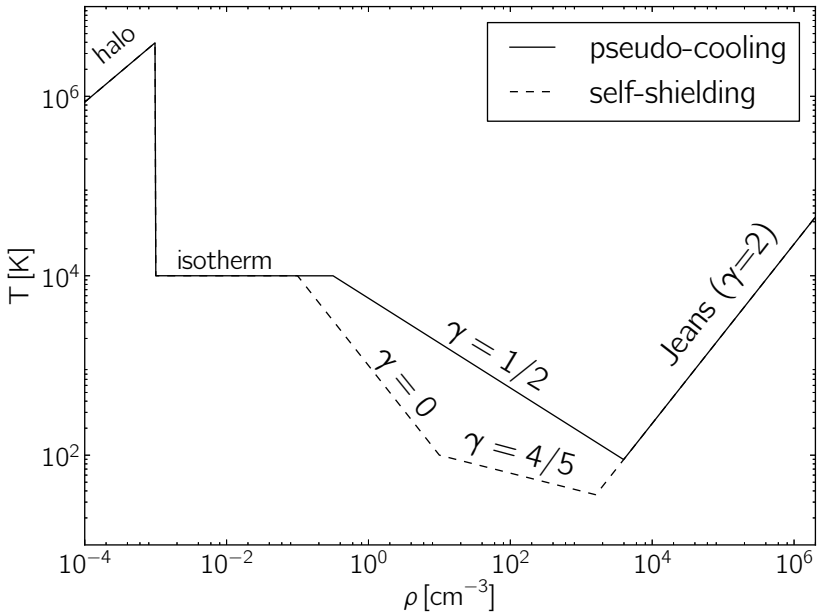

Figure 3.1

Effective EoS for pseudo-cooling (solid line) and self-shielding (dashed line). Pseudo-cooling EoS mimics detailed balance between cooling and heating processes at 1/3 solar metallicity. Self-shielding EoS models the ability of the gas clouds to reach even lower temperatures by absorbing the interstellar radiation in their outer layers. The low density regime ($\gamma = 5/3$) corresponds to the hot virialized gas in the stellar halo. The Jeans polytrope ($\gamma = 2$) dominates high density regions, avoiding artificial fragmentation.

LMC and SMC, respectively. The solar metallicity we have adopted in the $\mathrm{LMC}_{1.0\mathrm{Z}_\odot}$ simulation is higher than in the real LMC (1/2 $\mathrm{Z}_\odot$; Russell & Dopita, 1992, Rolleston et al., 1996), but fairly representative of low-redshift and low mass disk galaxy that we intend to model. The metallicity of 1/10 $\mathrm{Z}_\odot$ that we used in the $\mathrm{SMC}_{0.1\mathrm{Z}_\odot}$ simulation falls in the range of estimated values for the real SMC (1/5–1/20 $\mathrm{Z}_\odot$; Russell & Dopita, 1992, Rolleston et al., 1999).

3.3.2 Morphology

Figure 3.2 displays the surface gas density map of the three galaxies. $\mathrm{MW}_{\mathrm{PC}}$, a spiral galaxy, shows large variety of substructures: bar and spiral arms on the kpc-scale as well as dense clumps on the parsec scale (see Renaud et al., 2013, for details). Apart from regular structure of overdensity clumps – beads on a string, some spiral arms host a pattern of dense structures organized as spurs and resembling the features created by Kelvin-Helmholtz instabilities. $\mathrm{LMC}_{1.0\mathrm{Z}_\odot}$ is also a disk galaxy, just like real LMC (which is an irregular, perturbed disk galaxy), but with a much less pronounced structure of spiral arms and more diffuse gas present in the inter-arm regions compared to $\mathrm{MW}_{\mathrm{PC}}$. Our model of LMC is morphologically close to M33, the Triangulum Galaxy, which is a spiral with multiple substructures connecting the inner and the outer spiral features. $\mathrm{SMC}_{0.1\mathrm{Z}_\odot}$ is an irregular dwarf galaxy. Three major dense clumps can be seen within the irregular structure of the diffuse gas.

Table 1
SUMMARY OF MODEL PARAMETERS

	MW_{PC}[a]	$LMC_{1.0Z_\odot}$	LMC_{PC}	LMC_{SS}	$SMC_{0.1Z_\odot}$	$SMC_{0.3Z_\odot}$	$SMC_{1.0Z_\odot}$	SMC_{PC}	SMC_{SS}
EoS or metallicity[b] [$Z_\odot$]	PC	1.0	PC	SS	0.1	0.3	1.0	PC	SS
box length [kpc]	100	25			30				
AMR coarse level	9	8			8				
AMR fine level	21	14			15				
maximal resolution [pc]	0.05[c]	1.5			1.0				
DM halo									
mass [$\times 10^9$ $M_\odot$]	453.0	8.0			1.2				
particle number [$\times 10^5$]	300.0	3.49			5.0				
primordial stars[d]									
mass [$\times 10^9$ $M_\odot$]	46.0	3.1			0.35				
particle number [$\times 10^5$]	300.0	5.75			2.15				
gas									
mass [$\times 10^9$ $M_\odot$]	5.94	0.54			0.715				
cell number[e] [$\times 10^6$]	240	385	440	450	43	43	43	45	50
radial profile	exponential								
scale radius [kpc]	6	3			1.3				
radial truncation [kpc]	28	6			2.3				
vertical profile	exponential								
scale-height [kpc]	0.15	0.15			0.6				
vertical truncation [kpc]	1.5	0.45			1.3				
intergalactic density[f]	10^{-7}	10^{-7}			10^{-3}				
star formation									
ϵ	3%	3%			3%				
ρ_0 [cm^{-3}]	2×10^3	10^2			10^2				
stellar feedback									
photo-ionization	✓	-			-				
radiative pressure	✓	-			-				
SNe	kinetic	thermic	kinetic	kinetic	thermic	thermic	thermic	kinetic	kinetic

[a] simulations are labeled mnemonically, with their name having the value of the metallicity or EoS parameter in subscript: MW_{PC}, $LMC_{1.0Z_\odot}$, LMC_{PC}, LMC_{SS}, $SMC_{0.1Z_\odot}$, $SMC_{0.3Z_\odot}$, $SMC_{1.0Z_\odot}$, SMC_{SS}, SMC_{PC}

[b] metallicity is a meaningful parameter only when the heating and cooling processes are evaluated, the name of the EoS is given otherwise

[c] the analysis is performed by extracting the simulation data at the effective resolution of 1.5 pc (see text for details)

[d] stars initially present in simulation

[e] approximative AMR cell number

[f] fraction of density of gas at the edge of galaxy that is set beyond the truncation of the gas disk

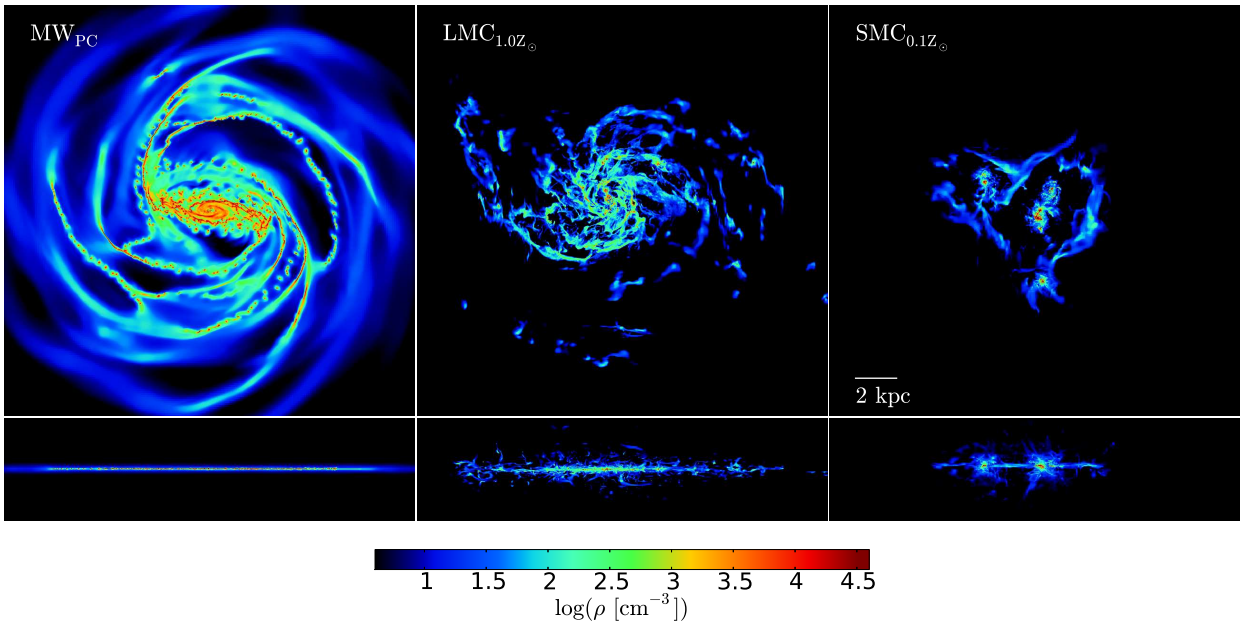

Figure 3.2

Surface density of gas of the galaxies for our three simulations: MW$_{PC}$ (left), LMC$_{1.0Z_\odot}$ (middle) and SMC$_{0.1Z_\odot}$ (right panel) seen face-on on the top and edge-on on the bottom panels. The box size of the face-on projection is 20×20 kpc^2 and that of the edge-on projection is 20×5 kpc^2.

3.3.3 Gas density PDF

The density probability distribution function (PDF) of the gas shows its fraction in different phases, from diffuse ISM to the densest clouds in the individual regions or over the entire galaxy. The mass-weighted PDF of the gas for MW$_{PC}$, LMC$_{1.0Z_\odot}$ and SMC$_{0.1Z_\odot}$ is shown in Figure 3.3. The MW$_{PC}$'s PDF has a log-normal shape, followed by a power-law tail at high densities ($\rho \gtrsim 1000$ cm^{-3}) probed thanks to the high resolution reached in this simulation. Similarly, the LMC$_{1.0Z_\odot}$'s PDF can be approximated by a log-normal functional form in the density range from 10^{-2} to 10^2 cm^{-3} with and excess of dense gas with respect to a log-normal fit above density of about 100 cm^{-3}. Truncation possibly due to the resolution limit is visible at a density of $\sim 2\times10^4$ cm^{-3}. The PDF of the SMC$_{0.1Z_\odot}$ is rather irregular with two components, one at low densities ($\sim 10^{-1}$ cm^{-3}) and the other one at high densities ($\sim 2\times 10^4$ cm^{-3}). Such irregular PDF reveals the density contrast between diffuse gas and several high density clumps.

The shape of the density PDF is determined by global properties of galaxies and physical processes of their ISM. As suggested by Robertson & Kravtsov (2008), the density PDF can vary from galaxy to galaxy and that of a multiphase ISM can be constructed by summing several log-normal PDFs, each representing approximately an isothermal gas phase. Similarly, Dib & Burkert (2005) showed that the PDF of a bistable two-phase medium evolves into a bimodal form with a power-law tail at the high density-end in the presence of self-gravity (see also Elmegreen, 2011, Renaud et al., 2013). However, in most cases, a single, wider log-normal functional form is a reasonably good approximation of the PDF of disk galaxies up to $\gtrsim 10^4$ cm^{-3} (see e.g. Tasker & Bryan, 2008).

Note that SMC$_{0.1Z_\odot}$, which has a lower metallicity than LMC$_{1.0Z_\odot}$, is able to reach the highest

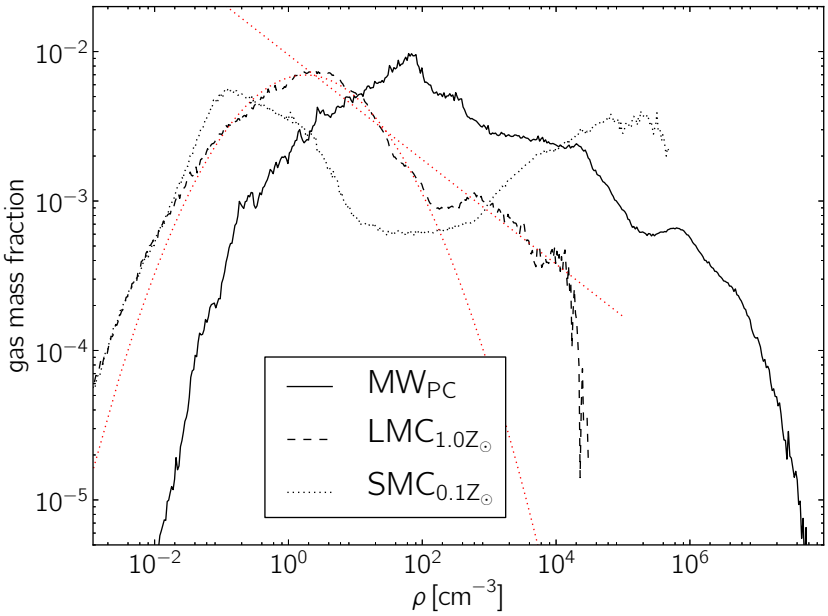

Figure 3.3

Comparison of the mass-weighted density PDF in MW$_{PC}$ at full resolution of 0.05 pc (solid line), LMC$_{1.0Z_\odot}$ (dashed line) and SMC$_{0.1Z_\odot}$ (dotted line). Approximated log-normal functional form and a power-law are shown for LMC$_{1.0Z_\odot}$ in red (see Renaud et al., 2013, Figure 10, for the best fit for MW$_{PC}$).

densities. Metallicity is important for cooling: the gas with higher metallicity is more efficient at cooling and should be able to reach higher densities. However, we do not observe such trend. This could indicate that factors other than thermal may be key in setting the gas distribution.

Another possible explanation could be due to the choice of threshold density ρ_0 for star formation and the metallicity in the LMC$_{1.0Z_\odot}$. If ρ_0 is chosen to be low, stars will form in an intermediate density medium, i.e. without the need of gravitational collapse of a cloud into a dense region. Furthermore, stellar feedback helps the destruction of the densest clumps which produces more intermediate-density gas and further prevents the gravitational contraction leading to high densities. The maximum density of the ISM is thus lower than with a high ρ_0 and the resulting PDF does not yield the classical high density power-law tail. However, in the case of LMC$_{1.0Z_\odot}$, the transition of the gas from high ($>10^3$ – 10^4 cm^{-3}) to intermediate densities ($10 - 10^2$ cm^{-3}, just below the actual ρ_0) due to the feedback would lead to a substantial reduction in the SFR (because of the $\rho_{SFR} \propto \rho^{3/2}$ used in our model, the SFR is dominated by high-density gas). Consequently, feedback itself would be substantially reduced.

Another, more likely explanation is that SMC$_{0.1Z_\odot}$ contains a much higher gas fraction compared to LMC$_{1.0Z_\odot}$ (see Table 1) leading to a much lower value of Toomre parameter ($Q \propto \Sigma_{gas}^{-1}$) which allows SMC$_{0.1Z_\odot}$ to reach higher densities than in LMC$_{1.0Z_\odot}$.

3.4 Analysis

To study the 100 pc scale properties of individual galaxies, analyzed regions are selected by examining the face-on projections of the gas distribution. We then consider sub-regions (hereafter referred to as beams) of 100×100 pc^2 in the galactic plane and with galaxy scale-height along the line of sight.

A study of the impact of the beam size is presented in Section 3.4.2. In order to have a significant amount of data, several snapshots in the analysis of the LMC and SMC galaxies are used.

3.4.1 Definitions

In a given beam, the effective Mach number $\mathcal{M}$ is defined as:

$$\mathcal{M} = \frac{\sigma_v}{\sqrt{3}} \frac{1}{c_s}, \tag{3.5}$$

Mach number

where σ_v and c_s are the mass-weighted 3D velocity dispersion and the mass-weighted sound speed with respect to the beam, respectively, calculated as follows

$$\sigma_v = \sqrt{\frac{\sum_i m_i v_i^2}{\sum_i m_i} - \left(\frac{\sum_i m_i v_i}{\sum_i m_i}\right)^2}, \tag{3.6}$$

and

$$c_s = \sqrt{\frac{\sum_i m_i T_i \gamma \frac{k_B}{m_H}}{\sum_i m_i}}. \tag{3.7}$$

Summations are done over all AMR cells in the analyzed beam and the index i refers to cell related quantities: T_i, m_i and v_i are the cell temperature, gas mass and speed, respectively. $\gamma = 5/3$ is the adiabatic index for monoatomic gas, m_H is the mass of the hydrogen atom and k_B the Boltzmann constant.

An alternative to the above "beam-based" average could be to compute the mass-weighted $\mathcal{M}$ with a cell velocity dispersion itself calculated with respect to its closest cells, but we find that this does not lead to a significant difference in the results.

Temperature in the beam is computed as mass-weighted average:

$$T = \frac{\sum_i m_i T_i}{\sum_i m_i}. \tag{3.8}$$

To estimate the actual thickness of the star-forming regions within each beam, we apply Gaussian fit to 1D projection of the gas density along one of the mid-plane axes. The thickness is then defined as the full width at half maximum of the resulting fit. Although the method to estimate the thickness parameter is simple, the obtained values are in good agreement with visual inspection of density maps of individual star-forming regions.

Note that in our analysis we don't use the SFR computed directly in the simulation. The main reason is that the conversion of gas into stars is modeled as a stochastic process leading to the discretization of the Σ_{SFR} values which make the analysis difficult by introducing more noise.

The SFR of a beam is estimated directly from the gas content of a cell by using Equation (3.1)[5]. Σ_{SFR} is then given by

$$\Sigma_{SFR} = \frac{\sum_i \rho_{\star i} V_i}{S}, \tag{3.9}$$

Σ_{SFR}

[5] only cells having $\rho > \rho_0$ are considered

where $\rho_{\star i}$ and V_i are the cell SFR density and volume, respectively and S is the surface of the beam. Similarly, $\Sigma_{\rm gas}$ is

$\Sigma_{\rm gas}$

$$\Sigma_{\rm gas} = \frac{\sum_i \rho_i V_i}{S}, \tag{3.10}$$

with ρ_i representing the cell gas density.

3.4.2 Tests

beam size effects

Our choice of the beam size is related to the structure of the ISM that is turbulence-driven. Log-normal probability distribution function is found to be a good description for supersonically turbulent isothermal gas (see 4.2.2 for more details). But once these hypotheses about the state of gas are relaxed, strictly log-normal PDF is not recovered. When all scales are considered, the PDFs of the density field in our sample of galaxies are close to, but not exactly log-normal functional forms (see Section 3.3.3). Consequently, individual beams should be large enough to be representative samples of star-forming regions at different evolutionary stages. In addition, the choice of the beam size is somehow linked to the turbulence and its cascade. Turbulence is injected at large scales and it cascades down to the small scales, where energy dissipation overcomes its transfer. In order to capture this turbulent cascade, the size of the beam should not be too small compared to the dissipation scale, nor too large compared to the injection scale[6]. In the former case, turbulence would be already dissipated, while in the latter case, the simulation would capture other processes than turbulence.

To estimate the impact of the size of the beam on the results in the $\Sigma_{\rm gas}$–$\Sigma_{\rm SFR}$ plane, we vary the beam width by a factor of 2.5 with respect to the one used in analysis. Figure 3.4 shows the comparison for the $\rm MW_{PC}$ simulation. Increased beam size leads to an overall reduction of $\Sigma_{\rm gas}$ for the beam, which can be understood as a consequence of decreased volume fraction occupied by the dense gas. On the contrary, for smaller beam size, higher values of $\Sigma_{\rm SFR}$ are reached. This comparison suggests that the considered spatial scale impacts the position of points in the $\Sigma_{\rm gas}$–$\Sigma_{\rm SFR}$ plane. Schruba et al. (2010) found such dependence in the study of the Local Group spiral galaxy M33. Similarly, Lada et al. (2013) found a more efficient SF at scales of molecular clouds, indicating that caution should be used when comparing SF relations involving different spatial scales. However, the global behavior of the $\Sigma_{\rm gas}$–$\Sigma_{\rm SFR}$ relation does not seem to be strongly affected by the size of the beam, at least for the range of sizes that we explored.

pc and sub-pc physics

We remind that the $\rm MW_{PC}$ simulation is analyzed at the resolution of 1.5 pc, closer to the resolution reached by other simulations in our sample, not at its maximal resolution of 0.05 pc. To study the impact of the resolution, we compare in Figure 3.5 the $\Sigma_{\rm gas}$–$\Sigma_{\rm SFR}$ relation for these two resolutions. Comparison shows, that sub-parsec physics does not influence our results at low and intermediate surface gas densities, but it plays a role in densest regions, where it leads to higher values of $\Sigma_{\rm SFR}$. The increased resolution leads to the modification of structures mainly at high densities which translates into higher values of $\Sigma_{\rm SFR}$ computed at fixed 100 pc scale.

3.5 Global parameters: Metallicity vs EoS

We would like to study what is the impact of the gas metallicity on the $\Sigma_{\rm SFR}$. To this purpose, we compare our three simulations of SMC with different metallicities. The left panel of Figure 3.6

[6] i.e. about the scale-height of the gas disk (Bournaud et al., 2010, Renaud et al., 2013).

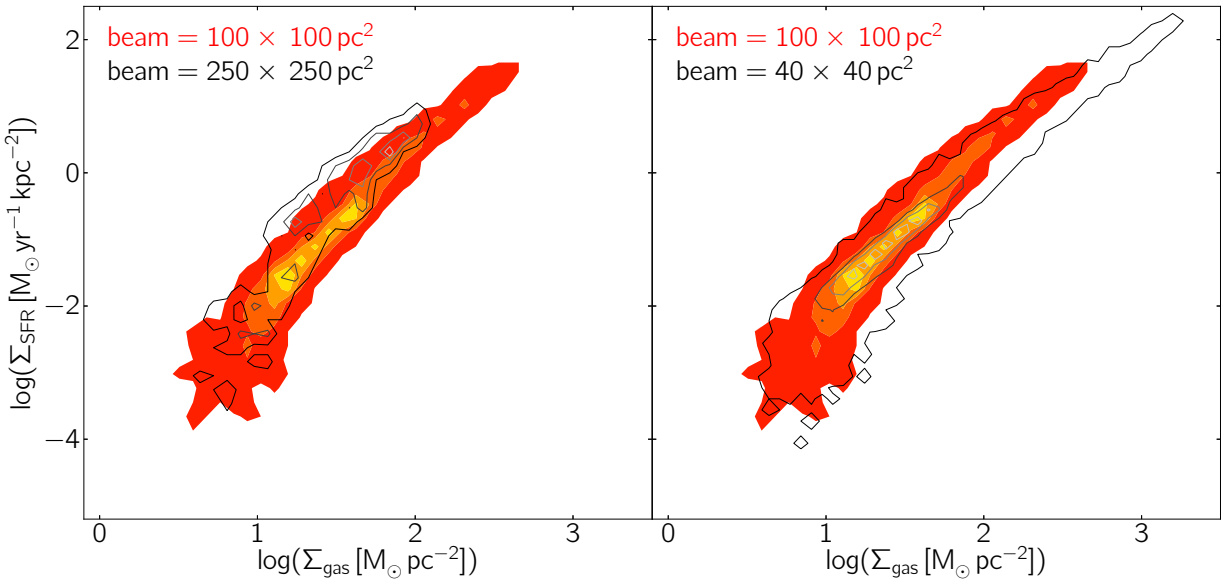

Figure 3.4

The effect of beam size on the Σ_{gas}–Σ_{SFR} relation in the MW_{PC} simulation. The two panels show the effect of varying the beam width by a factor of 2.5 (black contours) with respect to the one used in analysis (colored filled contours). When increasing the beam size, the dense gas represents smaller and smaller volume fraction which leads to an overall reduction of Σ_{gas} for the beam. The color coding of the two-dimensional normalized histogram corresponds to the 0.3, 0.5, 0.8 and 1.0 contour levels.

shows two systems with similar metallicities, 0.1 $Z_\odot$ and 0.3 $Z_\odot$, while on the right panel, two more extreme metallicities are compared, 0.1 $Z_\odot$ and 1.0 $Z_\odot$. In the region below the break, higher metallicity systems tend to have higher Σ_{SFR} for a fixed value of Σ_{gas} than systems with lower metallicity.

We are next interested how the fact of using an EoS instead of evaluating the heating and cooling processes influences the SFR. In Figure 3.7, the $SMC_{0.1Z_\odot}$ simulation is compared to that of SMC_{PC}, using the EoS of pseudo-cooling and to that of SMC_{SS} with the EoS of self-shielding. The similarity of two contour plots on the left panel suggests that the pseudo-cooling EoS is a good approximation to the actual heating and cooling processes even for a slightly lower metallicity in this case (we remind that the pseudo-cooling EoS is derived using the metallicity of 1/3 $Z_\odot$; see Section 3.2.2). In the case of the self-shielding EoS, for a given value of Σ_{gas}, Σ_{SFR} tends to be higher compared to that of the simulation with metallicity of 0.1 $Z_\odot$.

We remind that we do not assume any metallicity gradient in the gas, nor chemical evolution. The model for self-shielding used in our simulations does not contain any implicit metallicity dependence, similarly to the work of Dobbs et al. (2008). As shown in Figure 3.7, the self-shielding EoS leads to higher Σ_{SFR} for fixed Σ_{gas} compared to the model of SMC with metallicity of 0.1 $Z_\odot$.

The *existence* of the break in the Schmidt-Kennicutt relation in our models does not seem to depend on self-shielding effects. The exact position of this break is however sensitive to metallicity: the slope at low Σ_{gas}, i.e. below the break, is higher in metal-poor galaxies as shown on Figure 3.6. Similar metallicity dependent position of the break is present in the theoretical model of Krumholz et al. (2009) including the effect of hydrogen self-shielding which in turn determines the amount

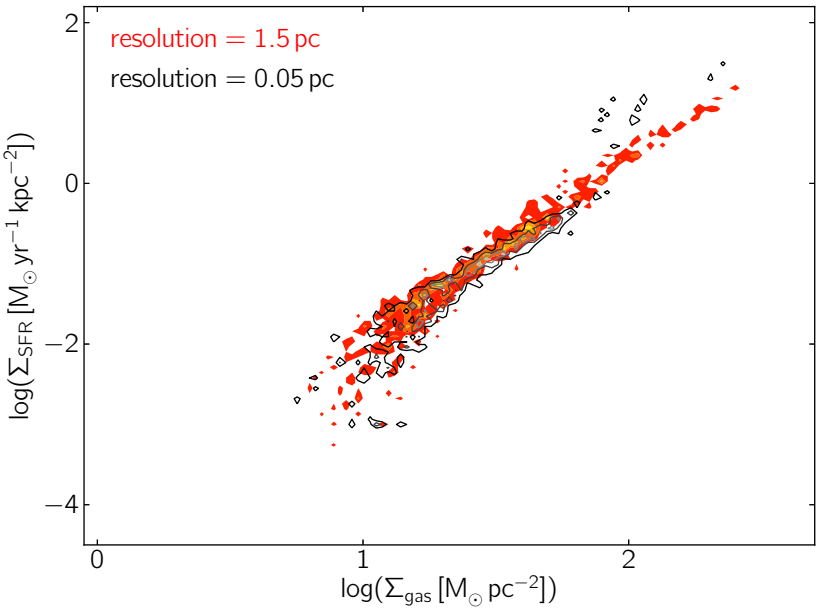

Figure 3.5

The impact of resolution on the Σ_{gas}–Σ_{SFR} relation in the MW_{PC} simulation. The maximal resolution of 0.05 pc (black contours) is compared to the resolution of 1.5 pc (colored filled contours), at which the entire analysis is performed. No significant difference is noticeable at low and intermediate surface densities of gas. At high Σ_{gas}, Σ_{SFR} tends to be higher at the resolution of 0.05 pc. The color coding of contour levels is as in Figure 3.4.

of gas in molecular form. In addition, Dib (2011) explored the metallicity-dependent feedback and found that it can lead to a modification of the position of the break for a given metallicity-dependent molecular gas fraction. It is clear that self-shielding has an impact on the Schmidt-Kennicutt relation (see right panel of the Figure 3.7), but it does not seem to be the only factor determining the presence of the break.

3.6 Local parameters: Mach number & Vertical scale of the gas

Mach number

We turn now our attention to the local properties of individual regions of simulated galaxies. In Figure 3.8 we show how the Σ_{gas}–Σ_{SFR} relation depends on the Mach number, temperature and velocity dispersion calculated using the Equations (3.5), (3.8) and (3.6), respectively. The example of MW_{PC} is shown, but we obtain qualitatively similar results for all other galaxies. For the sake of completeness, the Mach number dependence for our most realistic cases of SMC and LMC galaxies, $SMC_{0.1Z_\odot}$ and $LMC_{1.0Z_\odot}$, is displayed in Figure 3.9 in addition to that of MW_{PC}.

Two regimes in the star formation relation can be typically identified. The points located in the region below the break have typically Mach numbers with values below unity. Furthermore, for a given Σ_{gas}, Σ_{SFR} increases with increasing Mach number. At high surface densities of gas, Σ_{SFR} and Σ_{gas} are found to be correlated. The gas reservoirs that happen to be in this regime of efficient star formation tend to have supersonic velocity dispersions.

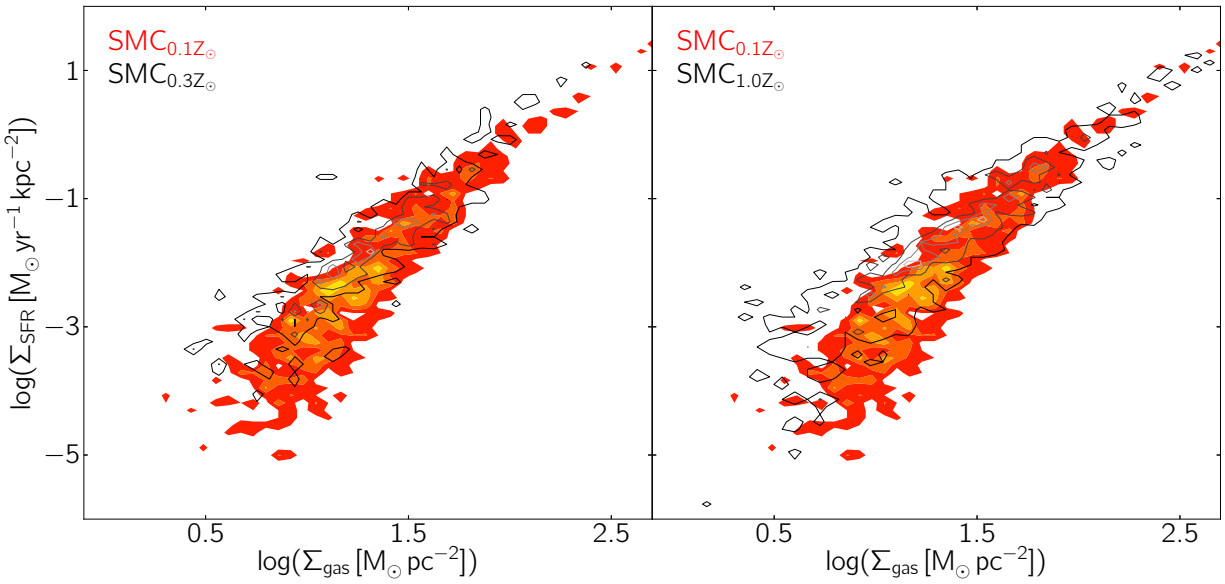

Figure 3.6

The impact of gas metallicity on the Σ_{gas}–Σ_{SFR} relation in the model of SMC. The left panel shows two simulations of the SMC with comparable metallicities: 0.1 $Z_\odot$ (colored filled contours) and 0.3 $Z_\odot$ (black contours). The right panel compares the effect of gas metallicity of 0.1 $Z_\odot$ with that of 1.0 $Z_\odot$. Gas cooling rates increase with metallicity, which translates into increased Σ_{SFR} for a fixed value of Σ_{gas} in the region of the break. The color coding of contour levels is as in Figure 3.4.

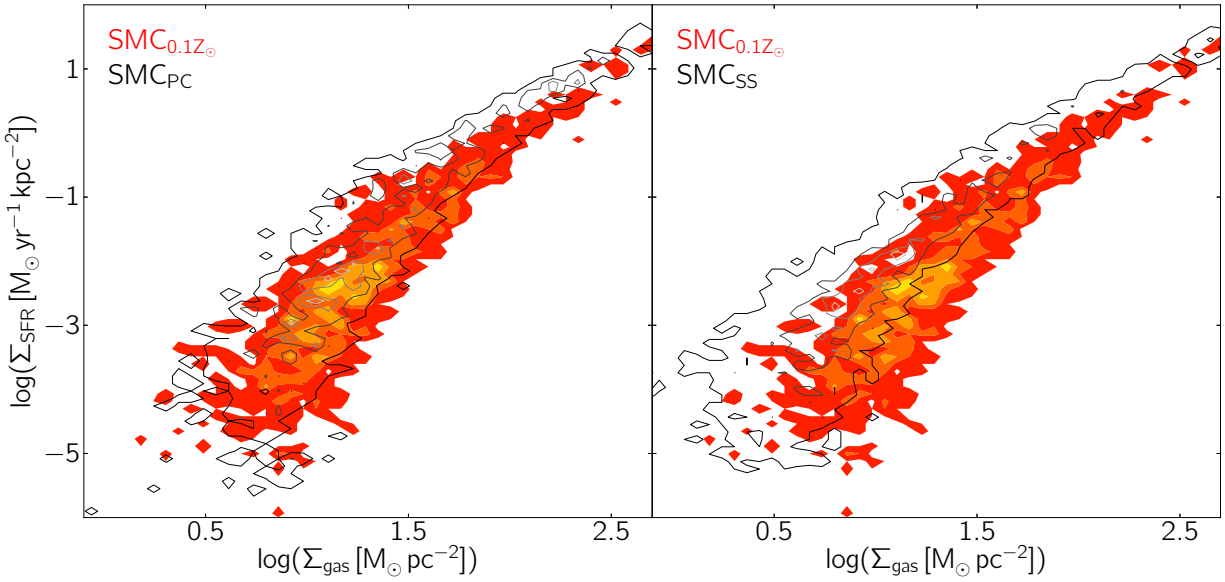

Figure 3.7

Comparison of the Σ_{gas}–Σ_{SFR} relation in $SMC_{0.1Z_\odot}$ (colored filled contours) to that of SMC_{PC} (black contours) in the left panel and to that of SMC_{SS} (black contours) in the right panel. The color coding of contour levels is as in Figure 3.4.

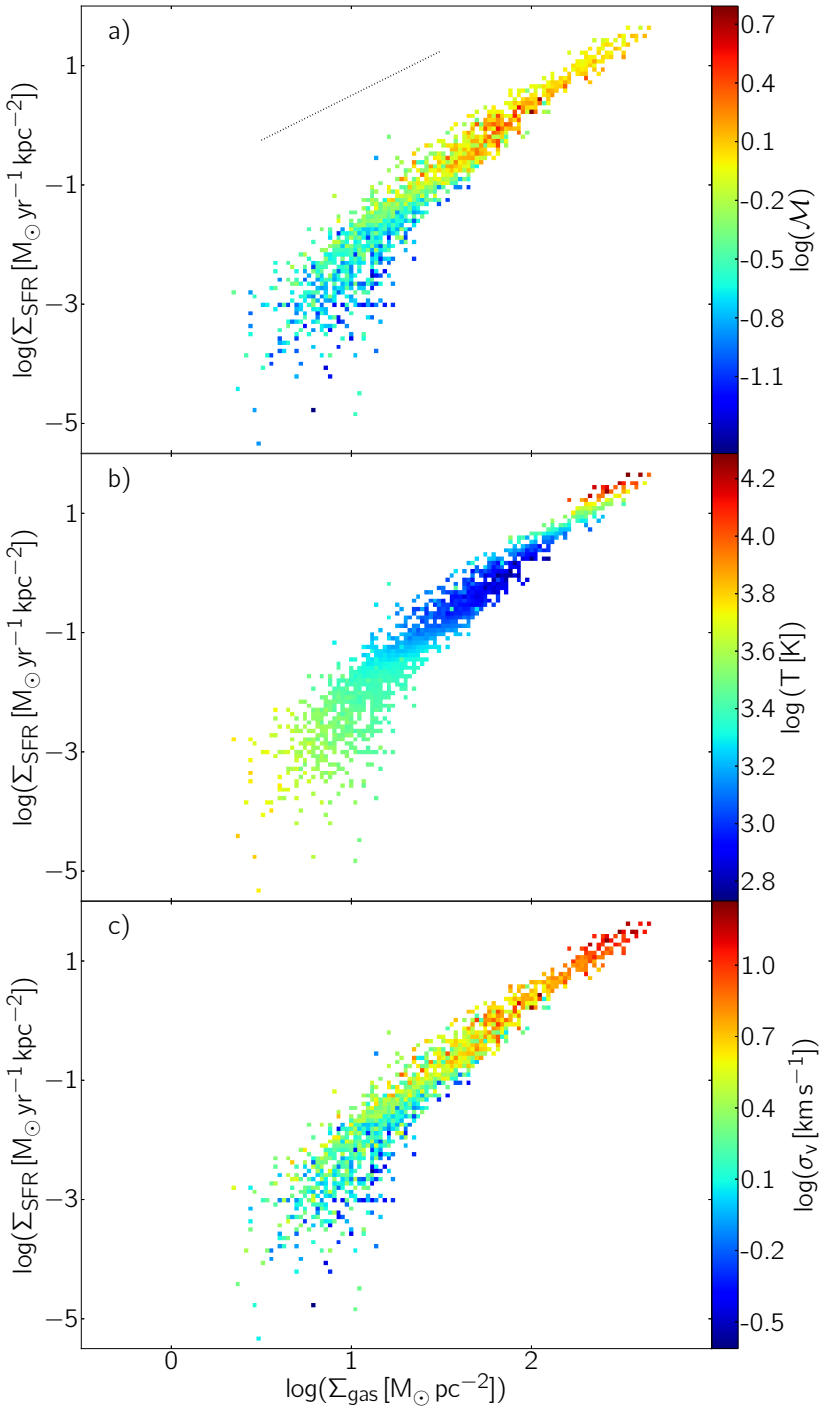

Figure 3.8

The local surface density of the star formation rate as a function of surface density of gas for the MW_{PC} model. The color indicates the Mach number (panel a), temperature (panel b) and velocity dispersion (panel c) in each beam. The dotted line indicates a power-law of index 3/2. Note that regions at high Σ_{gas} and high Σ_{SFR} that have high temperatures (on panel b) represent unresolved dense gas situated on the Jeans polytrope (see Section 3.2.2).

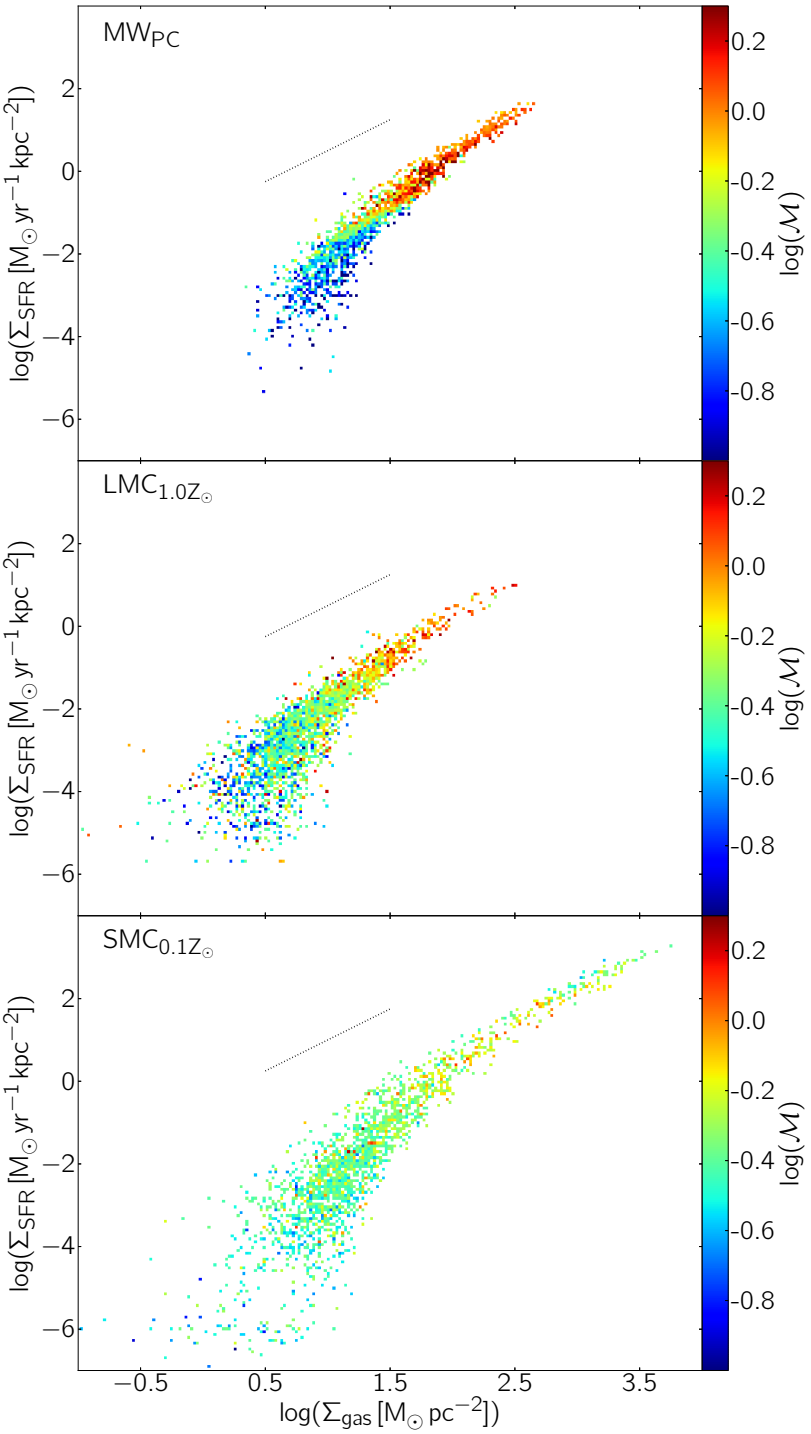

Figure 3.9

The local surface density of the star formation rate as a function of surface density of gas for MW$_{PC}$ (top panel), LMC$_{1.0Z_\odot}$ (middle) and SMC$_{0.1Z_\odot}$ (bottom). The color indicates the Mach number. The dotted line indicates a power-law of index 3/2.

Both the temperature and velocity dispersion contribute to the resulting Mach number dependence in the star formation relation. Despite the variation in temperature, the overall variation in Mach

number relies on σ_v. The velocity dispersion of the ISM can be increased by several processes. Among them Bournaud et al. (2010) found, in simulations similar to those analyzed here, self-gravity to play the dominant role, compared to stellar feedback. Therefore, by increasing the velocity dispersion, self-gravity sets the level of turbulence, i.e. the compression of gas and thus the SF. This suggests that the power-law part of the Σ_{gas}–Σ_{SFR} relation arises from self-gravity at high Mach number, while this connection is weaker in the break.

vertical scale

Another local parameter we are interested in and which is related to the geometry of individual star-forming regions is their scale-height. Figure 3.10 shows the variation of the Σ_{gas}–Σ_{SFR} relation with the thickness of the star-forming regions in $SMC_{0.1Z_\odot}$. For a given surface gas density, thicker regions tend to have lower surface star formation density. This relation between Σ_{SFR} and the thickness parameter at fixed Σ_{gas} results from the Equation (3.1) relating the volume density of gas with that of star formation rate.

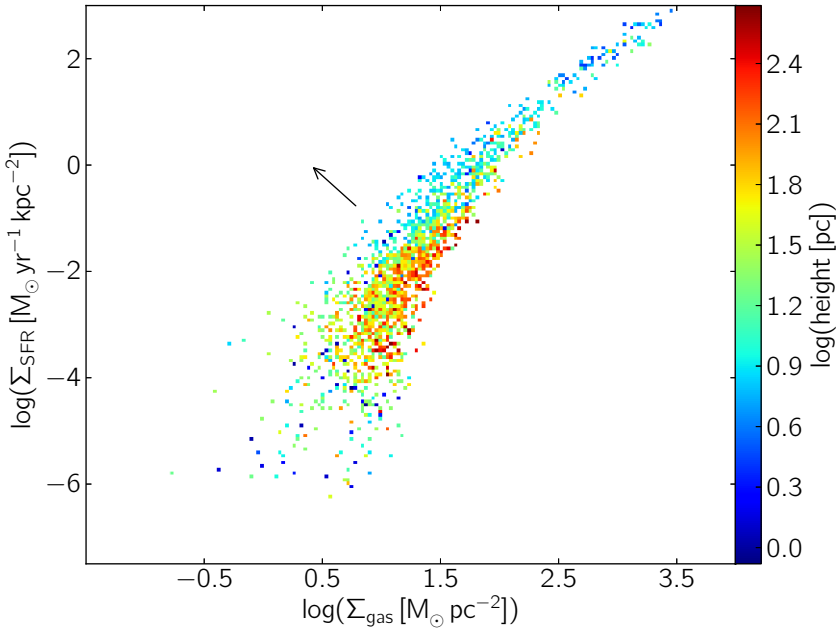

Figure 3.10

The local surface density of the star formation rate as a function of surface density of gas for the $SMC_{0.1Z_\odot}$ model. The color represents the thickness of star-forming region. The arrow indicates the direction in the measured scale-height of the gas from higher to lower values.

3.7 Comparison with observations

Most spatially resolved studies of spiral galaxies find the presence of a power-law Σ_{gas}–Σ_{SFR} relation with a break at surface gas densities of the order of a few $M_\odot\,pc^{-2}$ (see Kennicutt & Evans, 2012, and references therein). The slope of the power-law relation in the high surface-density regime is found to be in the range 1.2–1.6 when total (molecular plus atomic) gas surface density is considered.

Less agreement about the power-law slope in observations is reached when molecular-gas surface density is considered solely. Some recent studies (e.g. Eales et al., 2010, Rahman et al., 2011,

Leroy et al., 2013) have reported an approximately linear relation between the surface density of star formation rate and the surface density of molecular gas. Other studies (e.g. Kennicutt et al., 2007, Verley et al., 2010, Liu et al., 2011) have found a much steeper relation, with a slope in the range 1.2–1.7, similar to that of integrated measurements (Kennicutt, 1998). This discrepancy between different results in observations is still debated. A possible interpretation of the sublinear relation was recently proposed by Shetty et al. (2013). They suggest that the CO emission used in the estimation of Σ_{gas} is not all necessarily associated with SF. Not subtracting off such a diffuse component could lead to a slope close to unity.

The distribution of data points from the observations of the SMC (Bolatto et al., 2011) in the Σ_{gas}–Σ_{SFR} plane has a similar shape than that of spiral galaxies, but is noticeably shifted toward higher total Σ_{gas}.

In Figure 3.11, we show three of our models: MW_{PC}, $SMC_{0.1Z_\odot}$ and $LMC_{1.0Z_\odot}$ in the Σ_{gas}–Σ_{SFR} plane. The MW_{PC} and the $LMC_{1.0Z_\odot}$ models lie in the loci of observed spiral galaxies (e.g. Kennicutt, 1998, Kennicutt et al., 2007, Bigiel et al., 2008). Our $SMC_{0.1Z_\odot}$ model has a lower Σ_{SFR} for a given Σ_{gas} when compared to both the MW_{PC} and the $LMC_{1.0Z_\odot}$ models. The region below the break of our $SMC_{0.1Z_\odot}$ model is located at slightly lower Σ_{gas} than the real Small Magellanic Cloud, but its displacement with respect to spiral galaxies (MW and LMC) is well reproduced (Figure 3.11). In our simulations, Equation (3.1) sets the slope of power-law relation with the value of 1.5. A shallower relation, closer to the observed values, might be reached by accounting for a stronger regulation of star formation (e.g. pre-SN stellar feedback, see Renaud et al., 2012), but this slope change has not been probed in simulations yet.

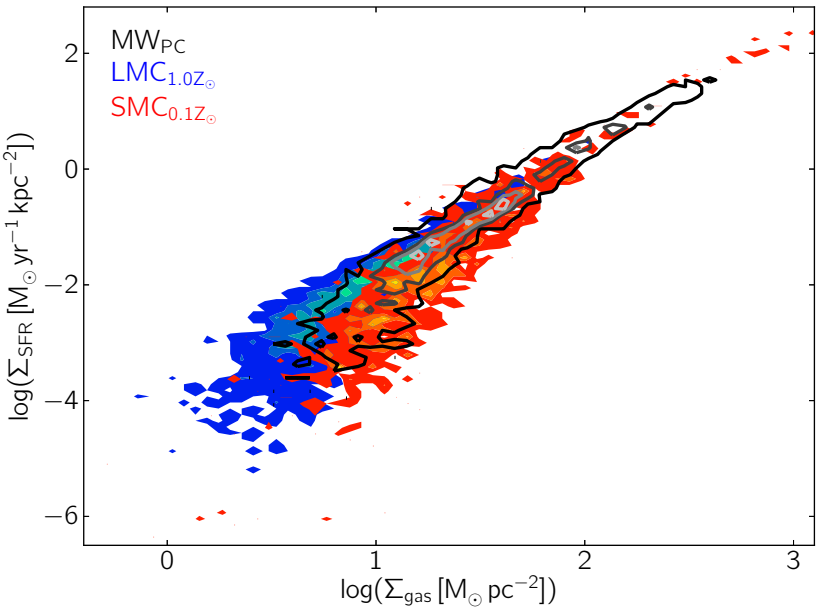

Figure 3.11

Comparison of MW_{PC}, $LMC_{1.0Z_\odot}$ and $SMC_{0.1Z_\odot}$. The color coding of contour levels is as in Figure 3.4.

3.8 Threshold interpretation

The *existence* of the break in the Σ_{gas}–Σ_{SFR} relation is, in our models, equivalent of having a non-zero value of the volume density threshold in the local, three dimensional star formation relation. Setting no threshold leads to a power-law relation without a break.

ρ_0 threshold

Figure 3.12 shows that the value of the density threshold ρ_0 that we have used in our analysis has an impact on the Σ_{gas}–Σ_{SFR} relation. Changing the value of ρ_0 changes the slope at low Σ_{gas} in the Σ_{gas}–Σ_{SFR} relation. This could suggest that the transition from the inefficient to the power-law regime could be due to the density threshold ρ_0 we imposed by hand in the star formation law (see Equation (3.1)). However, we have checked that the deviation from the power-law regime occurs at $\mathcal{M} \approx 1$, independently of ρ_0. In addition, in Figure 3.9, we have shown that beams located in the break tend to have $\mathcal{M}$ below unity, while regions at high Σ_{gas} are mostly supersonic.

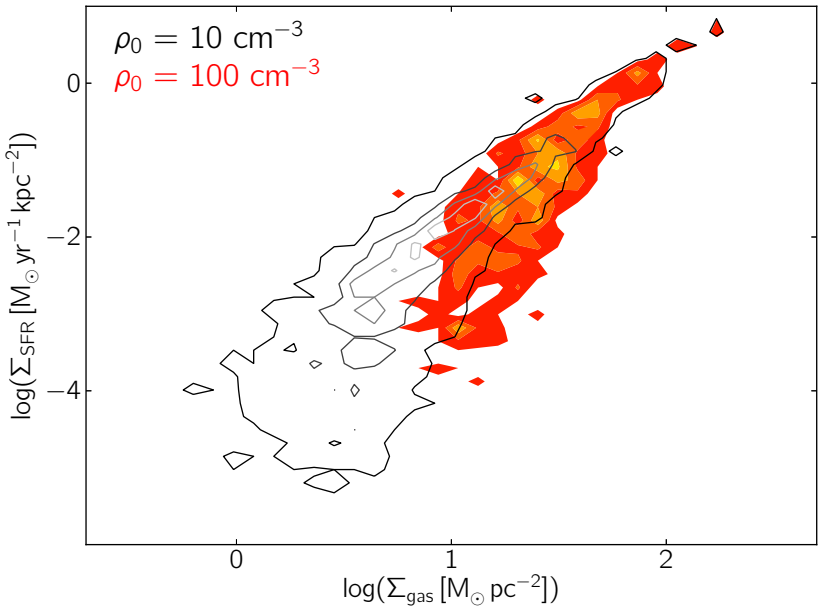

Figure 3.12

Comparison of the Σ_{gas}–Σ_{SFR} relation in the LMC$_{1.0Z_\odot}$ simulation with the star formation volume density threshold ρ_0=10 cm^{-3} (black contours) to that with ρ_0=100 cm^{-3} (colored filled contours). The color coding of contour levels is as in Figure 3.4.

To better understand the behavior of the ISM in our simulations, we show in Figure 3.13 the Mach number as a function of average volume density of gas[7] $\langle\rho\rangle$ in the beam for MW$_{PC}$. The Mach number varies with the average density as $\mathcal{M} \propto \langle\rho\rangle^{0.5}$, similarly to the two-phase turbulent flow studied by Audit & Hennebelle (2010). Although caution should be used when doing such comparison (temperature and velocity dispersion vary with density differently in both models), the onset of the supersonic regime, i.e. the transition from an inefficient regime to a power-law, happens at densities of ≈ 10 cm^{-3} (see also Audit & Hennebelle, 2010, their Figures 4 and 9).

radius

Other interpretations of the observed break are possible. The Σ_{gas}–Σ_{SFR} relation could be an

[7] computed as the mass-weighted average density of the gas in each beam

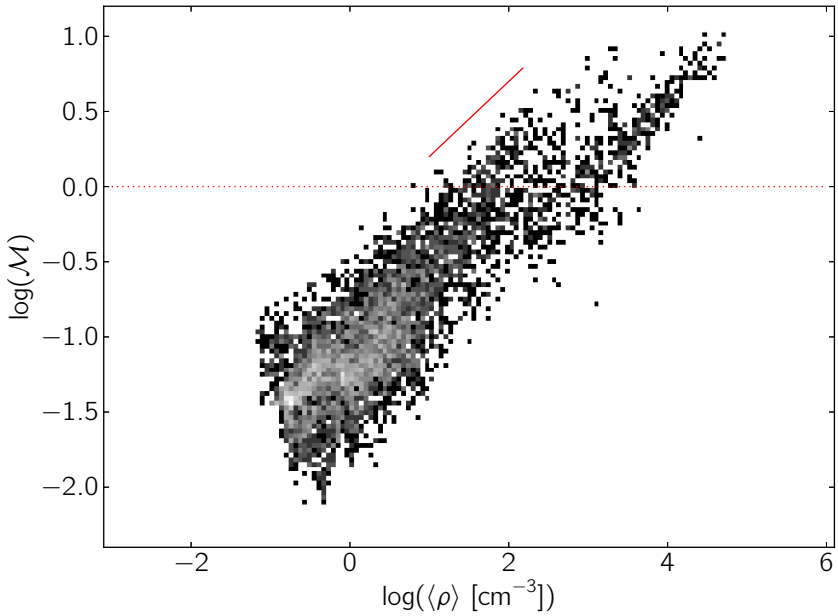

Figure 3.13

The Mach number as a function of the average volume density of gas computed in beams of 100×100×100 pc^3, for MW_{PC}. The solid line indicates the slope ($\mathcal{M} \propto \langle\rho\rangle^{0.5}$) found in small scale simulations of Audit & Hennebelle (2010) (their Figure 9).

effect of the galactic radial distance with low Σ_{gas} at large radius and high Σ_{gas} at small radius, as found by Kennicutt et al. (2007) and Bigiel et al. (2008). The break could then be explained as a consequence of the drop in the average volume density in the outer regions of galaxies as proposed by Barnes et al. (2012). However, Figure 3.14 shows no such radial dependence for Σ_{gas} nor Σ_{SFR}. Star-forming regions in outer parts of a galaxy can exhibit both star formation regimes. A possible explanation why we do not see any radial dependence in our simulations may be a missing metallicity gradient. The outer regions of our simulated galaxies have the same metallicity than the innermost regions, thus the metallicity is probably too high at the edge of disk and allows for an efficient cooling and consequently an efficient star formation while it may lie in the break regime otherwise.

When azimuthally averaged, Σ_{gas} and Σ_{SFR} both decline steadily as a function of radius in many galaxies despite different morphologies (see Bigiel et al. 2008 for a sample of nearby spiral galaxies and Leroy et al. 2009 for CO intensity radial profiles for the same sample). Figure 3.15 shows Σ_{gas} and Σ_{SFR} as functions of radius for $LMC_{1.0Z_\odot}$. Both radial profiles decline with galactic radius as in observed spiral galaxies.

HI to H_2 transition

Another alternative explanation for the existence of the break is that it corresponds to the transition from atomic to molecular hydrogen (Krumholz et al., 2009). According to this scenario, the transition from atomic to molecular hydrogen and the subsequent star formation depend on local conditions that vary with galactic radius, e.g. metallicity, gas pressure and shear[8]. Bigiel et al. (2008) found such radial dependence in the sample of nearby galaxies in agreement with the findings

[8]Shear dictates whether molecular clouds can form (e.g. Leroy et al., 2008, Elson et al., 2012), but if they do form, shear does not seem to influence the efficiency at which they convert their gas into stars (Dib et al., 2012).

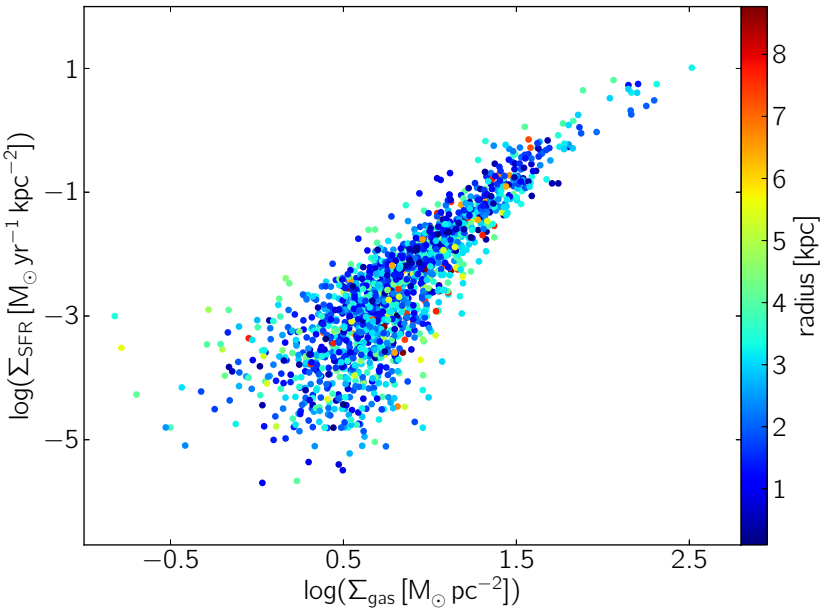

Figure 3.14

The local surface density of the star formation rate as a function of surface density of gas for $LMC_{1.0Z_\odot}$. Color indicates the radial distance of the beam in kpc.

of Wong & Blitz (2002) and the threshold interpretations of e.g. Kennicutt (1989), Martin & Kennicutt (2001) and Leroy et al. (2008). Similar results are reproduced in some simulations, e.g. Halle & Combes (2013), who find that molecular gas is a better tracer of star formation than atomic gas and plays an important role in the low surface density regions of galaxies by allowing for more efficient star formation. However, our models that do not include chemodynamics, are able to reproduce the observed break at low Σ_{gas}. Therefore, this seems to indicate that the presence of molecules is not a necessary condition to *trigger* the process of star formation. However, we acknowledge numerous observational evidences showing that molecules are involved at a later stage of the SF process.

metallicity

At this point, it is worth reconsidering the metallicity and its impact on the Σ_{gas}–Σ_{SFR} relation. In Figure 3.6, we have shown that the exact position of the break in the Σ_{gas}–Σ_{SFR} plane depends on metallicity. A comparison of different metallicities in otherwise identical systems shows that the slope at low Σ_{gas} has a greater value in metal-poor galaxies. Figure 3.3 suggests that metallicity is not the only factor determining the gas density distribution in our simulations. Similar lack of direct dependence of the fraction of dense gas on metallicity is found when simulations of the SMC with different metallicities are compared (not shown here). Thus the slope at low Σ_{gas} cannot be explained by the presence of a higher fraction of dense gas in systems with higher metallicity compared to systems with lower metallicity. However, metallicity has an impact on star formation, even though indirect. Metallicity directly influences the temperature of the gas: higher the metallicity, more efficient the cooling and therefore lower the temperature, which in turn, impacts the Mach number. In Figure 3.16, we show Mach numbers for $SMC_{1.0Z_\odot}$ and $SMC_{0.1Z_\odot}$. Higher values of Mach number are reached in galaxy with higher metallicity.

This work does not include metallicity-dependent self-shielding and feedback. Accounting for them, Dib (2011) showed that both the fraction of gas in molecular form and the efficiency of star

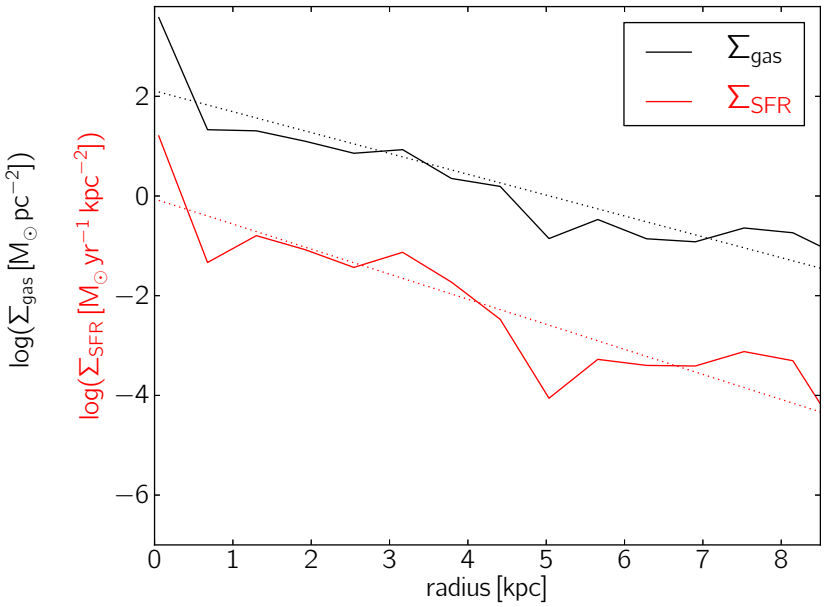

Figure 3.15

Radial profiles of azimuthally averaged Σ_{gas} (black) and Σ_{SFR} (red) for $LMC_{1.0Z_\odot}$. Dotted lines correspond to exponential fits.

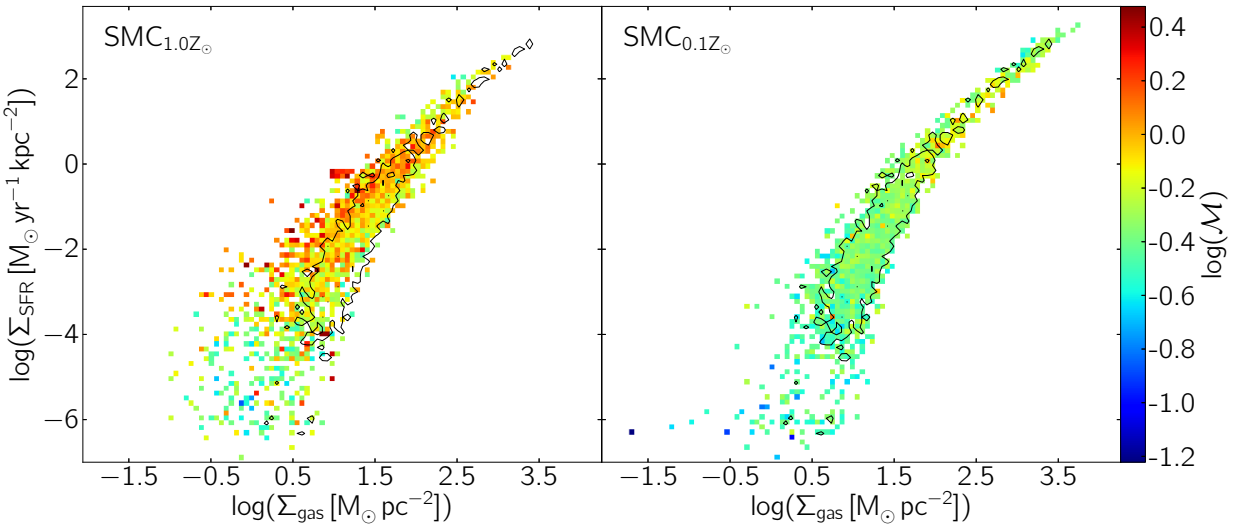

Figure 3.16

As in Figure 3.6, the effect of gas metallicity on the Σ_{gas}–Σ_{SFR} relation in the model of SMC is represented. Colors indicate the Mach number in the simulation of the SMC with metallicity of 1.0 $Z_\odot$ on the left panel and the simulation of the SMC with metallicity of 0.1 $Z_\odot$ on the right panel. In both panels the black contours are those of the simulation of the $SMC_{0.1Z_\odot}$, shown for reference.

formation per unit time depend on metallicity. This leads to the metallicity dependent Σ_{gas}–Σ_{SFR} relation at any Σ_{gas}.

turbulence

To summarize, we consider two representative beams having the same Σ_{gas}, but different Σ_{SFR} (Figure 3.17). These beams have similar average volume densities $\langle\rho\rangle$ which can be several orders of magnitude smaller than ρ_0. However, the beam that happens to have the highest Σ_{SFR} has always the highest Mach number, as previously suggested by Figure 3.9. We have argued above that the density threshold ρ_0, the thickness of the star-forming regions and the molecules do not have impact on the transition from the regime of inefficient star formation to the efficient power-law regime. The role of the artificial threshold ρ_0 imposed in the simulations is to set a frontier between the diffuse non-star-forming gas and the star-forming component, but not to tune the efficiency of star formation per se. Therefore at a given Σ_{gas}, this efficiency depends mostly on the level of turbulence ($\mathcal{M}$), i.e. the compression of the ISM, which determines the efficiency of star formation: higher turbulence results in higher Σ_{SFR}.

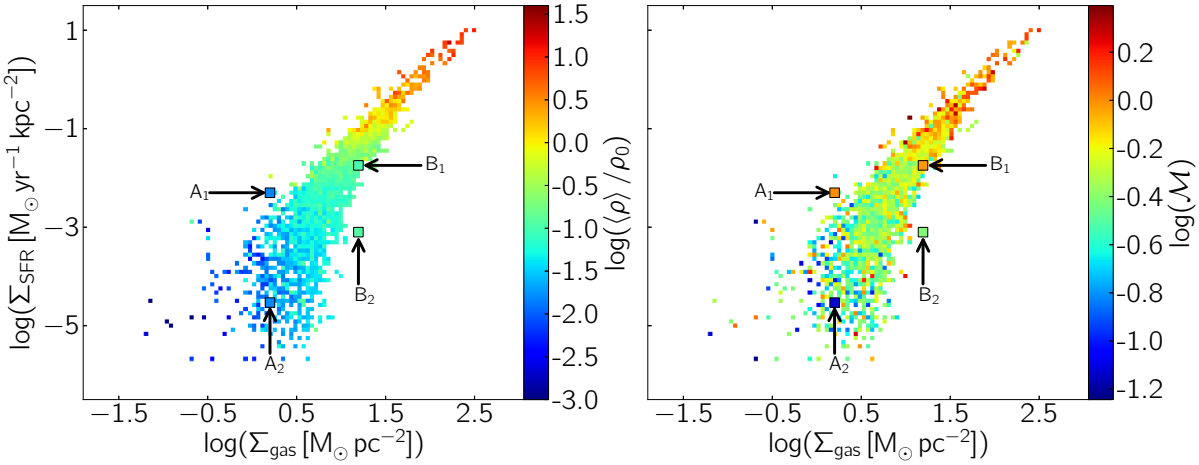

Figure 3.17

The volume density normalized to the threshold density ρ_0=10 cm^{-3} (left panel) and the Mach number (right panel) for the LMC$_{1.0Z_\odot}$ simulation, as in Figure 3.9. Two pairs of beams (A_1–A_2 and B_1–B_2) are highlighted in each panel. Within each pair, the two beams are chosen to have the same value of Σ_{gas} and a similar value of $\langle\rho\rangle/\rho_0$. Beams with higher Σ_{SFR} at fixed Σ_{gas} have a higher Mach number. The two pairs of beams have larger size for clarity reasons.

3.9 Comparison to merger-driven star formation

In previous Section we argued that the onset of supersonic turbulence in dense gas could contribute to the interpretation of the observed break in the Σ_{gas}–Σ_{SFR} relation by analyzing isolated disk and irregular galaxies. As suggested by observations (Irwin, 1994, Elmegreen et al., 1995), the (supersonic) ISM turbulence typically increases by a factor of a few in interacting and merging galaxies. Galaxy mergers are thus ideal laboratories to study the impact of the turbulent ISM on the star formation activity.

There is an observational body of evidence that interacting and merging disk galaxies can experience increased star formation activity (e.g. Sanders et al., 1988, Genzel et al., 1998, Barton et al.,

2000, Veilleux et al., 2002, Nikolic et al., 2004, Ellison et al., 2008).

Galaxy interactions induce non-axisymmetric gas distributions resulting in gravitational torques that build high gas concentrations at the nucleus by driving material inwards. Consequently, star formation rate is predicted to increase, resulting thus in a centralized or nuclear starburst. This is what is known as a standard theory of merger-induced starbursts, based on the results of major-mergers simulations (Barnes & Hernquist, 1991, Mihos & Hernquist, 1996, Cox et al., 2006, 2008, Karl et al., 2010). Such description explains well observed centrally concentrated starbursts (e.g. Sanders et al., 1988, Kewley et al., 2006, Ellison et al., 2010), however, there is also mounting evidence for a clustered component of merger-induced star formation that is not confined to the central regions and can be spatially extended. A well-known example of such spatially extended star formation are the Antennae galaxies (Whitmore & Schweizer, 1995), where majority of star formation occurs in the off-nuclear regions (in a few big star-forming clumps in extended disks and in the bridge between the two galaxies, Wang et al., 2004). Many other examples of extended star formation are known both in observed (e.g. Elmegreen et al., 1995, Wang et al., 2004, Weilbacher et al., 2000, Cullen et al., 2006, Smith et al., 2008, Hancock et al., 2009) and modeled systems (e.g. Barnes, 2004, Chien & Barnes, 2010). Moreover, star formation activity can be intense even in early interaction phases (Ellison et al., 2008) as well as in post-merger galaxies (Ellison et al., 2013), and it has been shown that SFR enhancements are not limited to closest pairs ($\lesssim$ 30 kpc), but are clearly found to occur at much larger separations as well (Scudder et al., 2012, Patton et al., 2013, Ellison et al., 2013).

There are further indications that the "standard" model cannot explain all aspects of merger-induced star formation. Firstly, a factor of only a few for an average enhanced SFR, as quantified in simulations of equal-mass mergers (Di Matteo et al., 2007, 2008), seems, in spite of debated observational estimates, to indicate too low intensity of merger-induced starbursts compared to observations (Bournaud, 2010). Secondly, physical processes involved in starbursting mergers cannot be limited to the global gas compression increasing the gas surface density only. This can be deduced from observationally suggested existence of two different modes in galaxy-averaged star formation relations (Daddi et al., 2010b, Genzel et al., 2010): a regime of normal disk galaxies and a regime of starbursts with an order of magnitude shorter depletion timescales for similar gas surface densities (Saintonge et al., 2012). In the absence of other physical mechanism, increased value of $\Sigma_{\rm gas}$ would move the system to the increased $\Sigma_{\rm SFR}$ along the sequence of normal galaxies. Thus, in addition to the standard mechanism that certainly takes places in real mergers as suggested by existing evidence for nuclear merger-driven starbursts, more complex physical processes need to be involved as well.

Gas inflows-induced increase of the gas surface density is not the only change in the structure of the ISM triggered by mergers. The ISM turbulence increases in interacting and merging galaxies, and could thus, by compressing the diffuse gas reservoirs, control the starburst activity. The increased velocity dispersions (few tens of km s^{-1}) of the cold gas component were observed already long time ago (Irwin, 1994, Elmegreen et al., 1995, Wei et al., 2012), however, merger simulations have started to resolve ISM turbulence only recently (Teyssier et al., 2010, Powell et al., 2013). In particular, the work of Teyssier et al. (2010) suggests that the main reason why previous models of galaxy mergers studying the properties of merger-induced star formation do not allow to understand the physical processes driving the starburst mode is missing resolved ISM turbulence and clustered star formation. In spite of this progress, several questions remained without answers. Such as, whether the small-scale physics and structures are resolved sufficiently so that convergence on the global starburst activity is reached, what physical processes increase or modify the ISM turbulence in mergers and why such changes lead to starburst activity.

By resolving the structure and small-scale physics[9] of the ISM, Renaud et al. (2014) reached the convergence of the global SFR at parsec-scale resolution, which allowed to perform a study of integrated properties of the tides, turbulence and star formation. Our findings point toward the compressive turbulence being the principal agent in driving the merger to the starburst sequence. We suggest that turbulence is injected into the ISM by the increased gas mass fraction in compressive tides in extended volumes during the interaction. The resulting increased compressive turbulence mode (which overcomes the solenoidal one) leads to an excess of dense gas which translates into enhanced star formation activity bringing the system into the regime of starburst in the Schmidt-Kennicutt diagram.

In the remainder of this Chapter, I focus mainly on some of the spatially resolved properties in the model of merging galaxies of Renaud et al. (2014) that resembles Antennae galaxies (NGC 4038/39), but is a fairly representative case of many other mergers. Simulation of this major galaxy merger was run with the same code as in the case of galaxies described in Section 3.2. The included physical processes are also very similar: heating and cooling at solar metallicity, stellar feedback in the form of photo-ionization, radiative pressure and SNe. The maximal resolution reached is 1.5 pc, but the same merger model was run also at lower resolutions (6 and 24 pc). In addition, as a control sample, the progenitor galaxies were run in isolation too.

The evolution of the system in the Σ_{gas}–Σ_{SFR} plane is shown in Figure 3.18. The isolated progenitors as well as pre-merger galaxies are initially close to the sequence of disk galaxies (local spirals and high redshift disks; see Daddi et al. 2010b). During the first encounter, system starts to move toward the sequence of starbursts, while the surface density of gas is significantly enhanced only after the second encounter. The interpretation of this behavior was given in Renaud et al. (2014). We have shown that during the first encounter global inflows didn't have enough time to increase the surface density of gas yet, even though Σ_{SFR} is significantly increased due to the increased compressive turbulence. On the other hand, the increased Σ_{gas} at the second encounter results from gravitational torques and gas inflows that operate in addition to previously developed compressive turbulence. After the coalescence, system starts to go back to the disk sequence, but before reaching it definitively, it experiences another come-back to the sequence of starbursts after which it returns toward the disk regime again. This second ascension to the starburst regime lasts much longer than the first one and it is characterized by the steady decrease of the surface density of gas, while the surface density of star formation rate increases. This could be caused by the material previously expulsed during the interaction that is now falling back to the merger remnant.

Let us now focus on the small-scale, local properties of the galactic system. For the small-scale analysis, we choose four different snapshots corresponding to four different time periods throughout the interaction sequence: $\approx$ 6 Myr before the first pericentre passage (pre-merger), $\approx$ 20 Myr after the first pericentre passage, $\approx$ 20 Myr before the second pericentre passage and $\approx$ 2 Myr after the second pericentre passage. The respective density maps of gas are shown in Figure 3.19. The choice is motivated by the combination of values of Σ_{gas} and Σ_{SFR} reached at these periods. As can be seen from Figure 3.18, the two first snapshots correspond to comparable integrated Σ_{gas}, while their Σ_{SFR} trace two different regimes, disks and starbursts, respectively. At two other epochs, galaxies are close to the starburst sequence, but have significantly different surface density of gas. In Figures 3.20-3.22, the dependence of the Σ_{gas}–Σ_{SFR} relation on the Mach number, divergence of velocity field and distance to the closest center of mass, respectively, is shown for these four different

[9] Resolution of $\sim$ 1 pc is needed in order to allow gas cooling down $\lesssim$ 100 K and to reach high Mach numbers ($\sim$ 10). Other physics that may be important, but consequences of which only start to be explored, such as magnetic fields or cosmic rays, are not included.

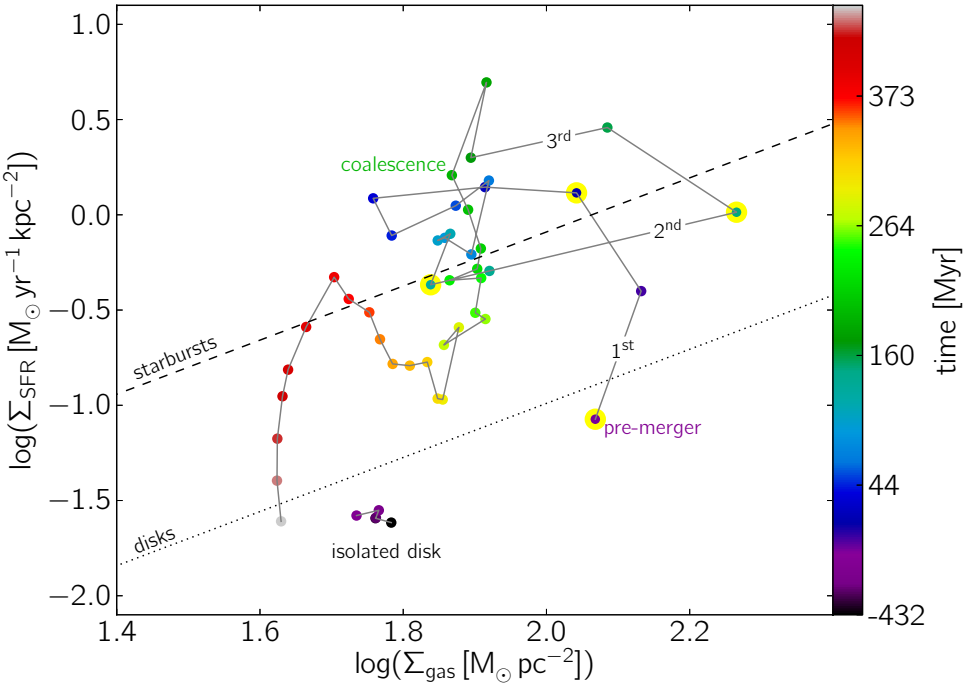

Figure 3.18

Evolution of surface density of gas and star formation inside the half-mass radius of galaxies every ≈ 10 Myr. The overplotted numbers indicate the three pericentre passages at t=0, 146 and 171 Myr. The final coalescence begins at ≈ 190 Myr. Time for isolated disk is arbitrary. The dashed and dotted lines indicates the sequence of starbursts and disks, respectively, as in Daddi et al. (2010b).

snapshots.

The Σ_{gas}–Σ_{SFR} relation shows qualitatively very similar dependence on the Mach number (Figure 3.20) to the one obtained for isolated galaxies (to be compared with Figure 3.9). Irrespectively of the stage of merging, regions located below the break tend to be have Mach numbers below unity, while the regime of efficient star formation is characterized by Mach numbers greater than unity.

Renaud et al. (2014) measured the turbulence energy carried by compressive and solenoidal mode in the simulation of Antennae galaxies. We found that during the collision the energy in compressive mode rises more significantly than that in solenoidal mode (factor of ≈ 12 for the compressive mode and factor of ≈ 5 for the solenoidal mode). Here, we explore the spatially resolved properties of star formation and their relation to those of turbulent flow. Figure 3.21 shows the dependence of the Σ_{gas}–Σ_{SFR} relation on the divergence of velocity field, computed, similarly to other local properties, as a mass-weighted average in each beam. Here, we do not compare directly the compressive mode with the solenoidal one, however we can get a global picture on the importance of the compressive turbulence in the resolved Schmidt-Kennicutt diagram. Regions of efficient star formation tend to have higher absolute values of the velocity divergence. In addition, below the break, at fixed Σ_{gas}, regions with higher Σ_{SFR} tend to be more compressive (their divergence of the velocity field is lower).

Finally, we wish to explore if there exists a correlation between the distance of the beam from the center of the mass of the system and its position in the Schmidt-Kennicutt diagram. Figure 3.22 shows the dependence of the Σ_{gas}–Σ_{SFR} relation on the distance of the beam to the closest center

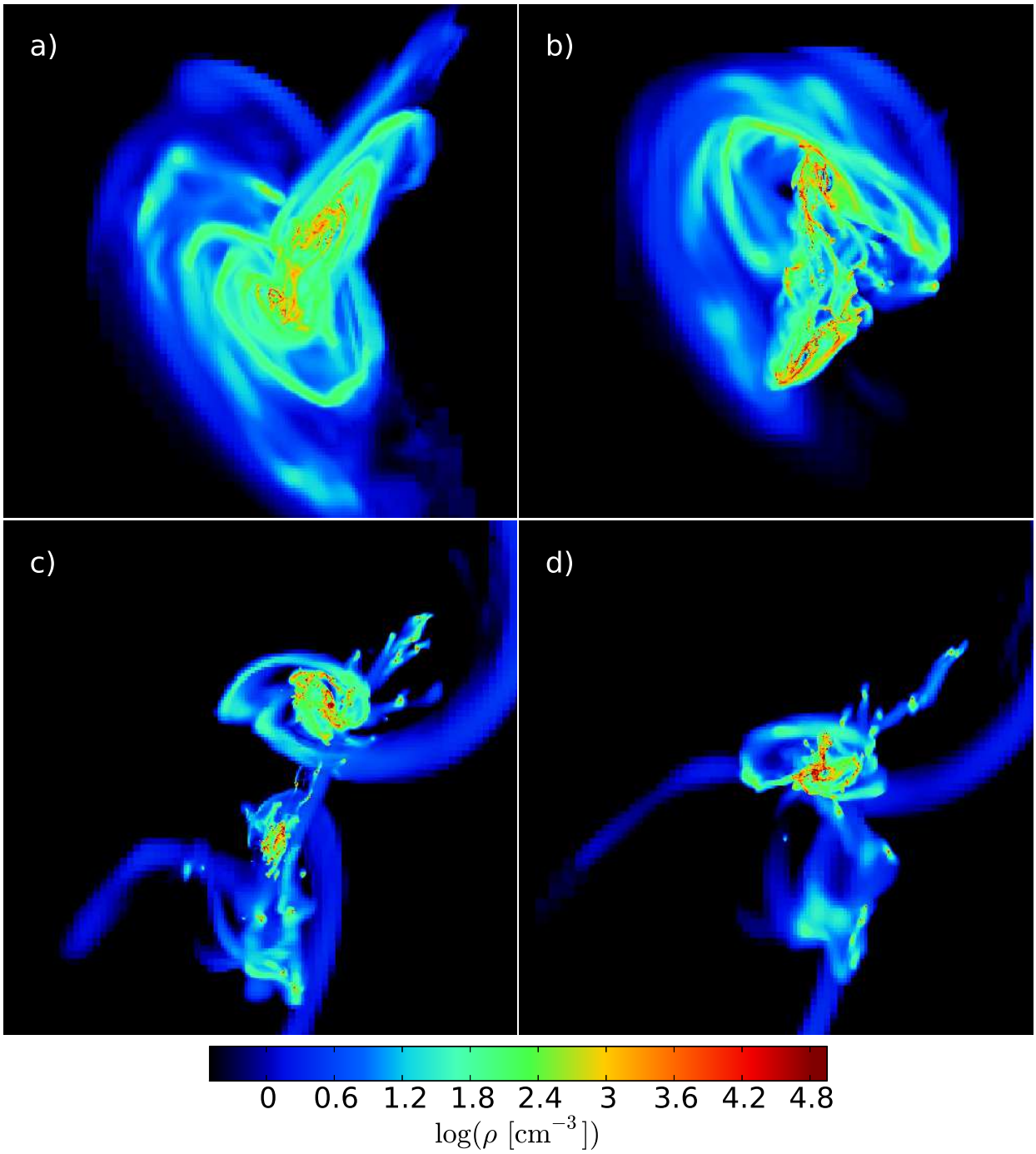

Figure 3.19

Surface density of gas of the Antennae galaxies in the central 30×30 kpc^2 at four different stages of the merger: pre-merger (panel a), ≈ 20 Myr after the first pericentre passage (panel b), ≈ 20 Myr before the second pericentre passage (panel c) and ≈ 2 Myr after the second pericentre passage (panel d).

of the mass at given stage of merger. We do not find any clear trend with regard to this dependence. As a matter of fact, highest star formation activity is in the center of galaxies, but the triggered

star formation is spatially extended, not limited to nuclear regions only. At any epoch of merging, star-forming regions can exhibit both star formation regimes, no matter how far away they are from the closest center of mass.

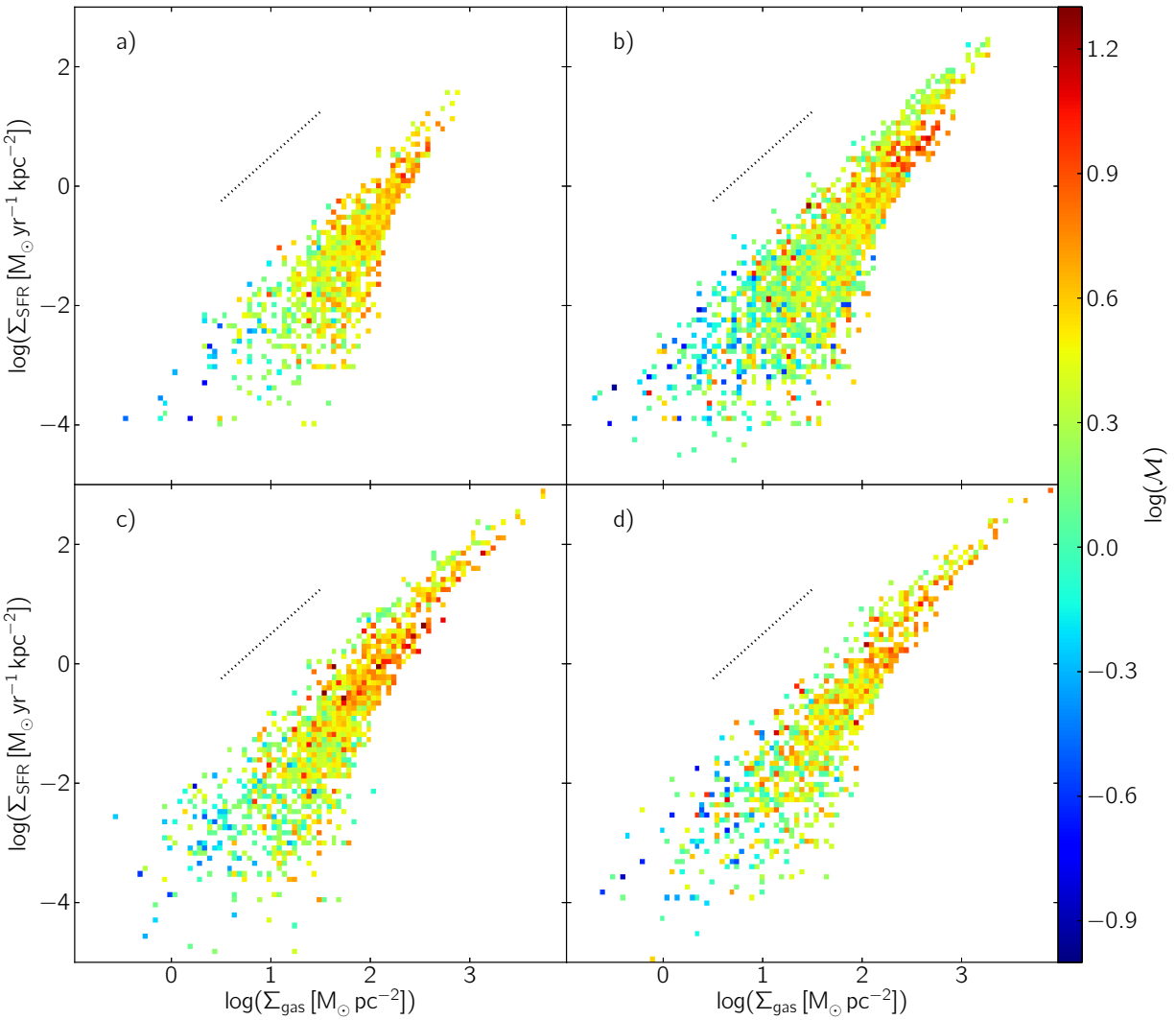

Figure 3.20

The local surface density of star formation rate as a function of surface density of gas at four different stages of merger (highlighted with yellow circles in Figure 3.18): pre-merger (panel a), ≈ 20 Myr after the first pericentre passage (panel b), ≈ 20 Myr before the second pericentre passage (panel c) and ≈ 2 Myr after the second pericentre passage (panel d). The color indicates the Mach number in each beam. The dotted lines display a power-law of index 3/2.

3.10 Summary

A study of the star formation relations and thresholds at 100 pc scale in a sample of low-redshift simulated galaxies was presented. These include simulations representative of Milky Way-like spiral

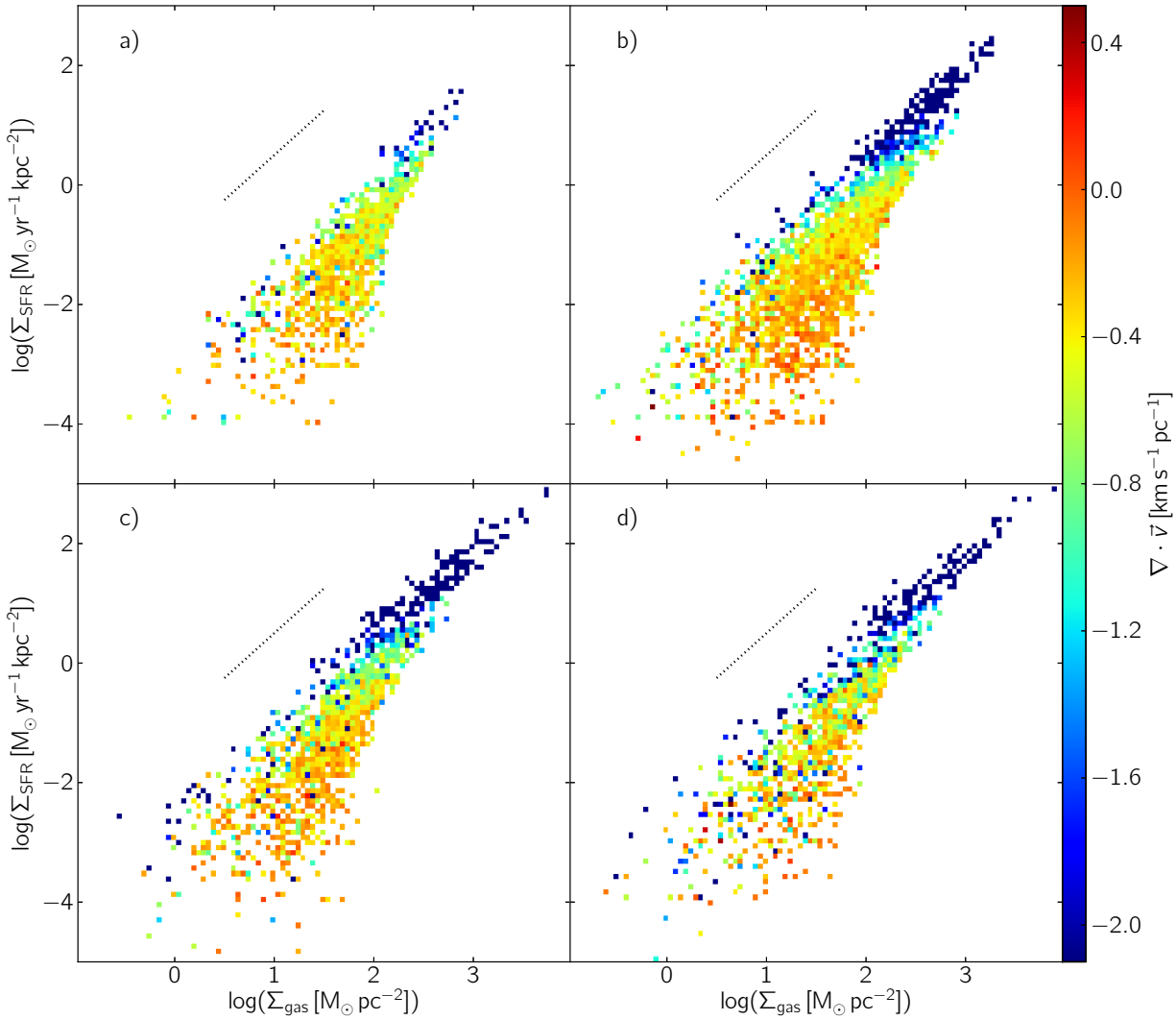

Figure 3.21

The local surface density of star formation rate as a function of surface density of gas at four different times, as in Figure 3.20. The color indicates the divergence of velocity field for each beam.

galaxy, the Large and the Small Magellanic Clouds. We analyzed the role of interstellar turbulence, gas cooling, and geometry in drawing these relations, by investigating the dependence of the star formation on three parameters: the Mach number, the thickness of the star-forming region and the star formation volume density threshold.

Our main findings are as follows:

① Our simulations point toward a contribution of the onset of supersonic turbulence in dense gas to the surface density threshold for efficient star formation. For all analyzed systems, galaxy merger included, we obtain qualitatively the same result: regions located below the break are dominated by subsonic turbulence, while turbulence tends to be supersonic in those located in the power-law regime.

② The distribution of the ISM of a galaxy in the Σ_{gas}–Σ_{SFR} plane (mainly the position of the

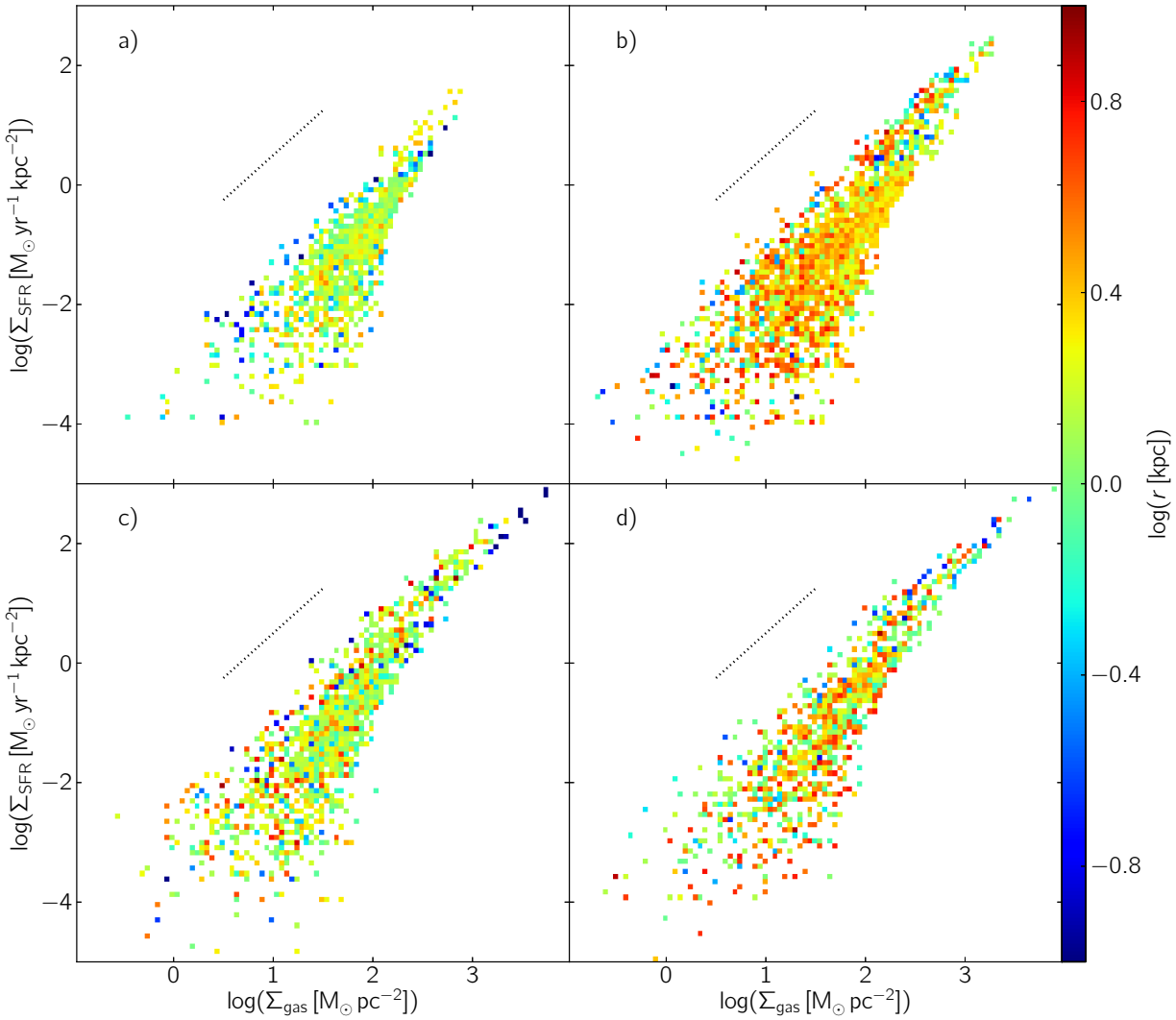

Figure 3.22

The local surface density of star formation rate as a function of surface density of gas at four different times, as in Figure 3.20. The color indicates the distance of each beam to the closest center of mass.

break) is sensitive to metallicity, but always correlated with the Mach number as detailed above. When different metallicities are considered for otherwise identical systems, Σ_{SFR} increases with the metallicity. When different systems with same metallicities are considered (compare Figure 3.11 for $LMC_{1.0Z_\odot}$ and Figure 3.6 for $SMC_{1.0Z_\odot}$), roughly the same position in the Σ_{gas}–Σ_{SFR} diagram is obtained. This can explain observations of low-efficiency star formation in relatively dense gas in SMC-like dwarf galaxies. The driving physical parameter is still the onset of supersonic turbulence, but this onset is harder to reach at moderate gas densities in lower-metallicity systems that can preserve warmer gas.

③ During galaxy merger, the system evolves from the disk to the starburst regime in the Σ_{gas}–Σ_{SFR} diagram. As shown by Renaud et al. (2014), this is due to the excess of dense gas generated by the increased compressive turbulence which is triggered by compressive tides

during the interaction. Regions located in the power-law regime are found to have higher level of compressive turbulence compared to those located below the break.

④ Merger-enhanced star formation activity is not limited to the nuclear region, beams with high Σ_{SFR} can be easily found at larger distances as well.

Several other models (e.g. Krumholz et al., 2009) have proposed that self-shielding alone is efficient at producing giant molecular clouds and triggering SF. Indeed, this effect cools the gas down at high density, thus enhancing the fragmentation of the ISM, but also lowering the sound speed, i.e. increasing the level of turbulence. Both the compression of the ISM by supersonic turbulence and the fragmenting effect from self-shielding increase with metallicity. Having neglected the dependence of self-shielding on metallicity, our results emphasize the role of supersonic turbulence in our most metal rich examples. Combining the two effects would lead to a higher efficiency of star formation than either effect alone.

At the scale of clouds, the gravitational collapse is known to trigger SF. However, at larger scales, in galactic structures like spiral arms, we found that the injection of turbulence by self-gravity (and possibly by other processes like shear and feedback) can drive the compression of the gas, leading to SF. In this view, an external trigger like supersonic turbulence could be a sufficient condition to from stars, without necessarily invoking the collapse of large galactic regions ($\sim$ 100 pc) prior to turbulent compression – only compressed regions need to eventually collapse into stars.

Chapter 4

Star formation laws and thresholds

The role of turbulence - theory

> *In order to avoid simply describing experiments that have been done, we have to propose laws beyond their observed range. There is nothing wrong with that, despite the fact that it makes science uncertain. If you thought before that science was certain–well, that is just an error on your part.*
>
> — Richard P. Feynman, *The Character of Physical Laws*

4.1 Introduction

Here, we aim at developing an analytic model, based on simple assumptions, describing the star formation relations and thresholds as a function of the presence of the supersonic turbulence that shapes the ISM in different types of galaxies.

4.2 Theory

4.2.1 Analytical formalism

Let us start by considering a region of surface S and thickness h, total mass M of which is distributed according to a mass-weighted probability distribution function (PDF) f. The volume of such region can be written as the sum of the volumes occupied by the gas at all possible densities ρ as

$$\begin{aligned} V = hS &= \int_0^\infty \frac{Mf(x)}{\rho}\, dx \\ &= \frac{M}{\overline{\rho}} \int_0^\infty \frac{f(x)}{x}\, dx, \end{aligned} \tag{4.1}$$

where in the second line the normalization of the local gas volume density ρ, $x = \rho/\overline{\rho}$, was used. $\overline{\rho}$ then reads

$$\begin{aligned} \overline{\rho} &= \frac{M}{\mathrm{h}S} \int_0^\infty \frac{f(x)}{x}\, dx \\ &= \frac{\Sigma}{\mathrm{h}} \int_0^\infty \frac{f(x)}{x}\, dx, \end{aligned} \tag{4.2}$$

where $\Sigma = M/S$ is gas surface density of considered region.

The surface density of SFR (Σ_{SFR}) can be similarly written as

$$\begin{aligned} \Sigma_{\mathrm{SFR}} = \frac{M_{\mathrm{SFR}}}{S} &= \frac{1}{S} \int_0^\infty \frac{Mf(x)}{\rho} \rho_{\mathrm{SFR}}(x)\, dx \\ &= \frac{\frac{M}{\overline{\rho}} \int_0^\infty f(x) x^{-1} \rho_{\mathrm{SFR}}(x)\, dx}{\frac{M}{\overline{\rho}\mathrm{h}} \int_0^\infty f(x) x^{-1}\, dx} \\ &= h \frac{\int_0^\infty f(x) x^{-1} \rho_{\mathrm{SFR}}(x)\, dx}{\int_0^\infty f(x) x^{-1}\, dx}, \end{aligned} \tag{4.3}$$

where M_{SFR} and ρ_{SFR} are the local mass and volume density of SFR, respectively. The second line simply takes the expression of S from Equation (4.1). In order to apply this generally valid expression for Σ_{SFR} to real systems, two ingredients need to be supplied: the density PDF f, telling us how the density field is distributed, and the density star formation rate ρ_{SFR}, i.e. the relation describing the process of the conversion of gas into stars.

4.2.2 Log-normal PDF

First ingredient required to compute the Σ_{SFR} that we discuss is the density PDF. The shape of the density PDF is determined by global properties of galaxies and physical processes of the ISM. Among them compressible turbulence and gravity seem to play dominant role in shaping the gas density distribution. Vázquez-Semadeni (1994) in his pioneering work suggested, based on a statistical argument and two-dimensional numerical simulation, that the density distribution in fully turbulent flow was consistent with a log-normal PDF. Since then, various simulations (e.g. Padoan et al., 1997, Passot & Vázquez-Semadeni, 1998, Nordlund & Padoan, 1999, Klessen, 2000, Kritsuk et al., 2007, Federrath et al., 2008, 2010, Price & Federrath, 2010, Konstandin et al., 2012) have established

that the density PDF of *supersonic non-gravitating isothermal turbulent* gas is well represented by a log-normal functional form

$$f_\sigma(x) = \frac{1}{x\sqrt{2\sigma^2\pi}} \exp\left[-\frac{\left(\ln(x) - \frac{\sigma^2}{2}\right)^2}{2\sigma^2}\right], \tag{4.4}$$

where the width σ is related to the Mach number $\mathcal{M} = v_{rms}/c_s$[1] through the relation $\sigma^2 = \ln(1 + b^2\mathcal{M}^2)$ with the empirical parameter b, which depends on the nature of the turbulence. Using simulations of driven isothermal supersonic turbulence, Federrath et al. (2008, 2010) studied two limiting cases of turbulence driving: compressive (curl-free) and solenoidal (divergence-free). They confirmed the result by Passot & Vázquez-Semadeni (1998) of $b \approx 1$ for the case of compressive forcing and found $b \approx 1/3$ for solenoidal forcing, in agreement with e.g. Kritsuk et al. (2007), Beetz et al. (2008).

Let us now discuss the two conditions under which the supersonic turbulence generates the log-normal PDF, the isothermal and non-gravitating gas. Already Scalo et al. (1998) pointed out that the density PDF is strictly log-normal only for isothermal supersonic gas. Indeed, PDF cannot be exactly log-normal for non-isothermal flows as the condition of the independence of the mean density is no longer satisfied. Studies of two-phase gas (e.g. Gazol et al., 2005, Vázquez-Semadeni et al., 2006, Audit & Hennebelle, 2010) showed that the density PDF of such medium is not log-normal anymore, instead, two peaks typically develop, one at low density ($\sim$ a few cm^{-3}) and one at high density ($\sim$ a few hundreds of cm^{-3}). Similarly, deviations from log-normal PDF were found for the gas described by the polytropic equation of state. Simulations of driven supersonic turbulence for such gas produced skewed PDFs (e.g. Passot & Vázquez-Semadeni, 1998, Nordlund & Padoan, 1999). This result can be understood qualitatively: the dense gas that happens to be colder than the average has higher Mach number which leads to broader PDF. As a consequence, the PDF has a more extended high-density wing than in the isothermal case. However, PDFs of polytropic supersonic turbulence are not far from log-normal and show a high density tail that formally approaches power-law (Nordlund & Padoan, 1999).

What about gravity? Gravity leads to collapse and thus is expected to have a strong impact on the density PDF. Simulations show that once gravity becomes important and takes over, some gas is collapsing which leads to a high density tail in the PDF (e.g. Klessen, 2000, Slyz et al., 2005, Hennebelle & Chabrier, 2008, Kritsuk et al., 2011, Collins et al., 2012). Empirically, this high density tail approaches power law, but the region around the maximum of the PDF remains well described by a log-normal functional form (Nordlund & Padoan, 1999). Moreover, this gravitational tail evolves with time: it develops first at high density part of the PDF and advances steadily to ever lower densities. Girichidis et al. (2014) proposed a simple analytic model based on spherical free-fall collapse according to which only very dense regions (with densities much higher than the mean density) will be affected. This is because the free-fall time ($t_{ff} \propto \rho^{-1/2}$) of gas at densities well below the mean density is very long compared to the evolutionary time scales.

The density field cannot be directly observed, however, the integrated density along the line of sight, the column density, can be used instead to compare models with observations. The column density PDFs inferred from observations of molecular clouds seem to support theoretical predictions for the density PDFs. The column density distribution of clouds without active star formation are well-fitted by log-normal functional forms, while active star-forming clouds show a power-law excess

[1] v_{rms} and c_s denote the root mean square velocity and the thermal sound speed, respectively

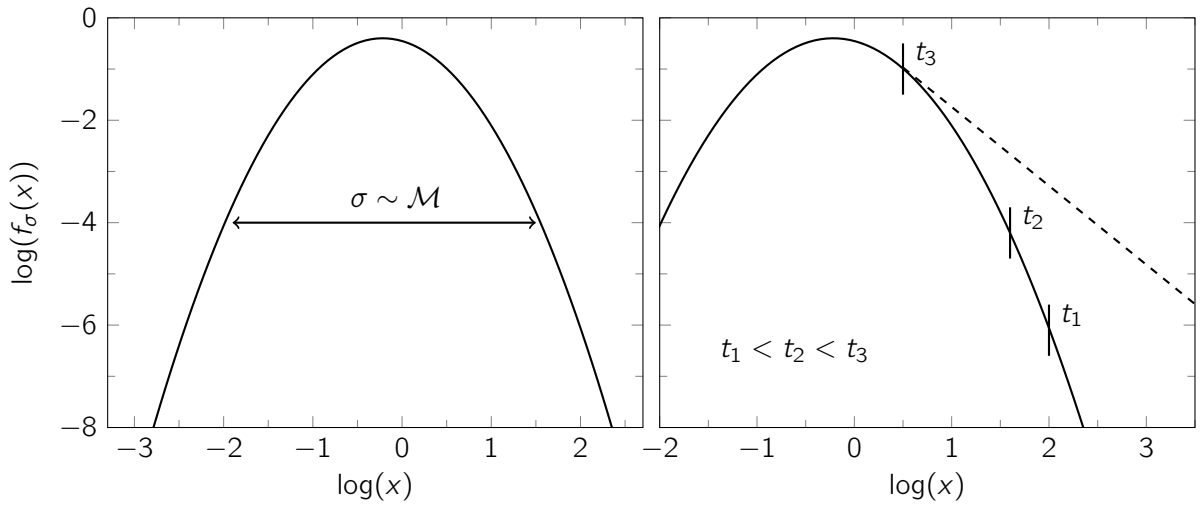

Figure 4.1

Left: Log-normal density PDF. The width of the PDF is related to the Mach number $\mathcal{M}$ through $\sigma^2 \approx \ln(1 + 3\mathcal{M}^2/4)$: the width increases with increasing $\mathcal{M}$. **Right:** Schematic view of log-normal density PDF with a high-density power-law tail. The switch (indicated by the vertical line) from a log-normal PDF to a tail that approximates a power-law tail advances with time from higher to ever lower densities.

of high column densities (Kainulainen et al., 2009, Froebrich & Rowles, 2010, Lombardi et al., 2010, André et al., 2011, Schneider et al., 2012).

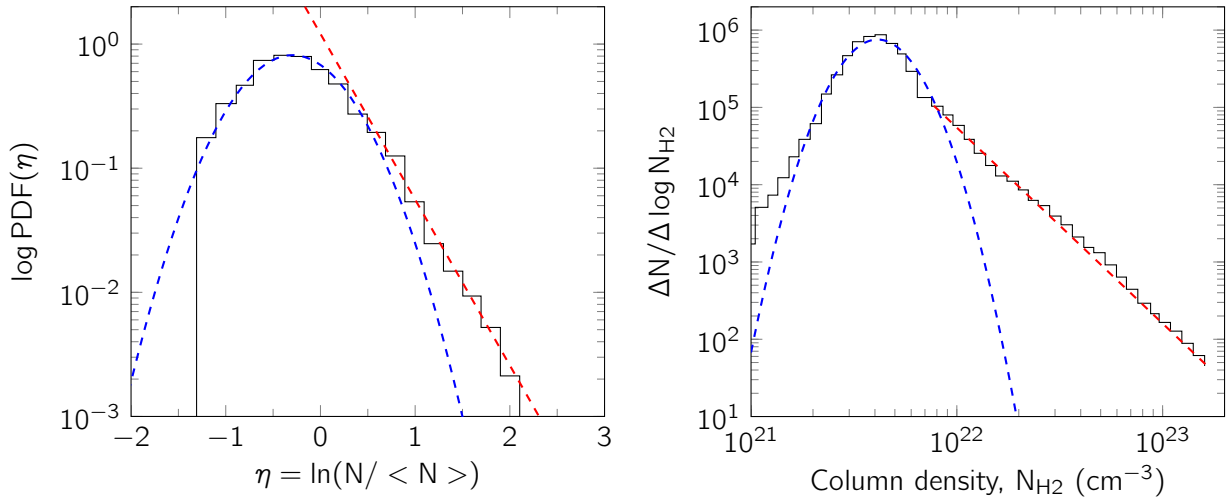

Figure 4.2

Probability density functions of column density inferred from observations. **Left:** The Rosette molecular cloud (from Schneider et al., 2012, their Figure 6). **Right:** The Aquila star-forming molecular cloud (from André et al., 2011, their Figure 5). Log-normal fit (blue) at low column densities and a power-law fit (red) at high column densities are superimposed.

It is established that most of the ISM mass is supersonically turbulent (see e.g. Burkert, 2006, and references therein), thus in the forthcoming application of the analytical formalism, the log-normal density PDF will be applied. Further discussion about the validity of this assumption can be found in

3.3.3.

4.2.3 Dynamical star formation

Second ingredient that need to be supplied to Equation (4.3) is ρ_{SFR}, encoding the information about the conversion of gas into stars. Schmidt (1959) pointed out that it would seem probable that the star formation rate depends on the gas density and proposed that the number of stars formed per unit interval of time scales as a power of the gas density.

To describe the process of star formation locally (at small scales), we use this empirical relation, with the assumption, that the relevant time scale for star formation is the local free-fall time t_{ff}. According to this scenario, a fraction of gas that becomes gravitationally unstable and collapses converts a constant fraction ϵ of its mass into stars per free-fall time. In addition, we assume the existence of a volume density threshold ρ_0 above which the gas density has to be in order to be eligible for star formation.

ρ_{SFR} can thus be written as

$$\rho_{SFR} = \begin{cases} 0 & \text{if} \rho \leq \rho_0 \\ \epsilon \frac{\rho}{t_{ff}} = \epsilon \sqrt{\frac{32G}{3\pi}} \rho^{3/2} & \text{else} \end{cases} \tag{4.5}$$

4.2.4 Σ_{gas}–Σ_{SFR} relation without stellar feedback

We now have at hand all the elements necessary to finally compute the expression for Σ_{SFR} from Equation (4.3). For a log-normal PDF and a local star formation given by Equation (4.5), Σ_{SFR} becomes (see Appendix A.1 for detailed derivation)

Σ_{SFR} without feedback

$$\Sigma_{SFR} = \epsilon \sqrt{\frac{8G}{3\pi}} \frac{\exp\left(\frac{3}{8}\sigma^2\right)}{\sqrt{h}} \Sigma_{gas}^{3/2} \operatorname{erfc}\left(\frac{\ln\left(\frac{\rho_0 h}{\Sigma_{gas}}\right) - \sigma^2}{\sqrt{2}\sigma} \right). \tag{4.6}$$

This expression, relating Σ_{gas} and Σ_{SFR} depends on three parameters: Mach number $\mathcal{M}$ (through the width σ of the PDF), thickness h of a region under consideration and ρ_0 which represents a volume density threshold above which star formation takes place. By examining the functional dependence of this expression on Σ_{gas}, we notice immediately two regimes, a power law with index 3/2, in which the the star formation relation in directly imprinted, and a complementary error function which is present only if ρ_0 is different from zero. To illustrate the behavior of Σ_{SFR}, we plot it in Figures 4.3a)-c) as a function of Σ_{gas} for different combinations of parameters $\mathcal{M}$, h and ρ_0, respectively. We recover a 3/2 index power law, which falls off at low surface densities (for any non-zero threshold ρ_0) resulting in break in Σ_{gas}–Σ_{SFR} relation, the shape and position of which depend on $\mathcal{M}$, h and ρ_0.

4.2.5 Σ_{gas}–Σ_{SFR} relation with regulation by stellar feedback

So far, we haven't considered any kind of regulation by stellar feedback. However, in dense cores, the conversion of gas into stars is limited by stellar feedback which can heat, ionize or even eject the gas and thus making it unavailable for star formation. Such gas can again participate in conversion

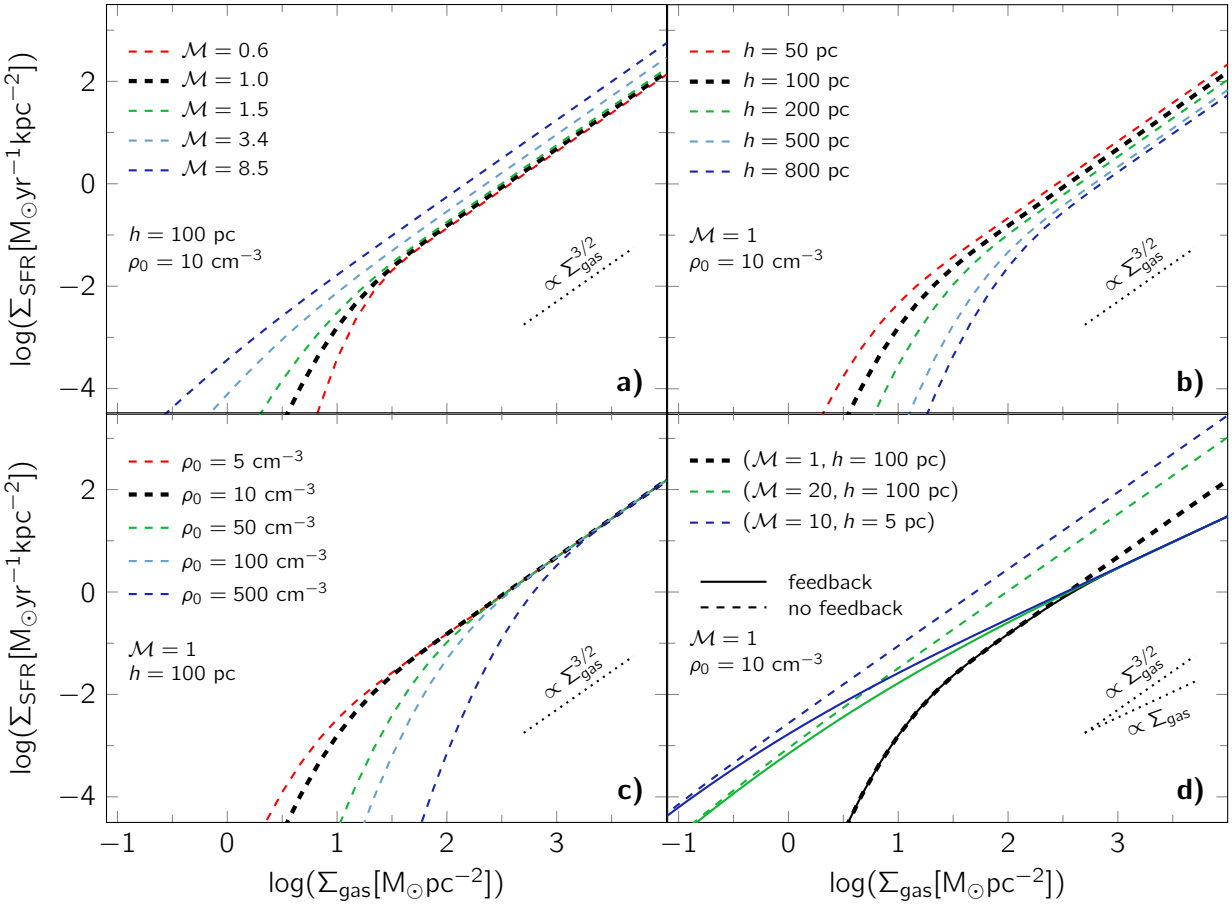

Figure 4.3

Surface density of the star formation rate as computed from Equation (4.6) with $\epsilon = 0.01$, showing its dependence on the Mach number $\mathcal{M}$ (panel a), the thickness h (panel b) and the density threshold ρ_0 (panel c). Panel d) illustrates the regulation due to stellar feedback, as computed from Equation (4.8) (solid lines), compared to no regulation (dashed lines in all panels).

to stars after a certain time t_s. Only a certain fraction ϵ_s of the gas mass can be consumed for star formation per timescale t_s (Bontemps et al., 1996, Matzner & McKee, 2000), which translates into a saturation in the local SF:

$$\rho_{SFR} = \begin{cases} 0 & \text{if } \rho \leq \rho_0 \\ \min\left(\epsilon\sqrt{\frac{32G}{3\pi}}\rho^{3/2}, \frac{\epsilon_s}{t_s}\rho\right) & \text{else} \end{cases} \tag{4.7}$$

In what follows, we will adopt the value of 100 Myr for t_s, which seems reasonable as the (re)formation of star-forming clouds is generally triggered by galactic-scale processes (e.g. Dobbs & Pringle, 2009 for spirals; Teyssier et al., 2010 for mergers; and Bournaud et al., 2007 at high redshift). This value represents for instance the interval between the compression by two spiral arms, or for giant clumps to collapse in high-redshift disks. In nuclear starbursts, where the dynamical timescale is much shorter ($\sim$ 10 Myr), the strong stellar feedback from OB-type stars takes over and also regulates SF, by limiting the conversion of gas into stars to $\epsilon_s \approx 0.3$ (Murray et al., 2010) over the duration of the starburst event, i.e., t_s = 100 Myr here again (Di Matteo et al., 2008).

By using this saturated star formation Equation (4.7) together with a log-normal PDF, Equation (4.3) leads to $\Sigma_{\rm SFR}$ of following form (see Appendix A.2 for detailed derivation)

$\Sigma_{\rm SFR}$ with feedback

$$\begin{aligned}\Sigma_{\rm SFR} =& \epsilon\sqrt{\frac{8G}{3\pi}}\frac{\exp\left(\frac{3}{8}\sigma^2\right)}{\sqrt{h}}\Sigma_{\rm gas}^{3/2}\left[\operatorname{erfc}\left(\frac{\ln\left(\frac{\rho_0 h}{\Sigma_{\rm gas}}\right)-\sigma^2}{\sqrt{2}\sigma}\right)\right.\\ &\left.-\operatorname{erfc}\left(\frac{\ln\left(\frac{\epsilon_s^2 3\pi h}{t_s^2 32G\epsilon^2\Sigma_{\rm gas}}\right)-\sigma^2}{\sqrt{2}\sigma}\right)\right]\\ &+\frac{\epsilon_s}{2t_s}\Sigma_{\rm gas}\operatorname{erfc}\left(\frac{\ln\left(\frac{\epsilon_s^2 3\pi h}{t_s^2 32G\epsilon^2\Sigma_{\rm gas}}\right)-\frac{\sigma^2}{2}}{\sqrt{2}\sigma}\right).\end{aligned} \tag{4.8}$$

As illustrated in Figure 4.3d), this corresponds to the flattening of the power law at high surface densities (power law of index 3/2 is followed by a power law of unity index at high $\Sigma_{\rm gas}$). This transition to the regime of feedback-regulation is shifted toward lower $\Sigma_{\rm gas}$ for higher $\mathcal{M}$ or smaller h.

4.2.6 $\Sigma_{\rm gas}$–$\Sigma_{\rm SFR}$ relation for starbursting mergers without stellar feedback

Due to the tidal interaction, the gas in merging galaxies is expected to have higher turbulent velocities. This modification of th ISM turbulence is directly imprinted in the gas density PDF in the form of excess of dense gas compared to a log-normal PDF. Such an excess of high-density components is found in the hydrodynamic simulations of mergers (Teyssier et al., 2010, Bournaud et al., 2011b, Renaud et al., 2014), even though the resulting PDFs are not necessarily log-normal. This behavior can be qualitatively understood by considering how the ISM turbulence affects the gas distribution and thus its PDF. The width of the PDF is to first order related to the Mach number through the parameter representing the type of turbulent mode. For purely compressive turbulence, the density PDF is roughly three times larger than for purely solenoidal one (Federrath et al., 2008). In isolated and pre-merger galaxies, the PDF of which is well described by a log-normal PDF, the equipartition is roughly reached, i.e. one third of turbulent energy is in compressive and two thirds in solenoidal mode (Federrath et al., 2008, 2010). During the merger, the turbulent energy raises and the maximum density increases significantly. When the compressive mode overcomes the solenoidal one, the system moves away from the equipartition and the PDF gets modified: secondary component at high density appears (as found in the simulation of Antennae galaxies by Renaud et al., 2014). To keep the analytic formalism as simple as possible, we will model the merger induced density PDF by a function that fits well the gas density probability distribution function in merging galaxies:

$$f(x) = (1-m)f_{\sigma_1}(x) + mf_{\sigma_2}(x/\exp\delta), \tag{4.9}$$

where f_σ is a log-normal functional form given by Equation (4.4). The parameter m represents a mass fraction of the initial PDF that is converted into a denser component, parametrized by a dimensionless parameter δ as shown in Figure 4.4. The free parameters m and δ are adjusted to

represent a good fit to PDFs obtained in the above mentioned simulations. In what follows, we adopt following values, $\sigma_1 = \sigma_2$, $m = 0.2$ and $\delta = 3$.

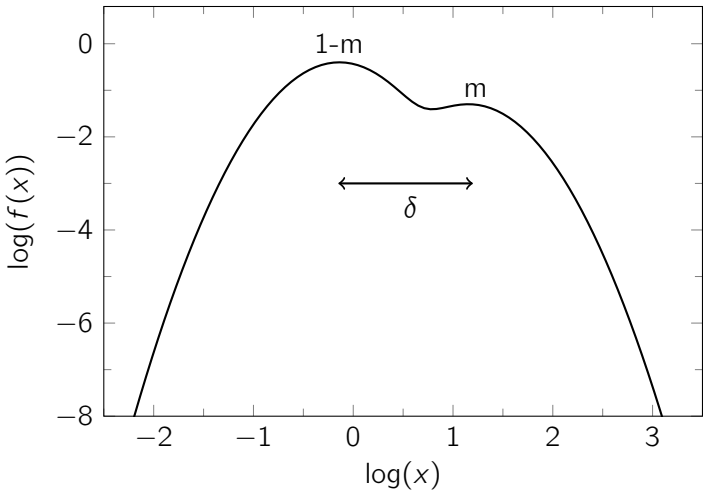

Figure 4.4

Density PDF of a merger modeled as a sum of two log-normal PDFs expressed by Equation (4.9). The adopted values of the parameters $m = 0.2$ and $\delta = 3$ are in a good agreement with PDFs obtained in hydrodynamic simulations (Teyssier et al., 2010, Bournaud et al., 2011b, Renaud et al., 2014).

Σ_{SFR} for starbursting mergers, computed from Equation (4.3) by adopting the expression for PDF in the form of Equation (4.9) and star formation in that of Equation (4.5), reads (see Appendix A.3 for more detailed derivation)

Σ_{SFR} merger without feedback

$$\Sigma_{SFR} = \epsilon \sqrt{\frac{8G}{3\pi}} \frac{\Sigma_{gas}^{3/2}}{\sqrt{h}} \left[(1-m) \exp\left(\frac{3}{8}\sigma_1^2\right) \operatorname{erfc}\left(\frac{\ln\left(\frac{\rho_0 h}{\Sigma_{gas}}\right) - \sigma_1^2}{\sqrt{2}\sigma_1} \right) + m \exp\left(\frac{3}{8}\sigma_2^2\right) \exp\left(\frac{3}{2}\delta\right) \operatorname{erfc}\left(\frac{\ln\left(\frac{\rho_0 h}{\Sigma_{gas}}\right) - \sigma_2^2 - \delta}{\sqrt{2}\sigma_2} \right) \right]. \quad (4.10)$$

In spite of increased complexity of this expression due to additional parameters coming from the modeling of the PDF of a merger, the main features of its behavior are the same: a single break at low surface densities followed at high surface densities by a power-law of index 3/2. The quantitative difference with respect to an isolated galaxy with a single log-normal PDF is in the position of the break, this is shifted toward lower surface gas densities in the case of a merger.

4.2.7 Σ_{gas}–Σ_{SFR} relation for starbursting mergers with stellar feedback

And finally with a regulation by stellar feedback, Σ_{SFR} in the case of starbursting mergers is given by

Σ_{SFR} merger with feedback

$$\begin{aligned}\Sigma_{SFR} = &\epsilon\sqrt{\frac{8G}{3\pi}}\frac{\Sigma_{gas}^{3/2}}{\sqrt{h}}(1-m)\exp\left(\frac{3}{8}\sigma_1^2\right)\left[\mathrm{erfc}\left(\frac{\ln\left(\frac{\rho_0 h}{\Sigma_{gas}}\right)-\sigma_1^2}{\sqrt{2}\sigma_1}\right)\right.\\ &\left.-\mathrm{erfc}\left(\frac{\ln\left(\frac{\epsilon_s^2 3\pi h}{t_s^2 32G\epsilon^2\Sigma_{gas}}\right)-\sigma_1^2}{\sqrt{2}\sigma_1}\right)\right]\\ &+(1-m)\Sigma_{gas}\frac{\epsilon_s}{2t_s}\,\mathrm{erfc}\left(\frac{\ln\left(\frac{\epsilon_s^2 3\pi h}{t_s^2 32G\epsilon^2\Sigma_{gas}}\right)-\frac{\sigma_1^2}{2}}{\sqrt{2}\sigma_1}\right)\\ &+\epsilon\sqrt{\frac{8G}{3\pi}}\frac{\Sigma_{gas}^{3/2}}{\sqrt{h}}m\exp\left(\frac{3}{2}\delta\right)\exp\left(\frac{3}{8}\sigma_2^2\right)\left[\mathrm{erfc}\left(\frac{\ln\left(\frac{\rho_0 h}{\Sigma_{gas}}\right)-\sigma_2^2-\delta}{\sqrt{2}\sigma_2}\right)\right.\\ &\left.-\mathrm{erfc}\left(\frac{\ln\left(\frac{\epsilon_s^2 3\pi h}{t_s^2 32G\epsilon^2\Sigma_{gas}}\right)-\sigma_2^2-\delta}{\sqrt{2}\sigma_2}\right)\right]\\ &+m\Sigma_{gas}\frac{\epsilon_s}{2t_s}\exp\delta\,\mathrm{erfc}\left(\frac{\ln\left(\frac{\epsilon_s^2 3\pi h}{t_s^2 32G\epsilon^2\Sigma_{gas}}\right)-\frac{\sigma_2^2}{2}-\delta}{\sqrt{2}\sigma_2}\right).\end{aligned} \tag{4.11}$$

This star formation relation yields as previously to a single break at low surface densities followed by a power-law of index 3/2, which is now flattened at high surface densities due to stellar feedback. This flattening is described by a power-law of unity index, as in the case of isolated galaxy with regulation by stellar feedback.

4.3 Comparison with observations

Next obvious step is the confrontation of the model with observations. To do so, we need to supply three parameters, the analytic model depends on, for each system we want to model. These are the Mach number $\mathcal{M}$, the thickness of a region of galaxy (or entire galaxy) and the star formation density threshold ρ_0. For each system that is to be used in our comparison, we choose the combination of these three parameters on observational bases, whenever possible, and we try to motivate the choice physically, otherwise. $\mathcal{M}$ and h are in principle observationally accessible. ρ_0 is hard one, as for the moment, we haven't said anything about its origin, nevertheless, we have seen that only its non-zero value leads to a surface density break that, as we will illustrate in this Section (and we have already discussed in Chapter 3), is found in observations. Encouraged by the results from galaxy simulations presented in Chapter 3, we propose that the local volume density threshold ρ_0 for star formation corresponds to a volume density above which, at small scale, cold enough gas becomes supersonically turbulent and hosts the shocks. Consequently, a fraction of gas becomes gravitationally unstable, collapses and is converted into stars. Calculations at galactic scale (Bournaud et al., 2010) have shown that at solar metallicity, for the velocity dispersions of $6-10$ km s^{-1}, typical for nearby spiral galaxies, gas can cool below 10^4 K and thus leading to supersonic ISM above a density of ≈ 10 cm^{-3}.

Similarly, a relation $\mathcal{M} \approx (\rho/10cm^{-3})^{1/2}$ was found in detailed models of ISM including turbulence and radiative transfer (Audit & Hennebelle, 2010).

spirals

We start the comparison with local spiral galaxies. The velocity dispersions of the large-scale HI and CO reservoirs of typical spirals in the local Universe are ~ 10 km s^{-1} (Combes et al., 2002). This corresponds, for temperatures of 10^{3-4} K, to $\mathcal{M} \approx 1$ and $h \approx 100$ pc. In the line with previous arguments, $\rho_0 = 10$ cm^{-3} is adopted for local spirals. Disks at high redshift ($z \sim 1-2$) have high velocity dispersions ($30-90$ km s^{-1} Förster Schreiber et al., 2009) suggesting the presence of a strong turbulence. This leads to a thicker disks (~ 1 kpc Elmegreen & Elmegreen, 2006) and higher surface densities of gas in such systems compared to their local counterparts.

These values lead to a very good agreement between the model and observations, as shown in Figure 4.5. The model naturally reproduces the break in the star formation relation observed in local spirals when both entire galaxy or its smaller regions are considered. At surface densities typical for these galaxies, the presence of the stellar feedback does not change the behavior of $\Sigma_{\rm gas}$–$\Sigma_{\rm SFR}$ relation. At higher surface densities, where high redshift disks are located, feedback induces a transition from the power-law of index 3/2 to that of unity matching the observational data. Note that for high-redshift disks, we have used the same value of ρ_0 than for local spirals. A lower value is probably more realistic as the onset of supersonic turbulence most likely occurs at a lower density threshold, but such value would modify mainly the break, i.e. the relation in a range of densities much lower than that of high-z galaxies here considered.

SMC

Let's now move to the Small Magellanic Cloud which is a system with properties in many aspects different from local spiral galaxies. First of all, it is a low-metallicity system (~ 0.2 Z$_\odot$ Bolatto et al., 2008) implying a less efficient cooling of the ISM compared to local spirals at solar metallicity. This translates, in this formalism, into a higher value of ρ_0 needed for ISM turbulence to become supersonic. Calculations similar to those of Bournaud et al. (2010) give an estimate of 100 cm^{-3}. It is not straightforward to establish the thickness h of the SMC. A calculation based on the hypothesis of an isothermal self-gravitating disk (Combes et al., 2002, Chapter 1), gives for a velocity dispersion of ≈ 20 km s^{-1} and a rotational speed of 40 km s^{-1} at the HI half-mass radius of 1.5 kpc (Stanimirović et al., 2004), an estimate of ~ 500 pc. The uncertainty on the scale-height parameter being rather high, different triplet of parameters ($\mathcal{M}$, h, ρ_0) matching the observations were explored. Among the most realistic ones, we select $\mathcal{M} = 2$, $h = 500$ pc and $\rho_0 = 100$ cm^{-3} (Renaud et al., 2012), matching the data as shown in Figure 4.5.

mergers

Starbursting mergers have at least twice more turbulent ISM than isolated galaxies both at low (Irwin, 1994, Elmegreen et al., 1995) and high redshift (Bournaud et al., 2011a) and consequently also thicker gas reservoirs, although not necessarily in all regions of the system. To compare the model with observations, we adopt doubled values of $\mathcal{M}$ and h compared to disks at the same redshift. In starbursting mergers feedback is found to be important already at low redshift, as opposed to spirals, where only at high redshift the regulation by stellar feedback is needed to reproduce the observed SF relation.

To sum up, the necessary ingredients in the proposed analytic model to reproduce the observed diversity of the star formation relations include the regulation by stellar feedback, the turbulence that increases with redshift, the PDF with an excess at high densities for starbursting mergers, and the higher density threshold in the local star formation relation.

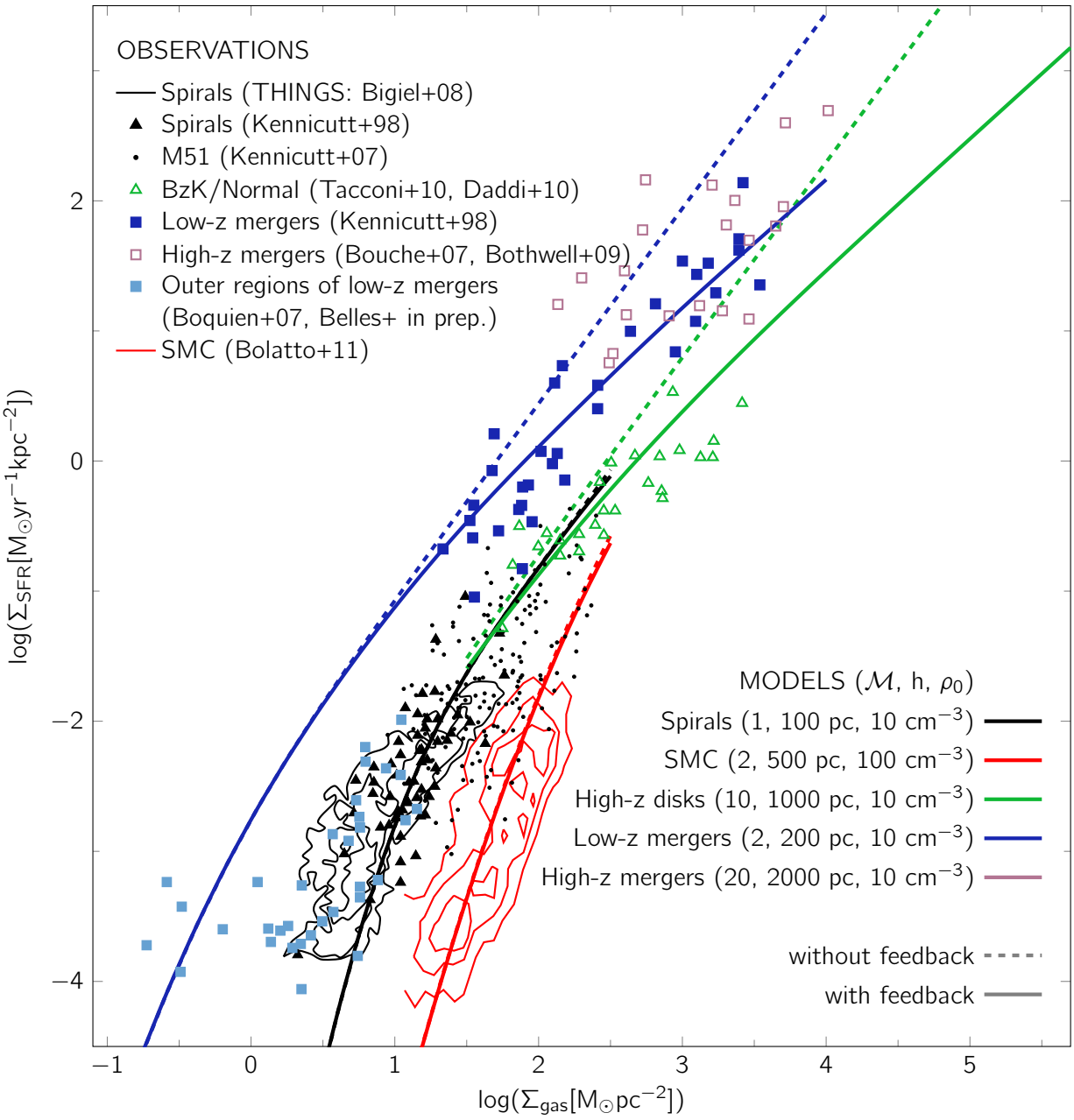

Figure 4.5

Comparison of models with observations of entire galaxies or their regions at low and high redshift. Colored curves are models of different galactic environments using physically motivated parameters, not fits to observational data. Dashed lines represent models without feedback, full lines models including the regulation by stellar feedback.

4.4 Comparison with simulations

By using typical values of ISM properties in different galactic environments, our model, based on the supersonic nature of the turbulence in the ISM, naturally explains observed relations. The formalism leads to an analytic expression relating Σ_{gas} and Σ_{SFR} that depends on three parameters: the Mach number, the star formation density threshold and the thickness of the star-forming regions. This idealized model is based on two assumptions. One assumption is the characterization of an entire star-forming region by a single set of three parameters, while wide ranges of them are more appropriate for describing the real ISM. Another assumption is the description of the gas volume density by a log-normal distribution, which was primarily found for isothermal supersonic turbulence (e.g. Vázquez-Semadeni, 1994, Nordlund & Padoan, 1999). A further test of this model is its comparison to galaxy simulations in which a wide diversity of parameters and density distributions consistent with the multiphase ISM is recovered.

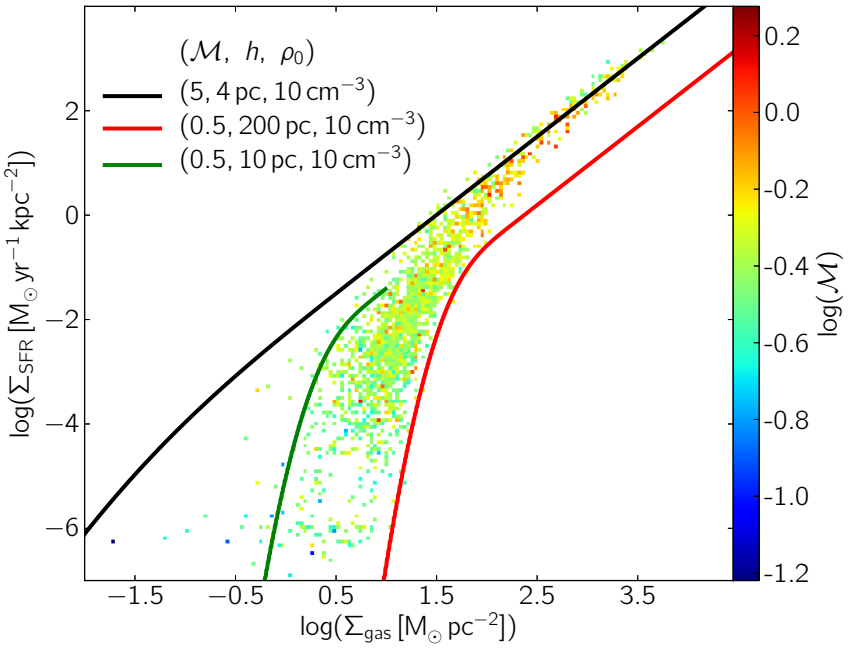

Figure 4.6

$SMC_{0.1Z_\odot}$: comparison with the model with three sets of parameters (indicated in the legend). The black curve matches the supersonic regime of efficient star formation, while the green and the red curves represent upper and lower limits for the regime of the break, where the star formation is inefficient. The h parameter is in agreement with values measured in the simulation (see Figure 3.10). The model with extreme parameters brackets the simulation results.

In Figures 4.6 and 4.7, we compare simulations of MW_{PC} and $SMC_{0.1Z_\odot}$ (presented in Chapter 3) with the analytic model of Renaud et al. (2012). We do not compare each individual star-forming region in the simulation with the model, but we are rather interested in what values these parameters should take to obtain upper and lower limits for simulated data[2]. The break is in the subsonic regime

[2]The numerical values we have adopted for Mach numbers and scale-heights represent plausible extremes for this

(measured values of $\mathcal{M}$ are below unity) which corresponds to the regime where the analytic model deviates from its asymptotic behavior (at high $\Sigma_{\rm gas}$). In this regime the scale-heights of the beams set the efficiency of star formation spanning the range given by the model and quantitatively in accordance with the values measured in the simulations (Figure 3.10). In the analytic model, the power-law regime can be reached even with the Mach number below unity (red curve). However, our simulations do not probe this area of the $\Sigma_{\rm gas}$–$\Sigma_{\rm SFR}$ plane: the data points in the power-law regime are exclusively supersonic and can only be described by a model with the Mach number above unity (black curve).

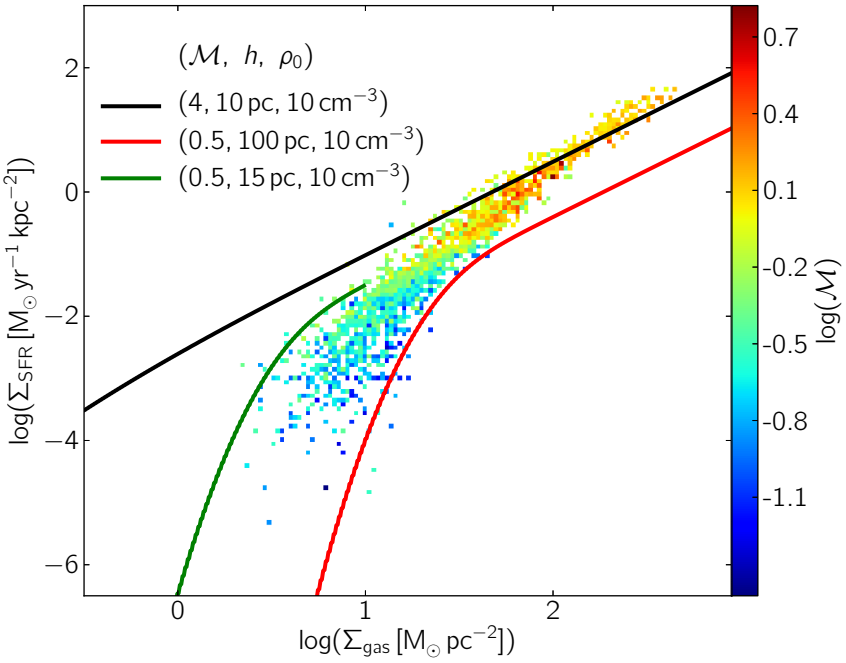

Figure 4.7

$\rm MW_{PC}$: comparison with the model. As in Figure 4.6, the supersonic regime is compared to the model prediction and similarly, the subsonic regime at low $\Sigma_{\rm gas}$ is situated between the curves characterized by the Mach number lower than unity for the measured thickness.

4.5 Summary

An analytic formalism relating the surface density of gas and the surface density of star formation rate was described. Its only two ingredients are the gas density PDF and the local star formation relation including a density threshold, interpreted here as the onset of supersonic turbulence, and a regulation by stellar feedback. Our main findings are as follows:

① Integration over entire galaxies or their regions leads to an analytic expression relating $\Sigma_{\rm gas}$ and $\Sigma_{\rm SFR}$ that depends on three parameters: the Mach number, the star formation density threshold

type of galaxy.

and the thickness of the star-forming regions. This local star formation threshold translates into a break at low surface densities in the Σ_{gas}–Σ_{SFR} plane. At higher surface densities, a 3/2 index power law of the local star formation is directly imprinted, followed by a slope of unity at even higher surface densities, where the feedback becomes a dominant regulation factor.

② By using the typical values of ISM properties, the analytic model is capable of reproducing observed diversity of star formation relation in different systems, such as spiral galaxies, the Small Magellanic Cloud or starbursting mergers, without any fitting or fine tuning of parameters.

③ Comparison with simulations of local spiral and irregular galaxies confirms that the interpretation of the surface density threshold for efficient star formation as the typical density for the onset of supersonic turbulence in dense gas is a viable explanation of the observed break in the Σ_{gas}–Σ_{SFR} relation.

④ The vertical spread in the Σ_{gas}–Σ_{SFR} plot is given by the interplay between different parameters of star-forming regions. Figures 4.6 and 4.7 show a reasonable agreement between simulations and the proposed analytic model, confirming that this idealized model provides a viable description of star formation in a turbulent ISM compared to more realistic simulations of self-gravitating systems with star formation and feedback. The values of the model parameters (Mach number, thickness and density threshold) characterizing the points in Σ_{gas}–Σ_{SFR} plane are close to the values measured in simulations.

Chapter 5

Alternative zoom-in resimulation with RAMSES

> *We have found it of paramount importance that in order to progress we must recognize our ignorance and leave room for doubt. Scientific knowledge is a body of statements of varying degrees of certainty–some most unsure, some nearly sure, but none absolutely certain.*
>
> — Richard P. Feynman, *What do you care what other people think?*

The method used to model the evolution of galaxies in cosmological context presented in Chapter 2 has shown to be able to produce galaxy morphologies comparable to observed ones in the same mass range. However, their stellar mass content is in tension with observational constraints. On the other hand, Chapters 3 and 4 have suggested that resolving the ISM is crucial for obtaining star formation relations in agreement with observations. This Chapter aims at combining the advantages of both approaches by using the same simulation technique as in the case of isolated galaxy simulations and adding an important physical ingredient, gas accretion and mergers, by means of the method used in the cosmological simulations.

5.1 Introduction

Galaxies are far from being isolated entities in our Universe. They are part of a large scale pattern, known as the cosmic web (e.g. Bond et al., 1996), the existence of which has been suggested by early attempts to map the galaxy distribution in the Universe (e.g. Jõeveer et al., 1978, Geller & Huchra, 1989, Shectman et al., 1996), and since then confirmed by large galaxy surveys (2dFGRS: Colless et al., 2003; SDSS: Tegmark et al., 2004; 2MASS: Huchra et al., 2005). In the framework of the cosmic web, four distinct categories of substructures are usually distinguished: voids, sheets, filaments and nodes. These nodes of dark matter filamentary structure are places where most galaxies

form. The dark matter filaments serve as tunnels along which the baryonic matter can be funneled into the galaxy (e.g. Katz et al., 1993, Katz & White, 1993, Bond et al., 1996, Shen et al., 2006). The exact way of how baryons, gas in particular, get into galaxy and how their accretion changes as the galaxy grows in mass are important, although not yet fully understood processes determining many properties of the galaxy.

Based on theoretical considerations and numerical simulations, two modes of accretion have been identified. The hot accretion mode, today considered as the traditional, classical model of galaxy formation, was described in early theoretical papers more than thirty years ago (Rees & Ostriker, 1977, Silk, 1977, White & Rees, 1978). In this picture, spherically infalling gas is shock heated to the virial temperature of the halo near the virial radius and creates a hot, pressure supported halo of gas. Depending on the cooling timescale, gas may then radiatively cool and accrete onto a galaxy forming in the center of dark matter halo (White & Frenk, 1991). However, only very massive haloes are found to easily sustain a virial shock that is stable against gas cooling leading to the shock-heating of the gas entering the halo. Both analytic studies (Binney, 1977, Birnboim & Dekel, 2003, Dekel & Birnboim, 2006) and hydrodynamic simulations (Katz et al., 2003, Kereš et al., 2005, 2009, Ocvirk et al., 2008) have established the existence of a critical mass below which shocks are unstable and cannot propagate outwards. In the absence of a stable virial shock, gas is accreted onto a halo (and galaxy) without being shock heated at the virial radius, thus referred to as a cold mode accretion. Such a scenario for gas accretion was shown to dominate both at high redshift and for low mass objects at low redshift. The cold gas can then be delivered to the central galaxy along the filaments penetrating deep inside the halo, the phenomenon dubbed cold flows (Kereš et al., 2005, Dekel & Birnboim, 2006, Dekel et al., 2009). For intermediate halo masses, some dense cold inflowing filaments were found to coexist with hot gas by resisting the pressure force exerted by this hot gaseous material (Ocvirk et al., 2008). All these studies suggest that the vast majority of high redshift galaxies grow by acquiring gas from cold streams and the question which naturally arises is what is confrontation with observations telling us about this prediction.

Observationally, putting the existence of the cold mode accretion, together with cold flows on a firm basis is complicated. Different possible signatures of cold mode accretion were suggested in the literature, such as low-ionization metal absorption lines (Kimm et al., 2011, Stewart et al., 2011a, Goerdt et al., 2012, van de Voort et al., 2012) or absorption lines offset from the galaxy's systematic velocity due to a very high specific angular momentum of the cold gas (Stewart et al., 2011b). Although some tentative observations have already been reported (Crighton et al., 2013), the clear observational evidence for cold flows in galaxies is still missing. Several reasons for cold flows being difficult to detect exist. Firstly, the covering fraction[1] of the filaments is typically low. The exact value of the covering fraction depends on the halo mass and redshift in the way that remains to be determined. Other criteria, such as gas temperature, column density and radial distance within which the calculation is performed, play also an important role. Dekel et al. (2009) reported the covering fraction of around 25 % for four simulated massive haloes ($\sim 10^{12}$ $M_{\odot}$) at $z \sim 2.5$, while other studies found a significantly lower values below $\sim$ 10 % (Kimm et al., 2011, Faucher-Giguère & Kereš, 2011). Secondly, cold filamentary gas is not the only source of low-ionization lines, galaxy's interstellar medium is an important absorber as well. Kimm et al. (2011) have shown that due to the small optical depth for the low-ionization transition from cold filamentary gas compared to that of the ISM of the host galaxy, it is extremely difficult to distinguish metal absorption lines arising from cold filaments and those caused by the ISM of high redshift galaxies. The third reason is related

[1]The covering fraction is usually constructed by considering the total fraction of sight lines within a given projected radius from the center of the galaxy and applying some column density criterion.

to the geometry of the accretion. For filaments to be detected, they need to be well aligned with the line of sight in order to maximize their column density and thus produce a strong absorption signal. Any misalignment lowers the probability of the filament detection. Finally, a low metallicity of filaments makes them transparent to metal line observations.

So even though an analytic formalism offers a fairly robust prediction concerning the cold mode accretion, observations haven't so far proposed a clear and equally robust evidence that such a mechanism is occuring in our Universe. Numerical simulations thus stay the main tool for studying the physical processes related to the deposition of gas into galaxies. However, the observational evidence is crucial as it is always possible that simulations miss some additional physics that could change or modify our current understanding, similarly to what has happened with the picture of the baryonic content of galaxies: simulations significantly overpredict the fraction of baryons locked up in galaxies (e.g. Guo et al., 2010, Behroozi et al., 2010) which has drawn more attention to outflows as a possible solution to this problem. Indeed, there are some issues related to numerical simulations that are worth noting. Firstly, different techniques are used in the selection of a cold mode gas accretion. In some studies this selection criterion is based on the comparison of maximum past temperature of gas with some temperature threshold (Kereš et al., 2005, 2009, van de Voort et al., 2012, Faucher-Giguère & Kereš, 2011) motivated by the location of a minimum in the bimodal distribution of this maximum temperature found by Kereš et al. (2005). This method is widely used in many simulations, however, Nelson et al. (2013) have shown that comparing the maximum past temperature of gas to a fixed temperature threshold is physically motivated approach only for haloes with virial temperature much higher than this threshold temperature, while for lower mass systems, some fraction of the virial temperature of the dark matter halo should be used instead. The use of the constant temperature criterion was also shown to lead to the previously reported existence of the mass (somewhat arbitrary, depending on the precise definition of the transition) of $10^{11.5} - 10^{12}$ $M_\odot$ marking the transition from cold to hot dominated accretion, while the comparison of the thermal history of gas to a fraction of virial temperature does not result in any sharp transition. Instead, cold gas fraction gradually declines from about 20% to 0% over the halo mass range $10^{10} - 10^{12}$ $M_\odot$. Another possibility, explored by Brooks et al. (2009), is to use entropy changes as a criterion to identify shocked gas. Although this method was found to yield very similar results when compared to constant temperature criterion, it should be explored in a full cosmological volume. Another approach, more used in AMR simulations[2] is to study instantaneous properties of gas (e.g. Ocvirk et al., 2008, Dekel et al., 2009, Agertz et al., 2009b).

In addition to analysis methodology, numerical technique seems also to play an important role in establishing the character and importance of cold gas accretion. By performing a comparison of cosmological simulations run with the SPH code GADGET (Springel, 2005) and the moving mesh code AREPO (Springel, 2010), Nelson et al. (2013) have shown that the relative contributions of hot and cold mode accretion is non-trivially modified by numerical shortcomings intrinsic to SPH simulations. GADGET simulations imply, in agreement with previous studies, that during accretion, only a small fraction of gas in forming galaxies in haloes with mass above 10^{11} $M_\odot$ heats to an considerable fraction of the virial temperature at $z = 2$. In AREPO simulations, at halo mass of 10^{11} $M_\odot$, the accretion of cold gas was found to decrease by a factor of about two, while the accretion rate of hot gas was found to be enhanced by an order of magnitude. Significant differences were

[2] As opposed to smoothed particle hydrodynamics (SPH) simulations, which are of (pseudo)-Lagrangian nature, the analysis of cosmological gas accretion in grid based simulations is limited because of their Eulerian nature. It is difficult to simply identify the trajectory of a given gas parcel due to the exchange of mass between the neighboring cells. This can be partly overcome using tracer particles (Dubois et al., 2012, Genel et al., 2013).

reported by these authors also for the geometry of filaments. In contrast to GADGET filamentary gas structures that tend to remain cold and flow coherently to small radii within a halo, or possibly produce large number of fragments of purely numerical origin, filaments in AREPO undergo important heating at comparable distances from the center and are more diffuse.

Another, non negligible issue simulations are constantly facing is the resolution. Resolving the details of cold flows is numerically very challenging and the impact of the resolution on the results that have been obtained so far has only recently started to be evaluated. Higher resolution ($\sim 50 - 100$ pc) simulations of galaxies forming at nodes of the cosmic web at high redshift (e.g. Ceverino et al., 2010) reveal disks surrounded by a region in which streams break up forming a "messy interaction" region. It is not clear what would be the impact of even higher resolution on the details of the disk gas supply through cold streams penetrating the hot halo along the dark matter filaments of the cosmic web.

The importance of the understanding of accretion modes lies also in its impact on the star formation, one of the most important physical processes of the galaxy formation and evolution. The way the gas is accreted determines its further availability for the star formation. On one hand, shock-heated gas has typically long cooling times, meaning that such gas will not be able to participate in the conversion to stars shortly after being accreted, however it will contribute to the buildup of the gas reservoir and thus influence later star formation rate. On the other hand, cold gas may fuel star formation immediately.

Star formation is ultimately connected with feedback. Effects of feedback and galactic scale outflows on gas inflow have started to be explored only recently (Oppenheimer et al., 2010, Faucher-Giguère et al., 2011, van de Voort et al., 2011). While cold mode accretion was not found to be substantially suppressed by the galactic outflows generated by SN events (Shen et al., 2013), ejection of hot gas from galaxies could add mass and thermal support to the halo and thus increase heating of cosmologically inflowing gas (Oppenheimer et al., 2010). Stellar feedback (SN and/or pre-SN) seems also to play an important role for storing of gas (Woods et al., 2014). Accreted gas can be (re-)cycled back into gas reservoir by feedback processes which allows the gas to be (re-)used at later times. As shown by Woods et al. (2014), in the case of relatively weak feedback, the accreted gas is used up earlier as the fraction of gas returning to the reservoir is lower, but when feedback is strong, galaxies can recycle more gas and also eject it which would lead to their lower final baryon and stellar content, and could shift the peak of star formation to lower redshifts (similarly to the findings of Scannapieco et al., 2012). Another feedback process, impact of which was studied in the context of cosmological accretion, is AGN feedback. While van de Voort et al. (2011) found AGNs to preferentially prevent hot mode gas from cooling, Dubois et al. (2013) report signatures of morphologically disturbed cold filamentary structures by AGN activity: AGNs are both destroying the connectivity of the filaments and bending them.

Even though the exact way outflows are powered by feedback still remains rather unclear, they are without doubt an essential ingredient to understanding of the circulation of baryons during galaxy formation. Observations of metal absorption and of Lyα emission lines provide compelling evidence that galactic-scale outflows with velocities of several hundred km/s are ubiquitous in star-forming galaxies at low and high redshift (e.g. Shapley et al., 2003, Tremonti et al., 2007, Weiner et al., 2009, Rubin et al., 2010), with mass-loading factors up to 10 (Steidel et al., 2010, Genzel et al., 2011). What is less known however is how far the expelled material travels and what is exactly its spatial distribution. As was previously mentioned, observational signatures of infall by cold accretion are very subtle. It is difficult to tell them apart from the feedback-driven outflows. Probably the most significant difference comes from kinematic-absorption line signatures: infalling material in galaxy

spectra is expected to be primarily redshifted, while outflowing material blueshifted and could reach much higher velocities with respect to the galaxy systemic redshift. However, Doppler shift alone is not enough since an outflow in the background produces the same signature as an inflow in the foreground. Additional physical constraints are thus needed.

Multi Unit Spectroscopic Explorer (MUSE; Bacon et al., 2010) at the Very Large Telescope was designed to improve the status of current observations. With its unique combination of high spectral and spatial resolution and contiguous integral field coverage, this integral field spectrograph is expected to detect fine structures in the Universe, such as spatial extended emission from the filamentary streams of cool gas and the outflowing material around star-forming galaxies.

It is clear that a lot of progress was made in our understanding of the physics of galaxy formation and growth since the early works. Until observations will be able to deliver a robust technique to study gas accretion and outflows, we have to rely on numerical simulations as the main tool for testing the theoretical predictions. It is however quite surprising to what extent different numerical schemes involving only hydrodynamics can lead to different results. In addition, various phenomenological approaches and subgrid recipes are employed in modeling of the associated star formation, feedback processes and resulting outflows, impact of which has to be thoroughly studied and understood. Apart from the uncertainty of these models resulting from our ignorance of details of these physical processes, their inclusion in the numerical simulation of cosmological volumes is computationally costly due to large range of temporal and spatial scales that has to be covered. The impact of gas streams on the disk morphology and its star formation was studied in the model of clumpy disks observed at high redshift (Ceverino et al., 2012). However, numerical simulations studying the details of interaction between cold flows and a galaxy disk in the local Universe are still missing. In more general, many aspects of disk-gas streams and inflow-outflow interactions are still debated. Among them, turbulence which may (Genel et al., 2012, Gabor & Bournaud, 2014) or may not (Hopkins et al., 2013b) be maintained by cold-flow accretion, the buildup of gas reservoirs around galaxies and its role in driving late-time star formation, the impact of feedback on the overall accretion at the virial radius or the mixing of cold and hot halo gas. In the light of the above mentioned results, a more detailed investigation is required to establish the exact way in which the cold streams evolve, interact with outflows and eventually merge with the central galaxy and influence its properties.

5.2 Resimulation method

The aim of this Section is to give a short outline of the resimulation method developed and presented in more details in Martig et al. (2009). It is a method that could in principle have various applications, but here the focus is on the resimulation of galaxy evolution in a cosmological context and can thus be thought of as an alternative to the traditional zoom-in technique. The method is based on the extraction of the merger and accretion histories of the main halo from the cosmological simulation in a given redshift range, from the initial redshift $z_{\rm max}$ to the final one $z_{\rm min}$, at the final virial radius ($R_{\rm vir}$). Typical resimulated volumes are thus of few $R_{\rm vir}$ following specific boundary conditions imposed by the cosmological simulation.

first phase

To guide the reader through the sequence of individual steps, Figure 5.1 shows an activity diagram, which illustrates the first phase of the resimulation method. The input to the method is a cosmological simulation, for example a dark matter-only cosmological simulation run with a set of given parameters. The second step includes the identification of dark matter haloes and particles that are not bound to any halo and that will be referred to as diffuse particles in each snapshot of simulation. In the next step, a halo, the evolution of which is to be resimulated, has to be chosen from the final snapshot,

for instance at $z = 0$. At this point, various selection criteria determining the evolution history of the galaxy can be applied. Once the main halo is selected, all of its most massive progenitors are identified in each snapshot and at same time all dark matter haloes and diffuse dark matter particles crossing a certain fixed spherical boundary around the main halo are recorded. This boundary is chosen to be the final virial radius (at $z = 0$) and for each dark matter halo or diffuse dark matter particle its mass, position, velocity, spin and time of boundary crossing are recorded. A file of initial conditions giving the information about all haloes and particles initially present inside the final virial radius and a catalog, which is just a list of all particles and interacting haloes crossing the final virial radius between the initial and final redshift, are thus obtained. So far, in each of these steps, any tool for particle identification, its tracing and recording the necessary information could have been used. The output of this first stage, namely the file of haloes and particles crossing the boundary at all times and those present inside this boundary at the beginning of the resimulation, becomes the input for the next stage, again illustrated in the form of an activity diagram that can be easily followed, shown in Figure 5.2.

second phase

At this point, another input, a set of model galaxies, is needed. This is because each previously identified dark matter halo has to be replaced with a galaxy made of gas, star and dark matter particles. The way this is done consists of choosing the model that is closest in mass from the set of galaxies. Furthermore, each previously identified diffuse particle has to be replaced with a blob of lower-mass, high-resolution gas and dark matter particles. In this way, the initial conditions and the catalog with all necessary information for resimulation of the galaxy are constructed. This information includes the time of the insertion of the blob or galaxy in the simulation, its position, velocity, spin, gas profile, mass, as is usually done in the case of an isolated galaxy simulation.

advantages

As this method is meant to be an alternative to the standard zoom-in simulation, it is worth mentioning its advantages, but also drawbacks. The main advantage of this resimulation technique is the low computation time, meaning that running a large number of simulations is much easier and thus statistical studies are possible.[3] Another advantage is the possibility to simulate galaxies with different types of merger histories, contrarily to zoom-in simulations, where typically all progenitors need to be initially present in the high-resolution sub-volume, which can become very large. Finally, decoupled evolution of the main galaxy from the expansion of the universe allows to keep the physical resolution constant as a function of time at no additional cost.

drawbacks

As far as drawbacks are concerned, probably the most important one is the large number of free parameters for the model galaxies. Even though these parameters are selected to be as close as possible to those of observed galaxies, a full diversity will never be recovered. Additional complication stems from the difficulty to obtain observational constrains for galaxies at high redshift. This drawback is intrinsically related to the method itself and can be partly overcome by discarding the early phase of the simulation in the analysis as it was shown (see Martig et al., 2009) that the initial assumptions do not make a big difference due to the redistribution of the initial baryons by mergers and instabilities especially at high redshift. Finally, an important limitation is linked with the existing implementation, which is a sticky-particle scheme that is known for poorly treating the hot gas phase, thus gas around galaxies and probably also gas inside galaxies heated by feedback processes. Consequently, massive haloes, for which the hot accretion mode is believed to be a dominant accretion channel, cannot be modeled correctly. This drawback can be overcome by implementing the resimulation method in a grid-based code that offers a better treatment of fluid instabilities, shocks and phase boundaries, such as for example RAMSES.

[3] This technique was used to obtain the sample of galaxies studied in Chapter 2. Just to give a rough idea, each simulation required about five days in terms of computation time.

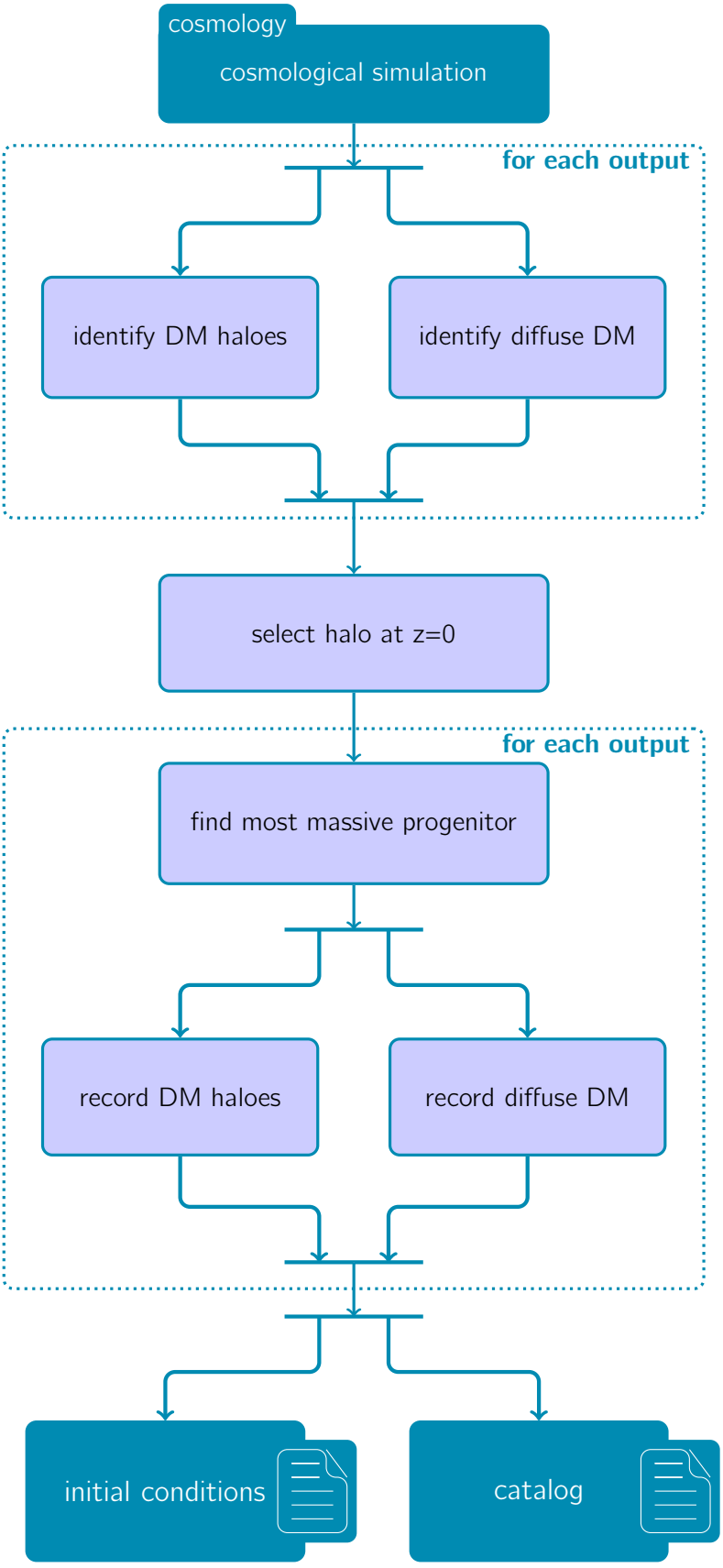

Figure 5.1

Activity diagram for the first phase of the resimulation method. Starting from a cosmological simulation, the initial conditions and catalog keeping track of dark matter haloes and dark matter diffuse particles necessary for the resimulation of the central galaxy are obtained.

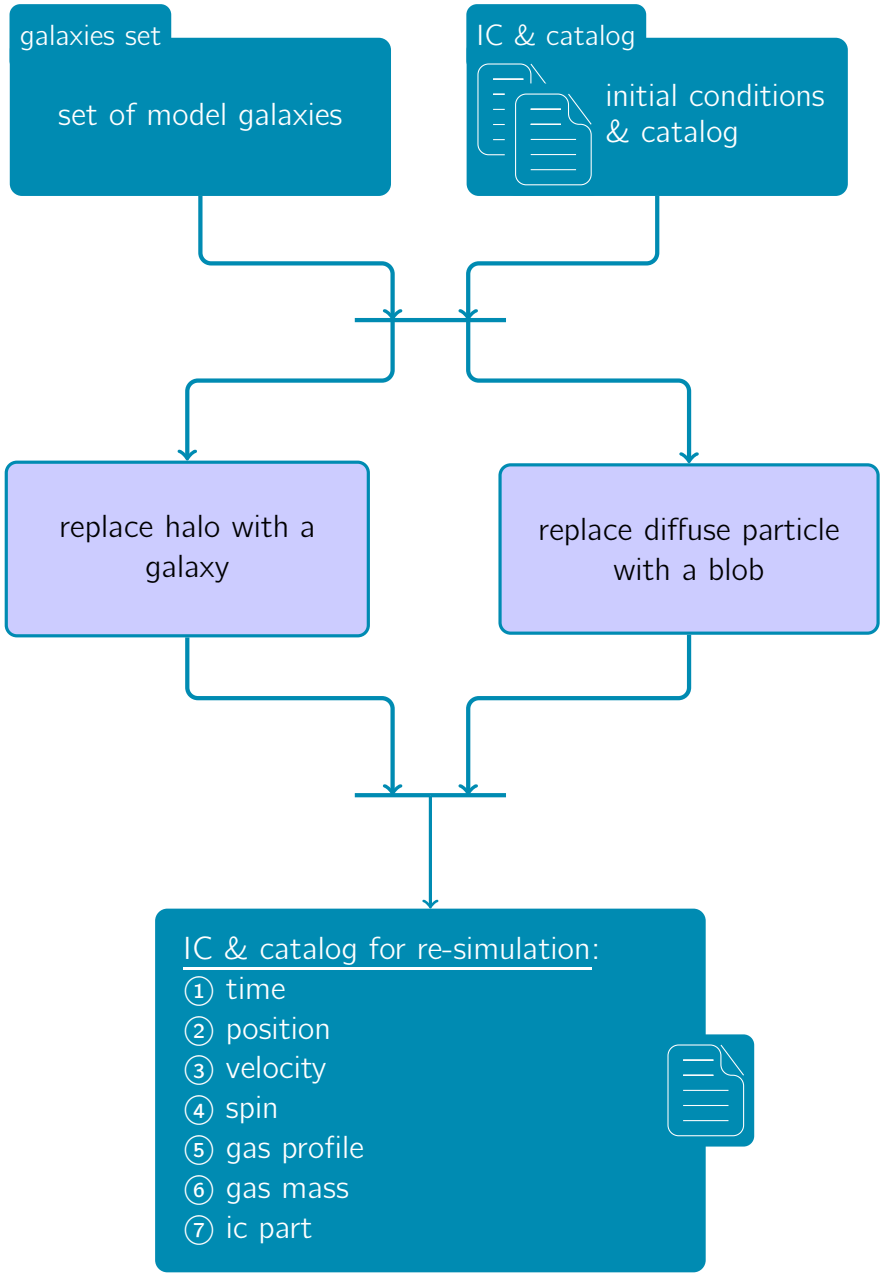

Figure 5.2

Activity diagram for the second phase of the resimulation method. Each dark matter halo identified in the previous phase is replaced with a galaxy made of dark matter, gas and stars while each particle, previously identified as diffuse, is replaced by a blob of gas and dark matter particles. The obtained catalog is ready to be used for the resimulation of the central galaxy.

5.3 Resimulation method with RAMSES

A small part of this thesis has been dedicated to the implementation of the resimulation method in massively parallel, grid-based adaptive mesh refinement hydrodynamic code RAMSES[4] (Teyssier, 2002), which is written in Fortran90.

5.3.1 RAMSES user's perspective

The default version of RAMSES contains various algorithms allowing to develop applications for computational astrophysics (see documentation[5] for more details about the current implementation). To parametrize the existing features of implemented algorithms, the RAMSES parameter file based on the Fortran "namelist" format is used.

To design advanced applications, the general philosophy in RAMSES community is to "patch the code". The basic idea of this approach is to create a new directory (typically in the RAMSES patch/ directory) where all files that need to be modified are copied. Simple path specification of this directory in the PATCH variable of the Makefile allows user to recompile the current version of the code with the key routines together with modified ones according to the needs of an application.

The default version of RAMSES does not provide an easy way to set up an isolated galaxy or several galaxies simulation. To this purpose, based on the work of Damien Chapon, Florent Renaud has developed a module allowing user to define the initial conditions for one or more galaxies in a very simple way through the definition of some parameters in a &GROUP_PARAMS block of the namelist file. These parameters are described in Appendix B, Table 5. The current implementation does not allow to introduce a galaxy in the simulation at arbitrary time. For the purposes of cosmological resimulation, it is not convenient to use namelist based list of all galaxies entering the simulation box (due to the large number of galaxies to be added). That is why the logic of the namelist file block &GROUP_PARAMS was modified and only the path to the catalog (containing all information necessary for galaxy initialization as well as for the insertion of blobs and/or other galaxies) is needed. The way this is done is shown in Table 2.

The catalog is an ASCII file, in which each line corresponds to one galaxy or blob extracted from the cosmological simulation and should have attributes described in Table 3.

5.3.2 RAMSES developer's perspective

The accretion of matter onto haloes is made through two channels: the smooth accretion of diffuse material and the mergers. From the implementation point of view, several questions arise in relation to the way diffuse gas is introduced into the simulation. The accretion of diffuse material is modeled as a blob of dark matter particles and gas component following the orbital and spin parameters given by the cosmological simulation. To allow the diffuse gas density field to be smooth, the mean density of the blob is chosen to be lower than the local density of the dark matter halo of the main galaxy so that each blob can be tidally disrupted when approaching the main galaxy.

The first issue that needs to be explored is whether we will be able to obtain enough collimated gas accretion, if it only follows dark matter. Before actually running a test simulation, we need to consider the time needed for gas to cool down and to concentrate into filamentary structure thinner than the one of dark matter before the instantaneous virial radius. Matter is introduced into simulation at the position corresponding to the final virial radius $R_{\mathrm{vir}(z_{\mathrm{min}})}$, let us say $z = 0$, which is

[4] Raffinement Adaptatif de Maillage Sans Effort Surhumain

[5] http://www.ics.uzh.ch/~teyssier/ramses/Documentation.html

Variable name, syntax and default value	**Fortran type**	**Description**
galaxy_list='galaxy_list'	Character LEN=512	Path to the catalog.
IG_density_factor=1.0D-5	Real	Density contrast for the intergalactic medium.
compatibility_vfactor=.false.	Logical	This is only for the particles velocities, not the gas, nor the galaxies. If compatibility_vfactor=.false. (i.e NOT defined in the GROUP_PARAMS in the namelist), velocities in 'ic_part' are in km/s (see also init_part.f90). If compatibility_vfactor=.true., velocities in 'ic_part' are in code units and no scaling will be done (see also init_part.f90).

Table 2

&GROUP_PARAMS BLOCK PARAMETERS DESCRIPTION FOR THE RESIMULATION PATCH

typically the case. This radius is larger than the instantaneous $R_{\rm vir}$ for higher redshifts ($z = 2 - 5$), thus between $R_{\rm vir(z=0)}$ and $R_{\rm vir(z>2)}$ gas could have enough time to reach the equilibrium in the gravitational potential well of dark matter filaments. We can make a crude estimation if this is indeed possible. For gas densities 0.01-0.1 cm^{-3}, free-fall time is of 100 Myr, at maximum of 500 Myr. Cooling time for gas at density of 0.01 cm^{-3}, metallicity of 0.1 Z$_\odot$ and temperature of 10^6 K is < 100 Myr. This implies that if injected at this temperature, gas should be able to cool and concentrate into a cold filament following the underlying dark matter structure in about 100 Myr, at maximum 500 Myr, before it reaches its actual $R_{\rm vir}$.

Second potential problem with this resimulation technique is the morphology of filaments. The implementation making use of sticky particle scheme for gas particles succeeded to obtain realistic thickness with respect to fully cosmological simulations. However it is not evident that this will be the case also for more realistic treatment of gas physics in the RAMSES code.

And finally, equation of state of gas at low densities, or the temperature floor at these low densities if cooling is used, needs to be modified. Typically, in galaxy simulations, the low density regime ($\rho < 10^{-3}$ cm^{-3}) is modeled with a polytropic EoS of form $T \propto \rho^{2/3}$, yielding a temperature of 4×10^6 K for density of 10^{-3} cm^{-3}, followed by an isotherm at 10^4 K (see Chapter 3.2.2). For densities of our interest (typical for cold flows or diffuse accretion in general), we can encounter a situation in which relatively dense (~ 0.1 cm^{-3}) and cool ($\sim 10^4$ K) gas moves through a gas with lower density (e.g. 5×10^{-4} cm^{-3}) which is more hot (2.5×10^6 K). This will create a pressure gradient opposing the motion of the flow/blob until eventually stopping its propagation. A solution that we will test is to use the isothermal temperature floor even for low densities ($\rho < 10^{-3}$ cm^{-3}).

To test our hypothesis, we have run a resimulation of a galaxy with an intermediate accretion history including only the diffuse components. We start with an initial uniform grid of 128^3 cells ($l_{\rm coarse} = 7$) in a 400 kpc box. Refinement is allowed up to a maximum resolution of 780 pc ($l_{\rm fine} = 9$) in the high density and/or Jeans unstable regions. Each AMR cell is refined into eight new cells if it contains more than 30 particles, or its baryonic mass content is larger than $5{\times}10^4$ M$_\odot$, or the local thermal Jeans length is smaller than four times the current cell size. Thermal evolution

Column	Variable	Description
1	time_in	Time of the insertion of the galaxy or blob (in Myr).
2	position_x	x-coordinate of the center of mass of the galaxy or blob (in kpc).
3	position_y	y-coordinate of the center of mass of the galaxy or blob (in kpc).
4	position_z	z-coordinate of the center of mass of the galaxy or blob (in kpc).
5	velocity_x	v_x-coordinate of the center of mass of the galaxy or blob (in km/s).
6	velocity_y	v_y-coordinate of the center of mass of the galaxy or blob (in km/s).
7	velocity_z	v_z-coordinate of the center of mass of the galaxy or blob (in km/s).
8	axis_x	x-component of the angular momentum of the galaxy or blob.
9	axis_y	y-component of the angular momentum of the galaxy or blob.
10	axis_z	z-component of the angular momentum of the galaxy or blob.
11	Mass_gas	Gaseous mass of the galaxy disk of blob (in 10^9 $M_\odot$).
12	rad_profile	Radial density profile of the disk ('exponential' or 'Toomre') or blob.
13	typ_radius	Characteristic radius of the disk or blob (in kpc).
14	cut_radius	Truncation radius of the disk or blob (in kpc).
15	z_profile	Vertical density profile of the disk or blob ('exponential' or 'gaussian').
16	typ_height	Characteristic height of the disk or blob (in pc).
17	cut_height	Truncation height of the disk or blob (in pc).
18	ic_part_file	File in the IC directory that contains the particle data (see also init_part.f90).
19	Vcirc_dat_file	File in the IC directory containing the velocity curves (col1 = radii in pc, col2 = Vcirc in km/s) [ORDERED IN RADIUS, NO DUPLICATED LINES].

Table 3
RESIMULATION CATALOG FILE ITEMS DESCRIPTION

is computed including atomic and fine-structure cooling assuming fixed metallicity of 0.1 $Z_\odot$ and heating from a uniform UV background (see Chapter 3 for details). We prevent gas to cool below 500 K. Other physical processes such as star formation and feedback are not included. Given the low resolution, we cannot resolve the central galaxy, but the main purpose of our test is to study the global behavior of accreting gas, not its interaction with galaxy itself and what we really need at this stage is to create the potential well allowing the accretion of diffuse gas as dictated by cosmological simulation. The resimulated galaxy is modeled with 7×10^5 dark matter particles with the total mass of 1.4×10^{12} $M_\odot$. The initial gas component has mass of 0.5×10^9 $M_\odot$, an exponential radial profile with the scale radius of 3.5 kpc and radial truncation of 5 kpc, and an exponential vertical profile with

scale-height of 1.6 kpc and vertical truncation of 3.2 kpc. Each blob representing diffuse material contains 117 dark matter particles with the mass of 5×10^4 $M_\odot$ each and its gas to total mass fraction is 0.17. Gaseous component of each blob has an exponential radial profile with the scale radius of 1 kpc and radial truncation of 2 kpc, and an exponential vertical profile with scale-height of 0.4 kpc and vertical truncation of 1 kpc.

We follow the evolution of the diffuse accretion from redshift 5 down to redshift 0.5. The simulation has been run for 3×10^4 cpu hours on 256 cpus. In Figure 5.3 we show maps of number density and temperature at maximum density along the line of sight in the entire resimulated volume at redshift $z \sim 3$. At large radii, coherent incoming streams penetrating toward the central galaxy can be visually identified both in density and temperature maps. Filaments have temperatures of $10^4 - 10^5$ K and densities in the range of $\sim$ 0.1 - 0.01 cm^{-3} at larger radial distances while in the vicinity of the central galaxy, temperature can rise up to 10^7 K.

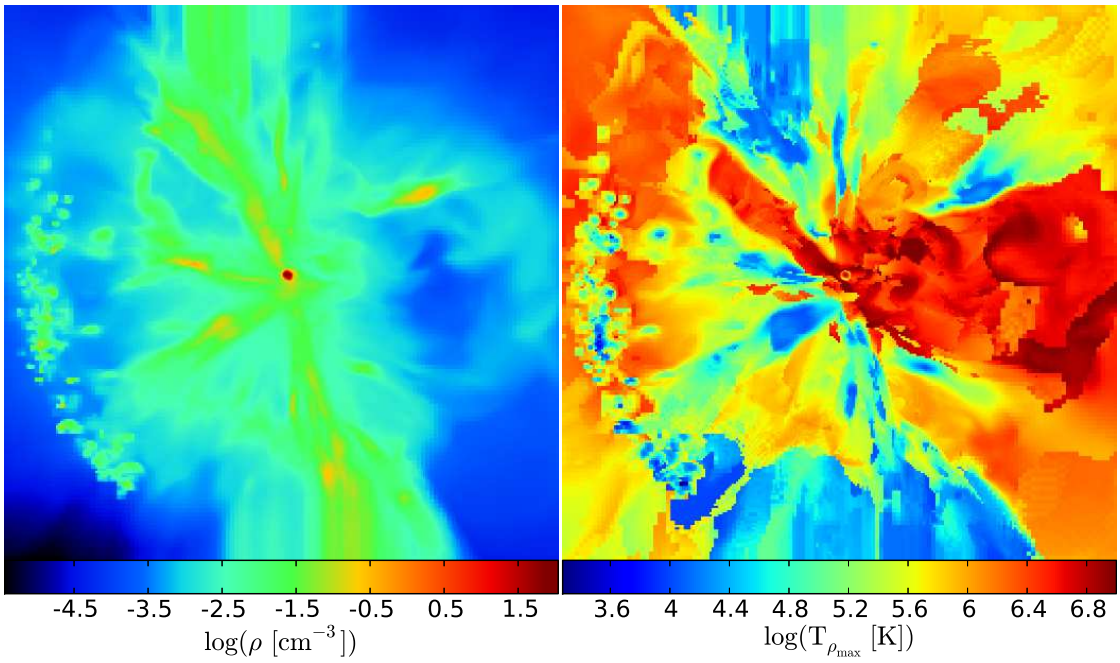

Figure 5.3

Visualization of gas number density (left) and temperature at maximum density along the line of sight (right) at redshift $z = 3$. The box size is 400 $\times$ 400 kpc^2.

We have also run the same model at higher resolution, 390 pc. Comparison of densities and temperatures at maximum density along the line of sight for two runs are shown in Figure 5.4. Both gas density and temperature show differences in their distribution. In the higher resolution run, gas is more fragmented along the filaments, making them loose their coherent structure extending beyond 100 kpc. Instead, they are feeding the central region with about 50 kpc in size. Temperatures where the density is maximum seem to be globally slightly lower except in the center, where larger high temperature region develop. More detailed analysis is required to understand these differences, however, it is interesting to see how relatively small change in resolution can lead to qualitatively different structures already at this stage.

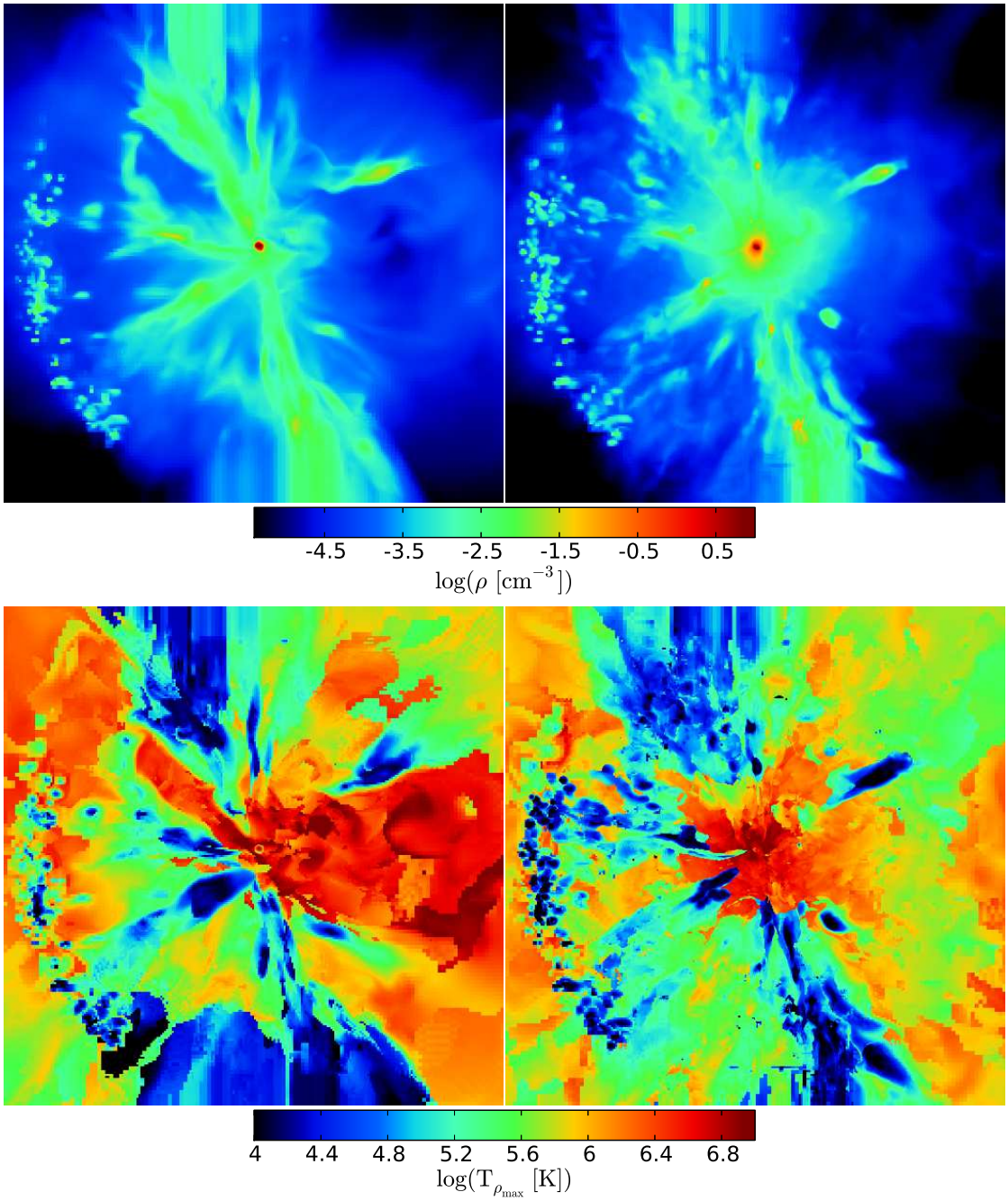

Figure 5.4

Number density of gas in the resimulated volume (top) and temperature at maximum density along the line of sight in the resimulated volume (bottom) are shown for two runs. The only difference is the resolution. At low resolution (left), filamentary structure of coherent incoming streams extends to large radial distances. At higher resolution (right), the gas fragments into denser clumps, making the filaments much more perturbed. Gas streams are thinner and a region of denser and hotter gas develops in central $\sim$ 50 kpc.

5.4 Perspectives

Studying the connection between the formation and evolution of internal structures of galaxies and large scale environment requires a galaxy model including cosmological background, including gas and associated physical processes such as cooling, star formation and feedback, and having sufficiently high resolution. Last but not least, it is helpful to be able to simulate a statistically significant sample of systems. These requirements may seem obvious, however it is much less obvious to satisfy them simultaneously in current cosmological hydrodynamic simulations.

Although our first tests including only diffuse accretion have shown to produce very encouraging results, in order to model accretion as dictated by cosmological evolution, the inclusion of mergers needs to be tested. Natural continuation is thus to run a resimulation of main galaxy using full catalog of initial conditions, including both diffuse accretion and mergers, as extracted from cosmological simulation. Possible problem that could be encountered at this stage is if multiple major mergers change orbital parameters of the main galaxy in such way, that it will gain a substantial bulk motion making it leave the simulation box. We cannot re-center the main galaxy and increasing the size of the box could be computationally costly solution.

The purpose of implementing the resimulation technique in the AMR code RAMSES is to combine on one side the advantages of the method itself, and on the other side the ability to treat gas phases with higher accuracy compared to the existing implementation involving the sticky particle scheme. Another improvement is the inclusion of star formation and various feedback processes such as SN, photoionization and radiation feedback that were used in simulations of isolated galaxies. As suggested by the results of our idealized galaxy simulations, in order to model the ISM properly, increased resolution to at least ~ 10 pc is necessary. Depending on concrete application, resolutions of 10-100 pc are conceivable for obtaining a sample of 20-30 resimulated galaxies at reasonable computation cost of about 20 million cpu hours. Another form of feedback that is not considered in our simulations is AGN feedback resulting from gas accretion onto a central black hole which can provide a large amount of energy and which is believed to play an important role in the assembly of high mass galaxies.

In order to characterize the history of accreted gas in galaxies, parcels of gas have to be tracked throughout their history in the simulation. The use of tracer particles, already used in the RAMSES code by e.g. Dubois et al. (2013), is probably inevitable if we do not want to be limited to the study of instantaneous properties only, but follow the history of accreted gas as well. The very first analysis that will be done with our simulations is to compute the mass in spherical shells of different radial bins in order to infer the inflow rate. Incoming gas provides the fuel for star formation. The importance of the mode of gas accretion lies in its determination of when this gas will be able to form stars. Instantaneous star formation rate depends on the current gas accretion rates, but also on previous accumulation of gas and on the mode of that accreted gas. Cold accreted gas is available for SF almost immediately. Hot accreted gas makes part of the gas reservoir that may fuel star formation at later times. This reservoir can be replenished by gas fountain – gas that joined the ISM, was heated and expelled from the galaxy by feedback. How far can this gas travel before cooling and becoming available for new star formation? And if it reaches the reservoir, what are typical delays for next star formation? Even though environment certainly plays a role, especially in dense regions where gas can be removed from the reservoir, feedback is extremely important for recycling of gas that was once accreted onto the galaxy. The role of feedback-driven outflows is twofold. On one hand outflows may interact with inflowing streams of gas and altering their properties and in general their ability to reach the central galaxy, on the other hand feedback may not only cycle the gas into the

reservoir, but if sufficiently strong, also eject it entirely. While strong outflows are found to affect most sensitively the accretion rate at the virial radius, it does not seem to have much effect on the accretion rate of cold gas to the center (Faucher-Giguère et al., 2011, Powell et al., 2011). However, AGN feedback was shown to be able to alter the properties of inflowing gas (Dubois et al., 2013). As far as the importance of feedback for storing of gas is concerned, Woods et al. (2014) have recently shown that strong feedback is able to make early star formation less efficient and shift the peak of star formation to lower redshifts, bringing a star formation history and stellar content of galaxies in better agreement with observations.

Simulations similar to those presented in this thesis (Bournaud et al., 2014) have shown that the physically motivated feedback model for photoionization, radiation pressure (Renaud et al., 2013) and SNe is able to produce realistic outflows. These simulations were however performed in isolation, without taking external accretion into account. The question that naturally arises is thus what is the result of the interaction of galactic-scale outflows with cosmic inflows. Do they interact at all? Are outflows able to disrupt inflows? Are they in steady-state?

Another interesting aspect is the ability of cold flows to actually reach the central galaxy. Results from the Illustris simulation seem to suggest that it is far from clear that cold flows manage easily to penetrate deep enough the halo to reach the disk of galaxy and supply it with gas. This statement is certainly mass and probably resolution dependent, however it is a good question to ask as it may indeed help to solve the problem of too high star formation at high redshift observed in almost all cosmological simulations of galaxy formation. We will also explore an alternative scenario proposed by Gabor & Bournaud (2014), in which inflow-increased turbulence delays star formation in high-redshift star-forming galaxies. Star formation efficiency is reduced as a consequence of increased turbulence velocity dispersions (Elmegreen & Burkert, 2010, Genel et al., 2012) which tend to increase the physical size of the galaxy gas distribution, lowering the gas density and thus SF efficiency.

Finally, it will also be possible to perform idealized simulations of cold flows in order to study their dynamical interactions with galactic outflows and the complicated physical processes that are taking place in the hot halo of galaxies.

Conclusion

In this thesis, I have made use of zoom-in cosmological simulations, high-resolution (parsec and sub-parsec) simulations of isolated galaxies and analytic technique to study links between galaxy evolution, morphology, and internal physical processes, namely star formation as the outcome of the turbulent multiphase ISM.

Standard scenario of galaxy formation tells us that galaxies form at the center of hierarchically merging dark matter halos. Formation of galaxies inside these haloes is however much more complicated than the formation of dark matter halos themselves because it involves dissipative, poorly understood baryonic processes.

In Chapter 2, I studied the evolution of barred galaxies with its mass dependence and accretion history of individual galaxies in a suite of zoom-in cosmological simulations (Martig et al., 2012), and compared to observations available to date, in the redshift range from two to zero. This work is based on the simulation sample of Milky-Way-mass galaxies, with present-day stellar masses ranging from 1×10^{10} to 2×10^{11} $M_{\odot}$, in low-density environments, with a broad variety of mass growth histories. I find that the fraction of bars declines with increasing redshift, from about 70 % at $z = 0$ to 10% - 20% at $z = 1$. Observable bars are rare and weak down to $z \simeq 1$ and almost absent from the progenitors of present-day spirals at $z > 1.5$, in agreement with the observed bar fraction evolution. The epoch of bar formation, $z \simeq 0.8 - 1$, traces the epoch of the emergence of the final thin disk of spiral galaxies, when today's spirals acquire their disk-dominated morphology. This corresponds to the transition between an early "violent" phase at $z > 1$ dominated by frequent mergers, violent disk instabilities and rapidly evolving structure, forming thick disks, bulges, and stellar halos, and late "secular" phase at $z < 0.8$, dominated by the slower growth and evolution of modern thin disks and limited bulge growth at late times. In general, bars do not contribute substantially to the late growth ($z < 1$) of (pseudo-)bulges in spiral galaxies. This late growth is dominated by continued cosmic infall and minor mergers rather than by bars. Another interesting finding is that while early bars (formed at $z > 1$) are often short-lived and may reform several times, bars that formed below $z \sim 1$ generally persist down to $z = 0$, some of them are intrinsically short-lived but maintained by late cosmological gas infall.

Contrarily to some other cosmological zoom-in simulations, models used in Chapter 2 successfully reproduce morphological diversity of galaxies with present-day stellar masses in the $10^{10} - 10^{11}$ $M_{\odot}$ range, in field and loose group environments. Large range of Hubble types can be found in the simulated sample at $z = 0$, from bulge-dominated galaxies to nearly bulgeless disks, with most of them having pseudo-bulges and 70% of them hosting a bar. At $z = 2$, galaxies tend to be very perturbed. If disks are present, they are often thick and sometimes unstable and clumpy. Another property of these galaxies reproduced in reasonable agreement with observations is their size. However, similarly to many other cosmological simulations, modeled galaxies form too many stars, with galaxy formation efficiency being three times higher than the one deduced from observations, and thus they cannot be a viable model for typical spiral galaxy formation. This has led me to study the process of star formation. To this purpose, I have performed a series of low-redshift galaxy simulations at parsec resolution in isolation, that I presented in Chapter 3 together with the study of the physical origin of their star formation relations and breaks. The analyzed sample includes simulations representative of the Large and Small Magellanic Clouds and the simulation of a Milky Way-like galaxy (Renaud et al., 2013) that reproduce the observed star formation relations and the relative variations of the

star formation thresholds. I studied the role of interstellar turbulence, gas cooling, and geometry in drawing these relations at 100 pc scale. I find that the onset of supersonic turbulence can be related to the surface density threshold for efficient star formation in the Σ_{gas}–Σ_{SFR} plane. Regions with efficient star formation are dominated by supersonic turbulence, while in the regime of the break, at low Σ_{gas}, turbulence tends to be subsonic.

Even though the distribution of the ISM of a galaxy in the Σ_{gas}–Σ_{SFR} plane, mainly the position of the break, is sensitive to metallicity, it is always correlated with the Mach number. This can explain observations of low-efficiency star formation in relatively dense gas in SMC-like dwarf galaxies. The driving physical parameter is still the onset of supersonic turbulence, but this onset is harder to reach at moderate gas densities in lower-metallicity systems that can preserve warmer gas.

Observations of galaxy-averaged star-formation relations seem to find evidence of bimodality according to which normal disk galaxies convert their gas into stars within a depletion time up to 10 times longer than galaxy mergers in starburst phase. I investigated this observational findings in the model of merging galaxies resembling Antennae galaxies (Renaud et al., 2014), but being a fairly representative case of many other mergers. Merging galaxies are found to move from the sequence of disks in the pre-merger phase to the sequence of starbursts reached during the interaction in the Σ_{gas}–Σ_{SFR} plane. This is interpreted as being due to the excess of dense gas generated by the increased compressive turbulence which is triggered by compressive tides during the interaction (Renaud et al., 2014).

I also studied properties of the ISM in these interacting galaxies at 100 pc scale at different stages of the merger, from pre-merger to the period ≈ 2 Myr after the second pericentre passage. I find qualitatively similar results concerning the role of ISM turbulence identified in models of isolated galaxies: efficient power-law regime is characterized by Mach numbers above unity and larger absolute values of divergence of the velocity field compared to the region of the break. This is interpreted as a signature of supersonic turbulence contributing to the transition from inefficient conversion of gas to stars at low Σ_{gas} to efficient star formation regime at high Σ_{gas}. Another interesting result of this study is that the merger-enhanced star formation activity is spatially extended. Increased star formation activity is found not only in nuclear region, as expected by "standard" theory of merger-induced starbursts, but also at larger distances.

The findings form these idealized simulations showing the importance of structure of the ISM shaped by the supersonic turbulence on star formation led us to propose an idealized analytic model (Renaud, Kraljic & Bournaud, 2012) relating the surface density of gas and star formation rate as a function of three parameters: the Mach number, the thickness of the star-forming regions and the star formation density threshold. I present the model (Renaud, Kraljic & Bournaud, 2012) in Chapter 4, and compare it with observations as well as simulations of isolated galaxies presented in Chapter 3. This model predicts a break at low surface densities in the Σ_{gas}–Σ_{SFR} plane, due to the local star formation threshold, that is followed by a 3/2 index power-law regime at high densities that can be flattened under the effects of stellar feedback at even higher surface densities, where the feedback becomes a dominant regulation factor. Comparison of model predictions with observations reveals the strength of this model: it is able to explain the observed diversity of star formation laws and thresholds in different systems such as nearby spirals, the Small Magellanic Cloud, high redshift disks, low and high redshift mergers. I next compare the model with simulations and find that the vertical spread in the Σ_{gas}–Σ_{SFR} diagram is given by the interplay between different model parameters of star-forming regions. Reasonable agreement between simulations and the proposed analytic model confirms that this idealized model provides a viable description of star formation in a turbulent ISM compared to more realistic simulations of self-gravitating systems with star formation and feedback.

One important implication of this work, focused on star formation, is to pose constraints on galaxy formation simulations. I find that it is crucial to resolve and model correctly the multiphase ISM in order to possibly solve the problems related to stellar masses that hamper cosmological simulations of galaxy evolution, such as those analyzed in Chapter 2 using the alternative cosmological zoom-in technique (Martig et al., 2009). This method, that has been able to reproduce realistic morphologies, has the advantage to model properly the properties of the star-forming interstellar medium in spite of relatively low resolution of ~ 100 pc (typically reached in the this kind of simulations). However, it is not able to treat gas around, and possibly also inside galaxies correctly – it neglects thermal pressure, especially in hot halos which may play crucial role in modeling high mass systems. This can be remedied by coupling the resimulation method with a grid-based hydrodynamic code which is known to model fluid dynamics better than particle based codes. In Chapter 5, I present the basic features of the resimulation technique, consisting in resimulating, at high resolution, the accretion history of a galaxy extracted in a low-resolution cosmological simulation, and its implementation in the Adaptive Mesh Refinement code RAMSES (Teyssier, 2002). I find that very first results including smooth accretion of resimulated galaxy only are indeed encouraging: gas filaments are well able to reach correct physical state in the gravitational potential well of the underlying dark-matter structure with their distribution in cold flows being established by the same process as in the fully cosmological simulation. In the future, I plan to include full accretion history, including both smooth and clumpy components, and more physics and investigate in detail the relative contribution of cold and hot mode accretion, interaction of inflows and outflows and their impact on the star formation at different stages of galaxy evolution.

Publications

Renaud F., Bournaud F., **Kraljic K.**, Duc P.-A.
Starbursts triggered by intergalactic tides and interstellar compressive turbulence.
MNRAS, 442, L33, 2014 arXiv:1403.7316

Kraljic K., Renaud F., Bournaud F., Combes F., Elmegreen B., Emsellem E., Teyssier R.
The role of turbulence in star formation laws and thresholds.
ApJ, 784, 112, 2014 arXiv:1402.1680

Bournaud F., Perret V., Renaud F., Dekel A., Elmegreen B., Elmegreen D., Teyssier R., Amram P., Daddi E., Duc, P.-A., Elbaz D., Epinat B., Gabor J., Juneau S., **Kraljic K.**, Le Floch' E.
The long lives of giant clumps and the birth of outflows in gas-rich galaxies at high redshift.
ApJ, 780, 57, 2014 arXiv:1307.7136

Renaud F., Bournaud, F., Emsellem, E., Elmegreen, B., Teyssier, R., Alves, J., Chapon, D., Combes, F., Dekel, A., Gabor, J., Hennebelle, P., **Kraljic, K.**
A sub-parsec resolution simulation of the Milky Way: global structure of the interstellar medium and properties of molecular clouds.
MNRAS, 2414, 2013 arXiv:1307.5639

Renaud F., **Kraljic K.**, Bournaud F.
Star formation laws and thresholds from interstellar medium structure and turbulence.
ApJ, 760, L16, 2012 arXiv:1210.2355

Kraljic K., Bournaud F., Martig M.
The two-phase formation history of spiral galaxies traced by the cosmic evolution of the bar fraction.
ApJ, 757, 60, 2012 arXiv:1207.0351

Table 4

LIST OF MAIN ACRONYMS AND SYMBOLS USED THROUGHOUT THE TEXT

Acronym	Expansion
AGN	Active galactic nucleus
AM	Angular momentum
AMR	Adaptive mesh refinement
CDM	Cold dark matter
CR	Corotation
DM	Dark matter
EoS	Equation of state
ILR	Inner Lindblad resonance
ISM	Interstellar medium
LMC	Large Magellanic Cloud
MW	Milky Way
OLR	Outer Lindblad resonance
PC	Pseudo-cooling
PDF	Probability distribution function
SF	Star formation
SFMS	Star formation main sequence
SFR	Star formation rate
$\Sigma_{\rm gas}$	Surface density of gas
$\Sigma_{\rm SFR}$	Surface density of star formation rate
SMC	Small Magellanic Cloud
SN, SNe	Supernova, Supernovae
SS	Self-shielding
UV	Ultraviolet
z	Redshift
Z	Metallicity

Appendix A

Σ_{gas}–Σ_{SFR} relations

A.1 Σ_{gas}–Σ_{SFR} relation without stellar feedback

Let us start with the calculation of the denominator of Equation (4.3)

$$\begin{aligned}
\int_0^\infty f(x)x^{-1}\,dx &= \int_0^\infty \frac{1}{x^2\sqrt{2\sigma^2\pi}}\exp\left[-\frac{\left(\ln(x)-\frac{\sigma^2}{2}\right)^2}{2\sigma^2}\right]dx \\
&= \frac{1}{\sqrt{2\sigma^2\pi}}\int_{-\infty}^\infty \exp(-y)\exp\left[-\frac{\left(y-\frac{\sigma^2}{2}\right)^2}{2\sigma^2}\right]dy \\
&= \frac{1}{\sqrt{2\sigma^2\pi}}\int_{-\infty}^\infty \exp\left[-\frac{\left(y+\frac{\sigma^2}{2}\right)^2}{2\sigma^2}\right]dy \\
&= \frac{1}{\sqrt{\pi}}\int_{-\infty}^\infty \exp\left(-t^2\right)\,dt \\
&= 1.
\end{aligned} \tag{A.1}$$

The complementary error function erfc defined by

$$\operatorname{erfc}(z) \equiv 1-\operatorname{erf}(z) = \frac{2}{\sqrt{\pi}}\int_z^\infty \exp\left(-t^2\right)\,dt \tag{A.2}$$

is invoked to go to the last line.

Using the expression for ρ_{SFR} as expressed by Equation (4.5), the numerator of Equation (4.3) reads as

$$\int_0^\infty f(x)x^{-1}\rho_{SFR}\,dx = \underbrace{\frac{\epsilon\alpha}{\sqrt{2\sigma^2\pi}}\int_{\frac{\rho_0}{\bar{\rho}}}^\infty \frac{1}{x^2}\exp\left[-\frac{\left(\ln(x)-\frac{\sigma^2}{2}\right)^2}{2\sigma^2}\right]\rho^{3/2}\,dx}_{\mathbf{I}_1(\sigma,\,\frac{\rho_0}{\bar{\rho}})} \tag{A.3}$$

$$
\begin{aligned}
I_1(\sigma, \frac{\rho_0}{\overline{\rho}}) &= \frac{\epsilon\alpha\overline{\rho}^{3/2}}{\sqrt{2\sigma^2\pi}} \int_{\ln\left(\frac{\rho_0}{\overline{\rho}}\right)}^{\infty} \exp\left(\frac{y}{2}\right) \exp\left[-\frac{\left(y-\frac{\sigma^2}{2}\right)^2}{2\sigma^2}\right] dy \\
&= \frac{\epsilon\alpha\overline{\rho}^{3/2}}{\sqrt{2\sigma^2\pi}} \exp\left(\frac{3}{8}\sigma^2\right) \int_{\ln\left(\frac{\rho_0}{\overline{\rho}}\right)}^{\infty} \exp\left[-\frac{\left(y-\sigma^2\right)^2}{2\sigma^2}\right] dy \\
&= \frac{\epsilon\alpha\overline{\rho}^{3/2}}{\sqrt{\pi}} \exp\left(\frac{3}{8}\sigma^2\right) \int_{\frac{\ln\left(\frac{\rho_0}{\overline{\rho}}\right)-\sigma^2}{\sqrt{2}\sigma}}^{\infty} \exp\left(-z^2\right) dz \\
&= \frac{\epsilon\alpha\overline{\rho}^{3/2}}{2} \exp\left(\frac{3}{8}\sigma^2\right) \operatorname{erfc}\left(\frac{\ln\left(\frac{\rho_0}{\overline{\rho}}\right)-\sigma^2}{\sqrt{2}\sigma}\right),
\end{aligned} \tag{A.4}
$$

where α is $\sqrt{\frac{32G}{3\pi}}$. To go from first to second line, the normalization $x = \rho/\overline{\rho}$ and transformation $y = \ln(x)$ were invoked. To go from third to fourth line, the transformation $z = \frac{y-\sigma^2}{\sqrt{2}\sigma}$ was used.

Σ_{SFR} than reads

Σ_{SFR} without feedback

$$
\Sigma_{SFR} = \epsilon\sqrt{\frac{8G}{3\pi}} \frac{\Sigma_{gas}^{3/2}}{\sqrt{h}} \exp\left(\frac{3}{8}\sigma^2\right) \operatorname{erfc}\left(\frac{\ln\left(\frac{\rho_0 h}{\Sigma_{gas}}\right)-\sigma^2}{\sqrt{2}\sigma}\right), \tag{A.5}
$$

where according to Equations (4.2) and (A.1) $\overline{\rho} = \Sigma_{gas}/h$.

A.2 Σ_{gas}–Σ_{SFR} relation with feedback regulation

We have defined the saturation in the local SF as follows

$$
\rho_{SFR} = \begin{cases} 0 & \text{if } \rho \leq \rho_0 \\ \min\left(\epsilon\sqrt{\frac{32G}{3\pi}}\rho^{3/2}, \frac{\epsilon_s}{t_s}\rho\right) & \text{else} \end{cases} \tag{A.6}
$$

This can be written equivalently as

$$
\rho_{SFR} = \begin{cases} 0 & \text{if } \rho \leq \rho_0 \\ \epsilon\sqrt{\frac{32G}{3\pi}}\rho^{3/2} & \text{if } \rho_0 < \rho \leq \rho_1 \\ \frac{\epsilon_s}{t_s}\rho & \text{else} \end{cases} \tag{A.7}
$$

where

$$
\rho_1 = \left(\frac{\epsilon_s}{t_s}\frac{1}{\epsilon\sqrt{\frac{32G}{3\pi}}}\right)^2. \tag{A.8}
$$

For a log-normal PDF and according to Equation (4.3), Σ_{SFR} becomes

$$\begin{aligned}\Sigma_{SFR} &= h\int_0^\infty f(x)x^{-1}\rho_{SFR}\,dx \\ &= h\frac{\epsilon\alpha}{\sqrt{2\sigma^2\pi}}\int_{\frac{\rho_0}{\overline{\rho}}}^{\frac{\rho_1}{\overline{\rho}}}\frac{1}{x^2}\exp\left[-\frac{\left(\ln(x)-\frac{\sigma^2}{2}\right)^2}{2\sigma^2}\right]\rho^{3/2}\,dx \\ &+ \underbrace{h\frac{\epsilon_s}{t_s\sqrt{2\sigma^2\pi}}\int_{\frac{\rho_1}{\overline{\rho}}}^{\infty}\frac{1}{x^2}\exp\left[-\frac{\left(\ln(x)-\frac{\sigma^2}{2}\right)^2}{2\sigma^2}\right]\rho\,dx}_{I_2(\sigma,\frac{\rho_1}{\overline{\rho}})} \\ &= h\left[I_1(\sigma,\frac{\rho_0}{\overline{\rho}}) - I_1(\sigma,\frac{\rho_1}{\overline{\rho}}) + I_2(\sigma,\frac{\rho_1}{\overline{\rho}})\right] \end{aligned} \tag{A.9}$$

$$\begin{aligned} I_2(\sigma) &= \frac{\epsilon_s}{t_s}\frac{\overline{\rho}}{\sqrt{2\sigma^2\pi}}\int_{\ln\left(\frac{\rho_1}{\overline{\rho}}\right)}^{\infty}\exp\left(-\frac{\left(y-\frac{\sigma^2}{2}\right)^2}{2\sigma^2}\right)\,dy \\ &= \frac{\epsilon_s}{t_s}\frac{\overline{\rho}}{\sqrt{\pi}}\int_{\frac{\ln\left(\frac{\rho_1}{\overline{\rho}}\right)-\frac{\sigma^2}{2}}{\sqrt{2}\sigma}}^{\infty}\exp\left(-z^2\right)\,dz \\ &= \frac{\epsilon_s}{t_s}\frac{\overline{\rho}}{2}\,\mathrm{erfc}\left(\frac{\ln\left(\frac{\rho_1}{\overline{\rho}}\right)-\frac{\sigma^2}{2}}{\sqrt{2}\sigma}\right). \end{aligned} \tag{A.10}$$

Finally, Σ_{SFR} becomes

Σ_{SFR} with feedback

$$\begin{aligned}\Sigma_{SFR} &= \epsilon\sqrt{\frac{8G}{3\pi}}\frac{\Sigma_{gas}^{3/2}}{\sqrt{h}}\exp\left(\frac{3}{8}\sigma^2\right)\left[\mathrm{erfc}\left(\frac{\ln\left(\frac{\rho_0 h}{\Sigma_{gas}}\right)-\sigma^2}{\sqrt{2}\sigma}\right)\right. \\ &\left. - \mathrm{erfc}\left(\frac{\ln\left(\frac{\epsilon_s^2 3\pi h}{t_s^2 32G\epsilon^2\Sigma_{gas}}\right)-\sigma^2}{\sqrt{2}\sigma}\right)\right] \\ &+ \frac{\epsilon_s}{2t_s}\Sigma_{gas}\,\mathrm{erfc}\left(\frac{\ln\left(\frac{\epsilon_s^2 3\pi h}{t_s^2 32G\epsilon^2\Sigma_{gas}}\right)-\frac{\sigma^2}{2}}{\sqrt{2}\sigma}\right). \end{aligned} \tag{A.11}$$

A.3 Σ_{gas}–Σ_{SFR} relation for starbursting mergers without stellar feedback

Σ_{gas}–Σ_{SFR} relation for starbursting mergers without stellar feedback

Modeling the merger induced density PDF by a function expressed by the Equation (4.9) and using the Equation (4.5) for ρ_{SFR}, according to Equation (4.3), Σ_{SFR} (without stellar feedback) becomes

$$\begin{aligned}\Sigma_{SFR} &= h\left[(1-m)\int_0^\infty f_{\sigma_1}(x)x^{-1}\rho_{SFR}\,dx + m\int_0^\infty f_{\sigma_2}(x/\exp\delta)x^{-1}\rho_{SFR}\,dx\right]\\ &= h(1-m)\frac{\epsilon\alpha}{\sqrt{2\sigma_1^2\pi}}\int_{\frac{\rho_0}{\overline{\rho}}}^\infty \frac{1}{x^2}\exp\left[-\frac{\left(\ln(x)-\frac{\sigma_1^2}{2}\right)^2}{2\sigma_1^2}\right]\rho^{3/2}\,dx\\ &+ hm\frac{\epsilon\alpha}{\sqrt{2\sigma_2^2\pi}}\int_{\frac{\rho_0}{\overline{\rho}}}^\infty \frac{1}{x\,(x/\exp\delta)}\exp\left[-\frac{\left(\ln(x/\exp\delta)-\frac{\sigma_2^2}{2}\right)^2}{2\sigma_2^2}\right]\rho^{3/2}\,dx\\ &= h(1-m)I_1(\sigma_1,\frac{\rho_0}{\overline{\rho}}) + hm\exp\left(\frac{3}{2}\delta\right)I_1(\sigma_2,\frac{\rho_0}{\overline{\rho}\exp\delta})\end{aligned} \tag{A.12}$$

Σ_{SFR} merger without feedback

$$\begin{aligned}\Sigma_{SFR} = \epsilon\sqrt{\frac{8G}{3\pi}}\frac{\Sigma_{gas}^{3/2}}{\sqrt{h}}\Bigg[&(1-m)\exp\left(\frac{3}{8}\sigma_1^2\right)\operatorname{erfc}\left(\frac{\ln\left(\frac{\rho_0 h}{\Sigma_{gas}}\right)-\sigma_1^2}{\sqrt{2}\sigma_1}\right)\\ &+ m\exp\left(\frac{3}{8}\sigma_2^2\right)\exp\left(\frac{3}{2}\delta\right)\operatorname{erfc}\left(\frac{\ln\left(\frac{\rho_0 h}{\Sigma_{gas}}\right)-\sigma_2^2-\delta}{\sqrt{2}\sigma_2}\right)\Bigg]\end{aligned} \tag{A.13}$$

A.4 Σ_{gas}–Σ_{SFR} relation for starbursting mergers with stellar feedback

Modeling the merger induced density PDF by a function expressed by the Equation (4.9) and writing ρ_{SFR} as in A.2, according to Equation (4.3), Σ_{SFR} with stellar feedback becomes

$$\begin{aligned}\Sigma_{SFR} &= h\int_0^\infty f(x)x^{-1}\rho_{SFR}\,dx\\ &= h\left[(1-m)\int_0^\infty f_{\sigma_1}(x)x^{-1}\rho_{SFR}\,dx + m\int_0^\infty f_{\sigma_2}(x/\exp\delta)x^{-1}\rho_{SFR}\,dx\right]\\ &= h(1-m)\left[I_1(\sigma_1,\frac{\rho_0}{\overline{\rho}}) - I_1(\sigma_1,\frac{\rho_1}{\overline{\rho}})\right]\\ &+ hm\exp\left(\frac{3}{2}\delta\right)\left[I_1(\sigma_2,\frac{\rho_0}{\overline{\rho}\exp\delta}) - I_1(\sigma_2,\frac{\rho_1}{\overline{\rho}\exp\delta})\right] + hm\exp\delta I_2(\sigma_2,\frac{\rho_1}{\overline{\rho}\exp\delta})\end{aligned} \tag{A.14}$$

$$\Sigma_{SFR} = \epsilon\sqrt{\frac{8G}{3\pi}}\frac{\Sigma_{gas}^{3/2}}{\sqrt{h}}(1-m)\exp\left(\frac{3}{8}\sigma_1^2\right)\left[\operatorname{erfc}\left(\frac{\ln\left(\frac{\rho_0 h}{\Sigma_{gas}}\right)-\sigma_1^2}{\sqrt{2}\sigma_1}\right)-\operatorname{erfc}\left(\frac{\ln\left(\frac{\epsilon_s^2 3\pi h}{t_s^2 32G\epsilon^2\Sigma_{gas}}\right)-\sigma_1^2}{\sqrt{2}\sigma_1}\right)\right]$$
$$+(1-m)\Sigma_{gas}\frac{\epsilon_s}{2t_s}\operatorname{erfc}\left(\frac{\ln\left(\frac{\epsilon_s^2 3\pi h}{t_s^2 32G\epsilon^2\Sigma_{gas}}\right)-\frac{\sigma_1^2}{2}}{\sqrt{2}\sigma_1}\right)$$
$$+\epsilon\sqrt{\frac{8G}{3\pi}}\frac{\Sigma_{gas}^{3/2}}{\sqrt{h}}m\exp\left(\frac{3}{2}\delta\right)\exp\left(\frac{3}{8}\sigma_2^2\right)\left[\operatorname{erfc}\left(\frac{\ln\left(\frac{\rho_0 h}{\Sigma_{gas}}\right)-\sigma_2^2-\delta}{\sqrt{2}\sigma_2}\right)-\right.$$
$$\left.-\operatorname{erfc}\left(\frac{\ln\left(\frac{\epsilon_s^2 3\pi h}{t_s^2 32G\epsilon^2\Sigma_{gas}}\right)-\sigma_2^2-\delta}{\sqrt{2}\sigma_2}\right)\right]+m\Sigma_{gas}\frac{\epsilon_s}{2t_s}\exp\delta\operatorname{erfc}\left(\frac{\ln\left(\frac{\epsilon_s^2 3\pi h}{t_s^2 32G\epsilon^2\Sigma_{gas}}\right)-\frac{\sigma_2^2}{2}-\delta}{\sqrt{2}\sigma_2}\right) \tag{A.15}$$

Σ_{SFR} mergers with feedback

$$\Sigma_{SFR} = \epsilon\sqrt{\frac{8G}{3\pi}}\frac{\Sigma_{gas}^{3/2}}{\sqrt{h}}(1-m)\exp\left(\frac{3}{8}\sigma_1^2\right)\left[\operatorname{erfc}\left(\frac{\ln\left(\frac{\rho_0 h}{\Sigma_{gas}}\right)-\sigma_1^2}{\sqrt{2}\sigma_1}\right)\right.$$
$$\left.-\operatorname{erfc}\left(\frac{\ln\left(\frac{\epsilon_s^2 3\pi h}{t_s^2 32G\epsilon^2\Sigma_{gas}}\right)-\sigma_1^2}{\sqrt{2}\sigma_1}\right)\right]$$
$$+(1-m)\Sigma_{gas}\frac{\epsilon_s}{2t_s}\operatorname{erfc}\left(\frac{\ln\left(\frac{\epsilon_s^2 3\pi h}{t_s^2 32G\epsilon^2\Sigma_{gas}}\right)-\frac{\sigma_1^2}{2}}{\sqrt{2}\sigma_1}\right)$$
$$+\epsilon\sqrt{\frac{8G}{3\pi}}\frac{\Sigma_{gas}^{3/2}}{\sqrt{h}}m\exp\left(\frac{3}{2}\delta\right)\exp\left(\frac{3}{8}\sigma_2^2\right)\left[\operatorname{erfc}\left(\frac{\ln\left(\frac{\rho_0 h}{\Sigma_{gas}}\right)-\sigma_2^2-\delta}{\sqrt{2}\sigma_2}\right)-\right.$$
$$\left.-\operatorname{erfc}\left(\frac{\ln\left(\frac{\epsilon_s^2 3\pi h}{t_s^2 32G\epsilon^2\Sigma_{gas}}\right)-\sigma_2^2-\delta}{\sqrt{2}\sigma_2}\right)\right]$$
$$+m\Sigma_{gas}\frac{\epsilon_s}{2t_s}\exp\delta\operatorname{erfc}\left(\frac{\ln\left(\frac{\epsilon_s^2 3\pi h}{t_s^2 32G\epsilon^2\Sigma_{gas}}\right)-\frac{\sigma_2^2}{2}-\delta}{\sqrt{2}\sigma_2}\right) \tag{A.16}$$

Appendix B

RAMSES patches

B.1 Patch: group

Author: Florent Renaud
Date: March 17, 2011
Aim: Initial conditions to set up one or more galaxies.
Location: &GROUP_PARAMS block of the namelist.
Namelist settings: Each array variable is a list (one item per galaxy). Maximum number of galaxies that can be initialized is 10.

Variable name, syntax and default value	Fortran type	Description
gal_center_x=100.0,100.0,...	Real arrays	x-coordinates of the centers of mass of the galaxies (in kpc).
gal_center_y=0.0,0.0,...		y-coordinates of the centers of mass of the galaxies (in kpc).
gal_center_z=0.0,0.0,...		z-coordinates of the centers of mass of the galaxies (in kpc).
v_gal_x=100.0,100.0,...	Real arrays	v_x-coordinates of the centers of mass of the galaxies (in km/s).
v_gal_y=0.0,0.0,...		v_y-coordinates of the centers of mass of the galaxies (in km/s).
v_gal_z=0.0,0.0,...		v_z-coordinates of the centers of mass of the galaxies (in km/s).
gal_axis_x=0.0E0,0.0E0,...	Real arrays	x-components of the angular momentum of the disks.
gal_axis_y=0.0E0,1.0E0,...		y-components of the angular momentum of the disks.
gal_axis_z=1.0E0,0.0E0,...		z-components of the angular momentum of the disks.
Mgas_disk=2.5D0,5.0D0,...	Real arrays	Gaseous masses of the disks (in 10^9 $M_\odot$).
typ_radius=6.0D0,6.0D0,...	Real arrays	Characteristic radii of the disks (in kpc).
cut_radius=6.0D0,6.0D0,...	Real arrays	Truncation radii of the disks (in kpc).
typ_height=6.0D0,6.0D0,...	Real arrays	Characteristic heights of the disks (in pc).
cut_height=6.0D0,6.0D0,...	Real arrays	Truncation heights of the disks (in pc).
rad_profile=N*'exponential'	Character LEN=16 arrays	Radial density profile of the disks ('exponential' or 'Toomre').
z_profile=N*'exponential'	Character LEN=16 arrays	Vertical density profile of the disks ('exponential' or 'gaussian').
Vcirc_dat_file=N*'Vcirc.dat'	Character LEN=16 arrays	Path to the files containing the velocity curves (col1 = radii in pc, col2 = Vcirc in km/s) [ORDERED IN RADIUS, NO DUPLICATED LINES].
ic_part_file=N*'init_part'	Character LEN=512 arrays	File in the IC directory that contains the particle data (see also init_part.f90).
IG_density_factor=1.0D-5	Real	Density contrast for the intergalactic medium.
compatibility_vfactor=.false.	Logical	This is only for the particles velocities, not the gas, nor the galaxies. If compatibility_vfactor=.false. (i.e. NOT defined in the GROUP_PARAMS in the namelist), velocities in 'ic_part' are in km/s (see also init_part.f90). If compatibility_vfactor=.true., velocities in 'ic_part' are in code units and no scaling will be done (see also init_part.f90).

Table 5
&GROUP_PARAMS BLOCK PARAMETERS DESCRIPTION FOR THE GROUP PATCH

Bibliography

Abraham R. G., Merrifield M. R., Ellis R. S., et al., 1999, MNRAS, 308, 569
Agertz O., Lake G., Teyssier R., et al., 2009a, MNRAS, 392, 294
Agertz O., Teyssier R., Moore B., 2009b, MNRAS, 397, L64
Agertz O., Teyssier R., Moore B., 2011, MNRAS, 410, 1391
Agertz O., Kravtsov A. V., Leitner S. N., et al., 2013, ApJ, 770, 25
Aguerri J. A. L., Beckman J. E., Prieto M., 1998, AJ, 116, 2136
Aguerri J. A. L., Méndez-Abreu J., Corsini E. M., 2009, A&A, 495, 491
André P., Men'shchikov A., Könyves V., et al., 2011, in Alves J., Elmegreen B. G., Girart J. M., Trimble V., editors, Computational Star Formation volume 270 of IAU Symposium, Origin of the prestellar core mass function and link to the IMF - Herschel first results. pages 255–262
Athanassoula E., 1999, in Sellwood J. A., Goodman J., editors, Astrophysical Discs - an EC Summer School volume 160 of Astronomical Society of the Pacific Conference Series, N-body Simulations of Interacting Disc Galaxies. page 351
Athanassoula E., 2002, ApJ, 569, L83
Athanassoula E., 2003, MNRAS, 341, 1179
Athanassoula E., 2005, MNRAS, 358, 1477
Athanassoula E., . page 305. 2013
Athanassoula E., Sellwood J. A., 1986, MNRAS, 221, 213
Athanassoula E., Machado R. E. G., Rodionov S. A., 2013, MNRAS, 429, 1949
Audit E., Hennebelle P., 2010, A&A, 511, A76
Bacon R., Accardo M., Adjali L., et al., 2010, in Society of Photo-Optical Instrumentation Engineers (SPIE) Conference Series volume 7735 of Society of Photo-Optical Instrumentation Engineers (SPIE) Conference Series, The MUSE second-generation VLT instrument
Barazza F. D., Jogee S., Marinova I., 2008, ApJ, 675, 1194
Barnes J. E., 1988, ApJ, 331, 699
Barnes J. E., 2004, MNRAS, 350, 798
Barnes J. E., Hernquist L. E., 1991, ApJ, 370, L65
Barnes K. L., van Zee L., Côté S., et al., 2012, ApJ, 757, 64
Barton E. J., Geller M. J., Kenyon S. J., 2000, ApJ, 530, 660
Barway S., Wadadekar Y., Kembhavi A. K., 2011, MNRAS, 410, L18
Bate M. R., Bonnell I. A., Price N. M., 1995, MNRAS, 277, 362
Beetz C., Schwarz C., Dreher J., et al., 2008, Physics Letters A, 372, 3037
Behroozi P. S., Conroy C., Wechsler R. H., 2010, ApJ, 717, 379
Behroozi P. S., Wechsler R. H., Conroy C., 2013, ApJ, 770, 57
Belokurov V., Walker M. G., Evans N. W., et al., 2008, ApJ, 686, L83
Belokurov V., Walker M. G., Evans N. W., et al., 2010, ApJ, 712, L103
Benson A. J., Frenk C. S., Lacey C. G., et al., 2002, MNRAS, 333, 177
Benson A. J., Bower R. G., Frenk C. S., et al., 2003, ApJ, 599, 38
Berentzen I., Shlosman I., 2006, ApJ, 648, 807
Berentzen I., Athanassoula E., Heller C. H., et al., 2003, MNRAS, 341, 343
Berentzen I., Athanassoula E., Heller C. H., et al., 2004, MNRAS, 347, 220
Bigiel F., Leroy A., Walter F., et al., 2008, AJ, 136, 2846

Binney J., 1977, ApJ, 215, 483
Birnboim Y., Dekel A., 2003, MNRAS, 345, 349
Block D. L., 2012, in Holder R. D., Mitton S., editors, Astrophysics and Space Science Library volume 395 of Astrophysics and Space Science Library, Georges Lemaître and Stigler's Law of Eponymy. page 89
Block D. L., Bournaud F., Combes F., et al., 2002, A&A, 394, L35
Boissier S., Prantzos N., Boselli A., et al., 2003, MNRAS, 346, 1215
Bolatto A. D., Leroy A. K., Rosolowsky E., et al., 2008, ApJ, 686, 948
Bolatto A. D., Leroy A. K., Jameson K., et al., 2011, ApJ, 741, 12
Bond J. R., Kofman L., Pogosyan D., 1996, Nature, 380, 603
Bonnell I. A., Dobbs C. L., Smith R. J., 2013, MNRAS, 430, 1790
Bontemps S., Andre P., Terebey S., et al., 1996, A&A, 311, 858
Bournaud F., 2010, in Smith B., Higdon J., Higdon S., Bastian N., editors, Galaxy Wars: Stellar Populations and Star Formation in Interacting Galaxies volume 423 of Astronomical Society of the Pacific Conference Series, Star Formation and Structure Formation in Galaxy Interactions and Mergers. page 177
Bournaud F., Combes F., 2002, A&A, 392, 83
Bournaud F., Combes F., 2003, A&A, 401, 817
Bournaud F., Combes F., Semelin B., 2005, MNRAS, 364, L18
Bournaud F., Elmegreen B. G., Elmegreen D. M., 2007, ApJ, 670, 237
Bournaud F., Elmegreen B. G., Martig M., 2009, ApJ, 707, L1
Bournaud F., Elmegreen B. G., Teyssier R., et al., 2010, MNRAS, 409, 1088
Bournaud F., Chapon D., Teyssier R., et al., 2011a, ApJ, 730, 4
Bournaud F., Powell L. C., Chapon D., et al., 2011b, in Brummell N. H., Brun A. S., Miesch M. S., Ponty Y., editors, IAU Symposium volume 271 of IAU Symposium, Star formation in galaxy mergers: ISM turbulence, dense gas excess, and scaling relations for disks and starbusts. pages 160–169
Bournaud F., Juneau S., Le Floc'h E., et al., 2012, ApJ, 757, 81
Bournaud F., Perret V., Renaud F., et al., 2014, ApJ, 780, 57
Boylan-Kolchin M., Bullock J. S., Kaplinghat M., 2011, MNRAS, 415, L40
Boylan-Kolchin M., Bullock J. S., Kaplinghat M., 2012, MNRAS, 422, 1203
Brooks A. M., Governato F., Quinn T., et al., 2009, ApJ, 694, 396
Brooks A. M., Kuhlen M., Zolotov A., et al., 2013, ApJ, 765, 22
Bullock J. S., 2010, ArXiv e-prints
Bureau M., Freeman K. C., 1999, AJ, 118, 126
Burkert A., 1995, ApJ, 447, L25
Burkert A., 2006, Comptes Rendus Physique, 7, 433
Cameron E., Carollo C. M., Oesch P., et al., 2010, MNRAS, 409, 346
Cappellari M., Emsellem E., Krajnović D., et al., 2011, MNRAS, 416, 1680
Ceverino D., Dekel A., Bournaud F., 2010, MNRAS, 404, 2151
Ceverino D., Dekel A., Mandelker N., et al., 2012, MNRAS, 420, 3490
Chiappini C., 2009, in Andersen J., Nordströara m B., Bland-Hawthorn J., editors, IAU Symposium volume 254 of IAU Symposium, The chemical evolution of the Galactic thick and thin disks. pages 191–196
Chien L.-H., Barnes J. E., 2010, MNRAS, 407, 43
Colín P., Valenzuela O., Klypin A., 2006, ApJ, 644, 687

Colless M., Dalton G., Maddox S., et al., 2003, VizieR Online Data Catalog, 7226, 0
Collins D. C., Kritsuk A. G., Padoan P., et al., 2012, ApJ, 750, 13
Combes F., Elmegreen B. G., 1993, A&A, 271, 391
Combes F., Sanders R. H., 1981, A&A, 96, 164
Combes F., Boisse P., Mazure A., et al., 2002, Galaxies and cosmology
Conn A. R., Lewis G. F., Ibata R. A., et al., 2013, ApJ, 766, 120
Courant R., Friedrichs K., Lewy H., 1928, Mathematische Annalen, 100, 32
Courty S., Alimi J. M., 2004, A&A, 416, 875
Cox T. J., Jonsson P., Primack J. R., et al., 2006, MNRAS, 373, 1013
Cox T. J., Jonsson P., Somerville R. S., et al., 2008, MNRAS, 384, 386
Crighton N. H. M., Hennawi J. F., Prochaska J. X., 2013, ApJ, 776, L18
Croton D. J., Springel V., White S. D. M., et al., 2006, MNRAS, 365, 11
Cullen H., Alexander P., Clemens M., 2006, MNRAS, 366, 49
Curir A., Mazzei P., Murante G., 2006, A&A, 447, 453
Daddi E., Dickinson M., Morrison G., et al., 2007, ApJ, 670, 156
Daddi E., Bournaud F., Walter F., et al., 2010a, ApJ, 713, 686
Daddi E., Elbaz D., Walter F., et al., 2010b, ApJ, 714, L118
Dalcanton J. J., Bernstein R. A., 2002, AJ, 124, 1328
Dale J. E., Ngoumou J., Ercolano B., et al., 2013, MNRAS, 436, 3430
de Blok W. J. G., McGaugh S. S., Rubin V. C., 2001, AJ, 122, 2396
de Vaucouleurs G., 1959, Handbuch der Physik, 53, 275
de Vaucouleurs G., 1974, in Shakeshaft J. R., editor, The Formation and Dynamics of Galaxies volume 58 of IAU Symposium, Structures of Central Bulges and Nuclei of Galaxies. page 335
de Vaucouleurs G., de Vaucouleurs A., Corwin Jr. H. G., et al., 1991, Third Reference Catalogue of Bright Galaxies. Volume I: Explanations and references. Volume II: Data for galaxies between 0^h and 12^h. Volume III: Data for galaxies between 12^h and 24^h.
Debattista V. P., Sellwood J. A., 2000, ApJ, 543, 704
Dekel A., Birnboim Y., 2006, MNRAS, 368, 2
Dekel A., Silk J., 1986, ApJ, 303, 39
Dekel A., Woo J., 2003, MNRAS, 344, 1131
Dekel A., Birnboim Y., Engel G., et al., 2009, Nature, 457, 451
Del Popolo A., Lima J. A. S., Fabris J. C., et al., 2014, J. Cosmology Astropart. Phys., 4, 21
Delgado-Serrano R., Hammer F., Yang Y. B., et al., 2010, A&A, 509, A78
Di Matteo P., Combes F., Melchior A.-L., et al., 2007, A&A, 468, 61
Di Matteo P., Bournaud F., Martig M., et al., 2008, A&A, 492, 31
Dib S., 2011, ApJ, 737, L20
Dib S., Burkert A., 2005, ApJ, 630, 238
Dib S., Piau L., Mohanty S., et al., 2011, MNRAS, 415, 3439
Dib S., Helou G., Moore T. J. T., et al., 2012, ApJ, 758, 125
Dobbs C. L., Pringle J. E., 2009, MNRAS, 396, 1579
Dobbs C. L., Glover S. C. O., Clark P. C., et al., 2008, MNRAS, 389, 1097
Dobbs C. L., Burkert A., Pringle J. E., 2011, MNRAS, 417, 1318
Dubinski J., Chakrabarty D., 2009, ApJ, 703, 2068
Dubois Y., Teyssier R., 2008, A&A, 477, 79
Dubois Y., Pichon C., Haehnelt M., et al., 2012, MNRAS, 423, 3616
Dubois Y., Pichon C., Devriendt J., et al., 2013, MNRAS, 428, 2885

Eales S. A., Smith M. W. L., Wilson C. D., et al., 2010, A&A, 518, L62
Efstathiou G., 2000, MNRAS, 317, 697
El-Zant A., Shlosman I., Hoffman Y., 2001, ApJ, 560, 636
Elbaz D., Daddi E., Le Borgne D., et al., 2007, A&A, 468, 33
Ellison S. L., Patton D. R., Simard L., et al., 2008, AJ, 135, 1877
Ellison S. L., Patton D. R., Simard L., et al., 2010, MNRAS, 407, 1514
Ellison S. L., Mendel J. T., Patton D. R., et al., 2013, MNRAS, 435, 3627
Elmegreen B. G., 2002, ApJ, 577, 206
Elmegreen B. G., 2011, ApJ, 731, 61
Elmegreen B. G., Burkert A., 2010, ApJ, 712, 294
Elmegreen B. G., Elmegreen D. M., 2006, ApJ, 650, 644
Elmegreen B. G., Parravano A., 1994, ApJ, 435, L121
Elmegreen B. G., Elmegreen D. M., Hirst A. C., 2004, ApJ, 612, 191
Elmegreen B. G., Elmegreen D. M., Knapen J. H., et al., 2007a, ApJ, 670, L97
Elmegreen B. G., Elmegreen D. M., Fernandez M. X., et al., 2009, ApJ, 692, 12
Elmegreen D. M., Kaufman M., Brinks E., et al., 1995, ApJ, 453, 100
Elmegreen D. M., Elmegreen B. G., Ravindranath S., et al., 2007b, ApJ, 658, 763
Elson E. C., de Blok W. J. G., Kraan-Korteweg R. C., 2012, AJ, 143, 1
Epinat B., Tasca L., Amram P., et al., 2012, A&A, 539, A92
Eskridge P. B., Frogel J. A., Pogge R. W., et al., 2000, AJ, 119, 536
Fall S. M., Efstathiou G., 1980, MNRAS, 193, 189
Faucher-Giguère C.-A., Kereš D., 2011, MNRAS, 412, L118
Faucher-Giguère C.-A., Kereš D., Ma C.-P., 2011, MNRAS, 417, 2982
Federrath C., 2013, MNRAS, 436, 3167
Federrath C., Klessen R. S., 2012, ApJ, 761, 156
Federrath C., Klessen R. S., Schmidt W., 2008, ApJ, 688, L79
Federrath C., Roman-Duval J., Klessen R. S., et al., 2010, A&A, 512, A81
Fisher D. B., Drory N., Fabricius M. H., 2009, ApJ, 697, 630
Förster Schreiber N. M., Genzel R., Bouché N., et al., 2009, ApJ, 706, 1364
Friedli D., Benz W., 1993, A&A, 268, 65
Froebrich D., Rowles J., 2010, MNRAS, 406, 1350
Gabor J. M., Bournaud F., 2014, MNRAS, 437, L56
Gao Y., Solomon P. M., 2004, ApJ, 606, 271
Garrison-Kimmel S., Rocha M., Boylan-Kolchin M., et al., 2013, MNRAS, 433, 3539
Gazol A., Vázquez-Semadeni E., Kim J., 2005, ApJ, 630, 911
Geller M. J., Huchra J. P., 1989, Science, 246, 897
Genel S., Dekel A., Cacciato M., 2012, MNRAS, 425, 788
Genel S., Vogelsberger M., Nelson D., et al., 2013, MNRAS, 435, 1426
Genel S., Vogelsberger M., Springel V., et al., 2014, ArXiv e-prints
Genzel R., Lutz D., Tacconi L., 1998, Nature, 395, 859
Genzel R., Tacconi L. J., Gracia-Carpio J., et al., 2010, MNRAS, 407, 2091
Genzel R., Newman S., Jones T., et al., 2011, ApJ, 733, 101
Gerin M., Combes F., Athanassoula E., 1990, A&A, 230, 37
Gilmore G., Reid N., Hewett P., 1985, MNRAS, 213, 257
Girichidis P., Konstandin L., Whitworth A. P., et al., 2014, ApJ, 781, 91
Gnedin N. Y., 2000, ApJ, 542, 535

Gnerucci A., Marconi A., Cresci G., et al., 2011, A&A, 528, A88
Goerdt T., Moore B., Read J. I., et al., 2010, ApJ, 725, 1707
Goerdt T., Dekel A., Sternberg A., et al., 2012, MNRAS, 424, 2292
Governato F., Willman B., Mayer L., et al., 2007, MNRAS, 374, 1479
Governato F., Brook C., Mayer L., et al., 2010, Nature, 463, 203
Guedes J., Callegari S., Madau P., et al., 2011, ApJ, 742, 76
Gunn J. E., Gott III J. R., 1972, ApJ, 176, 1
Guo Q., White S., Li C., et al., 2010, MNRAS, 404, 1111
Haardt F., Madau P., 1996, ApJ, 461, 20
Halle A., Combes F., 2013, A&A, 559, A55
Hammer F., Flores H., Puech M., et al., 2009, A&A, 507, 1313
Hancock M., Smith B. J., Struck C., et al., 2009, AJ, 137, 4643
Hasan H., Norman C., 1990, ApJ, 361, 69
Hasan H., Pfenniger D., Norman C., 1993, ApJ, 409, 91
Heller C. H., Shlosman I., Athanassoula E., 2007, ApJ, 671, 226
Hennebelle P., Chabrier G., 2008, ApJ, 684, 395
Hennebelle P., Chabrier G., 2011, ApJ, 743, L29
Hernquist L., 1992, ApJ, 400, 460
Herrington J., Bell E., CANDELS Team 2012, in American Astronomical Society Meeting Abstracts #219 volume 219 of American Astronomical Society Meeting Abstracts, No Significant Evolution in the Bar Fraction in Large Disk Galaxies From z=1.8 to z=0.6. page 429.06
Heyer M. H., Corbelli E., Schneider S. E., et al., 2004, ApJ, 602, 723
Hoeft M., Yepes G., Gottlöber S., et al., 2006, MNRAS, 371, 401
Hohl F., 1971, ApJ, 168, 343
Holley-Bockelmann K., Weinberg M., Katz N., 2005, MNRAS, 363, 991
Hopkins P. F., Quataert E., Murray N., 2011, MNRAS, 417, 950
Hopkins P. F., Keres D., Onorbe J., et al., 2013a, ArXiv e-prints
Hopkins P. F., Kereš D., Murray N., 2013b, MNRAS, 432, 2639
Hopkins P. F., Narayanan D., Murray N., 2013c, MNRAS, 432, 2647
Hubble E., 1925, Contributions from the Mount Wilson Observatory / Carnegie Institution of Washington, 304, 1
Hubble E., 1929, Proceedings of the National Academy of Science, 15, 168
Hubble E., Humason M. L., 1931, ApJ, 74, 43
Hubble E. P., 1926, ApJ, 64, 321
Hubble E. P., 1936, Realm of the Nebulae
Huchra J., Jarrett T., Skrutskie M., et al., 2005, in Fairall A. P., Woudt P. A., editors, Nearby Large-Scale Structures and the Zone of Avoidance volume 329 of Astronomical Society of the Pacific Conference Series, The 2MASS Redshift Survey and Low Galactic Latitude Large-Scale Structure. page 135
Hunter D. A., Elmegreen B. G., Baker A. L., 1998, ApJ, 493, 595
Ibata R., Mouhcine M., Rejkuba M., 2009, MNRAS, 395, 126
Ibata R. A., Lewis G. F., Conn A. R., et al., 2013, Nature, 493, 62
Inoue S., Saitoh T. R., 2011, MNRAS, 418, 2527
Irwin J. A., 1994, ApJ, 429, 618
Irwin M. J., Belokurov V., Evans N. W., et al., 2007, ApJ, 656, L13
Ishiyama T., Rieder S., Makino J., et al., 2013, ApJ, 767, 146

Jõeveer M., Einasto J., Tago E., 1978, MNRAS, 185, 357
Jeans J. H., 1902, Royal Society of London Philosophical Transactions Series A, 199, 1
Jogee S., Barazza F. D., Rix H.-W., et al., 2004, ApJ, 615, L105
Joung M. K. R., Mac Low M.-M., 2006, ApJ, 653, 1266
Jungwiert B., Combes F., Palouš J., 2001, A&A, 376, 85
Kainulainen J., Beuther H., Henning T., et al., 2009, A&A, 508, L35
Karl S. J., Naab T., Johansson P. H., et al., 2010, ApJ, 715, L88
Katz N., 1992, ApJ, 391, 502
Katz N., White S. D. M., 1993, ApJ, 412, 455
Katz N., Quinn T., Gelb J. M., 1993, MNRAS, 265, 689
Katz N., Keres D., Dave R., et al., 2003, in Rosenberg J. L., Putman M. E., editors, The IGM/Galaxy Connection. The Distribution of Baryons at z=0 volume 281 of Astrophysics and Space Science Library, How Do Galaxies Get Their Gas?. page 185
Kauffmann G., White S. D. M., Guiderdoni B., 1993, MNRAS, 264, 201
Kay S. T., Pearce F. R., Frenk C. S., et al., 2002, MNRAS, 330, 113
Kennicutt R. C., Evans N. J., 2012, ARA&A, 50, 531
Kennicutt Jr. R. C., 1989, ApJ, 344, 685
Kennicutt Jr. R. C., 1998, ApJ, 498, 541
Kennicutt Jr. R. C., Calzetti D., Walter F., et al., 2007, ApJ, 671, 333
Kereš D., Katz N., Weinberg D. H., et al., 2005, MNRAS, 363, 2
Kereš D., Katz N., Fardal M., et al., 2009, MNRAS, 395, 160
Kereš D., Vogelsberger M., Sijacki D., et al., 2012, MNRAS, 425, 2027
Kewley L. J., Geller M. J., Barton E. J., 2006, AJ, 131, 2004
Kim C.-G., Kim W.-T., Ostriker E. C., 2011, ApJ, 743, 25
Kim J., Balsara D., Mac Low M.-M., 2001, Journal of Korean Astronomical Society, 34, 333
Kimm T., Slyz A., Devriendt J., et al., 2011, MNRAS, 413, L51
Klessen R. S., 2000, ApJ, 535, 869
Klypin A., Kravtsov A. V., Valenzuela O., et al., 1999, ApJ, 522, 82
Knapen J. H., Shlosman I., Peletier R. F., 2000, ApJ, 529, 93
Konstandin L., Federrath C., Klessen R. S., et al., 2012, Journal of Fluid Mechanics, 692, 183
Kormendy J., 1982, ApJ, 257, 75
Kormendy J., Kennicutt Jr. R. C., 2004, ARA&A, 42, 603
Koyama H., Ostriker E. C., 2009, ApJ, 693, 1346
Kragh H., Smith R. W., 2003, History of Science, 41, 141
Kritsuk A. G., Norman M. L., Padoan P., et al., 2007, ApJ, 665, 416
Kritsuk A. G., Norman M. L., Wagner R., 2011, ApJ, 727, L20
Kroupa P., Theis C., Boily C. M., 2005, A&A, 431, 517
Krumholz M. R., McKee C. F., 2005, ApJ, 630, 250
Krumholz M. R., McKee C. F., Klein R. I., 2004, ApJ, 611, 399
Krumholz M. R., McKee C. F., Tumlinson J., 2009, ApJ, 699, 850
Lada C. J., Lombardi M., Roman-Zuniga C., et al., 2013, ApJ, 778, 133
Laine S., Shlosman I., Knapen J. H., et al., 2002, ApJ, 567, 97
Lamers H. J. G. L. M., Cassinelli J. P., 1999, Introduction to Stellar Winds
Larson R. B., 1974, MNRAS, 169, 229
Larson R. B., Tinsley B. M., Caldwell C. N., 1980, ApJ, 237, 692
Laurikainen E., Salo H., Rautiainen P., 2002, MNRAS, 331, 880

Laurikainen E., Salo H., Buta R., 2004, ApJ, 607, 103
Lecureur A., Hill V., Zoccali M., et al., 2007, A&A, 465, 799
Lee B., Giavalisco M., Williams C. C., et al., 2013, ApJ, 774, 47
Lee G.-H., Park C., Lee M. G., et al., 2012, ApJ, 745, 125
Lemaître G., 1927, Annales de la Societe Scietifique de Bruxelles, 47, 49
Leroy A. K., Walter F., Brinks E., et al., 2008, AJ, 136, 2782
Leroy A. K., Walter F., Bigiel F., et al., 2009, AJ, 137, 4670
Leroy A. K., Walter F., Sandstrom K., et al., 2013, AJ, 146, 19
Li Y., Mac Low M.-M., Klessen R. S., 2006, ApJ, 639, 879
Little B., Carlberg R. G., 1991, MNRAS, 251, 227
Liu G., Koda J., Calzetti D., et al., 2011, ApJ, 735, 63
Lombardi M., Lada C. J., Alves J., 2010, A&A, 512, A67
Lovell M. R., Eke V. R., Frenk C. S., et al., 2011, MNRAS, 413, 3013
Lynden-Bell D., 1976, MNRAS, 174, 695
Lynden-Bell D., Kalnajs A. J., 1972, MNRAS, 157, 1
Mac Low M.-M., Ferrara A., 1999, ApJ, 513, 142
Mac Low M.-M., Klessen R. S., 2004, Reviews of Modern Physics, 76, 125
Machado R. E. G., Athanassoula E., 2010, MNRAS, 406, 2386
Maiolino R., Mannucci F., Cresci G., et al., 2010, The Messenger, 142, 36
Maller A. H., Dekel A., 2002, MNRAS, 335, 487
Mandelbaum R., Seljak U., Kauffmann G., et al., 2006, MNRAS, 368, 715
Martig M., Bournaud F., 2010, ApJ, 714, L275
Martig M., Bournaud F., Teyssier R., et al., 2009, ApJ, 707, 250
Martig M., Bournaud F., Croton D. J., et al., 2012, ApJ, 756, 26
Martin C. L., 2005, ApJ, 621, 227
Martin C. L., Kennicutt Jr. R. C., 2001, ApJ, 555, 301
Martinez-Valpuesta I., Shlosman I., Heller C., 2006, ApJ, 637, 214
Martizzi D., Teyssier R., Moore B., et al., 2012, MNRAS, 422, 3081
Martizzi D., Teyssier R., Moore B., 2013, MNRAS, 432, 1947
Matzner C. D., McKee C. F., 2000, ApJ, 545, 364
McMillan P. J., Dehnen W., 2005, MNRAS, 363, 1205
Melvin T., Masters K., Lintott C., et al., 2014, MNRAS, 438, 2882
Menéndez-Delmestre K., Sheth K., Schinnerer E., et al., 2007, ApJ, 657, 790
Metz M., Kroupa P., Jerjen H., 2007, MNRAS, 374, 1125
Metz M., Kroupa P., Libeskind N. I., 2008, ApJ, 680, 287
Metz M., Kroupa P., Jerjen H., 2009, MNRAS, 394, 2223
Mihos J. C., Hernquist L., 1996, ApJ, 464, 641
Miwa T., Noguchi M., 1998, ApJ, 499, 149
Mo H., van den Bosch F. C., White S., 2010, Galaxy Formation and Evolution
Monaco P., Murante G., Borgani S., et al., 2012, MNRAS, 421, 2485
Moore B., 1994, Nature, 370, 629
Moore B., Katz N., Lake G., et al., 1996, Nature, 379, 613
Moore B., Ghigna S., Governato F., et al., 1999a, ApJ, 524, L19
Moore B., Quinn T., Governato F., et al., 1999b, MNRAS, 310, 1147
More S., van den Bosch F. C., Cacciato M., 2009, MNRAS, 392, 917
Moster B. P., Naab T., White S. D. M., 2013, MNRAS, 428, 3121

Murray N., Quataert E., Thompson T. A., 2005, ApJ, 618, 569
Murray N., Quataert E., Thompson T. A., 2010, ApJ, 709, 191
Narayanan D., Bothwell M., Davé R., 2012, MNRAS, 426, 1178
Navarro J. F., Benz W., 1991, ApJ, 380, 320
Navarro J. F., Steinmetz M., 2000, ApJ, 538, 477
Navarro J. F., White S. D. M., 1993, MNRAS, 265, 271
Navarro J. F., White S. D. M., 1994, MNRAS, 267, 401
Navarro J. F., Eke V. R., Frenk C. S., 1996, MNRAS, 283, L72
Navarro J. F., Frenk C. S., White S. D. M., 1997, ApJ, 490, 493
Navarro J. F., Ludlow A., Springel V., et al., 2010, MNRAS, 402, 21
Negroponte J., White S. D. M., 1983, MNRAS, 205, 1009
Neistein E., van den Bosch F. C., Dekel A., 2006, MNRAS, 372, 933
Nelson D., Vogelsberger M., Genel S., et al., 2013, MNRAS, 429, 3353
Nikolic B., Cullen H., Alexander P., 2004, MNRAS, 355, 874
Noeske K. G., Weiner B. J., Faber S. M., et al., 2007, ApJ, 660, L43
Noguchi M., 1987, MNRAS, 228, 635
Nordlund Å. K., Padoan P., 1999, in Franco J., Carraminana A., editors, Interstellar Turbulence The Density PDFs of Supersonic Random Flows. page 218
Ocvirk P., Pichon C., Teyssier R., 2008, MNRAS, 390, 1326
Ogiya G., Mori M., 2012, ArXiv e-prints
Oh S.-H., de Blok W. J. G., Brinks E., et al., 2011, AJ, 141, 193
Okamoto T., Eke V. R., Frenk C. S., et al., 2005, MNRAS, 363, 1299
Okamoto T., Gao L., Theuns T., 2008, MNRAS, 390, 920
Oppenheimer B. D., Davé R., 2006, MNRAS, 373, 1265
Oppenheimer B. D., Davé R., Kereš D., et al., 2010, MNRAS, 406, 2325
Ostriker J. P., Peebles P. J. E., 1973, ApJ, 186, 467
Padoan P., Nordlund Å., 2011, ApJ, 730, 40
Padoan P., Nordlund A., Jones B. J. T., 1997, MNRAS, 288, 145
Passot T., Vázquez-Semadeni E., 1998, Phys. Rev. E, 58, 4501
Patton D. R., Torrey P., Ellison S. L., et al., 2013, MNRAS, 433, L59
Pawlowski M. S., Pflamm-Altenburg J., Kroupa P., 2012, MNRAS, 423, 1109
Peebles P. J. E., 1969, ApJ, 155, 393
Peng C. Y., Ho L. C., Impey C. D., et al., 2002, AJ, 124, 266
Peng C. Y., Ho L. C., Impey C. D., et al., 2010, AJ, 139, 2097
Pfenniger D., 1991, in Sundelius B., editor, Dynamics of Disc Galaxies Dissolution of a Bar by Merging. page 191
Pfenniger D., Friedli D., 1991, A&A, 252, 75
Pfrommer C., Chang P., Broderick A. E., 2012, ApJ, 752, 24
Piontek F., Steinmetz M., 2011, MNRAS, 410, 2625
Pontzen A., Governato F., 2012, MNRAS, 421, 3464
Powell L. C., Slyz A., Devriendt J., 2011, MNRAS, 414, 3671
Powell L. C., Bournaud F., Chapon D., et al., 2013, MNRAS, 434, 1028
Price D. J., Federrath C., 2010, MNRAS, 406, 1659
Puech M., Hammer F., Flores H., et al., 2010, A&A, 510, A68
Quilis V., Moore B., Bower R., 2000, Science, 288, 1617
Quinn T., Katz N., Efstathiou G., 1996, MNRAS, 278, L49

Quirk W. J., 1972, ApJ, 176, L9
Rahimi A., Kawata D., 2012, MNRAS, 422, 2609
Rahman N., Bolatto A. D., Wong T., et al., 2011, ApJ, 730, 72
Read J. I., Gilmore G., 2005, MNRAS, 356, 107
Reddy B. E., Lambert D. L., Allende Prieto C., 2006, MNRAS, 367, 1329
Rees M. J., Ostriker J. P., 1977, MNRAS, 179, 541
Renaud F., Kraljic K., Bournaud F., 2012, ApJ, 760, L16
Renaud F., Bournaud F., Emsellem E., et al., 2013, MNRAS, 436, 1836
Renaud F., Bournaud F., Kraljic K., et al., 2014, MNRAS, 442, L33
Reynolds J. H., 1920, MNRAS, 80, 746
Robertson B., Yoshida N., Springel V., et al., 2004, ApJ, 606, 32
Robertson B., Bullock J. S., Cox T. J., et al., 2006, ApJ, 645, 986
Robertson B. E., Kravtsov A. V., 2008, ApJ, 680, 1083
Robitaille T. P., Whitney B. A., 2010, ApJ, 710, L11
Rolleston W. R. J., Brown P. J. F., Dufton P. L., et al., 1996, A&A, 315, 95
Rolleston W. R. J., Dufton P. L., McErlean N. D., et al., 1999, A&A, 348, 728
Romano-Díaz E., Shlosman I., Heller C., et al., 2008, ApJ, 687, L13
Roškar R., Teyssier R., Agertz O., et al., 2013, ArXiv e-prints
Rubin K. H. R., Prochaska J. X., Koo D. C., et al., 2010, ApJ, 712, 574
Russell S. C., Dopita M. A., 1992, ApJ, 384, 508
Saintonge A., Tacconi L. J., Fabello S., et al., 2012, ApJ, 758, 73
Salim S., Rich R. M., Charlot S., et al., 2007, ApJS, 173, 267
Salpeter E. E., 1955, ApJ, 121, 161
Sandage A., 1961, The Hubble atlas of galaxies
Sanders D. B., Soifer B. T., Elias J. H., et al., 1988, ApJ, 325, 74
Sargent M. T., Carollo C. M., Lilly S. J., et al., 2007, ApJS, 172, 434
Scalo J., Vazquez-Semadeni E., Chappell D., et al., 1998, ApJ, 504, 835
Scannapieco C., Tissera P. B., White S. D. M., et al., 2006, MNRAS, 371, 1125
Scannapieco C., White S. D. M., Springel V., et al., 2009, MNRAS, 396, 696
Scannapieco C., Wadepuhl M., Parry O. H., et al., 2012, MNRAS, 423, 1726
Schaye J., 2004, ApJ, 609, 667
Schmidt M., 1959, ApJ, 129, 243
Schneider A., Anderhalden D., Macciò A. V., et al., 2014, MNRAS, 441, L6
Schneider N., Csengeri T., Hennemann M., et al., 2012, A&A, 540, L11
Schruba A., Leroy A. K., Walter F., et al., 2010, ApJ, 722, 1699
Schuster K. F., Kramer C., Hitschfeld M., et al., 2007, A&A, 461, 143
Schwarz M. P., 1981, ApJ, 247, 77
Scudder J. M., Ellison S. L., Torrey P., et al., 2012, MNRAS, 426, 549
Sellwood J. A., 1980, A&A, 89, 296
Sellwood J. A., 1981, A&A, 99, 362
Sellwood J. A., 1989, MNRAS, 238, 115
Sellwood J. A., 2008, ApJ, 679, 379
Sérsic J. L., 1963, Boletin de la Asociacion Argentina de Astronomia La Plata Argentina, 6, 41
Seth A. C., Dalcanton J. J., de Jong R. S., 2005, AJ, 130, 1574
Shapley A. E., Steidel C. C., Pettini M., et al., 2003, ApJ, 588, 65
Shectman S. A., Landy S. D., Oemler A., et al., 1996, ApJ, 470, 172

Shen J., Sellwood J. A., 2004, ApJ, 604, 614
Shen J., Abel T., Mo H. J., et al., 2006, ApJ, 645, 783
Shen S., Madau P., Guedes J., et al., 2013, ApJ, 765, 89
Sheth K., Regan M. W., Scoville N. Z., et al., 2003, ApJ, 592, L13
Sheth K., Elmegreen D. M., Elmegreen B. G., et al., 2008, ApJ, 675, 1141
Sheth K., Melbourne J., Elmegreen D. M., et al., 2012, ApJ, 758, 136
Shetty R., Ostriker E. C., 2012, ApJ, 754, 2
Shetty R., Kelly B. C., Bigiel F., 2013, MNRAS, 430, 288
Silk J., 1977, ApJ, 211, 638
Silk J., Norman C., 2009, ApJ, 700, 262
Silk J., Rees M. J., 1998, A&A, 331, L1
Simon J. D., Geha M., 2007, ApJ, 670, 313
Skibba R. A., Engelbracht C. W., Aniano G., et al., 2012, ApJ, 761, 42
Slipher V. M., 1917, Proceedings of the American Philosophical Society, 56, 403
Slyz A. D., Devriendt J. E. G., Bryan G., et al., 2005, MNRAS, 356, 737
Smith B. J., Struck C., Hancock M., et al., 2008, AJ, 135, 2406
Sparre M., Hayward C. C., Springel V., et al., 2014, ArXiv e-prints
Spekkens K., Giovanelli R., Haynes M. P., 2005, AJ, 129, 2119
Springel V., 2005, MNRAS, 364, 1105
Springel V., 2010, MNRAS, 401, 791
Springel V., White S. D. M., Jenkins A., et al., 2005, Nature, 435, 629
Springel V., Frenk C. S., White S. D. M., 2006, Nature, 440, 1137
Stanimirović S., Staveley-Smith L., Jones P. A., 2004, ApJ, 604, 176
Steidel C. C., Erb D. K., Shapley A. E., et al., 2010, ApJ, 717, 289
Stewart K. R., Kaufmann T., Bullock J. S., et al., 2011a, ApJ, 735, L1
Stewart K. R., Kaufmann T., Bullock J. S., et al., 2011b, ApJ, 738, 39
Stinson G., Seth A., Katz N., et al., 2006, MNRAS, 373, 1074
Stinson G. S., Bailin J., Couchman H., et al., 2010, MNRAS, 408, 812
Stinson G. S., Brook C., Macciò A. V., et al., 2013, MNRAS, 428, 129
Struck C., Smith D. C., 1999, ApJ, 527, 673
Swaters R. A., Madore B. F., van den Bosch F. C., et al., 2003, ApJ, 583, 732
Tabor G., Binney J., 1993, MNRAS, 263, 323
Tacconi L. J., Genzel R., Neri R., et al., 2010, Nature, 463, 781
Tacconi L. J., Neri R., Genzel R., et al., 2013, ApJ, 768, 74
Tamburro D., Rix H.-W., Leroy A. K., et al., 2009, AJ, 137, 4424
Tan J. C., 2000, ApJ, 536, 173
Tasker E. J., Bryan G. L., 2008, ApJ, 673, 810
Tegmark M., Blanton M. R., Strauss M. A., et al., 2004, ApJ, 606, 702
Teyssier R., 2002, A&A, 385, 337
Teyssier R., Chapon D., Bournaud F., 2010, ApJ, 720, L149
Teyssier R., Pontzen A., Dubois Y., et al., 2013, MNRAS, 429, 3068
Thacker R. J., Couchman H. M. P., 2000, ApJ, 545, 728
Tollerud E. J., Boylan-Kolchin M., Bullock J. S., 2014, MNRAS, 440, 3511
Toomre A., 1963, ApJ, 138, 385
Toomre A., Toomre J., 1972, ApJ, 178, 623
Tremonti C. A., Moustakas J., Diamond-Stanic A. M., 2007, ApJ, 663, L77

Truelove J. K., Klein R. I., McKee C. F., et al., 1997, ApJ, 489, L179
Vale A., Ostriker J. P., 2004, MNRAS, 353, 189
van de Voort F., Schaye J., Booth C. M., et al., 2011, MNRAS, 414, 2458
van de Voort F., Schaye J., Altay G., et al., 2012, MNRAS, 421, 2809
van den Bergh S., 1960, ApJ, 131, 215
van den Bergh S., 2002, AJ, 124, 782
van den Bosch F. C., Burkert A., Swaters R. A., 2001, MNRAS, 326, 1205
Vázquez-Semadeni E., 1994, ApJ, 423, 681
Vázquez-Semadeni E., Ryu D., Passot T., et al., 2006, ApJ, 643, 245
Veilleux S., Kim D.-C., Sanders D. B., 2002, ApJS, 143, 315
Verley S., Corbelli E., Giovanardi C., et al., 2010, A&A, 510, A64
Vogelsberger M., Genel S., Springel V., et al., 2014, ArXiv e-prints
Wada K., Norman C. A., 2007, ApJ, 660, 276
Wadepuhl M., Springel V., 2011, MNRAS, 410, 1975
Wang Z., Fazio G. G., Ashby M. L. N., et al., 2004, ApJS, 154, 193
Wei L. H., Keto E., Ho L. C., 2012, ApJ, 750, 136
Weil M. L., Eke V. R., Efstathiou G., 1998, MNRAS, 300, 773
Weilbacher P. M., Duc P.-A., Fritze v. Alvensleben U., et al., 2000, A&A, 358, 819
Weinberg M. D., 1985, MNRAS, 213, 451
Weinberg M. D., Katz N., 2002, ApJ, 580, 627
Weinberg M. D., Katz N., 2007, MNRAS, 375, 460
Weiner B. J., Coil A. L., Prochaska J. X., et al., 2009, ApJ, 692, 187
White S. D. M., 1978, MNRAS, 184, 185
White S. D. M., Frenk C. S., 1991, ApJ, 379, 52
White S. D. M., Rees M. J., 1978, MNRAS, 183, 341
Whitmore B. C., Schweizer F., 1995, AJ, 109, 960
Whyte L. F., Abraham R. G., Merrifield M. R., et al., 2002, MNRAS, 336, 1281
Wilke K., Klaas U., Lemke D., et al., 2004, A&A, 414, 69
Wong T., Blitz L., 2002, ApJ, 569, 157
Woods R. M., Wadsley J., Couchman H. M. P., et al., 2014, MNRAS, 442, 732
Yang Y., Flores H., Hammer F., et al., 2008, A&A, 477, 789
Yoachim P., Dalcanton J. J., 2006, AJ, 131, 226
Zentner A. R., Kravtsov A. V., Gnedin O. Y., et al., 2005, ApJ, 629, 219
Zoccali M., Lecureur A., Barbuy B., et al., 2007, in Vazdekis A., Peletier R., editors, IAU Symposium volume 241 of IAU Symposium, Abundances in the Galactic Bulge: evidence for fast chemical enrichment. pages 73–77